Studies of Alloy Nanoclusters and Their Influence on Growth of Carbon Nanotubes

A thesis submitted in partial fulfillment of the requirement for the Degree of

Doctor of Philosophy in Physics

at the
University of Canterbury

by

Domagoj Belić

Department of Physics and Astronomy

2012

Abstract

With the many advances and astonishing breakthroughs that have recently happened, nanotechnology has become one of the most promising fields of physical sciences, showing a great potential for various applications that may soon change our everyday life. As a part of this growing discipline, nanocluster science has positioned itself at the forefront. In particular, alloy nanoclusters are especially interesting due to numerous combinations of sizes and compositions that give rise to a plethora of different properties.

In this work we examine $Ag_{0.85}Au_{0.15}$ and $Ni_{0.85}Cu_{0.15}$ nanoclusters: their structural, compositional, and morphological characteristics are investigated in detail. These clusters are produced by the inert gas aggregation (IGA) method from magnetron sputtered alloy targets, in an UHV compatible system. The design of the system is optimized for production and deposition of the clusters with size in the range 5 nm $< D <$ 10 nm. In order to increase the flux of sub-5 nm clusters in the system, we conducted modeling and experimental studies of cluster motion: the simulations showed that skimmers with wider internal angles might significantly improve the flux of smaller nanoclusters; however, the experimental study revealed a major influence of the background gas on scattering of such nanoclusters which consequently led to the loss of their flux.

A comprehensive study of $Ag_{0.85}Au_{0.15}$ nanoclusters was conducted over a period of more than 2 years. Nanoclusters with sizes in the range 3 nm $< D <$ 10 nm were deposited onto a-C films at various surface coverages and systematically investigated by transmission electron microscopy. We found that $Ag_{0.85}Au_{0.15}$ nanoclusters initially exhibited icosahedral and decahedral structural motifs, with a very small fraction of face centered cubic nanoclusters present. This may suggest that the source conditions used in the experiments (primarily Ar flow) left $Ag_{0.85}Au_{0.15}$ nanoclusters kinetically trapped in structures which correspond to local thermodynamic minima, rather than global energetically favoured atomic configurations.

When left exposed to ambient conditions, over time $Ag_{0.85}Au_{0.15}$ nanoclusters exhibited structural, morphological, and compositional changes: core-shell and Janus nanoclusters were observed in aged samples, as well as fragmentation of bigger par-

ticles. We attribute these changes to oxidation of the Ag component and increased diffusion of Ag_2O over the substrates. The final morphology of aged nanocluster-based thin films is governed by a combination of diffusion, Ostwald ripening, and the Plateau-Rayleigh instability.

High resolution transmission electron microscopy confirmed the presence of five-fold symmetric structures in $Ni_{0.85}Cu_{0.15}$ nanoclusters; however, their higher oxidation rate may have influenced the structures from the outset. In addition, when these nanoclusters were exposed to the electron beam, crystalline artifacts (nanochimneys) started to grown on them, with a structure corresponding to the NiO structure. $Ni_{0.85}Cu_{0.15}$ nanoclusters are subsequently used as catalysts in a pilot study of carbon nanotube synthesis which confirmed that such alloy nanoclusters are catalytically active for single wall and multi wall carbon nanotube growth.

Contents

List of Figures

List of Tables

Parts of the thesis contain results that originate from very successful collaborations with other researchers:

- Chapter 3 contains results of Monte Carlo simulations that were fully performed by P. A. Skovorodko from the Institute of Thermophysics, Novosibirsk, Russia
- Chapter 4 contains HR-STEM and HAADF images obtained by R.L. Chantry and Z. Li at the University of Birmingham, UK
- Chapter 5 contains results of thermal CVD growth of multi wall carbon nanotubes conducted by J. Ke and V. Golovko from the Department of Chemistry, University of Canterbury, Christchurch, New Zealand. In addition, CVD syntheses of single wall carbon nanotubes, as well as their SEM and Raman characterization were carried out by K. Edgar from the School of Chemical and Physical Sciences, Victoria University of Wellington, New Zealand

Parts of the thesis have been published or are being prepared for publications:

- Belić, D., Chantry, R.L., Li, Z.Y., Brown, S.A. (2011) "Ag-Au Nanoclusters: Structure and Phase Segregation", *Applied Physics Letters* **99**, 171914; doi: 10.1063/1.3656244
- Skovorodko, P.A., Brown, S.A., Belić, D. (2011) "Gas Dynamic Considerations for Performance of Nanocluster Deposition System", *AIP Conference Proceedings* **1333**, 203-208. doi: 10.1063/1.3562649
- Belić, D., Chantry, R.L., Li, Z.Y., Brown, S.A. (2012) "Ag-Au Nanoclusters: Evolution of Structures and Phases", *in preparation*
- Belić, D., Edgar, K., Ingham, B., Brown, S.A. (2012) "Induced Growth of NiO Nanorods on Ni-Cu Nanoclusters", *in preparation*

Chapter 1

Introduction

Nanoscale physics means huge differences. Nanoscale physics means great excitement. Nanoscale physics means endless possibilities. There is nothing small about nanoscale physics. In this thesis we will reveal new insights into alloy nanoclusters – a tiny portion of a vast, booming field of physical sciences – nanotechnology.

Nanotechnology deals with manipulation of matter on the nanoscale i.e. with objects whose dimensions are comparable to the distance of 1 nm: atoms, molecules, and atomic clusters. In systems of such small dimensions rules common to macroscopic systems fail; instead one needs to apply a new set of laws – quantum physics, which in turn gives birth to many extraordinary phenomena only seen on the nanoscale. Moreover, various nanoscale systems whose only point of difference is their size may exhibit very different characteristics. This brings us to the situation where by appropriately designing a nanosystem, one could tailor its properties, which could then be used in specific applications.

This study goes in the same direction – we tried to reveal structural, morphological and compositional properties of alloy nanoclusters that may be correlated to their size. In addition, in the second part of the study we attempted to exploit some of these properties of alloy nanoclusters for tailored growth of carbon nanotubes.

1.1 Nanoclusters

As suggested by the name, nanoclusters are aggregates of atoms whose size is less than 100 nm, i.e. they are comprised of 2 to $\sim 10^7$ atoms. Such small systems are very interesting because they have properties that are very different to those of their bulk counterparts. For instance, the melting temperature of nanoclusters is significantly lower than the melting temperature of bulk metals[1]. Consequently, well established bulk phase diagrams need to be reassessed for nanoscale systems.

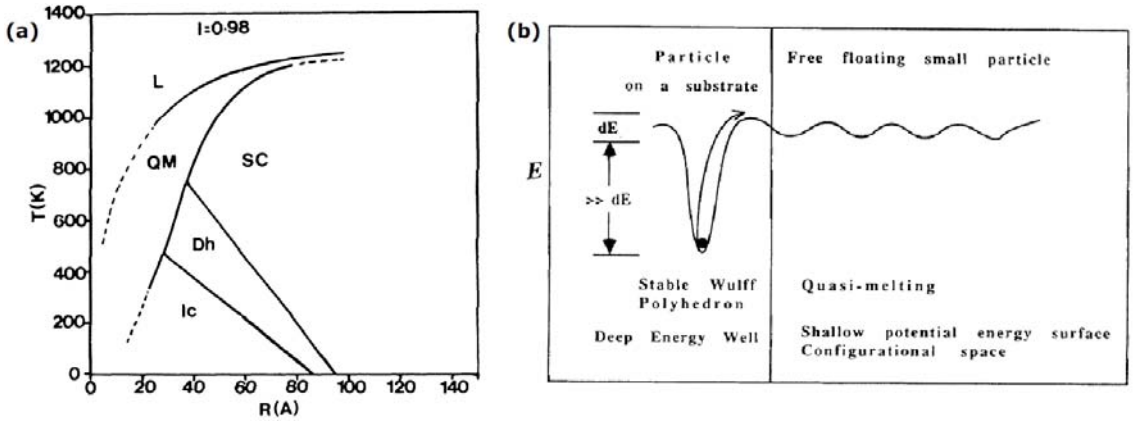

Figure 1.1: (a) Proposed nanoscale phase diagram for small Au particles.[5] (b) Schematics explaining behaviour of small Au particles: there exist a deep well i.e. global energy minimum which corresponds to a stable structure; however, if the particle is not in the global minimum, its structure may fluctuate between shallow local minima.[6]

Similarly, the structure of nanoclusters may differ from the structure of bulk metals, since the boundary conditions affect more atoms. For example, Ino[2] and Ino and Ogawa[3] demonstrated that Au atoms form nanosized multiply-twinned particles (MTP) – decahedra (Dh) and icosahedra (Ih), comprised of 5 and 20 face centered cubic (FCC) tetrahedra (Th), respectively; similar objects were later seen in the case of Ag[4]. Ajayan and Marks[5,6] expanded this investigation on sub-10 nm clusters and proposed a general nanoscale structural phase diagram (see Fig. 1.1) which suggested that fivefold symmetric structures are favoured for such small clusters at room temperature. More recently, Doye and Calvo[7] developed a structural phase diagram for the case of Ag (see Fig. 1.2) which also suggests that Ih and Dh structures should dominate for clusters smaller than ∼11 nm.

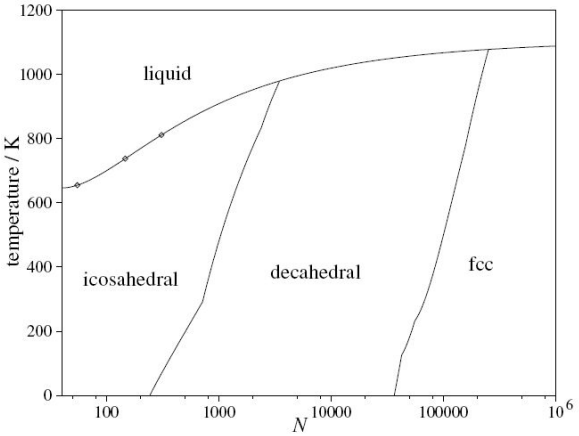

Figure 1.2: Structural phase diagram for Ag nanoclusters containing N atoms.[7]

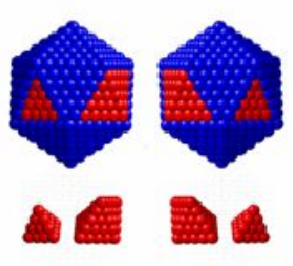

Figure 1.3: Illustration of chiral alloy icosahedral nanoclusters with phase segregated components. Credits: Shaun Hendy, IRL, Lower Hutt, New Zealand

1.2 Alloy Nanoclusters

In the previous section we focused on size-dependent structural characteristics of nanoclusters. If one considers alloy nanoclusters containing 2 or more metals, in addition to size effects, one needs to take into account effects of composition on nanocluster properties. For instance, due to the presence of various atomic species with different thermodynamic properties (such as surface energy), alloy nanoclusters might exhibit a tendency to form core-shell structures.

Ih nanoclusters are comprised of 20 basic building blocks – FCC tetrahedra, so that, since such an atomic configuration is not space-filling, internal strain is inherent in these nanoclusters. In order to relieve some of that strain and consequently lower its potential energy, an alloy nanosystem may prefer to phase-segregate. For example, if the nanosystem is an icosahedron with a composition of 85:15 at.%, possible phase segregation might result in formation of 3 tetrahedra of the minor component, surrounded by 17 tetrahedra of the major component, as illustrated in Fig. 1.3. Note that such nanoclusters would posses intrinsic chirality arising from the ordering of their basic Th building blocks.

In this thesis we focus on two alloys – $Ag_{0.85}Au_{0.15}$ and $Ni_{0.85}Cu_{0.15}$. The latter system looks very interesting from the point of view of chirality. Namely, since Ni is commonly used as nanocatalyst in carbon nanotube (CNT) synthesis[8–10], it would be advantageous to exploit possible $Ni_{0.85}Cu_{0.15}$ nanocluster chirality for selective production of chiral single wall carbon nanotubes (SWCNTs) by affecting how a graphene sheet that makes up the tube is rolled (see Fig. 1.4). As a consequence, this will determine whether the grown CNTs are preferentially metallic or semiconducting[11], which looks very appealing from the point of view of applications.

Alloy nanoclusters studied in this work were produced by inert gas aggregation (IGA) of magnetron-sputtered atoms from alloy targets. In order to examine their structural and compositional properties by *ex-situ* characterization techniques, nan-

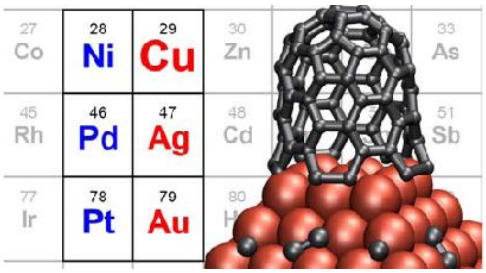

Figure 1.4: Illustration of CNT growth over a chiral alloy nanocluster, indicating that the CNT structure may be tailored by nanocluster chirality.[12]

oclusters were deposited onto substrates and exposed to air. In those conditions nanoclusters are likely to experience compositional modifications, as well as possible diffusion over the surface of the support and hence exhibit time dependent morphology changes. For that reason in the next sections we outline a few topics relevant to behaviour of nanoclusters deposited onto substrates.

1.3 Diffusion on Surfaces

As previously stated, in this work we investigated nanoclusters deposited onto substrates. For the purpose of transmission electron microscopy (TEM) investigations, amorphous carbon (a-C) films were used as a support for nanoclusters. Although relatively rough, a-C substrates are nevertheless smooth enough to allow a slow surface diffusion of material, which over time may change the morphology of the sample[13–15]. For example, Werner et al.[16] showed that the interaction of Au nanoclusters with a-C surfaces (placed in the x-y plane) could be described by a modified Lennard-Jones potential of the following form:

$$V_{L-J}(z) = V_0 \left(\frac{297}{(z/r_0 - 1.2)^{12}} - \frac{34.5}{(z/r_0 - 1.2)^6} \right) \tag{1.1}$$

where z is the distance from the nanocluster to the a-C plane, $V_0 = 0.3$ eV and $r_0 = 2.885$ Å. Their molecular dynamics (MD) modeling showed aggregation of Au nanoclusters on a-C films over time, as well as formation of thin islands and restructuring of initial Ih clusters (see Fig. 1.5). Based on these reports, one might expect similar behaviour for alloy nanoclusters deposited onto a-C. In Chapter 4 we present evidence which indicate that surface diffusion played an important role in morphological changes that happened in $Ag_{0.85}Au_{0.15}$ nanocluster-based thin films deposited onto a-C.

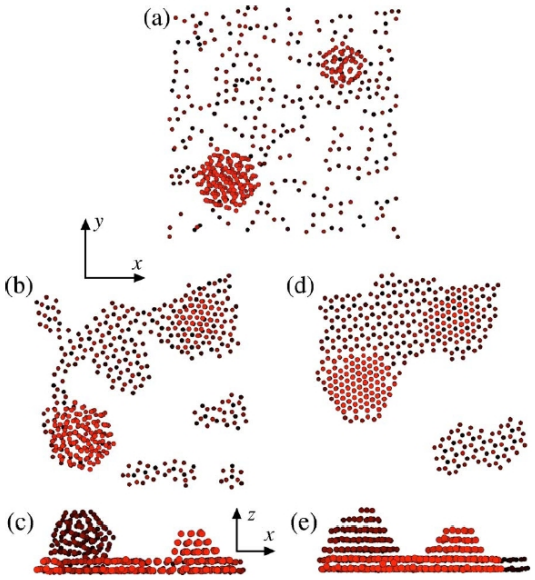

Figure 1.5: MD simulation results for diffusion of Au nanoclusters and atoms on a-C substrate: (a) initially there were 298 Au atoms, and two nanoclusters containing 55 and 147 atoms; (b) system configuration after 60 000 MC steps; (c) configuration after 1 180 000 MC steps. Images (d) and (e) show side views of configurations presented in (b) and (c), respectively. [16]

1.4 Ostwald Ripening

Another phenomenon common to ensembles of particles of various sizes is Ostwald ripening (OR). From the point of view of energetics, for a given amount of material, a system containing larger particles is favoured over a system with smaller particles, since it inevitably leads to minimization of energy. In other words, there exists a natural tendency for each system to maximize the number of bigger particles at the expense of smaller ones, as illustrated in Fig. 1.6. The classical Lifshitz, Slyozov, and Wagner (LSW) theory of OR[17,18] states that, for the case of slow diffusion, average radius of particles in the ensemble grows in time according to the following relation:

$$\langle r \rangle^3 = \frac{8\gamma s_\infty D v^2}{9RT} t \tag{1.2}$$

where $\langle r \rangle$ is average radius of particles, γ is its surface tension, s_∞ is solubility of the particle material, D is diffusion coefficient of the particle material, and v is molar volume of the particle material. In a case where the growth is limited by the attachment and detachment rates of material, instead of equation 1.2 the following

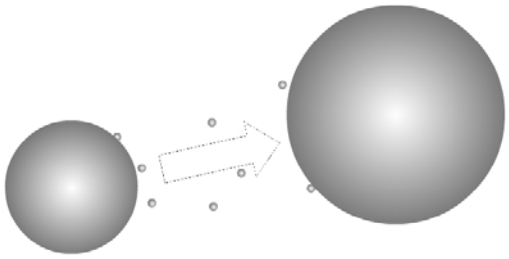

Figure 1.6: Illustration of particle growth through Ostwald ripening.

relation holds:

$$\langle r \rangle^2 = \frac{64\gamma s_\infty K v^2}{81RT} t \tag{1.3}$$

where K is rate constant of attachments of material.

For this reason one might expect coarsening of the size distribution of particles in a sample over time. Although above mentioned equations are derived for the case of particles in a liquid solution, qualitatively very similar reasoning may apply in the case of ensembles of particles deposited onto surfaces, such as a-C.

1.5 Plateau-Rayleigh Instability

For a given amount of material, the smallest surface to volume ratio is attained for spherical shape. Translated into the standpoint of thermodynamics, since every surface has associated energy, the system will tend minimize its energy by adopting a shape more similar to a sphere. In 1871. Plateau experimentally investigated the behaviour of a continuous stream of falling liquid and realized that the initially cylindric stream was susceptible to breaking into droplets when the wavelength λ of the perturbation of its radius R_0 was greater than its circumference. Lord Rayleigh gave the first theoretical explanation of this phenomenon that was later named Plateau-Rayleigh instability.

The above reasoning can also be applied in the case of solid cylinders[19] of initial radius exhibiting sinusoidal perturbation of the following form:

$$r = R_0 + \delta sin(2\pi x) \tag{1.4}$$

Over time perturbations with wavelength $\lambda > 2\pi R_0$ will prevail so that the cylinder eventually splits into spheres of diameter $d = 3.78R_0$ with the average distances between them $\lambda_m = 8.89R_0$, $9.02R_0$, and $12.96R_0$, for various mechanisms of mass

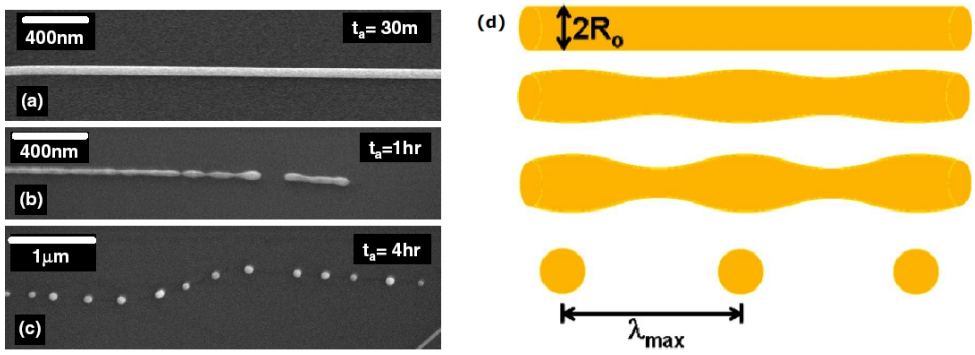

Figure 1.7: SEM images showing fragmentation of Au nanowire annealed at 500 °C, in a process similar to Plateau-Rayleigh instability: (a) $t = 0.5$ hour; (b) $t = 1$ hour: (c) $t = 4$ hours. Illustration of the process is shown in (d).[20]

transport: surface diffusion, internal volume diffusion, and external volume diffusion, respectively.

As an example relevant to our case of nanocluster-based thin films, it is worth mentioning a study of Karim et al.[20] who investigated the instability of Au nanowires subjected to annealing. They demonstrated (see Fig. 1.7) that the nanowires became unstable at the temperatures *far below the melting point* of bulk Au, exhibiting behaviour very similar to the Plateau-Rayleigh instability.

1.6 Thesis Outline

This thesis is focused on transmission electron microscopy (TEM) investigations of $Ag_{0.85}Au_{0.15}$ and $Ni_{0.85}Cu_{0.15}$ nanoclusters and nanocluster-based thin films. In total over 250 samples suitable for TEM imaging were deposited during the course of the study, as well as over 100 samples that were used in CNT growth experiments.

Chapter 2 describes the UHV-compatible inert gas aggregation (IGA) magnetron sputtering system used for production of alloy nanoclusters. In the first part of the chapter, basic working principles of the IGA system are explained more in detail, as well as its design, with the emphasis on the nozzle-skimmer configuration. The second part of the chapter contains results of nanocluster size distribution measurements for various source conditions, for Sn, Ag, $Ag_{0.85}Au_{0.15}$, and $Ni_{0.85}Cu_{0.15}$ sputter targets used in these experiments. At the end of this chapter we give some information about the main characterization techniques used in our study.

Chapter 3 gives results of the nanocluster velocity study: firstly, we present findings of numerical simulations of nanocluster motion inside the system during their deposition, which are then followed by an experimental investigation of cluster velocities, when skimmers with wider internal angles were used in the system. These

measurements were performed for various source conditions and nanocluster sizes in order to optimize the flux of sub-5 nm clusters to the deposition chamber.

Chapter 4 is the key chapter of this thesis – it outlines the most important results of a comprehensive study of $Ag_{0.85}Au_{0.15}$ nanoclusters and nanocluster-based thin films. Bright field high resolution transmission electron microscopy (HRTEM), high-angle annual dark field scanning transmission electron microscopy (HAADF STEM), and energy-dispersive X-ray spectroscopy (EDX) were utilized in order to investigate samples over longer periods, with the emphasis on their structural, morphological, and compositional properties. The collected information are analyzed in detail and a model is proposed for the observed phenomena.

Chapter 5 comprises results of the study of $Ni_{0.85}Cu_{0.15}$ nanoclusters, in a similar fashion given in chapter 4 for $Ag_{0.85}Au_{0.15}$ nanoclusters. The second part of this chapter is devoted to a preliminary investigation of single wall and double wall carbon nanotube (SWCNT and MWCNT) growth by catalytic chemical vapour deposition (CVD), in which $Ni_{0.85}Cu_{0.15}$ nanoclusters are used as catalysts. The CNT samples were extensively investigated by means of scanning electron microscopy (SEM). The focus here was on the optimization of CNT growth experimental conditions so that future studies might benefit from our initial findings.

Chapter 6 summarizes the main results of the studies of alloy nanoclusters and CNTs presented throughout this thesis. It also gives an outlook for future work on these topics within the Nanocluster group at the University of Canterbury.

Chapter 2

Experimental Methods

Principles of operation of the inert gas aggregation (IGA) magnetron sputtering system are presented in this chapter. We utilized the system to produce monometallic and alloy bimetallic nanoclusters in the size range 3–15 nm and to conduct a systematic *in-situ* mass spectrometry investigation of the influence of various experimental parameters (aggregation length, Ar flow rate, He dilution fraction, plasma generator power) on the cluster size distribution, for the case of Sn, Ag, $Ag_{0.85}Au_{0.15}$, $Ni_{0.85}Cu_{0.15}$ sputter targets. Later on these findings proved valuable for the optimized and straightforward production of clusters for subsequent *ex-situ* SEM and TEM characterization.

2.1 IGA Magnetron Sputtering System

Over the last decade an ultra high vacuum (UHV) compatible magnetron sputtering system (see Fig. 2.1) had been built at the University of Canterbury and utilized for the production of monometallic (Bi, Sb, Sn, Pb, Cu) nanoclusters by our group members[21–27]. A brief overview of the system is given here; for more detailed description see Ayesh[28] and Reichel[29] whose work on the system development is very much appreciated. The IGA magnetron sputtering system consists of four chambers (see Fig. 2.2) where a differential pumping is applied with the intention to create a pressure gradient needed for the successful production and deposition of clusters.

2.1.1 Source Chamber (1)

The source chamber is the core part of the system where cluster formation takes place (see Fig. 2.2). We employed a process generally known as sputtering: an alloy sputter target of 2" in diameter and 0.25" in thickness (see Fig. 2.3) is mounted on a movable holder (A) and a continuous flow of inert gas – Ar (or a mixture of Ar

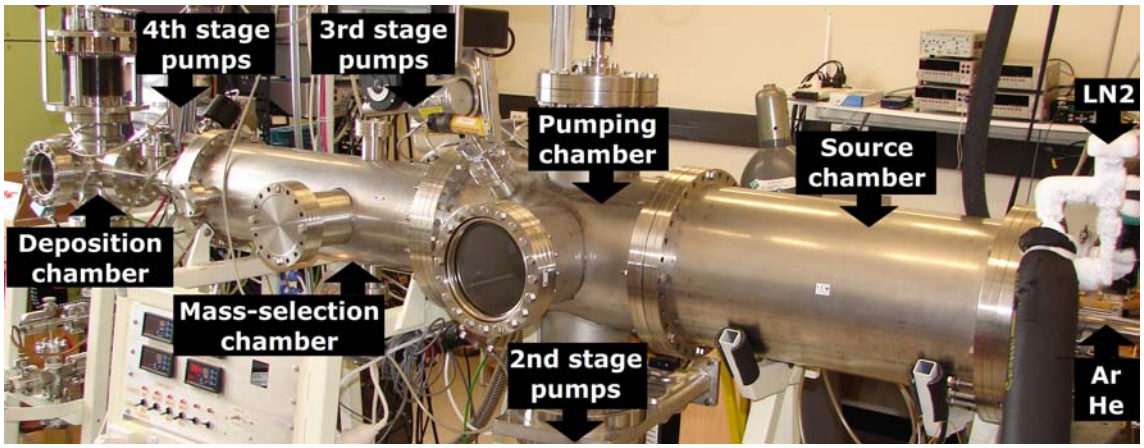

Figure 2.1: Photo of the inert gas aggregation (IGA) ultra high vacuum (UHV) compatible magnetron sputtering system used for the production of nanoclusters in our study.

and He) – is passed into the chamber between the target and a circular electrode. A magnet is placed just behind the sputter target so that, when DC voltage is applied between the alloy target and the electrode (the target is kept at a negative potential relative to the electrode placed ∼2 mm away), Ar plasma is created and Ar^+ ions start to accelerate in the electromagnetic field towards the target in a helical motion, hitting it with enough energy to eject some of the surface atoms into the chamber. During this process the sputter target heats up, so, in order to prevent melting, a water flow (room temperature) is used for cooling of the backside of the target.

When the atmosphere in the chamber gets supersaturated with metal atoms, homogeneous nucleation of clusters begins. This process can be described from the energetic point of view by considering the change of free Gibbs energy ΔG during

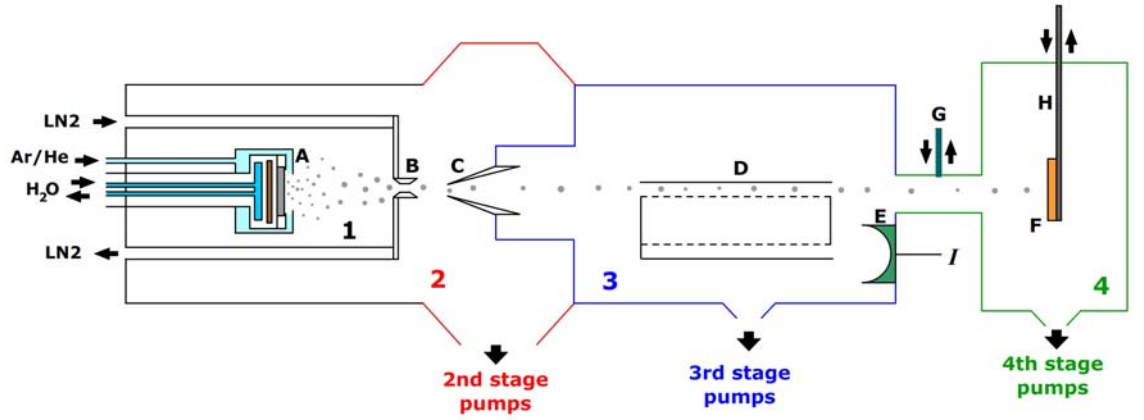

Figure 2.2: Schematics of the IGA magnetron sputtering system: 1 – source chamber; 2 – pumping chamber; 3 – mass-selection chamber; 4 – deposition chamber; A – sputter target holder; B – nozzle; C – skimmer; D – mass filter; E – Faraday cup, F – substrate; H – sample holder; G – gate valve.

Figure 2.3: $Ag_{0.85}Au_{0.15}$ sputter target used in our experiments, seen here mounted on the target holder that had been extruded from the cryostat for the target to be replaced.

the nucleation of clusters from the vapor phase:

$$\Delta G = 4\pi r^2\gamma - \frac{4}{3}r^3 cRTln(S) \tag{2.1}$$

In this relation r is radius of the created cluster, γ is its surface energy, c is the number of atoms enclosed in the cluster volume, R is gas constant, T is temperature of the vapour, and S is the saturation ratio i.e. the ratio between actual vapour pressure in the chamber and saturated pressure (at given temperature T). The first term in equation 2.1 corresponds to the increase of energy due to the formation of a cluster surface, while the second term refers to the decrease of energy when atoms precipitate from the vapor into the cluster of radius r. In order to have a preferential cluster growth (ΔG < 0), two conditions need to be satisfied:

1. $S > 1$ i.e. one needs to supersaturate the source chamber atmosphere with metal atoms

2. $r > \frac{2\gamma}{cRTln(S)}$ i.e. clusters need to be bigger than some critical radius

In reality this means we need to have a sufficient ejection rate of metal atoms from the surface of the sputter target in order to saturate the source chamber atmosphere with metal atoms. In addition, it is necessary to lower the temperature of the vapour in order to enhance the cluster nucleation rate. Therefore, our source chamber was designed as a liquid nitrogen cryostat.

Due to a difference between the source chamber (labeled 1 in Fig. 2.2) pressure ($p \sim 1$ Torr) and the pumping chamber (2 in Fig. 2.2) pressure ($p \sim 10^{-2}$ Torr), clusters will be carried away by the continuous inert gas flow through the nozzle (B). The size distribution of the clusters formed in the source chamber will depend upon several experimental parameters:

- Aggregation length (distance $|\overline{AB}|$ between the sputter target and the nozzle)
- Inert gas flow rate
- Inert gas mixture composition (ratio of Ar/He flow rates)
- Plasma generator power

We performed a detailed experimental study of the influence of these parameters on the size distribution of various monometallic and bimetallic clusters produced in the IGA magnetron sputtering system, with the results presented in § 2.3.

2.1.2 Pumping Chamber (2)

As mentioned earlier, a pressure gradient between the entrance and exit sections of the nozzle (see Fig. 2.4) is maintained by continuous pumping of the chamber surrounding the source chamber. In this space most of the inert gas is taken out of the system while clusters, being accelerated by the gas flow in the nozzle throat, gain momentum high enough to make them reach the skimmer located at a distance $L \lesssim 9$ mm downstream the nozzle (see Fig. 2.5) without being significantly deflected from their initial direction of motion at the nozzle exit. Geometrical properties of these two apertures define the cluster beam formed in the system. The choice of the nozzle-skimmer configuration shown in Fig. 2.5 is a result of the previous optimization of the system for a successful deposition of clusters ranging 5–10 nm in diameter[22,23].

The skimmer orifice represents the only connection between the pumping chamber and the mass-selection chamber (see Fig. 2.2). It is worthwhile saying that by changing the skimmer geometry and/or nozzle-skimmer distance L one can considerably affect the characteristics of the cluster beam, as well as the amount of inert gas which is transferred to the mass-selection chamber. Consequently, this will have a major effect on the mass-selection chamber pressure which, in turn, may significantly influence the cluster trajectory in that section of the system, in addition to the influence on the cluster velocity.

In order to investigate the influence of the skimmer geometry and the nozzle-skimmer distance on the cluster beam characteristics, we designed and tested new skimmers (see Fig. 2.6) with greater internal/external angles than the old one (presented in Fig. 2.4) whose geometry was optimized for high throughput of 5–10 nm clusters. By introducing these new wider skimmers one of the goals was to increase the flux of sub-5 nm clusters through the system. Both numerical and experimental studies were performed for the case of $Ag_{0.85}Au_{0.15}$ clusters; the results of that investigation are presented in the next chapter.

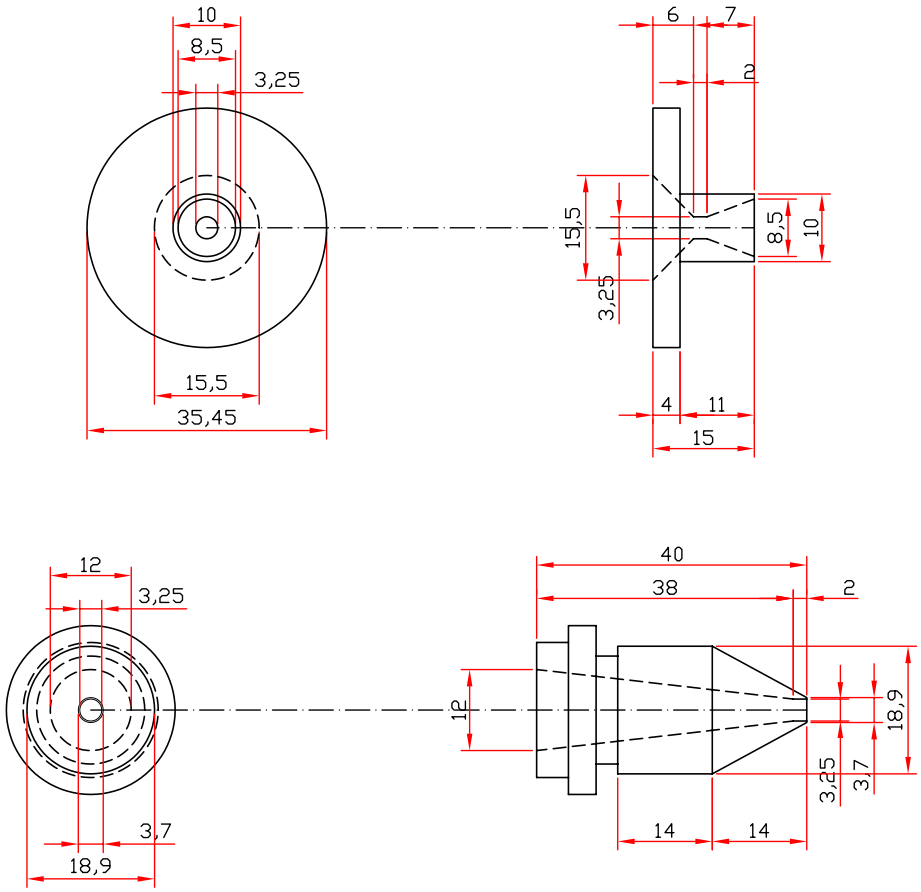

Figure 2.4: AutoCAD blueprints of the nozzle and original skimmer used in our experimental system. Values are given in millimeters. Based on this data, the internal and external angle of this skimmer were found to be 7.1°and 28.5°, hence the notation 7/30 skimmer.

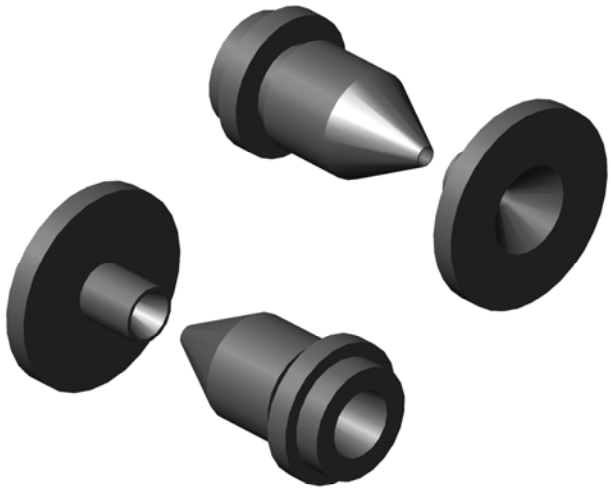

Figure 2.5: AutoCAD Sketch of the nozzle and 7/30 skimmer configuration standardly used in our experimental system. The nozzle-skimmer distance is set to $L = 9$ mm, but it could be shortened down to 5 mm. This configuration allows for the high throughput of the cluster in the size range 5–10 nm.

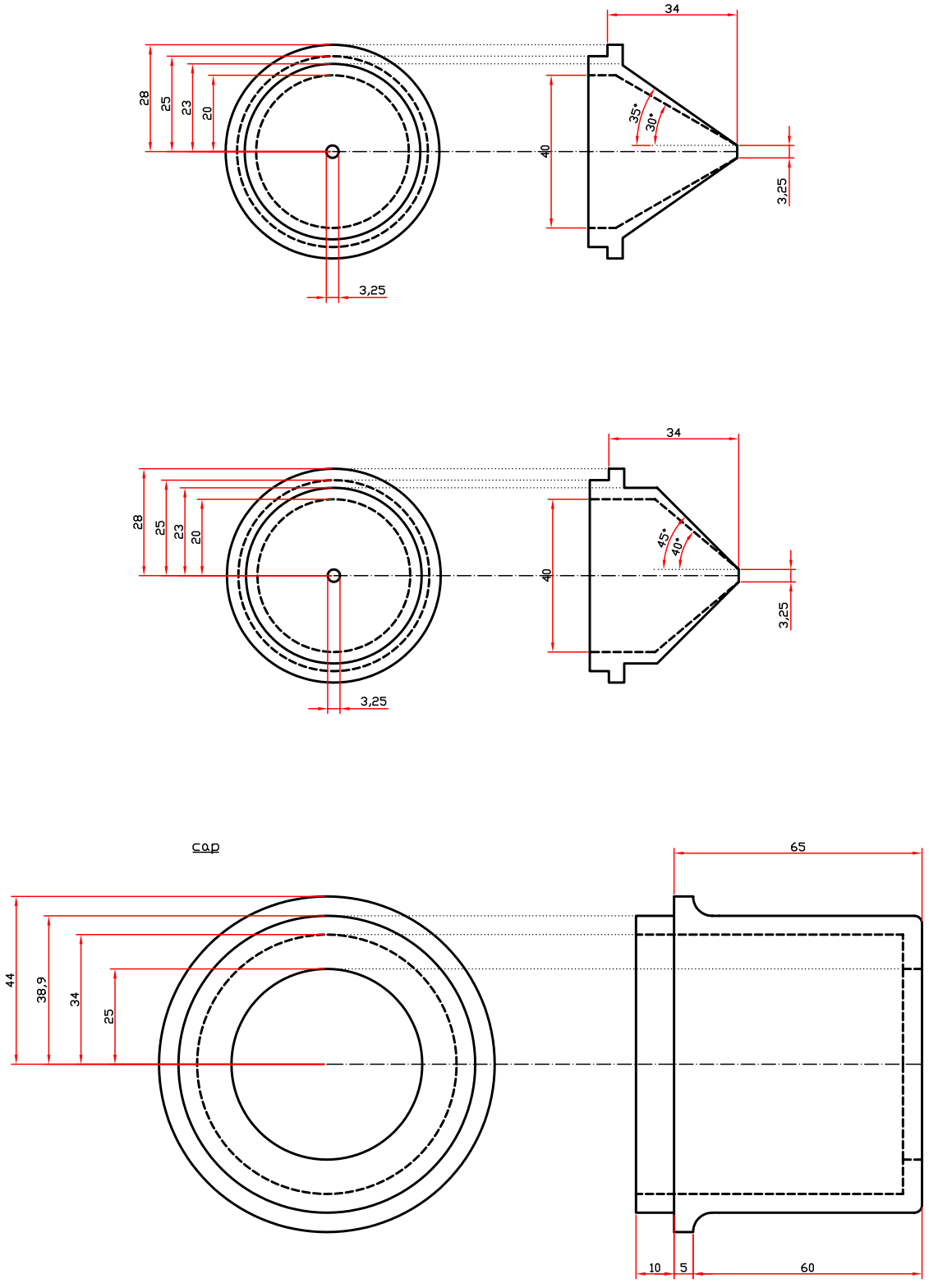

Figure 2.6: AutoCAD blueprints of the 30/35 (top) and 40/45 skimmers (middle) used in our experimental system. (bottom) A new skimmer holder of a bigger diameter had to be machined to support the new skimmers with greater internal/external angles. All values are in millimeters.

2.1.3 Mass-selection Chamber (3)

Having passed the skimmer (labeled C in Fig. 2.2) clusters now enter the third stage of the IGA magnetron sputtering system – mass-selection chamber. The chamber was named after a mass filter (D) installed in its interior which can be used for mass (size) selection of clusters. In addition to that, it regularly serves as a probe for determination of the size distribution of clusters in the beam (e.g. see § 2.3). A detailed overview of the mass filter's operational principles and its performance can be found elsewhere[21,23,30]; here we present a brief description of it.

A mass filter of this type was initially designed and built by von Issendorff and Palmer[30]. It consists of four parallel metallic plates, aligned with the cluster beam (see Fig. 2.7). The beam is allowed to enter the filter between the two lower plates; these plates are connected to an external voltage pulse generator that applies a short voltage pulse U_a between the plates 1 and 2, thus creating an electric field which then deflects charged clusters from their beam centerline trajectory toward the upper plate. This plate is designed in such a way that it has a narrow long opening parallel to the cluster beam so that the deflected clusters can pass into the electric-field-free interior of the mass filter (between plates 2 and 3) and continue to move without being disturbed. Clusters then go through a corresponding opening in the third plate to reach the space between plates 3 and 4 where again a voltage

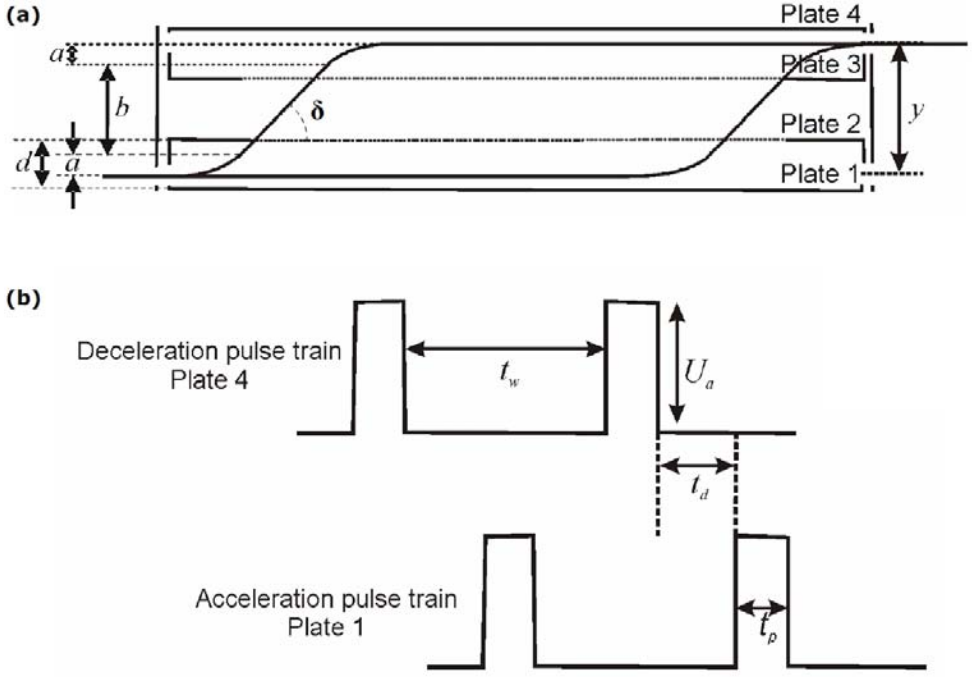

Figure 2.7: (a) Schematics of the mass filter used in our IGA system. (b) Timing of the voltage pulses applied to plates 1 and 4. Adapted from Ayesh[28].

pulse is applied to the plate 4. This pulse has the same size and length as the initial pulse between plates 1 and 2 and cancels out the lateral velocity that cluster gained from the first pulse. Consequently, the clusters retain only their axial velocity which allows them to exit the mass filter parallel to the original beam. These clusters then reach a Faraday cup (labeled E in Fig. 2.2) placed opposite the mass filter exit, where they contribute to the signal I measured by a Keithley picoammeter.

In order to select clusters of a certain mass m, one needs to set the proper values of the applied voltage U_a, duration of the pulse t_p, and delay time t_d between the pulses according to the following relations:

$$t_p = \frac{2a}{\sqrt{2E_p/m}} \tag{2.2}$$

$$t_d = \frac{b}{\sqrt{2E_p/m}} \tag{2.3}$$

where E_p is the energy that the clusters of charge e gain during the initial pulse that equals $E_p = \frac{a}{d}eU_a$. Here a represents the lateral distance that the clusters travel during the initial accelerating pulse, d is the separation between the plates 1 and 2, $b = y - 2a$ where y is the lateral distance between the slits of the mass filter (see Fig. 2.7). Note that a is also mass-dependent according to the following:

$$a = \frac{1}{2}m{v_0}^2\frac{d}{eU_a}tan^2\delta \tag{2.4}$$

where v_0 is the clusters' axial velocity and δ is the deflection angle.

In reality, a LabVIEW program is used to set the right pulses for clusters of a certain mass, when the values v_0, U_a, and δ are given. Through previous experiments[23,28] it was found that the following values should be used for the best performance of the mass filter: $v_0 = 210$ m/s, $U_a = 1400$ V, and $\delta = 45°$.

Since it is more convenient to use cluster size than mass (e.g. later on the size distribution can be checked by TEM imaging), the LabVIEW program calculates the cluster diameter according to:

$$D = \sqrt[3]{\frac{6}{\pi}\frac{m}{\rho_{eff}}} \tag{2.5}$$

where ρ_{eff} is the cluster effective density that is evaluated from the alloy composition (e.g. $\rho_{eff}(Ag_{0.85}Au_{0.15}) = 12.82$ g/cm^3). Here one needs to assume that all clusters in the beam have the same composition and that bulk density values still hold for clusters with $D > 3$ nm.

The measured signal I has to be additionally corrected to account for the mass filter resolution ($m/\Delta m = 6$). For that reason one needs to divide the signal I with mass m or more practical with D^3 to get the true cluster size distribution.

Note that *only charged clusters* can be mass selected. As a rule of thumb, one can expect that one third of the clusters from the beam are negatively charged, the other third are positively charged, and the rest are neutral clusters which are not affected by the mass filter operation.

From a practical point of view, two important consequences of the mass filtering (i.e. size selection) are immediately evident:

1. The flux of size-selected clusters is only a fraction of the flux of non size-selected clusters. Since it can take several minutes to deposit a typical non size-selected sample, the decrease in the cluster flux means that it may take several hours to deposit a sample of size-selected clusters, even in the case of samples with a very low surface coverage θ (surface coverage is the fraction of the total surface area covered by the clusters; the values above 100% correspond to the formation of multilayer structures).

2. Material is deposited onto the plates of the mass filter. Since the mass filter only allows passage of clusters of a certain mass (size), all other charged clusters will be rejected, which in reality means they are deposited within the mass filter interior. Over time this may pose a significant threat for the normal functioning of the mass filter.

Although most of the inert gas is taken from the system in the pumping chamber, a certain amount of it is still passed into the mass-selection chamber through the skimmer. Therefore a turbo molecular pump is attached to the chamber to minimize background gas pressure. However, because the flux of inert gas through the skimmer is dependent on the skimmer geometry (inlet diameter, internal/external angles), as well as on the nozzle-skimmer distance, in some cases mass-selection chamber pressure may rise considerably. Since by far the biggest portion of the cluster's total trajectory between the source and the substrate is in the mass-selection chamber, high background gas pressure here might have a significant influence on the cluster's motion: numerous cluster-gas collisions may decelerate and/or deflect the clusters from their straight trajectory – an effect that is highly undesirable. It is specially important to minimize this negative effect if one aims for a successful deposition of sub-5 nm clusters, which tend to be more susceptible to major trajectory deviations due to their smaller mass, with sub-2 nm cluster flux almost diminished by the time the beam gets to the exit point of the mass-selection chamber.

2.1.4 Deposition Chamber (4)

Having passed through the mass-selection chamber, clusters reach the deposition chamber (see Fig. 2.2) where they can be deposited onto substrates (labeled F). The deposition chamber is designed to allow for lowering and raising of the sample holder so that the holder is not blocking the cluster beam when the deposition rate is to be measured. This is done by a film thickness monitor using a quartz crystal microbalance sensor placed just behind the sample holder, on the path of the cluster beam.

The sample holder (see Fig 2.8) consists of 3 stencil-like ceramic plates mounted on a brass cryo finger. These ceramic plates are equipped with gold contacts to allow for *in-situ* electrical characterization of freshly deposited cluster-based devices. In our case however the focus was on the structural and morphological characterization of individual clusters, which was done *ex-situ* using scanning electron microscopy (SEM) or preferably transmission electron microscopy (TEM) (see § 2.5). For that reason it was enough to mount our samples directly onto the ceramic plates, utilizing a carbon tape. Samples for SEM characterization and for carbon nanotube (CNT) growth experiments were deposited onto Si_3N_4- or SiO_2-passivated Si wafers, whereas samples for TEM characterization were deposited onto various TEM grids (see Table 2.1 for specifications): continuous or holey amorphous carbon (a-C) film on Cu mesh, continuous a-C film on Au mesh, or highly oriented pyrolytic graphite (HOPG) flakes on oyster Cu or Au mesh.

In order to increase the sample production rate of our IGA system, a gate valve (labeled G in Fig. 2.2) is installed in between the mass-selection chamber and deposition chamber. Once the deposition of a set of samples is over, the gate valve can be closed which isolates the two chambers and allows for the deposition chamber

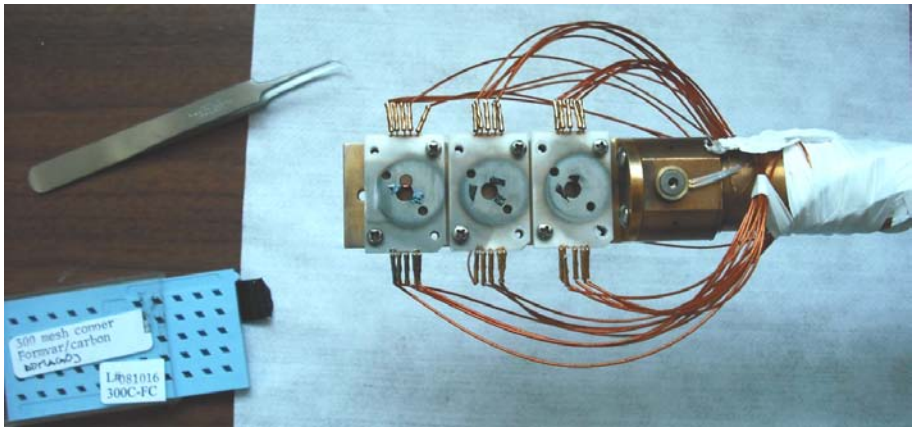

Figure 2.8: Photo of the sample holder used in our system. A standard a-C/Cu TEM grid can be seen mounted in the position 1.

TEM grid	film	mesh	supplier
GSCU300C	a-C/formvar	Cu	ProSciTech
GSAU300C	a-C/formvar	Au	ProSciTech
GYCU300	holey a-C	Cu	ProSciTech
GCU300	a-C	Cu	ProSciTech
GCU50-100	HOPG (home prepared)	oyster Cu	ProSciTech
GAU50-100	HOPG (home prepared)	oyster Au	ProSciTech

Table 2.1: Specifications of the TEM grids used in our experiments.

to be vented independently of the rest of the system. Since it takes ∼30 minutes to dismount a set of freshly deposited samples and mount a new set of substrates before placing the sample holder back into the deposition chamber, it is possible to deposit up to 6 sets or 18 samples per day – 6 times more than if the whole system is to be shut down and vented for each set of samples.

2.2 Stability of Experimental Conditions

As seen in Sec. 2.1.1, the source chamber of our IGA system needs to be cooled down in order to achieve successful cluster nucleation. This is done by cooling the walls of the chamber with liquid nitrogen. Since the chamber walls are made of steel, it takes some time to cool the whole chamber down to liquid nitrogen temperature $T = 77$ K. In addition to that, the water-cooled sputter target located inside the source chamber needs to reach equilibrium temperature, bearing in mind that the flows of room temperature water and inert gas slow the cooling process as well. Nevertheless, the cluster nucleation may begin even at temperature higher than 77 K, when the system has not yet reached thermodynamic equilibrium. These unstable experimental conditions affect the size distribution of clusters coming from the source chamber and, since the conditions slowly change over time as the system reaches stationary state, one can see variations of the cluster size distribution.

Fig. 2.9 shows the behaviour of the size distribution over time in the case of $Ag_{0.85}Au_{0.15}$ clusters, for the standard Ar flow rate $G = 100$ sccm. The first spectrum ($p = 659$ mTorr) was taken ∼1 hour after the source chamber cryostat was filled with liquid nitrogen. It took another ∼45 minutes until the source chamber pressure dropped to 600 mTorr. A series of spectra recorded in that period showed that the mean cluster size gradually increased by ∼10% overall while the source pressure had been dropping down from 659 mTorr to 600 mTorr, until the source chamber conditions slowly reached the equilibrium state.

Once the stable conditions are reached, source chamber pressure stabilizes and

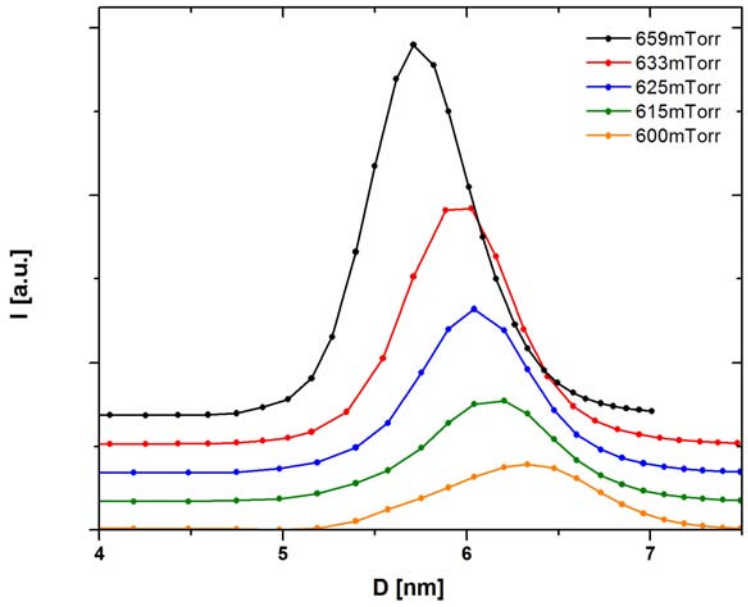

Figure 2.9: Behaviour of the $Ag_{0.85}Au_{0.15}$ cluster size distribution over time, under non-equilibrium source temperature and pressure. Ar flow rate was set to $G = 100$ sccm. Solid curves on this plot and all other plots throughout this chapter serve as a guide to the eye.

the cluster size distribution remains consistent for the whole duration of the experiment, as long as no other experimental parameter is modified.

It should be mentioned that there could be a small misalignment between the nozzle and skimmer (see § 2.1.2), which may primarily affect the intensity of the cluster size distribution, although a small shift of the distribution may also occur. Fortunately, our cryostat (see Fig. 2.2) is designed in such a way to allow a certain movement in both vertical and horizontal directions by means of rotation of 2 screws which support each side of the cryostat. In this fashion one can adjust the relative position of the nozzle to the skimmer and therefore increase the cluster intensity, which immediately shows up as an increase of the cluster deposition rate, seen on the film thickness monitor display.

The behaviour of the cluster size distribution when the system is in the stationary state for various experimental conditions is the topic of the next section.

2.3 *In-situ* Cluster Size Distribution Studies

We performed an experimental study of the influence of various parameters on the size distribution of clusters generated in the source chamber, for different sputter target materials used in the IGA system. As previously discussed in § 2.1.1, if one varies the experimental conditions in the source chamber by changing the values of the parameters, the cluster nucleation will be affected and, as a result, the cluster size

distribution will be modified to some extent. This is the main principle of gaining control over the cluster size in the IGA system, which is one of the key factors needed for a comprehensive experimental study of size-dependent characteristics of clusters, such as their shape and structure. This has been widely utilized in our investigation of $Ag_{0.85}Au_{0.15}$ and $Ni_{0.85}Cu_{0.15}$ clusters, presented in Chapters 4 and 5.

Here we give an overview of the experimental results of cluster size distribution behaviour in the case of two monometallic sputter targets – Sn and Ag – and two alloy bimetallic targets – $Ag_{0.85}Au_{0.15}$ and $Ni_{0.85}Cu_{0.15}$. It should be emphasized that *the cluster size distribution measured by the mass filter is not necessarily the size distribution of the clusters leaving the source chamber.* Namely, as discussed in § 2.1.2, the transfer of clusters through the skimmer is strongly dependent on the skimmer geometry and inert gas flow rate, meaning that for certain geometry-flow rate combinations some cluster sizes may be preferred, while others might be rejected, influencing the mass filter measurements.

2.3.1 Sn Nanoclusters

Sn cluster-based percolating films and nanodevices are studied extensively within our group[27,31,32], using Sn clusters that range 4–10 nm in diameter, produced in our IGA system. Based on our empirical observations, we have identified aggregation length (see Fig. 2.2) as the experimental parameter that is most suitable for controlling the Sn cluster size distribution, exploiting the advantage of having a movable sputter target holder installed in the system.

Commonly, we set the Ar flow rate to $G = 100$ sccm and plasma generator power to $P = 25$ W. Based on our earlier experimental observations, these values are found to be optimal for the successful deposition of 4–10 nm clusters at a sufficiently high deposition rate; these values are presumed in all of our experimental results that follow, unless stated differently. No He was added to the Ar flow in this case. We varied the aggregation length (AL) in a stepwise manner, starting from the value of $AL = 10$ cm down to the value of $AL = 5$ cm, and measured the cluster size distribution with our mass-filter (see Fig. 2.10). One can see that, as the AL is decreased, the cluster size distribution peak shifts from $D \sim 7$ nm for $AL = 10$ cm down to $D \sim 5.5$ nm for $AL = 5.6$ cm; at the same time, the peak intensity goes up. This behaviour is consistent with the expectation that, if the AL is relatively long, more Sn atoms are added to already nucleated clusters before they eventually leave the source chamber. Moreover, some of the clusters collide inside the source chamber forming "clusters of clusters", giving rise to an additional peak, as can be seen in Fig. 2.10 in the case of $AL = 10$ cm, where a side peak is located at

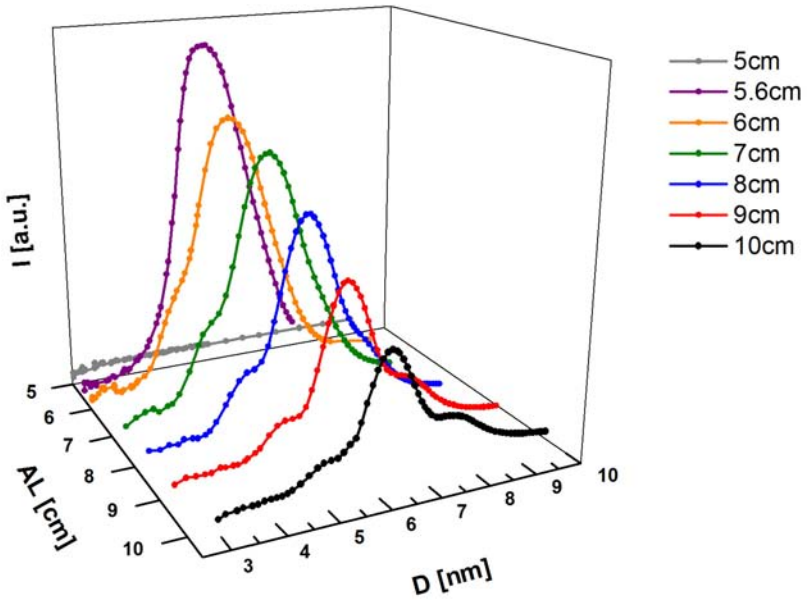

Figure 2.10: Sn cluster size distribution behaviour when AL is varied. Ar flow rate was set to $G_{Ar} = 100$ sccm, no He was added, and plasma generator power was set to $P = 25$ W.

$D \sim 8.5$ nm. On the other hand, this means that overall there are less clusters leaving the chamber, which results with the lower peak intensity. As the AL is shortened, more small clusters are produced in the source, showing as a peak shift toward the smaller cluster diameter, with the peak intensity increasing significantly.

For each sputter target there exists the shortest i.e. *cut-off* AL where an abrupt loss of mass filter signal occurs, indicating there are no (charged) clusters reaching the mass filter – in the case of Sn target (see Fig. 2.10), the cut-off occurs at $AL = 5$ cm. Possible explanations are:

1. The plasma plume has a certain length – for short AL the plume starts to touch the nozzle wall, allowing no space (or time) for efficient condensation of the sputtered atoms into clusters, so that effectively no clusters are generated.

2. Even if some clusters are generated in the source chamber, their size is such that the skimmer does not allow for a high throughput of these clusters.

3. Even if some smaller clusters pass through the skimmer, due to the background gas their trajectories deviate from the centerline so much that they do not reach the mass filter entrance.

Nevertheless, we have demonstrated here that one can effectively gain control over the (mean) cluster size by changing the aggregation length. Although the shift of the cluster size is relatively small ($\lesssim$3 nm), it is worth pointing out that we can control the nanocluster size *in the beam* i.e. *independently* of the sample surface

coverage – this is a significant advantage of the IGA system over most of other nanocluster fabrication techniques.

2.3.2 Ag Nanoclusters

Similar to the Sn case, we performed a study of nanocluster size distributions when Ag sputter target was used, with a more meticulous approach: the investigated AL range was broadened (4–13 cm) in comparison to the Sn case, and the AL values close to the cut-off AL were studied in more detail. All other experimental parameters were kept the same as in the Sn case.

The results of our measurements are presented in Fig. 2.11. Again one can see that behaviour of the cluster size distribution is very similar to the Sn case: when the AL was gradually shortened from $AL = 13$ cm down to $AL = 5$ cm, the peak position shifted from $D \sim 8.5$ nm to $D \sim 5.5$ nm. Meanwhile, the peak intensity rose by almost two orders of magnitude. When the AL was further shortened to below 5 cm, the peak intensity steadily weakened until it vanished completely at $AL < 4$ cm.

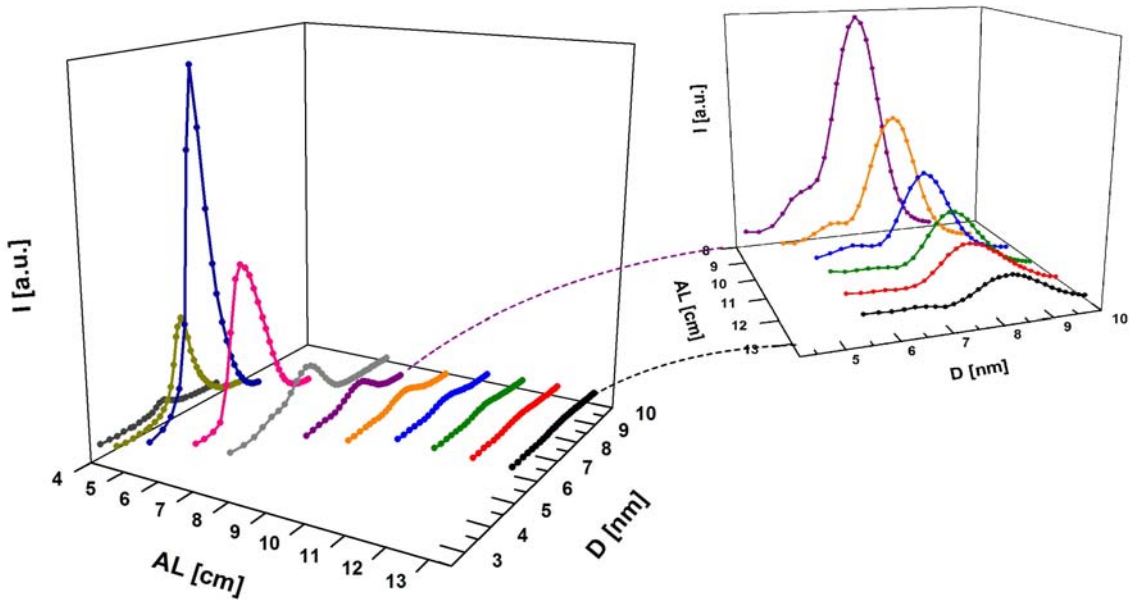

Figure 2.11: (left) Ag cluster size distribution behaviour when AL is varied. (right) For the sake of clarity, results for 8 cm $\leq AL \leq$ 13 cm are replotted with the intensity scale magnified 10×. Ar flow rate is set to $G_{Ar} = 100$ sccm, no He was added, and plasma generator power was set to $P = 25$ W.

2.3.3 $Ag_{0.85}Au_{0.15}$ Nanoclusters

The investigation of $Ag_{0.85}Au_{0.15}$ clusters and cluster-based thin films has been the focal point of the author's PhD work undertaken within the cluster group at the Physics and Astronomy Department, University of Canterbury (see Chapters 3 and 4). An abundance of experimental data related to $Ag_{0.85}Au_{0.15}$ nanoclusters has been gathered, including a comprehensive study of the influence of various experimental parameters on the cluster size distribution. Here we present a summary of these findings, which later on proved to be very useful and time-saving, serving as a recipe for a relatively quick deposition of samples of clusters of a desired size, with a high degree of reproducibility.

Unlike the previous cases of Sn and Ag clusters where only the influence of the AL on the cluster size distribution was investigated, for $Ag_{0.85}Au_{0.15}$ clusters we explored much wider range of the experimental four-dimensional phase space that is spanned by aggregation length (AL), Ar flow rate (G_{Ar}), He flow rate (G_{He}), and plasma generator power (P) axes.

Aggregation Length

Firstly, just like in the Sn and Ag cases, we varied the AL keeping all other parameters fixed at default values (G_{Ar} = 100 sccm, G_{He} = 0 sccm, P = 25 W). As one can see in Fig. 2.12, the $Ag_{0.85}Au_{0.15}$ cluster size distribution follows the same

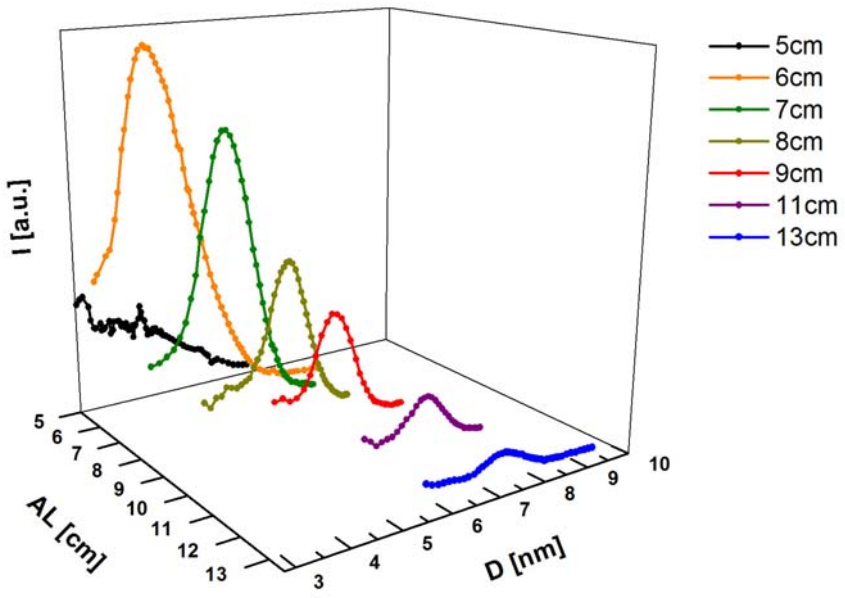

Figure 2.12: $Ag_{0.85}Au_{0.15}$ cluster size distribution behaviour when AL is varied. Inert gases flow rates are set to G_{Ar} = 100 sccm and G_{He} = 0 sccm; plasma generator power was set to P = 25 W.

behaviour as in Sn and Ag case – for longer AL values the size distribution peak is located at a bigger cluster diameter, whereas for shorter AL values the peak shifts toward a smaller cluster diameter, as expected. The peak intensity behaviour is also consistent with the previous cases – as the AL gets shorter, the peak intensity steadily grows and reaches its maximum for $AL \sim 6$ cm, before suddenly dropping to zero when the cut-off $AL \sim 5$ cm is attained.

As a useful experimental fact, it is worth mentioning that there seems to be no inter-cluster sticking so no "clusters of clusters" were generated at any AL within this set of experimental parameters values.

He Addition

We then studied the behaviour of $Ag_{0.85}Au_{0.15}$ cluster size distribution when He was added to Ar, comprising up to 80% of the total inert gas flow which was kept constant at $G_{Ar+He} = 100$ sccm. He atoms do not form a plasma in our IGA system and therefore do not contribute to the sputtering process – instead, they act as a heat transfer medium between the sputtered Ag(Au) atoms and the cryostat walls, promoting the nucleation of clusters even at low sputtering rates i.e. when the concentration of sputtered Ag(Au) atoms in the source chamber atmosphere is relatively low. Furthermore, the addition of He affects the characteristics of the gas mixture flow through the nozzle and skimmer, which may influence the measured size distribution.

Fig. 2.13 depicts this clearly: although the sputtering rate i.e. number of atoms

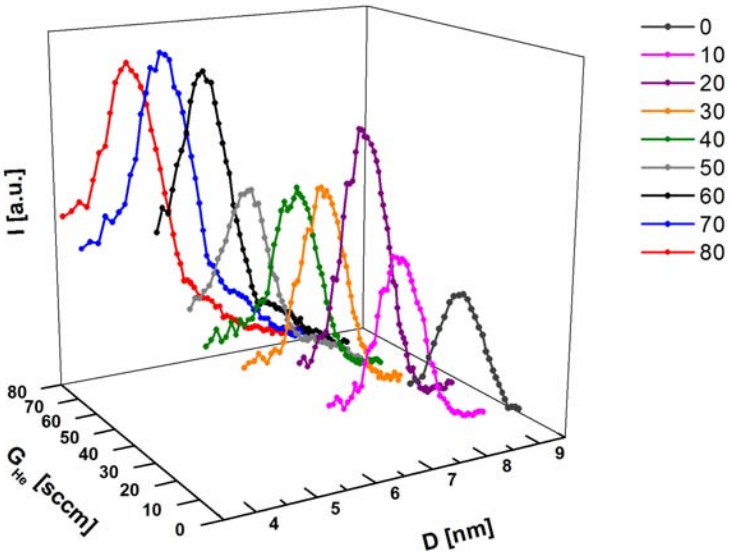

Figure 2.13: $Ag_{0.85}Au_{0.15}$ cluster size distribution behaviour when G_{He} is varied. Total inert gases flow rate is set to $G_{Ar+He} = 100$ sccm, with $AL = 13$ cm and $P = 25$ W.

ejected from the sputter target goes down with decreasing G_{Ar}, increasing G_{He} enhances their aggregation so that more clusters are nucleated in the source chamber. At the same time, the mean cluster size decreases from $D \sim 8$ nm for $G_{He} = 0$ sccm to $D \sim 5$ nm for $G_{He} = 80$ sccm. In the end one can conclude that the final size distribution is a result of a trade off between the reduction in number of sputtered atoms available for cluster nucleation on one side, and the enhancement of the cluster nucleation rate due to more He atoms on the other side.

Plasma Generator Power

Next we decided to move along the plasma generator power axis of our experimental phase space to investigate its effect on the cluster size distribution. The other parameters were fixed as follows: $AL = 9$ cm, $G_{Ar} = 100$ sccm, $G_{He} = 0$ sccm.

It should be noted that we have a bottom and top boundary value of plasma generator power – on one side there exists the minimum power P_{min} needed for the ignition of the plasma and on the other side we are limited by the fact that too much power used may lead to the melting of the sputter target. Although the sputter target cooling applied in our IGA system pushes the upper power boundary to some extent, there is still a maximum value allowed P_{max} after which the target starts to melt. Both of these boundary values are somewhat dependent on the G_{Ar} and G_{He}.

In our case (see Fig. 2.14) the minimum and maximum power values were

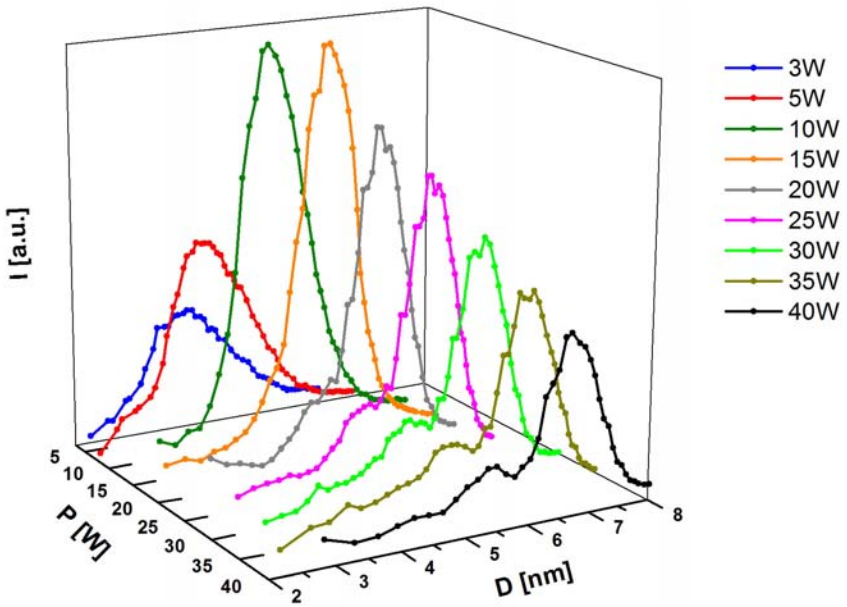

Figure 2.14: $Ag_{0.85}Au_{0.15}$ cluster size distribution behaviour when P is varied. Aggregation length was set to $AL = 9$ cm, with inert gases flow rates $G_{Ar} = 100$ sccm and $G_{He} = 0$ sccm.

$P_{min} = 3$ W and $P_{min} \sim 45$ W, respectively. As power was increased in this range, the cluster size distribution peak exhibited a shift toward bigger diameters. In a way this is expected since the more power one uses, the more Ag(Au) atoms will be ejected from the sputter target increasing their concentration in the source chamber, allowing more atoms to be added to already nucleated clusters.

Note that, as P values are increased, a small side peak is formed at $D \sim 5.5$ nm, giving rise to a bimodal cluster distribution, which is not desirable in our experiments.

Ar Flow Rate

Finally, we tested the behaviour of the cluster size distribution when the Ar flow rate was varied (see Fig. 2.15). It should be emphasized that this behaviour mostly reflects the performance of the 7/30 skimmer, rather than the actual source size distribution (although the increase in the concentration of Ar atoms in the source chamber will have some effect on it). A detailed study of the cluster velocity behaviour for various flow rates and skimmer geometries is presented in Chapter 3. As previously stated, one expects that the skimmer enhances the throughput of clusters of a certain size (favored for the given G_{Ar}) and suppresses the passage of clusters of other sizes, depending on the inert gas flow.

As can be seen in Fig. 2.15, the highest cluster intensity was measured at

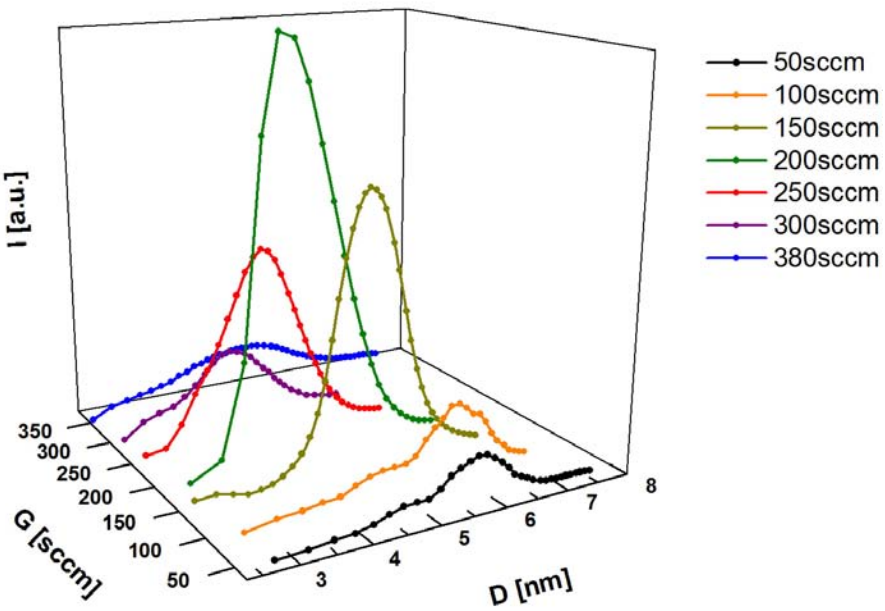

Figure 2.15: $Ag_{0.85}Au_{0.15}$ cluster size distribution behaviour when G_{Ar} is varied, without any He added ($G_{He} = 0$ sccm). Aggregation length was set to $AL = 9$ cm using plasma generator power $P = 25$ W.

$G_{Ar} = 200$ sccm for $D \sim 5$ nm clusters. For bigger G_{Ar} the peak intensity dropped significantly, eventually giving a smoother and wider distribution, highly undesirable for our sample deposition where a narrow cluster size distribution is of interest.

From the practical point of view, the variation of G_{Ar} can be beneficial for increasing the flux of clusters of a specific size. However, since this is mostly determined by the characteristics of the inert gas flow through the skimmer, we have limited freedom when choosing the cluster size.

Summary – $Ag_{0.85}Au_{0.15}$ Clusters

We studied the behaviour of $Ag_{0.85}Au_{0.15}$ cluster size distribution when the experimental parameters were varied, moving along various axes of the experimental phase space. We showed that it was possible to control the size of clusters in the range $4 \text{ nm} \leq D \leq 10$ nm by changing the parameter values. Although the volume of the phase space that was investigated was rather small, we acquired valuable insights of the cluster size distribution behaviour – this will be widely utilized in deposition of samples for *ex-situ* characterization, presented in Chapters 4 and 5.

2.3.4 $Ni_{0.85}Cu_{0.15}$ Nanoclusters

In addition to the studies of $Ag_{0.85}Au_{0.15}$ clusters, we investigated the size distribution behaviour of $Ni_{0.85}Cu_{0.15}$ clusters when aggregation length and plasma generator power were varied. Empirically it was immediately found that the intensity of the $Ni_{0.85}Cu_{0.15}$ cluster size distribution peak was approximately an order of magnitude weaker than in the case of $Ag_{0.85}Au_{0.15}$ clusters, when the same experimental conditions were used. The reason for this lies in the higher (bulk) cohesive energies of Ni and Cu compared to those of Ag and Au[33] – it means one needs to *invest* more energy to sputter the same number of Ni(Cu) atoms from the target than in the case of Ag(Au). Even though cohesive energy depends on the size and is generally smaller for nanoclusters than for bulk[34–36], as long as the cluster size is equal the relation between cohesive energies for different elements is still valid. This means that, when it comes to cluster aggregation, one needs to *take* more energy from the Ni(Cu) atoms floating in the source chamber atmosphere in order to nucleate the same number of clusters as in the case of Ag(Au) atoms. Consequently, the intensity of the $Ni_{0.85}Cu_{0.15}$ cluster beam will be considerably lower than the one for $Ag_{0.85}Au_{0.15}$, if the same experimental parameters values are used.

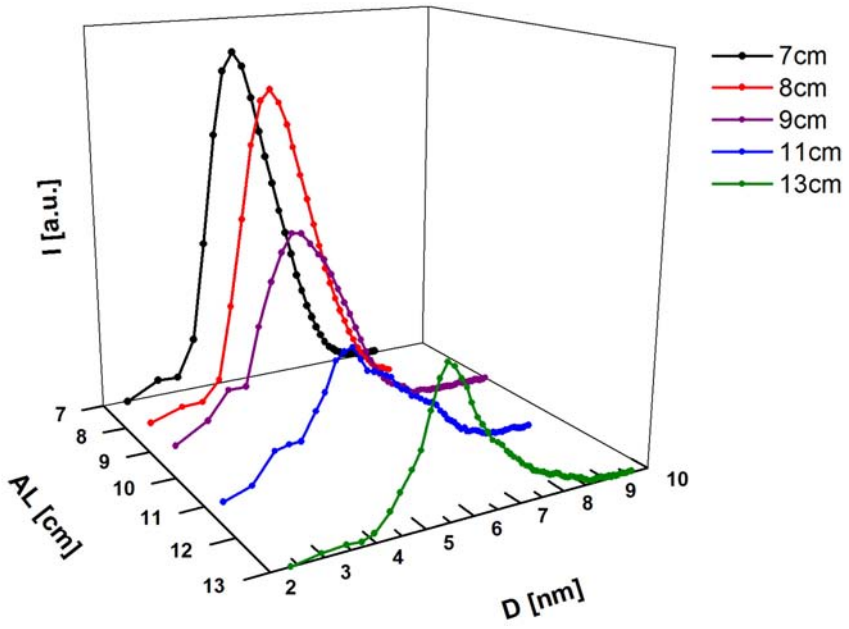

Figure 2.16: $Ni_{0.85}Cu_{0.15}$ cluster size distribution behaviour when AL is varied, keeping the other parameters fixed as follows: $P = 25$ W, $G_{Ar} = 150$ sccm, $G_{He} = 0$ sccm.

Aggregation Length

When the aggregation length was varied in the range 7 cm $\leq AL \leq$ 13 cm (see Fig. 2.16), the cluster size distribution peak exhibited almost no shift. Although the peak intensity showed some change, it was definitely much less than in any other sputter target material considered in our investigations (compare to Figs. 2.10, 2.11, and 2.12). For practical purposes it means that by changing the AL alone one will not be able to satisfactory control the size of $Ni_{0.85}Cu_{0.15}$ clusters.

Plasma Generator Power

The most reasonable way to boost the concentration of sputtered Ni(Cu) atoms in the source chamber atmosphere is to increase the plasma generator power. In our investigation plasma generator power was varied between $P = 15$ W and $P = 35$ W (see Fig. 2.17): the cluster size distribution peak intensity at first gradually increased, exhibited a maximum at $P = 25$ W and then decreased rapidly, practically diminishing at $P = 35$ W. The increase in the peak intensity can be explained straightforwardly by an increase in the number of Ar^+ ions hitting the sputter target, ejecting more Ni(Cu) atoms and thus saturating the source chamber atmosphere with Ni(Cu) atoms, which resulted with more nucleated clusters. On the other side, when more power is used in the system, more heat needs to be taken from the atmosphere in order to aggregate clusters. Since less Ar atoms are now available

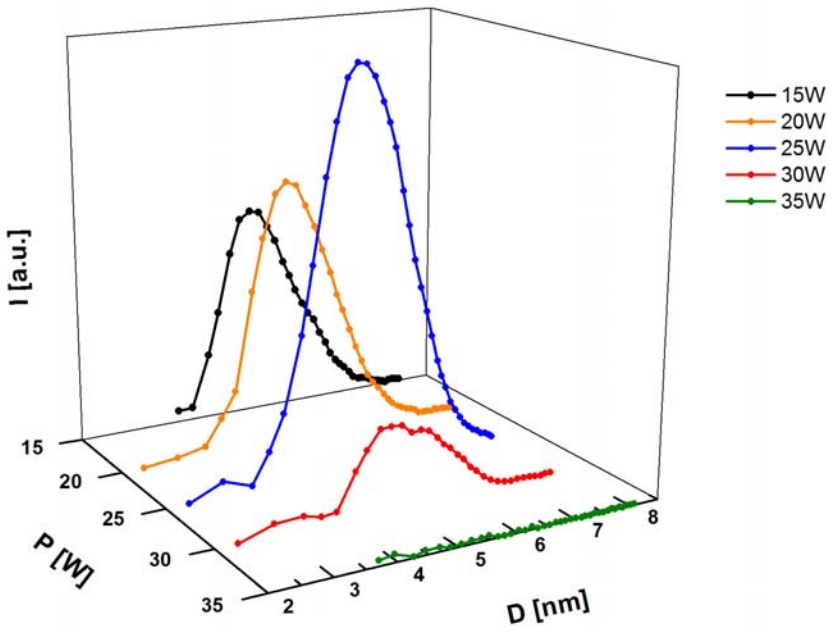

Figure 2.17: $Ni_{0.85}Cu_{0.15}$ cluster size distribution behaviour when P is varied. Other experimental parameters were as follows: $AL = 9$ cm, $G_{Ar} = 150$ sccm, $G_{He} = 0$ sccm.

for cooling purposes, the cluster aggregation is hampered. The overall nucleation is therefore a result of a trade off between the enhanced sputtering rate which promotes the cluster generation and the hindered cooling rate which diminishes the cluster generation.

He addition

Obviously neither change of AL nor P can provide satisfactory control over the $Ni_{0.85}Cu_{0.15}$ cluster size. As discussed in the previous section, the main difficulty here arises from the relatively high cohesive energy of Ni(Cu) which does not favor easy cluster nucleation. For that reason it is worthwhile introducing He into the source chamber atmosphere, since this generally enhances the heat transfer from atoms and clusters to the cryostat walls.

This assumption was investigated using the following set of experimental parameters: $G_{Ar+He} = 150$ sccm, $AL = 13$ cm and $P = 25$ W. As can be seen in Fig. 2.18, the addition of He had a major impact on the cluster aggregation – the number of clusters rose significantly, with the size distribution peak shifting toward a smaller cluster diameter, allowing for better control of the cluster sizes.

In reality, one needs to play around modifying all experimental parameters to gain control over the $Ni_{0.85}Cu_{0.15}$ cluster size in the range 3 nm $\leq D \leq$ 10 nm, finding the right combination of parametric values that will give a high intensity flux of clusters of a desired size.

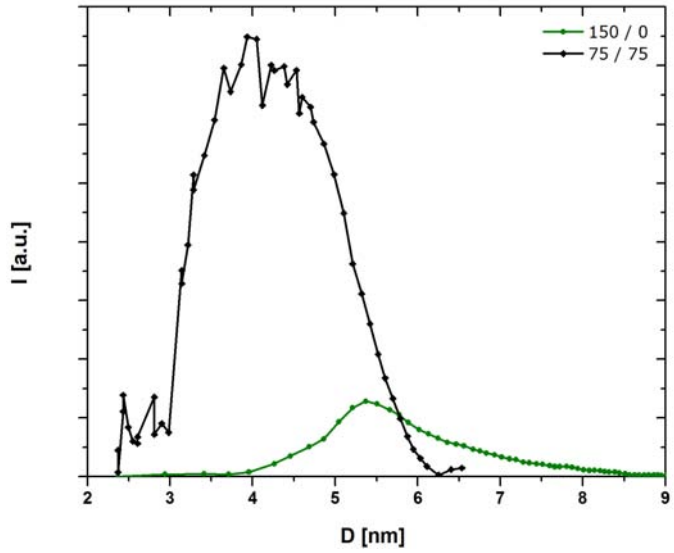

Figure 2.18: $Ni_{0.85}Cu_{0.15}$ cluster size distribution behaviour when He is added ($G_{He} = 75$ sccm). Total inert gases flow rate was set to $G_{Ar+He} = 150$ sccm, with $AL = 13$ cm and $P = 25$ W.

2.3.5 Summary

We conducted experimental studies of Sn, Ag, $Ag_{0.85}Au_{0.15}$, and $Ni_{0.85}Cu_{0.15}$ nanocluster size distribution behaviour with respect to various experimental parameters: aggregation length, plasma generator power, He addition, and Ar flow rate. It was found that by changing aggregation length one can gain control over the nanocluster size in the range 4 nm $\leq D \leq$ 10 nm (see Fig. 2.19, 2.20, and 2.21). There seems

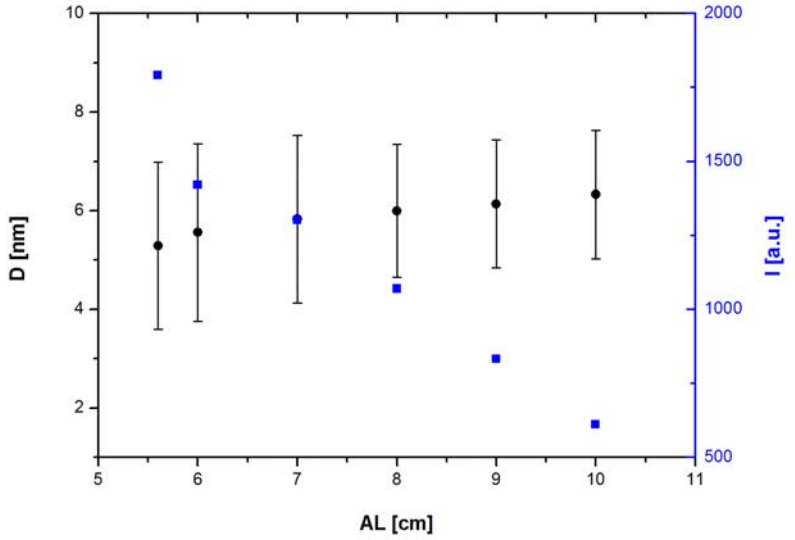

Figure 2.19: Sn cluster size (black circles) and peak intensity (blue squares) behaviour when AL is varied. The other experimental parameters were set as follows: $G_{Ar} = 100$ sccm, $G_{He} = 0$ sccm, $P = 25$ W. Error bars match FWHM of the corresponding size distributions from Fig. 2.10.

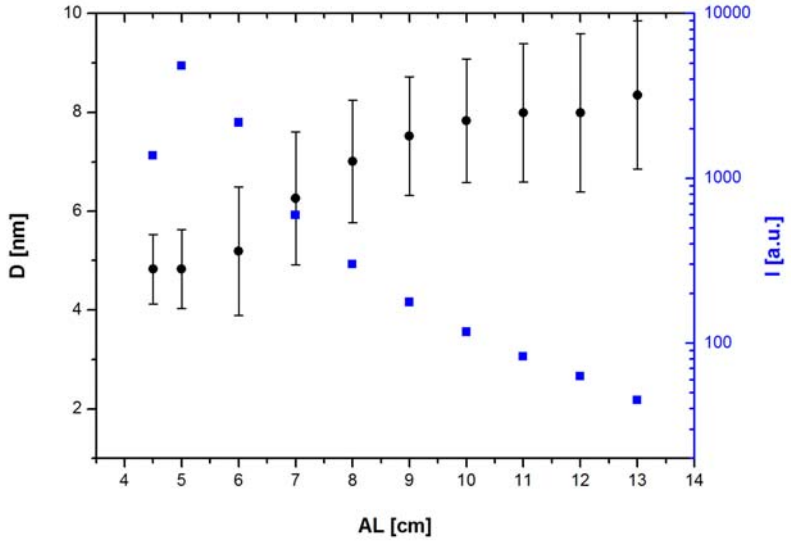

Figure 2.20: Ag cluster size (black circles) and peak intensity (blue squares) behaviour when AL is varied. The other experimental parameters were set as follows: $G_{Ar} = 100$ sccm, $G_{He} = 0$ sccm, $P = 25$ W.

to be a general trend that the mean cluster size decreases as aggregation length decreases – this is more pronounced in the case of Ag and $Ag_{0.85}Au_{0.15}$ than in Sn; at the same time the intensity i.e. number of clusters increases, which is expected from the point of view of mass conservation. This behaviour persists until the cut-off aggregation length is reached (usually ∼5 cm), when the cluster generation abruptly diminishes, as discussed in § 2.3.1.

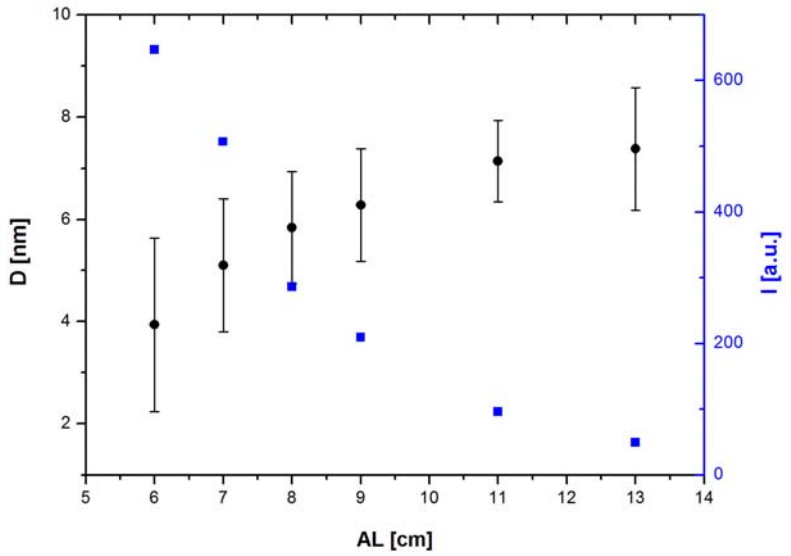

Figure 2.21: $Ag_{0.85}Au_{0.15}$ cluster size (black circles) and peak intensity (blue squares) behaviour when AL is varied. The other experimental parameters were set as follows: $G_{Ar} = 100$ sccm, $G_{He} = 0$ sccm, $P = 25$ W.

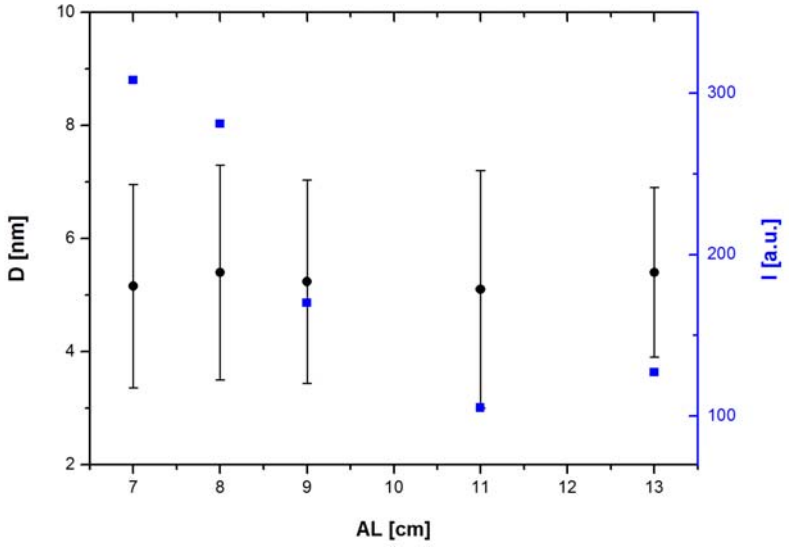

Figure 2.22: $Ni_{0.85}Cu_{0.15}$ cluster size (black circles) and peak intensity (blue squares) behaviour when AL is varied. The other experimental parameters were set as follows: $G_{Ar} = 150$ sccm, $G_{He} = 0$ sccm, $P = 25$ W.

However, the case of $Ni_{0.85}Cu_{0.15}$ represents an exception from the general trend seen in Sn, Ag, $Ag_{0.85}Au_{0.15}$ cases – the change of aggregation length did not visibly affect the position of the size distribution peak (see Fig. 2.22), preventing us from using this parameter as a way to control the cluster size. Interestingly, the $Ni_{0.85}Cu_{0.15}$ cluster intensity behaviour was quite similar to the other cases.

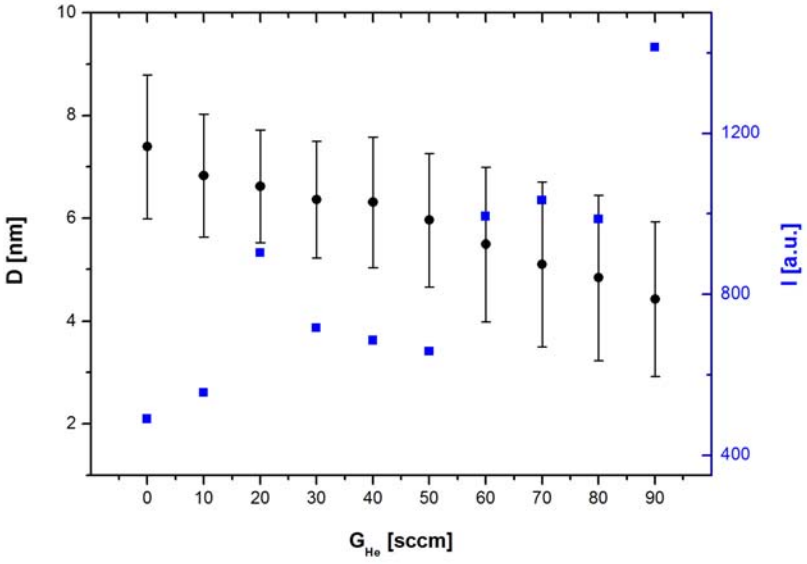

Figure 2.23: $Ag_{0.85}Au_{0.15}$ cluster size (black circles) and peak intensity (blue squares) behaviour when G_{He} is varied. The other experimental parameters were set as follows: $AL = 13$ cm, $G_{Ar+He} = 100$ sccm, $P = 25$ W.

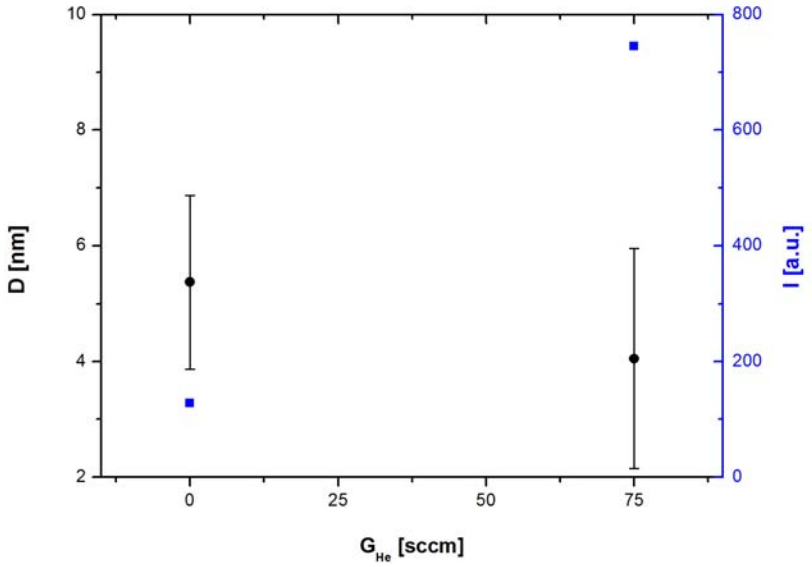

Figure 2.24: $Ni_{0.85}Cu_{0.15}$ cluster size (black circles) and peak intensity (blue squares) behaviour when G_{He} is varied. The other experimental parameters were set as follows: $AL = 13$ cm, $G_{Ar+He} = 150$ sccm, $P = 25$ W.

It is also interesting to see the effect of He addition on the cluster size and peak intensity (see Figs. 2.23 and 2.24): for both $Ag_{0.85}Au_{0.15}$ and $Ni_{0.85}Cu_{0.15}$ cases the mean cluster size decreases as more He is added. At the same time the peak intensity increases, in line with the expectation of mass conservation. Note that the addition of He can allow for a much better control of the $Ni_{0.85}Cu_{0.15}$ cluster size than the variation of aggregation length, seen in Fig. 2.22.

In reality, one needs to explore a wider range of the experimental phase space in order to find the optimal set of parameters that will yield the desired cluster size with a relatively narrow spread, while maintaining a satisfactory cluster intensity.

2.4 Experimental Set-up for CNT Growth

Metallic nanoclusters supported by various substrates are widely used as catalysts in carbon nanotube (CNT) synthesis, primarily by means of low temperature plasma enhanced chemical vapor deposition[37–45] (PECVD) or high temperature chemical vapor deposition[46–94] (CVD). The latter approach was utilized in order to study CNT syntheses catalyzed by $Ni_{0.85}Cu_{0.15}$ nanoclusters produced in our IGA magnetron sputtering system.

The CNT growth experiments were performed in collaboration with Jin Ke and Vladimir Golovko from the Chemistry Department, University of Canterbury, with a focus on fabrication of multi-wall carbon nanotubes (MWCNTs). We also collabo-

rated with Kirsten Edgar from the School of Chemical and Physical Sciences, Victoria University of Wellington, where the objective was to successfully grow single-wall carbon nanotubes (SWCNTs) using alloy nanoclusters as catalysts. In addition to the main goal – proving the concept that these alloy nanoclusters can be used as catalysts in CVD synthesis of SWCNTs and MWCNTs – the studies were performed with the intention of optimizing the growth conditions so that future work could be focused on investigations of the correlation between certain $Ni_{0.85}Cu_{0.15}$ nanocluster properties (e.g. size, shape, structure) and characteristics of grown CNTs (e.g. inner diameter, number of walls, chirality).

Here we give a brief outline of the CNT growth by CVD in the experimental system at the University of Canterbury; detailed description with recent advances in this popular method for CNT synthesis can be found elsewhere[95]. A sample containing catalytically active nanoclusters is inserted into a glass tube placed in an oven (see Fig. 2.25). The tube is flushed by a flow of inert gas (usually Ar) and slowly heated up to several hundred degrees Celsius. During the transfer of samples from the IGA deposition system to the CNT growth apparatus, clusters are exposed to air. Therefore, in the CNT growth experiments the clusters are initially oxidized and as such not suitable for successful CVD synthesis. In order to reduce the clusters before the CNT growth, a reducing agent, such as H or NH_3, is introduced into the reaction tube, alongside the inert gas. Note that the reduction temperature plays an important role in this process, hence its influence on the CNT growth was studied more in detail. After the reduction of clusters, a C-containing gas (in our case acetylene – C_2H_2) is added to the inert gas flow in order to supply

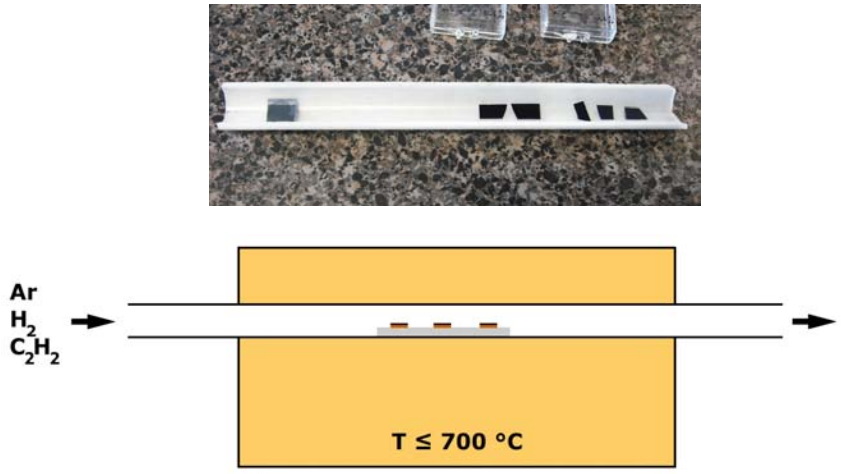

Figure 2.25: (top) Photo of a set of $Ni_{0.85}Cu_{0.15}/SiO_2$ samples placed in a quartz vessel ready for insertion into the CNT growth apparatus at UC. (bottom) Schematics of the experimental set-up for the growth of carbon nanotubes by chemical vapor deposition.

C atoms needed for the nucleation and growth of CNTs. At high temperatures metallic clusters act as catalytic centers for cracking of the C-containing gas into its base elements. During this process, concentration of C atoms on the cluster surfaces increases until a saturation point is reached when C atoms start to bond and form a C-cap around the cluster. Under favorable conditions the C-cap lifts off and CNT starts to grow either as a SWCNT or MWCNT, depending on the experimental conditions. The catalytic activity of nanoclusters for a successful synthesis of CNTs is known to depend on several factors: growth temperature[46–61], atmosphere composition[46,51,53,57,62–64], type of carbon-containing molecules used for CVD[65,66], size and shape of the clusters[59,67,68], concentration of dopant/impurity atoms in the (alloy) clusters[69–71], and characteristics of the cluster's supporting substrate[57,68,72].

As an example, a diagram showing experimental conditions used in the initial attempts of catalytic CVD synthesis of CNTs at UC is presented in Fig. 2.26. $Ni_{0.85}Cu_{0.15}$ nanoclusters had been produced in the IGA magnetron sputtering system and deposited onto cleaned SiO_2-passivated Si substrates (SiO_2/Si), ready to be used in the CNT growth experiments. In the first stage of the experiment presented in Fig. 2.26, the samples were heated up to 400 °C in an inert atmosphere. In the second stage a small amount of hydrogen is introduced in the inert atmosphere in order to reduce the oxidized clusters. After a couple of hours of reduction the temperature was further increased to 650 °C at which point acetylene was added to the gas mixture, initiating the CNT growth. In this case the CNT growth parameters were set with the intention of producing relatively long (> 5 μm) and thick (> 20 nm) CNTs, suitable for initial SEM and TEM characterization.

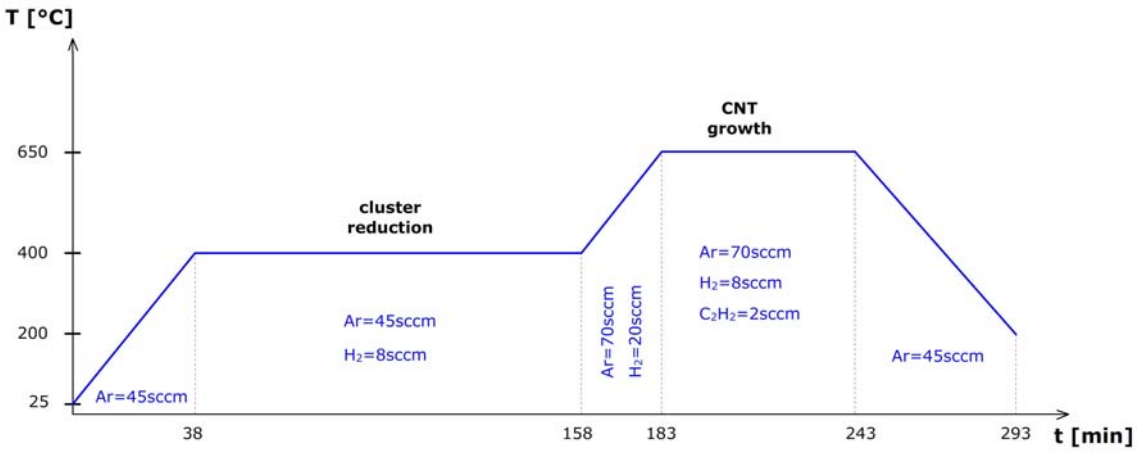

Figure 2.26: Diagram showing experimental conditions during the growth of CNTs by CVD synthesis at UC.[96]

2.5 Electron Microscopy Techniques

Scanning electron microscopy (SEM) and transmission electron microscopy (TEM) were the two main *ex-situ* characterization techniques used in our studies of alloy nanoclusters and carbon nanotubes. They provided insights into nanocluster properties such as size, shape, structure, composition, and surface coverage, as well as CNT properties such as length, diameter, number of walls, and crystallinity.

2.5.1 Scanning Electron Microscopy

SEM is a characterization technique in which an electron beam is raster scanning the surface of a specimen in order to reveal information about its topography, composition, or conductivity. Schematics of a typical scanning electron microscope are presented in Fig. 2.27. A thermionic or field emission electron gun (1) produces a monochromatic electron beam (2) which is compressed by a pair of condenser electromagnetic lenses (3,5). A condenser and objective aperture (4 and 5, respectively)

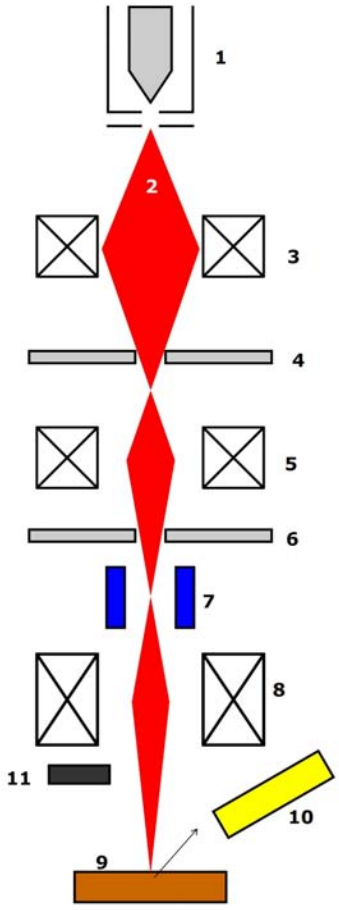

Figure 2.27: Schematics of a typical scanning electron microscope. Labels are explained in the text.

eliminate high-angle electrons from the beam so that it becomes thin and coherent before reaching the scanning coils (7) that control the raster scanning. Lastly, an objective lens (8) is used to focus the beam on a desired spot on the specimen (9). The interaction of the electron beam with the material in the specimen is a quite complex process which, among other species, gives rise to secondary and backscattered electrons (see Fig. 2.28). Secondary electrons are created by ionization of atoms in the specimen by the incident electron beam; their energy is usually < 5 eV so that only those electrons that are ejected near the surface (< 10 nm) can exit the material and be detected. Obviously, the topography of the sample will seriously affect the intensity of secondary electrons originating from each point on the surface - this is the main principle of image formation in scanning electron microscopy. It should be noted that the SEM magnification is purely a function of the size of the scanned area i.e. the SEM magnification is not achieved by the lenses used in the system.

Complementary to secondary electrons which enable the formation of topographical images, backscattered electrons can show the elemental composition of the scanned area since their intensity is directly proportional to the atomic number of the element present in the sample. Hence, the SEM is commonly equipped with both a secondary electron detector (10 in Fig. 2.28), as well as with a backscatter electron detector (11) that, in combination with the supporting computer system, can reveal the topography and composition of the scanned area.

Additionally, the SEM can be equipped with an energy-dispersive X-ray spectrometer that detects characteristic X-rays originating from the specimen exposed to the electron beam irradiation. This is another technique that can reveal the el-

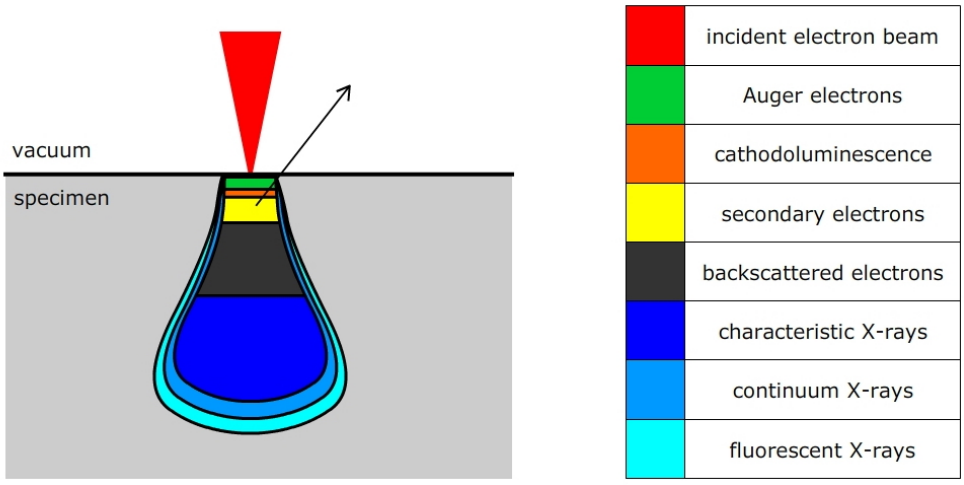

Figure 2.28: Illustration of resulting species from the electron beam - material interaction. Regions of origin of each specie are indicated by different colors.

emental composition of the sample; the basic principles of energy-dispersive X-ray spectroscopy (EDX) will be explained more in detail in § 2.5.3. For detailed description of SEM principles and recent advances in this technique see books from Goldstein[97] and Zhou and Wang[98].

SEM was primarily used for investigating the surface coverage of clusters deposited onto Si_3N_4/Si or SiO_2/Si wafers. In addition, we utilized SEM to study the effects of high temperature annealing of samples on the coalescence of deposited clusters. However, when the characteristics of individual nanoclusters are of interest, SEM exhibits a couple of shortcomings:

1. SEM has a relatively low resolution ($\sim$5 nm) – it is not suitable for detailed imaging on the atomic scale.

2. SEM is a surface-sensitive technique – it is not suitable for getting information about the inner structure of objects.

Nevertheless, SEM proved to be valuable in characterization of CNT samples where it was possible to quickly acquire information about spatial density of CNTs on the substrates, as well as to estimate their length and thickness.

In our SEM studies we used a JEOL 7000F field-emission scanning electron microscope equipped with a JEOL energy dispersive X-ray detector, located at the University of Canterbury Electron Microscopy Center (UCEM).

2.5.2 Transmission Electron Microscopy

For detailed examination of nanoclusters and CNTs we utilized high-resolution (HR) TEM. Apart from providing us with information about shape and size of clusters and CNTs, it also gave insights about their composition and inner structure.

Conceptually, the main difference to SEM is that in TEM one uses the transmitted part of the electron beam to form a magnified image or diffraction pattern. Obviously, a necessary requirement for successful atomic-resolution imaging is that the specimen must be sufficiently transparent to the electron beam, i.e. it must be sufficiently thin ($\lesssim$ 100 nm). For that reason, TEM specimens are usually prepared either by thinning of bulk samples or simply by deposition of samples onto commercially available TEM grids (see Fig. 2.29).

In our investigation, nanocluster TEM samples were deposited directly onto grids of various types – holey or continuous a-C film on Cu or Au mesh for Ag-Au or Ni-Cu samples, respectively, to enable accurate EDX measurements (see § 2.5.3). In addition, by peeling off flakes from bulk HOPG and clamping them in oyster Cu

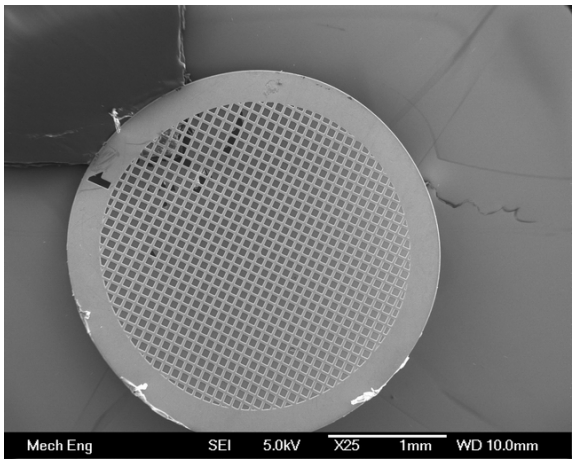

Figure 2.29: SEM image of a standard TEM grid (continuous a-C film supported on 300 Cu mesh: 85μm pitch, 54μm hole, 31μm bar), commonly used in our investigation; a-C film is on the bottom side.

and Au meshes we prepared grids that enabled TEM investigations of nanocluster coalescence on very smooth surfaces.

For TEM imaging of CNTs we first had to transfer the CNT samples from their original Si_3N_4/Si or SiO_2/Si substrates on which they were grown onto the TEM grids. We experimented with several procedures to optimize the preparation of TEM specimens; the following approach yielded the best results. The procedure was comprised of several steps: putting a drop of solvent onto the CNT sample, immersing a TEM grid into it and letting the drop evaporate before taking the grid off. This allowed for sticking of the CNTs to the a-C film by Van Der Waals forces, giving a relatively high surface coverage for satisfactory TEM imaging of the samples. Note that the success rate of this procedure strongly depends on the length and surface coverage of CNTs on the substrate that they are taken from.

As can be seen in Fig. 2.30, the section of a TEM above the specimen is quite similar to the upper section of a typical SEM (compare to Fig. 2.27): the electron gun in combination with a pair of condenser lenses defines the electron beam which strikes the specimen. The transmitted part of the beam is focused by the objective lens and magnified by the intermediate and projector lenses before it hits the fluorescent projection screen at the base of the column. The apertures can be inserted by will to block the part of the electron beam, either before (condenser aperture) or after (objective and selected area aperture) the beam strikes the specimen.

The two main operational modes of the TEM are diffraction pattern (DP) and imaging mode, presented schematically in Fig. 2.31 (a) and (b), respectively. In the diffraction pattern mode, the lenses are adjusted in such a way so that the back focal plane (bfp) of the objective lens serves as the object plane for the intermediate lens.

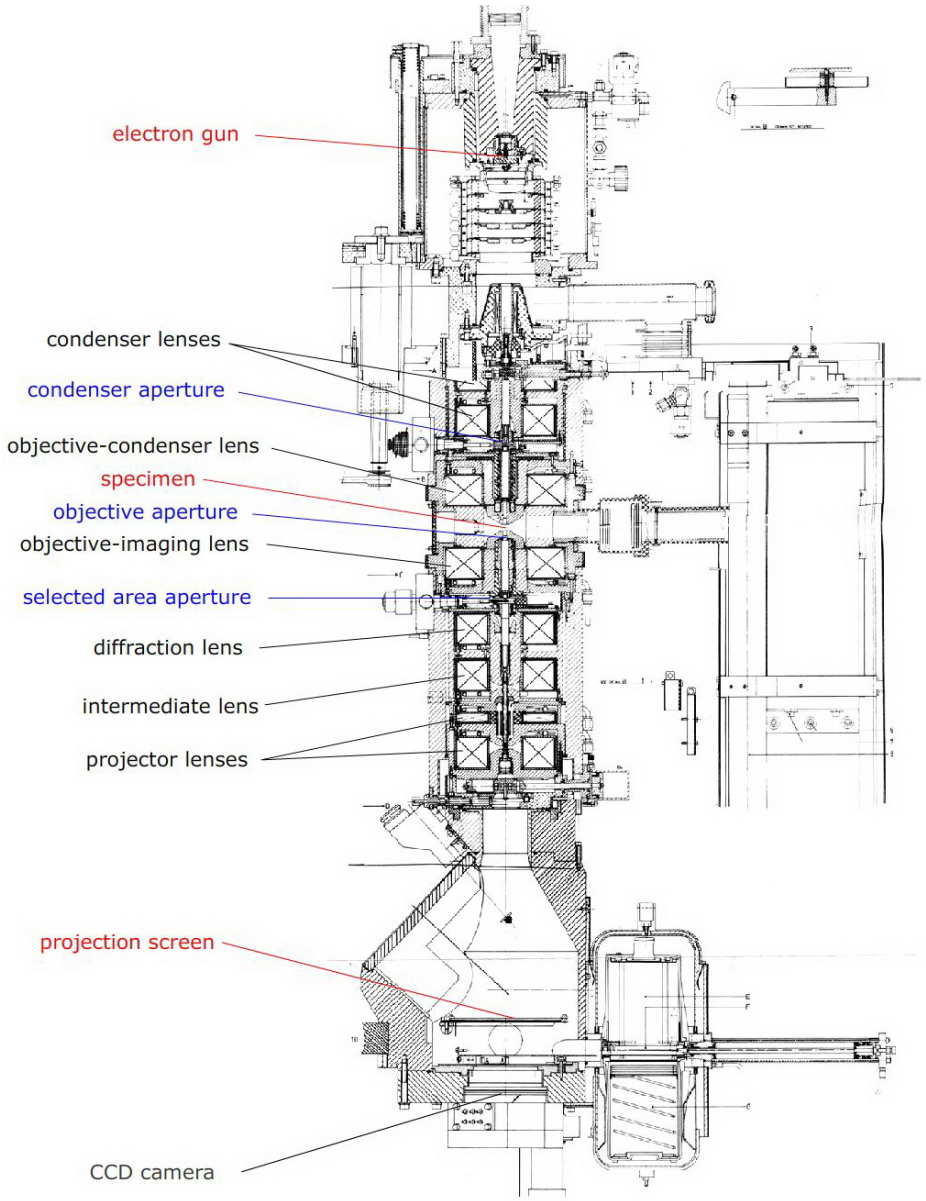

Figure 2.30: Schematics of a Philips CM200 analytical high-resolution microscope.

As a result, a diffraction pattern from the area bounded by the bottom aperture (hence the name *selected area* aperture) can be obtained on the projection screen.

In the imaging mode the intermediate lens needs to be adjusted so that its object plane coincides with the image plane of the objective lens. When this configuration is achieved, a magnified image of the specimen is visible on the projection screen.

The ray diagrams shown in Fig. 2.31 represent an idealized situation; in reality the electromagnetic lenses used in the TEM are not perfectly bending the electron beam so that the image is burdened with two major imperfections: *spherical* and *chromatic* aberration. As is illustrated in Fig. 2.32 (a), spherical aberration stems

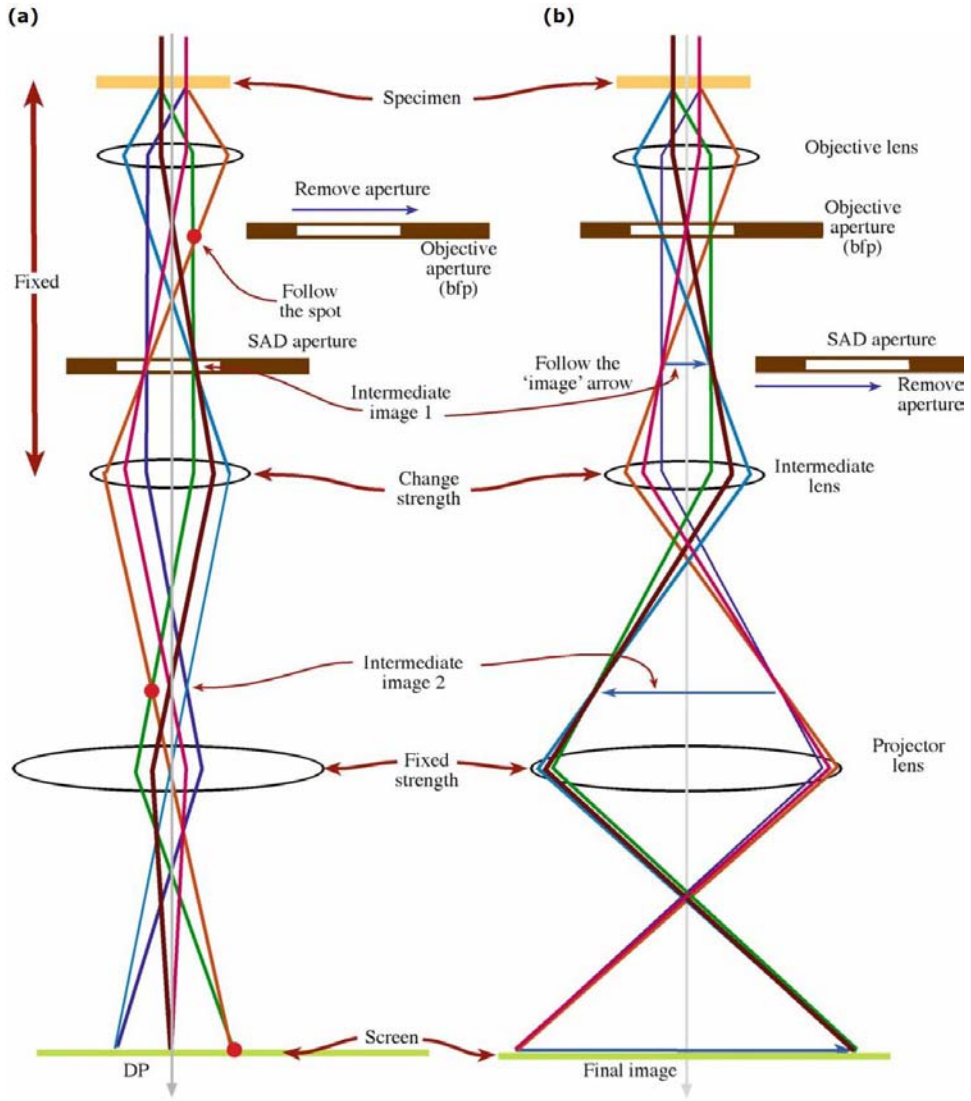

Figure 2.31: Ray diagrams illustrating two basic TEM modes: (a) electron diffraction and (b) imaging mode (adapted from Williams and Carter[99]).

from the inability of lenses to bend all electrons equally – the electrons further from the axis are bent more than those closer to the axis. Consequently, the image resolution is compromised so that the point object P gives an image P' of a disk of diameter $d = 2C_S\beta$ where C_S is the spherical aberration coefficient ($C_S = 3$ mm for our Philips CM200 TEM) and β is the collection angle of the lens.

On the other hand, chromatic aberration (see Fig. 2.32 (b)) is a consequence of the electron beam energy spread. Namely, in reality the electron beam is not perfectly monochromatic – the electrons from the electron gun can differ in energy up to several eV, which by itself is not a big issue. However, when the beam strikes the specimen, electrons with much broader range of energies emerge so that the lenses below the specimen are unable to bend all the electrons equally. Consequently, the

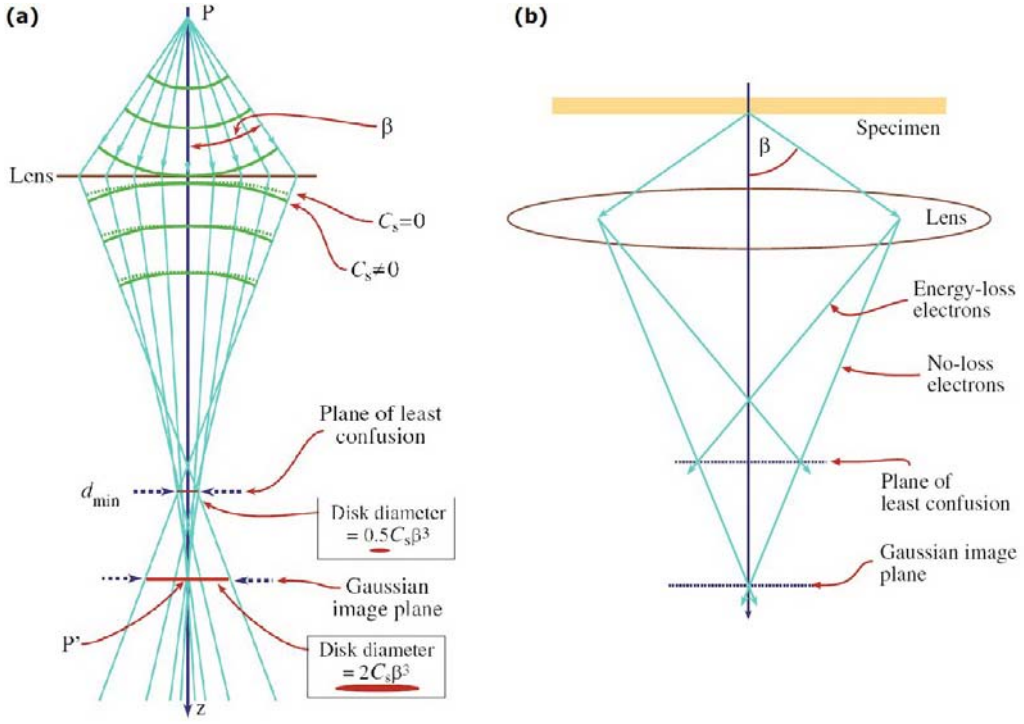

Figure 2.32: Ray diagrams illustrating two common shortcomings of lenses: (a) spherical aberration and (b) chromatic aberration. In both cases the rays bent by the lenses do not meet at a single point (adapted from Williams and Carter[99]).

image resolution is compromised.

In recent years many advances in aberration corrections have been reported[100–103] that have brought the real TEM resolution closer to the ultimate theoretical limit defined by the electron wavelength.

A typical TEM can be equipped with various detectors (see Fig. 2.33) that can record different signals originating from the electron beam – specimen interaction, just like in the case of SEMs. The most commonly acquired type of signal is the bright field (BF) signal which is recorded by a charged-coupled device (CCD) camera that produces standard (HR)TEM images. Newer models of the camera are also capable of capturing diffraction patterns that, in older TEMs, have been recorded on photographic films.

Modern scanning transmission electron microscopes (STEMs) are fitted with dark field (DF) detectors that capture highly deflected electrons. Since the intensity of deflected electrons is proportional to the atomic number of each element present in the sample[104], the contrast in DF images can reveal spatial distribution of elements in the sample (*elemental mapping*).

It should be noted here that STEMs have somewhat different principles of image acquisition: unlike conventional TEMs where the whole BF image is formed by a

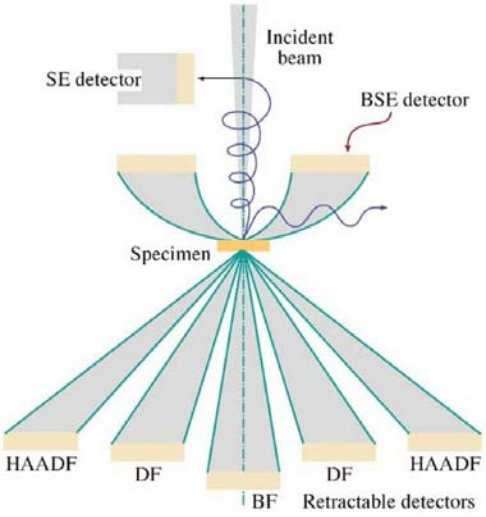

Figure 2.33: Illustration showing a possible detector configuration in a typical (S)TEM (adapted from Williams and Carter[99]).

relatively wide incident electron beam, STEMs use a finer, thinner electron beam that rasters the specimen, much like in SEM. A Faraday cup measures the intensity of the transmitted part of the incident electron beam so that the computer system can construct the image, pixel by pixel. And again like in SEM, the image magnification in STEMs is therefore a function of the size of the scanned area, whereas conventional TEMs use projector lenses to magnify the image.

In our study we utilized two transmission electron microscopes and associated equipment:

1. Philips CM200 high resolution analytical transmission electron microscope, located at UCEM. It is a non spherical aberration-corrected microscope with lanthanum hexaboride (LaB_6) cathode, operating at 200 kV, equipped with a Gatan Orius™ SC 200 CCD camera and an Oxford INCA energy-dispersive X-ray (EDX) analysis system.

2. JEOL JEM2100f scanning transmission electron microscope located at the University of Birmingham. It is a field-emission spherical aberration-corrected microscope, operating at 200 kV, equipped with a high-angle annular dark field (HAADF) detector. This part of TEM investigation was done by Ruth Chantry and Ziyou Li from the Nanoscale Physics Research Laboratory, School of Physics and Astronomy, University of Birmingham, United Kingdom.

Using these microscopes we acquired large amount of indispensable data about the fabricated nanoclusters and CNTs, summary of which is presented in Chapters 4 and 5.

ImageJ Analysis of HRTEM Images

Here we outline the basics of HRTEM image analysis using ImageJ software[105], with emphasis on the recognition of nanoclusters present on the images. The images were acquired on Philips CM200 TEM using Gatan Orius™ SC 200 CCD camera and accompanying Gatan DigitalMicrograph software[106] as 8-bit grayscale images (256 shades; with intensity 0 corresponding to black and intensity 255 corresponding to white). Such a raw image with 256 shades had to be binarized by carefully setting the threshold value so that all the pixels in the image with intensities below the threshold turn black (i.e. intensity is set to 0), while all the pixel above the threshold turn white (i.e. intensity is set to 255). An example is presented in Fig.2.34 where the threshold value is chosen so that the nanocluster area is reproduced with sufficient accuracy. Now the image is suitable for finding the surface coverage θ which is defined as the nanocluster projection area divided by the the total image area. In the next step one needs to remove all the undesired nanoclusters (coalesced or partially covered by the scalebar) in order to get an accurate size distribution of clusters.

Obviously, the accuracy of the analysis can be increased if one uses images taken at higher TEM magnifications. However, at the same time the number of nanoclusters on the image will decrease so that more images have to be analyzed for statistically significant results, which may then be time consuming. In our case it was found that the optimal magnification of images for this procedure is in the range 50 000 - 100 000 $\times$.

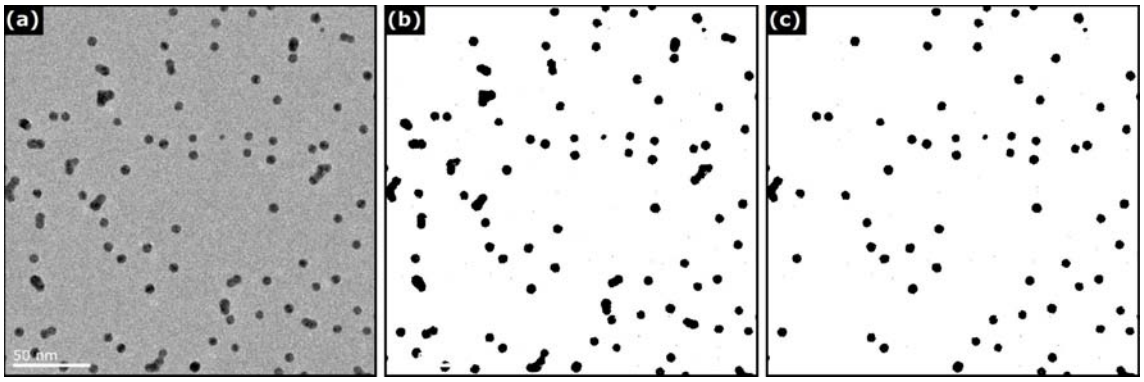

Figure 2.34: HRTEM image analysis in ImageJ software: (a) a raw 256 grayscale image as obtained in the TEM lab; (b) the same image after being binarized by setting the threshold value of 125 that gave the most accurate reproduction of nanocluster area; the surface coverage here is found to be $\theta = 4.8\%$ (c) the same image after the removal of coalesced clusters and those that were covered by the scalebar.

2.5.3 Energy-dispersive X-ray Spectroscopy

Since the Philips CM200 TEM used in our investigation was fitted with an EDX detector, it is worthwhile outlining its basic operational principles.

As previously said, when the electron beam hits the atoms within the specimen, the incident electrons can eject some of the electrons from the atoms. If, for instance, an electron is ejected from the K shell leaving a hole, then electrons from outer shells (L, M, N, O) can fill this hole. While doing so, they emit electromagnetic waves (X-rays) of energy that equals the difference between their initial and final state (see Fig. 2.35). Since the differences between energy levels are characteristic for each element, by measuring the X-ray energy spectra one can identify the elements present in the sample. Moreover, in most cases it is possible to perform a quantitative analysis that can show the fractional composition for each element in the sample.

Fig. 2.36 presents schematics of the Oxford INCA EDX system used in our investigation. Briefly, X-rays enter the Li-doped Si detector through the collimator and the window that separates the detector from the vacuum of the TEM column. On their path through the Si(Li) detector, the X-rays create electron-hole pairs whose number is directly proportional to the X-ray energy. This charge is accumulated at

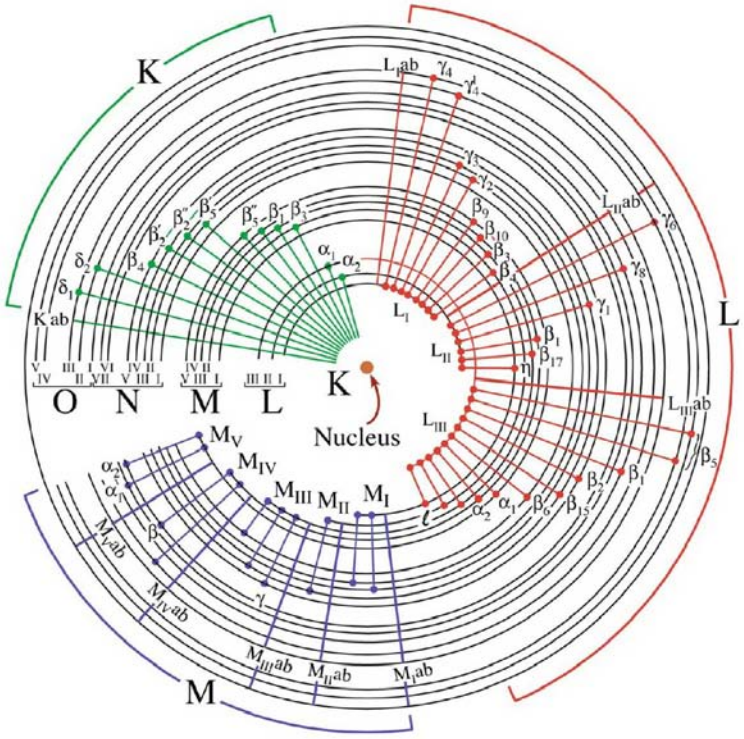

Figure 2.35: Illustration showing energy levels that electrons occupy in a heavy atom. A drop in the energy level is accompanied by the emission of a characteristic X-ray (adapted from Williams and Carter[99]).

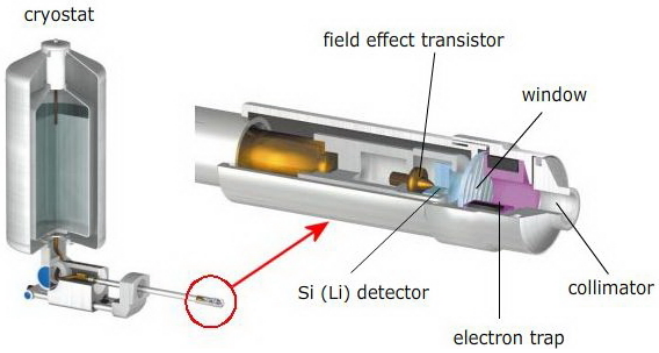

Figure 2.36: Schematics of the Oxford INCA EDX system used in our investigation (adapted from *http://www.x-raymicroanalysis.com/x-ray-microanalysis-explained/pages/tutorial1/system2.htm*).

the end of the detector giving a relatively weak signal which is then amplified by the field-effect transistor and transmitted to the computer system. The whole detector needs to be kept at low temperature to minimize the recombination of electron-hole pairs which will result with a loss of signal.

The main drawback of the whole system is the window (usually made of Be) that absorbs some of the X-ray energy even before they reach the detector. In general, the X-rays with energy < 1 keV will be seriously affected by the window absorption, and those with energy between 1 keV and 2 keV will be moderately affected. This is especially important for X-rays originating from light elements with the atomic number $Z < 11$, whose identification is therefore quite inaccurate.

A typical EDX spectrum taken from an alloy Ag-Au sample is given in Fig. 2.37, showing presence of Ag, Au, Cu, C, and O in the sample.

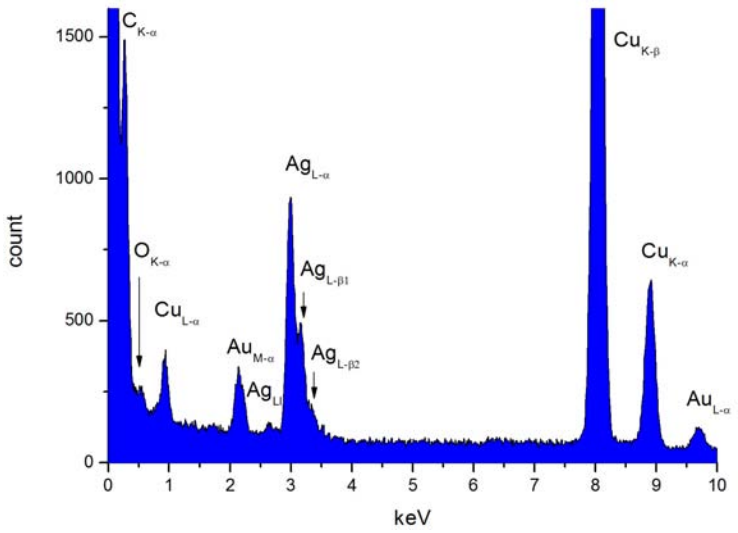

Figure 2.37: A typical EDX spectrum taken from a fresh alloy Ag-Au sample. Cu and C signals originate from the TEM grid, while some O is likely adsorbed on the a-C film.

Chapter 3

Cluster Velocity Measurements

This chapter outlines results of the velocity study for nanoclusters produced in the IGA magnetron sputtering system. Firstly, direct simulation Monte Carlo (DSMC) modeling was used to study the motion of clusters in the IGA system with respect to Ar flow, for different skimmer geometries used. The goal was to see if it was possible to increase the cluster velocity and consequently flux of sub-5 nm clusters to the deposition chamber, if alternative skimmer geometries were utilized in the IGA system. The modeling study was combined with experimental investigations – new wider skimmers were installed in the system and $Ag_{0.85}Au_{0.15}$ cluster size distributions and velocities were determined for different Ar flow rates. The performance of the new skimmers was compared to the experimental results for the original skimmer, as well as to the numerical calculations.

3.1 Cluster Velocity Optimization

Practical optimization of cluster deposition is a quite challenging issue. On their path from the source to the substrate, clusters deviate from the beam centerline due to collisions with the inevitable background gas particles. This effect is more pronounced for clusters of a smaller momentum i.e. for slower and smaller clusters. As a consequence, a considerable loss of sub-2 nm cluster flux and a partial loss of the total cluster flux occur between the source and deposition chamber. In addition, the deviations of cluster trajectories have a significant influence on the deposition of clusters onto substrates; for instance, clusters of a larger momentum might tend to land closer to the beam centerline, while those of a smaller momentum might be scattered in a wider angle. As a result, different parts of the substrate might contain clusters of different sizes. This spatial dependence is not desirable if one aims for fabrication of cluster-based devices by means of cluster deposition[21,24,26,107,108].

These problems might be minimized or completely eradicated if higher cluster velocities are achieved. However, if the velocities are too high, clusters might bounce off the substrate[109,110], severely deform or fragment upon impact[111–115], which is again highly undesirable. In addition, cluster velocity is one of the input parameters required for an efficient use of the mass filter of von Issendorff-Palmer type[30]. Hence, in order to optimize the deposition of nanoclusters, it is essential to accurately determine the cluster velocities which will enable us to asses the impact of various experimental parameters on the motion of clusters in the IGA system.

3.2 Nozzle and Skimmer Geometry

In order to achieve high deposition rates of clusters produced in IGA systems, it is necessary to form a well-defined cluster beam with a minimum spread angle, for any cluster size. For that reason IGA systems utilize a set of apertures (nozzles and/or skimmers), which can be further optimized geometrically to give collimated cluster beams of high intensity[116–122].

In our UHV-compatible IGA system (for detailed description see Chapter 2) the cluster beam is defined by a nozzle and skimmer (see Fig. 3.1). The nozzle and skimmer design that had been used in our experiments previously (see Fig. 3.1(b) – A and B) was a result of a ten year period of trial-and-error optimization which allowed for a high transmission of 5–10 nm clusters[23,29]. However, with the intention of improving the flux of sub-5 nm clusters, we decided to modify the skimmer geometry since, based on the previous work in this field[116], its internal angle was identified as the key factor in optimization of the cluster flux. The original 7/30 skimmer with the internal and external angles of 7° and 30°, respectively, was replaced by newly

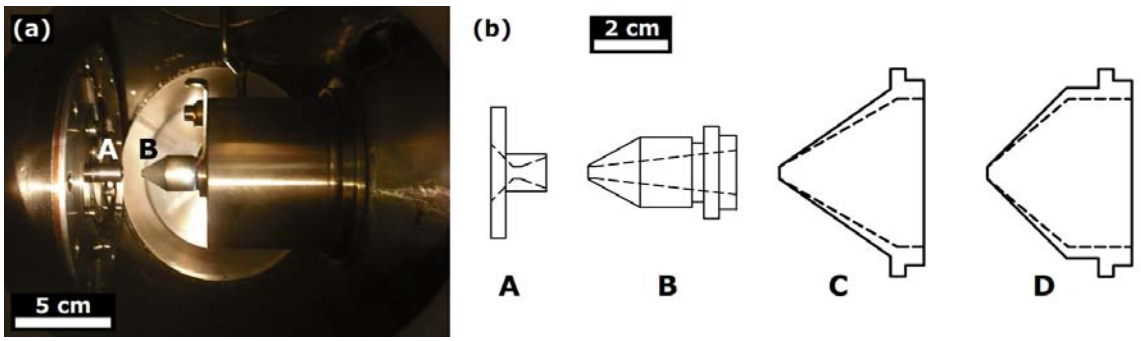

Figure 3.1: (a) Photo of the pumping chamber of our IGA system showing relative positions of the standard nozzle (A) and skimmer (B) between the source chamber and mass selection chamber. (b) A sketch of the standard nozzle (A) and standard 7/30 skimmer (B); sketches of suggested alternative skimmer geometries are also presented: 30/35 skimmer (C) and 40/45 skimmer (D).

designed skimmers of greater internal angles, while keeping the external angles as sharp as possible – such geometry minimizes the aerodynamic drag that clusters experience as they go through the skimmer. Consequently, this would increase the cluster velocities and give a higher throughput of sub-5 clusters that are otherwise severely affected by the drag. Two new skimmer designs were considered: 30/35 skimmer and 40/45 skimmer (see Fig. 3.1(b) – skimmers C and D).

3.3 Modeling of Cluster Behaviour in the IGA System

Before commencing experimental studies in our laboratory at UC, extensive modeling work on the performance of various skimmer geometries was conducted by Petr A. Skovorodko at the Institute of Thermophysics, Novosibirsk, Russia.

Numerical simulations of nanocluster motion in the carrier Ar gas were performed in two parts:

1. In the first part, the Ar flow through the nozzle and skimmer was simulated using a set of unsteady Navier-Stokes equations[123]. The nozzle-skimmer configuration used in these simulations is the one presented in Figs. 2.4 and 2.5. The main problem in modeling was that the Ar stagnation temperature T_0 (i.e. the inert gas temperature in the source chamber when the IGA system is in the stationary state) and the nozzle wall temperature T_W were unknown. For that reason, before proceeding any further, it was necessary to experimentally acquire the stagnation pressure p_0 of Ar in the source chamber, for various values of the Ar flow rate G so that the estimate of T_0 could be made. Fig. 3.2 shows the experimentally measured values (curve 1) alongside the two curves obtained by solving unsteady Navier-Stokes equations that assumed $T_0 = T_W = 77$ K (curve 2) and $T_0 = T_W = 120$ K (curve 3). It can be seen that the latter curve matched the experimental results considerably better than the former, suggesting that Ar used in our experiments is not cooled down to liquid nitrogen temperature, but to a higher temperature. Therefore the value $T_0 = T_W = 120$ K was adopted in subsequent modeling work as the best estimate. DSMC calculations were then used to model the Ar flow through the nozzle and skimmer. As noted above, the assumption was that the nozzle wall temperature was $T_W = 120$ K and that the skimmer wall was at room temperature ($T_S = 290$ K). Furthermore, it was assumed that solid surfaces of the walls were diffusely reflecting and the interaction between gas molecules was determined by the variable soft sphere (VSS) model[124] for a

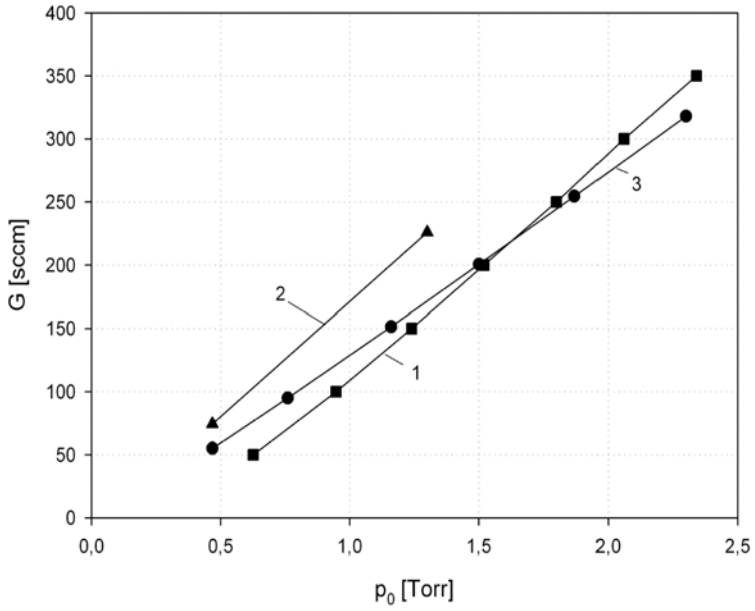

Figure 3.2: Correlation between the Ar pressure p_0 in the source chamber and the Ar flow rate G: experimentally measured values (1) and simulation results for two cases of Ar temperature: (2) $T_0 = 77$ K and (3) $T_0 = 120$ K. Here and throughout this chapter curves connecting datapoints serve as a guide to the eye for easier comparison.

repulsive potential between the molecules.

2. In the second part, the motion of clusters carried by the Ar flow was modeled using the expression for the free molecular drag coefficient of a spherical particle of diameter D moving with velocity v in the equilibrium gas of density ρ_∞ and temperature T_∞:

$$C_D = \frac{4F}{2\rho_\infty v^2 \pi D^2}$$

$$= \frac{2s^2+1}{\pi^{1/2}s^3} exp(-s^2) + \frac{4s^4+4s^2-1}{2s^4} erf(s) + \frac{2(1-\epsilon)\pi^{1/2}}{3s}\left(\frac{T_W}{T_\infty}\right)^{1/2}$$

where F is the drag force, $s{=}v/\sqrt{2RT_\infty}$ is the speed ratio, ϵ is the fraction of specular reflection of molecules on the particle surface whose temperature is T_W. In the simulation it is assumed that $\epsilon = 0$, $T_W = T_\infty$.

The simulations were performed for the $Ag_{0.85}Au_{0.15}$ clusters used in the experiments, with an approximation that the cluster density equaled the bulk alloy value ($\rho = 11.82$ g/cm^3). The second assumption was that the clusters are injected into the Ar flow field in the centerline of the nozzle neck with zero velocity.

3.3.1 Results for 7/30 Skimmer

Firstly, numerical simulations were performed for the original 7/30 skimmer with the intention of identifying possible shortcomings of that skimmer geometry. Investigations of the maximum lateral deviations r of sub-10 nm $Ag_{0.85}Au_{0.15}$ clusters from the beam centerline (see Fig. 3.3) in the skimmer region show that for the Ar flow rate of $G = 55$ sccm only clusters close to 2.5 nm in diameter efficiently pass through the skimmer without suffering large deflections. At the same time, clusters smaller and bigger than the preferred ~2.5 nm diameter tend to deviate more laterally from the central line. As a consequence of this cluster behaviour, a large portion of 1 nm $Ag_{0.85}Au_{0.15}$ clusters is lost over the ~1 m distance between the skimmer and deposition chamber. Obviously, this is a major drawback of the 7/30 skimmer geometry when the intention is to successfully deposit ~1 nm clusters.

Similar cluster behaviour was seen when the Ar flow rate was varied across a wider range of values, up to $G = 318$ sccm (see Fig. 3.4): for each given flow rate value, there exists a preferred $Ag_{0.85}Au_{0.15}$ cluster diameter for which the 7/30 skimmer has a focusing effect. For instance, at the Ar flow rate of $G = 55$ sccm the 7/30 skimmer will keep ~4 nm clusters on the beam centerline to such a precision that they will not deviate laterally more than a few millimeters over the length of ~1 m; at the Ar flow rate of $G = 200$ sccm a similar effect will occur for ~7 nm

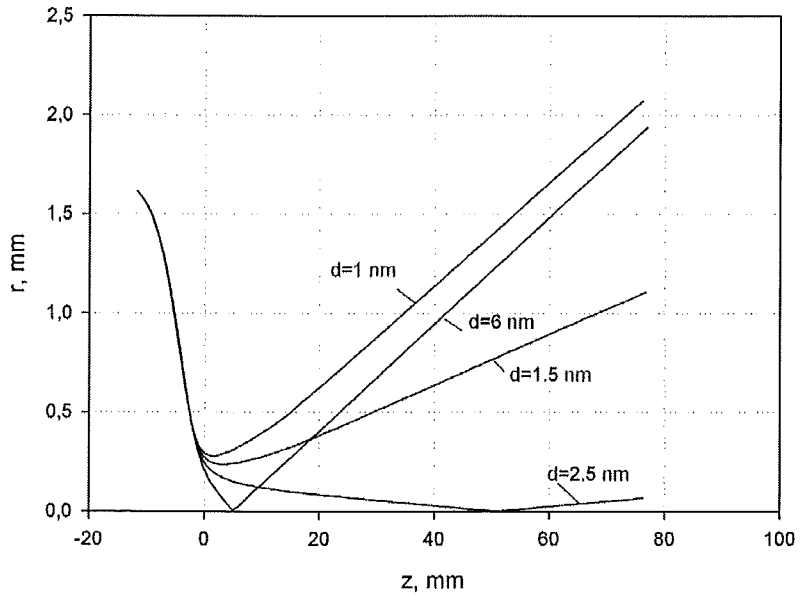

Figure 3.3: Maximum lateral deviation r from the centerline of $Ag_{0.85}Au_{0.15}$ clusters of various diameters in the 7/30 skimmer region, for the Ar flow rate $G = 55$ sccm. z is distance along the cluster beam centerline; $z = 0$ mm represents the entrance of the skimmer; $z = 40$ mm is the end point of the cluster trajectory through the skimmer.

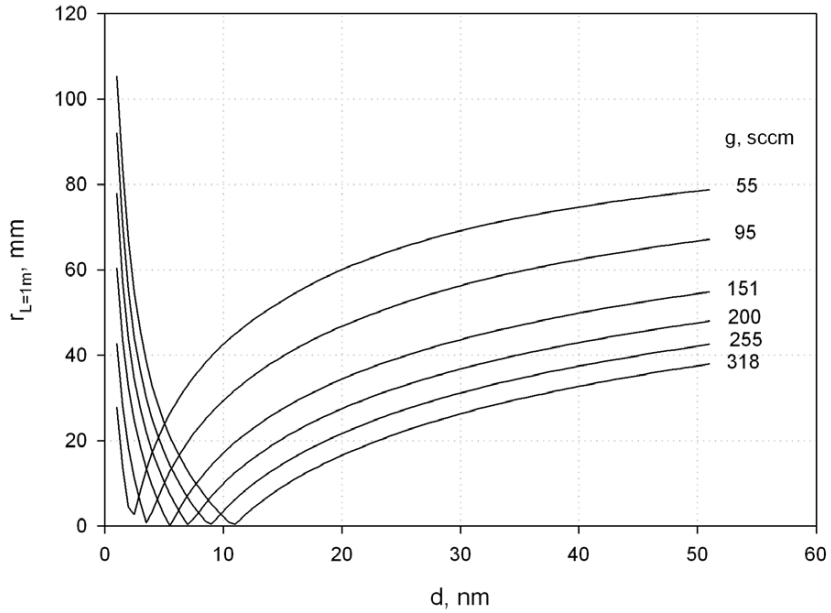

Figure 3.4: Maximum lateral deviation r from the centerline for Ag-Au clusters of diameter d at the distance of 1 m downstream the 7/30 skimmer, for various Ar flow rates G.

clusters. Conversely, one can see that clusters of other sizes are strongly deflected from the centerline – this effect is specially pronounced for sub-2 nm clusters – with the situation worsening for higher Ar flow rates. Therefore, if one aims for higher fluxes of these clusters, other skimmer geometries should be considered.

3.3.2 Results for 30/35 and 40/45 Skimmers

In order to increase the flux of sub-2 nm clusters arriving to the distance of 1 m (close to the real distance between the skimmer and the substrate in our UHV-compatible IGA system), performance of alternative skimmer geometries with 30/35 and 40/45 internal/external angles (see Fig. 3.1(b) – skimmers C and D) was simulated. Firstly, carrier Ar gas behaviour in and around the skimmer region was modeled: Fig. 3.5 presents flow fields of carrier gas axial velocities (z is distance along the cluster beam; r is radial distance from the beam centerline). When compared to the original 7/30 skimmer (Fig. 3.5 (a)), one can see a significant increase in the carrier gas axial velocities in the case of both 30/35 skimmer (Fig. 3.5 (b)) and 40/45 skimmer (Fig. 3.5 (c)). The increase is achieved within the new skimmers regions (16 mm $<$ z $<$ 56 mm), as well as in the region just behind them (z $>$ 56 mm). Note the subtle variations of carrier gas axial velocities between the 30/35 and 40/45 skimmer, in the region between z = 20 mm and z = 40 mm: in the latter case one gets higher values of carrier gas axial velocities a bit closer to the skimmer wall. This means that the effect of the aerodynamic drag is decreased as the internal skimmer angle

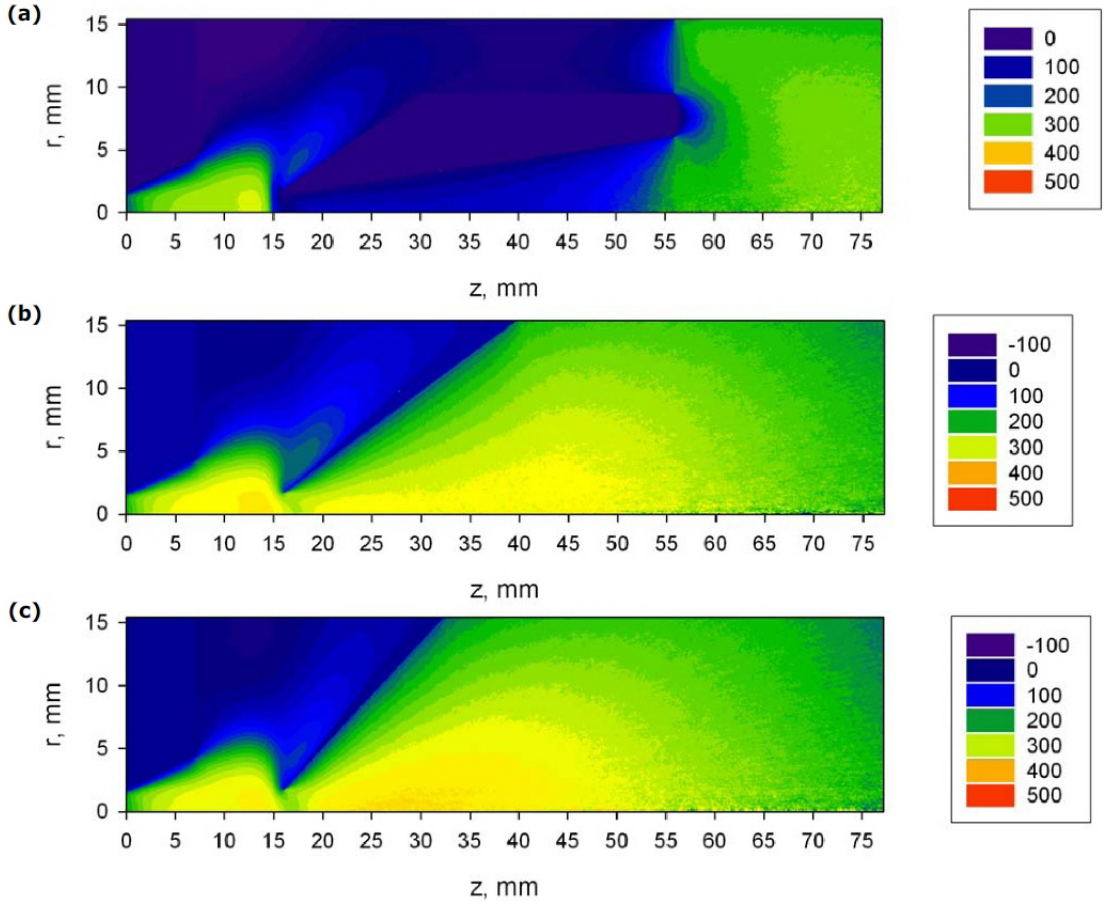

Figure 3.5: Flow fields of carrier Ar gas axial velocity for various skimmer geometries: (a) 7/30 skimmer; (b) 30/35 skimmer; (c) 40/45 skimmer. Ar flow rate is set to $G = 200$ sccm with $T_0 = 120$ K. $z = 0$ mm represents the end of the nozzle throat section of the radius $r = 1.68$ mm; $z = 7$ mm is the endpoint of the nozzle region; $z = 16$ mm is the entrance of the skimmer region. Axial velocity values are in m/s.

is increased.

As a consequence of the increased carrier gas axial velocity in the skimmer region, one might expect some enhancement of the cluster velocity as well. This hypothesis was tested by simulating the case of 6 nm $Ag_{0.85}Au_{0.15}$ clusters moving through each of the skimmer geometries (see Fig 3.6). It is evident that the cluster velocity inside the 30/35 and 40/45 skimmers ($z \geq 16$ mm) behaves differently than in the 7/30 skimmer case – it remains undisturbed and significantly higher ($\sim 20\%$) than in the case of the 7/30 skimmer where the cluster velocity drops steadily within the skimmer, which is attributed to a stronger aerodynamic drag for that skimmer geometry.

The behaviour of clusters inside the skimmers then in turn affects the values of cluster velocities at the distance of 1 m downstream the skimmers (see Fig. 3.7). Here numerical simulations of the velocity of clusters of a given diameter D show

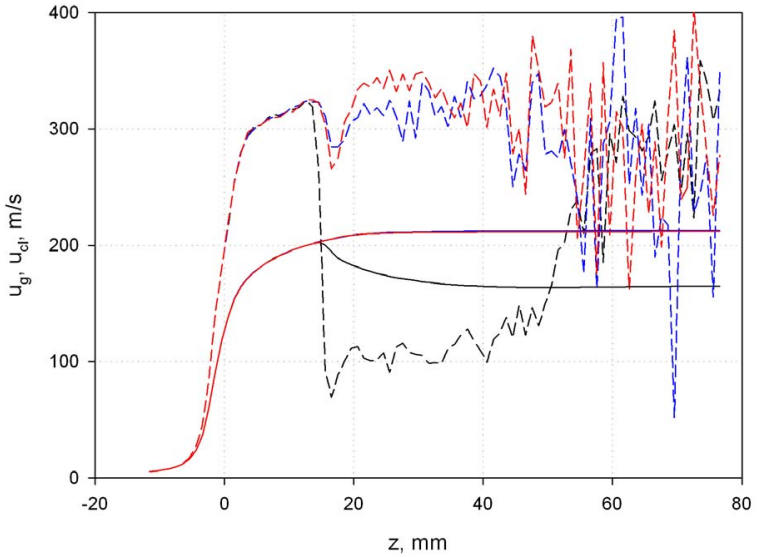

Figure 3.6: Numerical simulation results for the axial velocity of 6 nm $Ag_{0.85}Au_{0.15}$ clusters (solid lines) and carrier gas (dashed lines) on the beam centerline in the skimmer region: 7/30 skimmer (black), 30/35 skimmer (blue), 40/45 skimmer (red). $z = 16$ mm is the entrance of the skimmer. Ar flow rate was set to $G = 200$ sccm with the stagnation temperature assumed to be $T_0 = 120$ K.

a considerable increase for wider skimmers when compared to the values for the original 7/30 skimmer, even if the deceleration effect of the background gas in the mass-selection chamber is taken into account. Moreover, the biggest improvement in

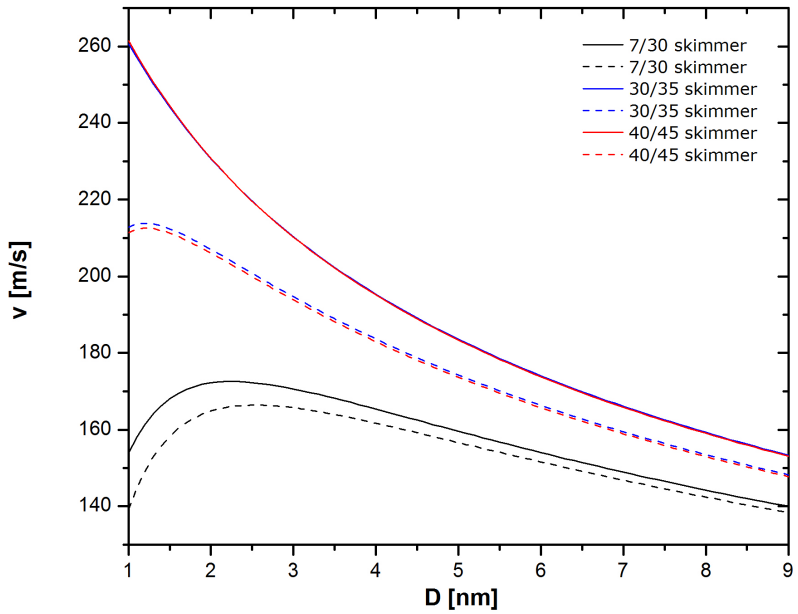

Figure 3.7: Numerical simulation results for the velocity of $Ag_{0.85}Au_{0.15}$ clusters of diameter D at distance of 1 m downstream the skimmer, for various skimmer geometries, without (solid lines) and with (dashed lines) the deceleration effect of the background gas in the mass selection chamber. Ar flow rate was set to $G = 100$ sccm.

the cluster velocity is expected for sub-2 nm clusters – from 30% to as much as 60%. This on the other hand means that sub-5 nm clusters have bigger momentum when the wider skimmers are utilized in the system, suggesting that one can expect smaller lateral deviations of cluster trajectories from the beam centerline at distance of 1 m from the nozzle. Consequently, the flux of sub-5 nm clusters should be enhanced, which was our main goal from the outset.

Increase in the carrier gas axial velocity for both 30/35 and 40/45 skimmer geometries (showed in Fig. 3.5 for the Ar flow rate $G = 200$ sccm) is expected for all flow rates in our experimental study (50–350 sccm). Again, this means that the velocity of clusters of a given diameter D is expected to be higher in the case of these new skimmer geometries, in comparison with the original 7/30 skimmer. Modeling of 7 nm $Ag_{0.85}Au_{0.15}$ cluster behaviour for various Ar flow rates (see Fig. 3.8) showed a considerable increase of the cluster velocity when these new skimmers were used, even if the deceleration effect of the background gas was considered.

Having performed numerical simulations that showed beneficial impacts of the 30/35 and 40/45 skimmers on the cluster velocities and, implicitly, on the flux of sub-5nm clusters, a decision was made to get these new skimmers machined and installed in our IGA sputtering system in order to experimentally test their performance and compare it to the modeling results.

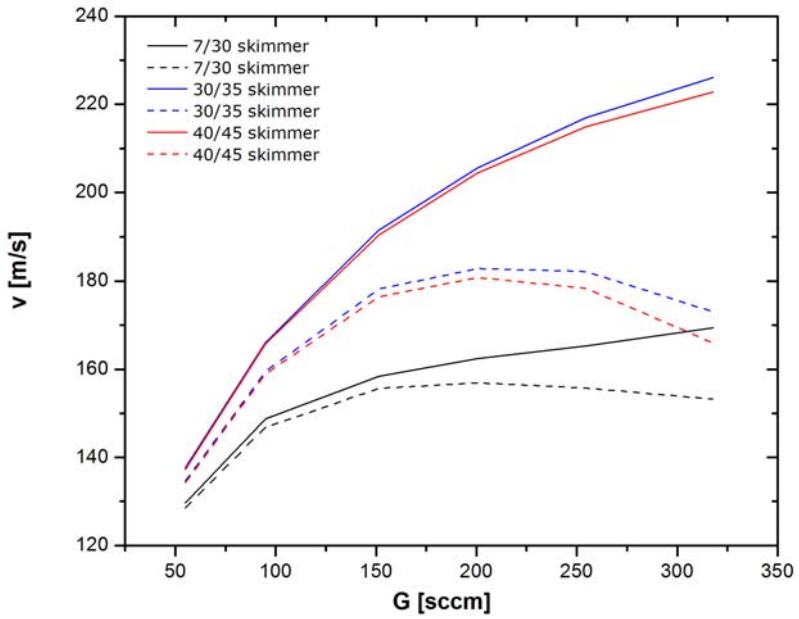

Figure 3.8: Numerical simulation results for the velocity of 7 nm $Ag_{0.85}Au_{0.15}$ clusters for various Ar flow rates G and skimmer geometries, without (solid lines) and with (dashed lines) the deceleration effect of the background gas in the mass selection chamber.

3.4 Experimental Set–up for Cluster Velocity Measurements

Our UHV-compatible IGA sputtering system[21] has been utilized for the production of $Ag_{0.85}Au_{0.15}$ nanoclusters and measurements of their velocity. Schematics of the experimental set-up for cluster velocity measurements is presented in Fig. 3.9 (for detailed description see Chapter 2). Briefly, $Ag_{0.85}Au_{0.15}$ nanoclusters are fabricated by IGA method inside the liquid nitrogen cooled source chamber (A), using a DC plasma generator operating at power of 25 W. The aggregation length i.e. the distance between the water-cooled alloy sputter target and the nozzle was varied between 6 and 13 cm, with the Ar flow rate in the range 50–350 sccm. These parameters define the size distribution of clusters leaving the source chamber i.e allow for the control of the mean cluster size. A continuous flow of Ar is maintained as the mixture of gas and clusters expands from the source (A) into the mass-selection chamber (D) through a pair of apertures – nozzle (B) and skimmer (C) – which define the cluster beam. In the differential pumping chamber located between these apertures much of the inert gas is removed from the system. This process is intended to take place without disturbing the cluster beam, but of course the nozzle/skimmer geometry significantly impacts the gas/cluster flow – this influence is the main subject of our study. While, experimentally, it has been demonstrated[22] that the system provides an intense flux of 5–10 nm clusters to a substrate, until now calculations that allow us to understand the process in detail have not been available, and it has not been possible to know whether further optimization is achievable. For the purpose of investigating the size dependency of cluster velocities, clusters that are injected into the mass-selection chamber (D) are filtered by the mass filter[30] that is set to select clusters of a specified size. It should be mentioned that the mass filter parameters used in our experiments are set in such a way that only negatively

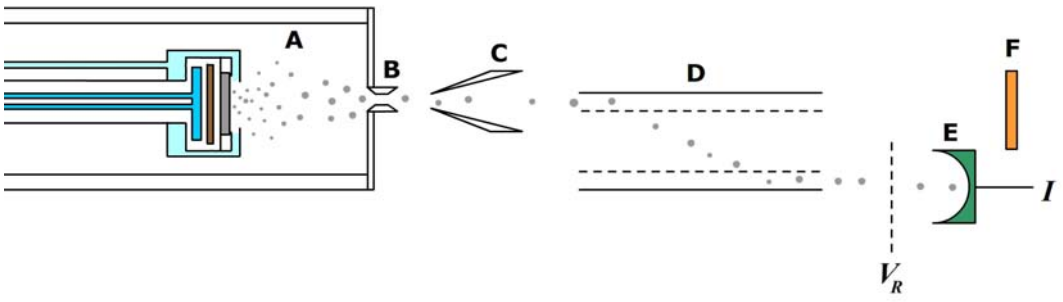

Figure 3.9: Schematics of the experimental set-up for measurements of cluster velocities. Labels are explained in the text.

charged clusters can be size-selected. These negatively charged size-selected clusters then reach a steel mesh positioned perpendicular to the cluster beam. The mesh is kept at a retarding voltage V_R which acts as a potential barrier – only clusters of a sufficient kinetic energy $E_K \geq eV_R$ will be able to pass through to the Faraday cup (E) where they will contribute to the signal I.

Note that the mass filter is commonly used as a probing tool for cluster size distribution measurements (see Chapter 2) and is switched off during the deposition of (non-selected) clusters for subsequent *ex-situ* characterization and applications (see Chapters 4 and 5).

In order to improve the signal-to-noise ratio when measuring the current I of size-selected clusters of a given diameter D, we had to maximize their intensity, keeping the Ar flow rate constant. This was achieved by adjusting the aggregation length that changed the effective aggregation volume of the source chamber, which in turn shifted the peak of the cluster size distribution toward the desired cluster diameter (a detailed study is presented in Chapter 2).

3.5 Cluster Velocity Determination

As previously stated, only charged clusters of the sufficient kinetic energy can pass the potential barrier imposed by the retarding voltage V_R:

$$\frac{1}{2}mv^2 = eV_R \tag{3.1}$$

where m is the cluster mass, v is its velocity, and e is elementary charge. Under the assumption that our clusters are spherical, the relation between the cluster velocity and retarding voltage is then:

$$v = 2\sqrt{\frac{3eV_R}{\pi\rho D^3}} \tag{3.2}$$

The density of each cluster ρ is defined by the atomic composition $Ag_{0.85}Au_{0.15}$ ($\rho = 11.82$ g/cm^3) and the cluster diameter D is determined by the mass filter. A LabVIEW controlled Keithley voltage source/picoammeter was used for setting the retarding voltage V_R and measurements of the current I from the Faraday cup at the same time.

I-V_R characteristics (a typical example is shown in Fig. 3.10) for each skimmer geometry were obtained, for various values of the argon flow rate G, cluster diameter D, and nozzle–skimmer distance L. Negatively charged clusters were passed through the mass filter and the maximum current was obtained for zero retarding voltage. As the absolute value of the retarding voltage was increased ("up" branch), the

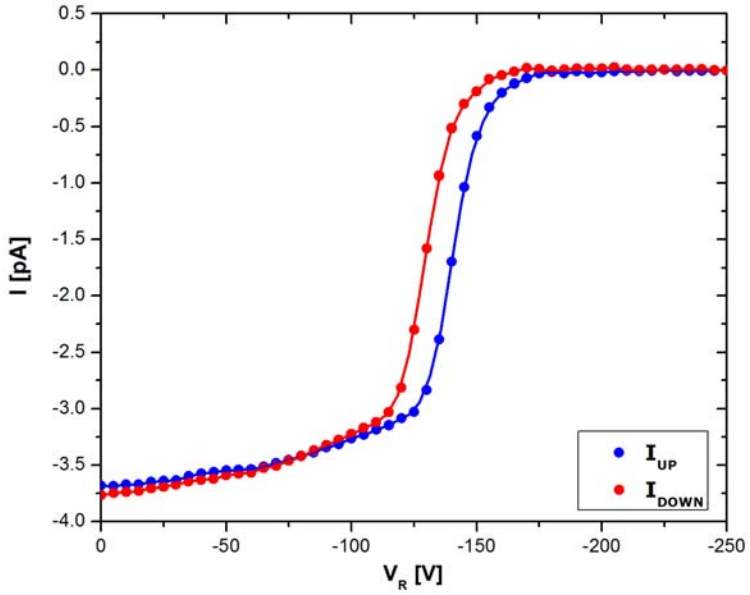

Figure 3.10: Current I from the Faraday cup as a function of retarding voltage V_R for 7 nm $Ag_{0.85}Au_{0.15}$ clusters and Ar flow rate G 250 sccm. Two branches were recorded as the retarding voltage was varied from 0 V to -250 V and back. Cluster velocities were obtained from the hysteresis-like behaviour of the curves, according to equations 3.2, 3.3, and 3.4.

energy barrier was raised which resulted with the current dropping down to zero. The retarding voltage is then decreased back to the initial zero value and the "down" branch is recorded. The mean velocity of the clusters in the beam v^* is determined by the "cut-off" retarding voltage V^* which corresponds to the steepest point on the slopes i.e. where the following relation holds:

$$\left.\frac{d^2 I}{dV_R{}^2}\right|_{V_R=V^*} = 0 \tag{3.3}$$

Finally, results were obtained in the following form:

$$v = (\bar{v} \ \pm \ \Delta v) \tag{3.4}$$

where

$$\bar{v} = \frac{v^*_{up} + v^*_{down}}{2}$$

and

$$\Delta v = \left| v^*_{up} - v^*_{down} \right|$$

3.6 Experimental Results

Following the recipe for determination of cluster velocities given in the previous section, we obtained velocity values for various skimmer geometries utilized in our experimental system. Correlation between the $Ag_{0.85}Au_{0.15}$ cluster velocity and cluster diameter D was investigated when the Ar flow rate was set to $G = 100$ sccm. In addition, cluster velocity behaviour was studied for various Ar flow rates G when the cluster diameter was set to $D = 7$ nm.

3.6.1 Cluster Velocity vs. Diameter

Fig. 3.11 shows the behaviour of cluster velocity with respect to cluster diameter D for three skimmer geometries considered. In general, it seems there has been some increase in the cluster velocity for the newly designed skimmers, although not very significant. It appears that the deceleration effect of the background gas in the mass-selection chamber might have been slightly underestimated – 30/35 and 40/45 skimmers allow more Ar to pass through so the mass-selection chamber pressure has increased significantly (by a factor of ∼3.5; see Table 3.1) and possibly counterbalanced most of the gains of using the wider skimmer angles. Since our simulations suggested the velocity increase of $\lesssim$10% in this cluster size range and the experimental error was somewhat similar, it is rather difficult to see overall benefits of the new skimmers. On the other hand, one can see that in all three cases

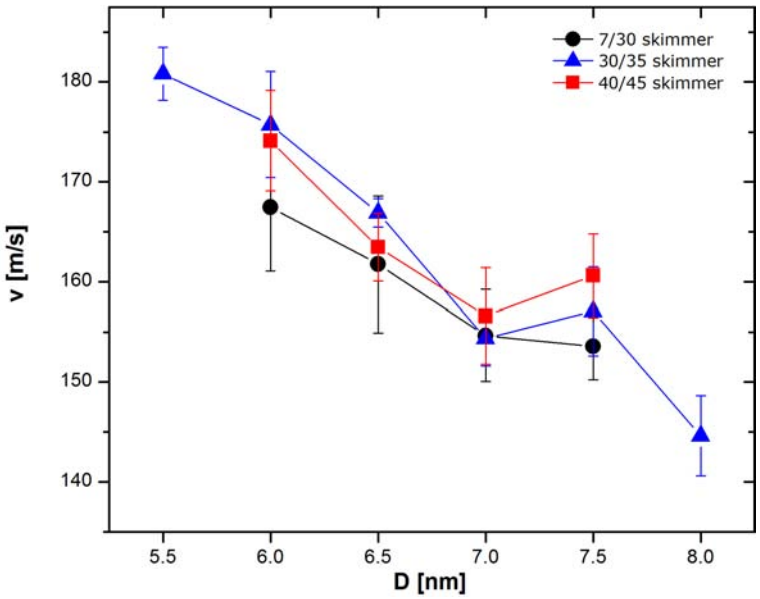

Figure 3.11: Velocity of $Ag_{0.85}Au_{0.15}$ clusters of diameter D, for different skimmer geometries used in our experiments. Ar flow rate was set to $G = 100$ sccm. The distance between the nozzle exit and skimmer inlet section was $L = 9$ mm.

Ar flow rate [sccm]	Mass-selection chamber pressure [10^{-4} Torr]		
	7/30 skimmer	30/35 skimmer	40/45 skimmer
50	0.3	1.0	1.0
100	0.7	2.2	2.3
150	1.3	4.4	4.6
200	2.2	7.5	7.8
250	3.7	> 10	> 10
300	5.8	> 10	> 10
350	> 10	> 10	> 10

Table 3.1: Mass-selection chamber pressure for various Ar flow rates, for various skimmer geometries. The distance between the nozzle exit and skimmer inlet section was $L = 9$ mm.

the cluster velocity drops for larger clusters, which is in a good agreement with the modeling results.

In order to study the cluster velocities by keeping the pressure in the mass-selection chamber at minimum, a modified version of the 40/45 skimmer with an inlet orifice diameter $d = 1$ mm was machined and installed in the system; all other skimmers used in our experiments have the inlet diameter $d = 3.25$ mm. Since the cross-sectional area of the modified skimmer's inlet is $\sim$10$\times$ smaller than in the case of any other skimmer, one could expect a significant drop in the mass-selection chamber pressure and, consequently, a considerable enhancement of the cluster velocity.

In addition, we decided to investigate the influence of the nozzle-skimmer distance L on the cluster velocity, as well as on the mass-selection chamber pressure. In this case we used the 40/45 skimmer with the inlet diameter of $d = 3.25$ mm which was brought closer to the nozzle to the distance of $L = 6$ mm. Since the flux of Ar (and clusters) increases rapidly as one gets closer to the nozzle exit (see Fig. 3.12), a considerable increase in the mass-selection chamber pressure is expected when the nozzle-skimmer distance is shortened from $L = 9$ mm to $L = 6$ mm.

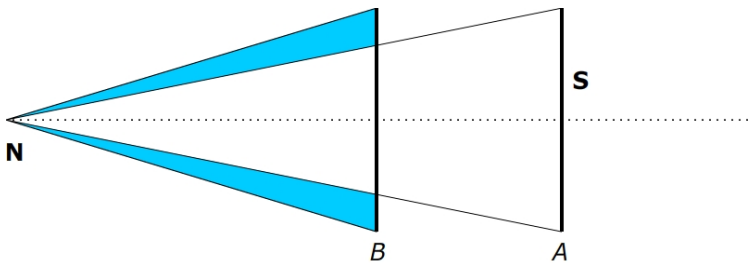

Figure 3.12: Schematics of the inert gas expansion from a nozzle **N** to a skimmer **S**: a simple geometrical reasoning can explain the increase of the inert gas flux (blue) through the skimmer when it is brought closer to the nozzle, from position *A* to *B*.

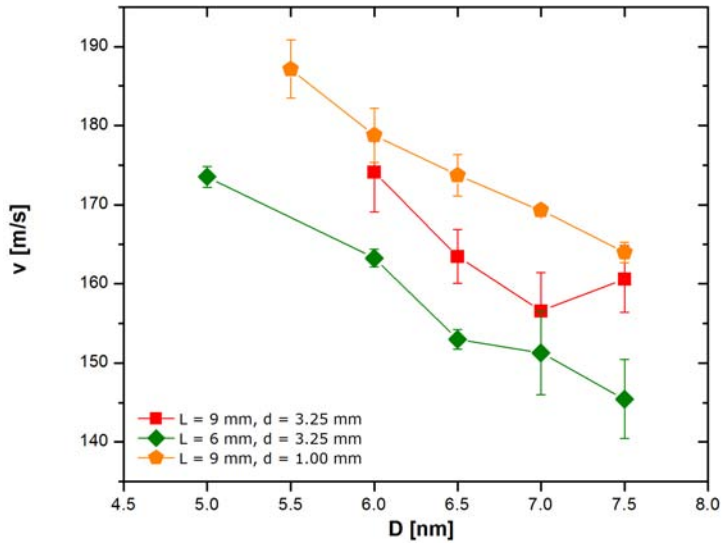

Figure 3.13: Velocity of $Ag_{0.85}Au_{0.15}$ clusters of diameter D, for 40/45 skimmer geometries: two nozzle-skimmer distances L and two skimmer inlet diameters d were tested. Ar flow rate was set to $G = 100$ sccm.

As one can see from the Fig. 3.13, in comparison with the original 40/45 skimmer, the cluster velocities were clearly greater when the modified 40/45 skimmer with the inlet diameter $d = 1$ mm was used. Conversely, when the original 40/45 skimmer with the inlet diameter $d = 3.25$ mm was used in a shorter nozzle-skimmer configuration ($L = 6$ mm), cluster velocities generally decreased below the values for the longer configuration ($L = 9$ mm).

The mass-selection chamber pressure decreased considerably for 40/45 skimmer with $d = 1$ mm in comparison with the original 40/45 skimmer with $d = 3.25$ mm (see Table 3.2) which is consistent with the increase in the cluster velocity seen when the latter skimmer was used. In opposition to that, the mass-selection chamber pressure for the short nozzle-skimmer distance increased to the values which are beyond the measuring range of our ion pressure gauge ($p > 10^{-3}$ Torr), which is

Ar flow rate [sccm]	Mass-selection chamber pressure [10^{-4} Torr]		
	L=9mm; d=3.25mm	L=9mm; d=1mm	L=6mm; d=3.25mm
50	1.0	0.1	>10
100	2.3	0.3	>10
150	4.6	0.5	>10
200	7.8	0.6	>10
250	>10	0.8	>10
300	>10	0.9	>10
350	>10	0.9	>10

Table 3.2: Mass-selection chamber pressure for various Ar flow rates, for 40/45 skimmers.

mainly responsible for the deceleration of the clusters on their ∼1 m trajectory inside the mass-selection chamber, as seen in Fig 3.13.

3.6.2 Cluster Velocity vs. Ar Flow Rate

In this set of experiments the cluster diameter was fixed to $D = 7$ nm so that the dependence of the cluster velocity on the Ar flow rate could be studied. Firstly, the study was performed using the 7/30, 30/35, and 40/45 skimmers that all have the inlet diameter of $d = 3.25$ mm, keeping the nozzle-skimmer distance at $L = 9$ mm. The results of the study are presented in Fig 3.14. We can immediately notice the lack of the expected enhancement of the cluster velocities when the 30/35 and 40/45 skimmers are used. In fact, some of the cluster velocities measured for these new wider skimmers actually sit below the velocities when the old 7/30 skimmer is used in the system. However, it is interesting to note that for the Ar flow rate range 50–150 sccm the biggest velocity values were obtained for the 40/45 skimmer, whereas the situation is reversed in the flow rate range 200–350 sccm where this skimmer geometry delivered the slowest clusters.

These results may again be explained by the behaviour of the mass-selection chamber pressure (see Table 3.1) – at low Ar flow rates the pressure stays relatively low and the deceleration effect is relatively small so that we can see some beneficial effects of using the 40/45 skimmer; at higher flow rates however the new skimmers allow more Ar to enter the mass-selection chamber increasing the background gas

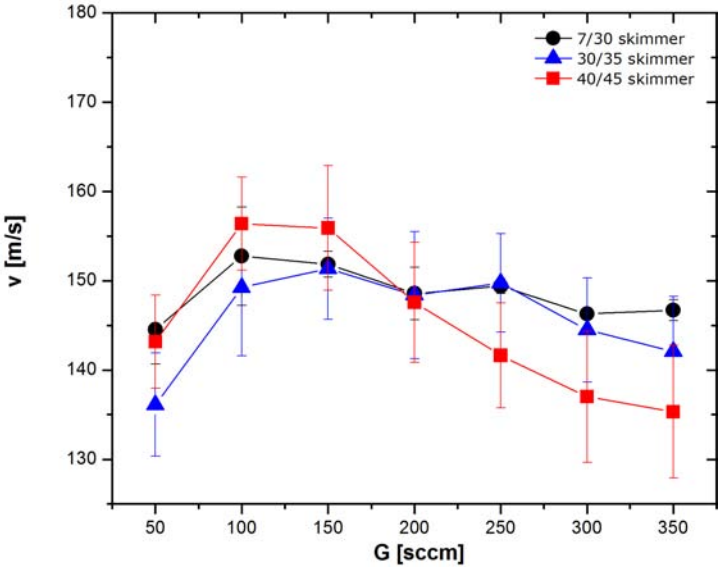

Figure 3.14: Velocity of 7 nm $Ag_{0.85}Au_{0.15}$ clusters for various Ar flow rates G, for different skimmer geometries used in our experiments. The nozzle-skimmer distance was $L = 9$ mm.

pressure, which, in turn, decelerates the clusters and counterbalances any gains in the cluster velocity that may have occurred in the skimmer. Just as in the case of the velocity–diameter study presented in the previous section, we again tested the influence of a shorter nozzle-distance configuration ($L = 6$ mm) on the velocity of 7 nm $Ag_{0.85}Au_{0.15}$ clusters for the 40/45 skimmer, for the whole range of Ar flow rates. Furthermore, we installed a 40/45 skimmer with a smaller inlet diameter of $d = 1$ mm and repeated the whole set of measurements (see Fig 3.15).

The shorter nozzle-skimmer configuration yielded cluster velocities somewhat lower than in the case of the longer distance, which is expected since more Ar is now passed into the mass-selection chamber, increasing the background pressure which decelerated the clusters. It is worthwhile noting that the difference between the cluster velocities for the two nozzle-skimmer configurations diminishes as the Ar flow rate is increased, suggesting that the gas flow through the 40/45 skimmer reaches a saturation level, which seems to be independent of the nozzle-skimmer distance.

In contrast, in the case of the 40/45 skimmer with a smaller inlet diameter ($d = 1$ mm) one can see a major improvement in the cluster velocities when compared to the 40/45 skimmer with a larger diameter ($d = 3.25$ mm). This boost was increased for the higher inert gas flow rates, reaching up to 50%. Obviously, the choice of a smaller inlet diameter resulted in a smaller Ar flow through the skimmer that consequently lowered the mass-selection chamber pressure (see Table 3.2) and therefore minimized the deceleration of the clusters.

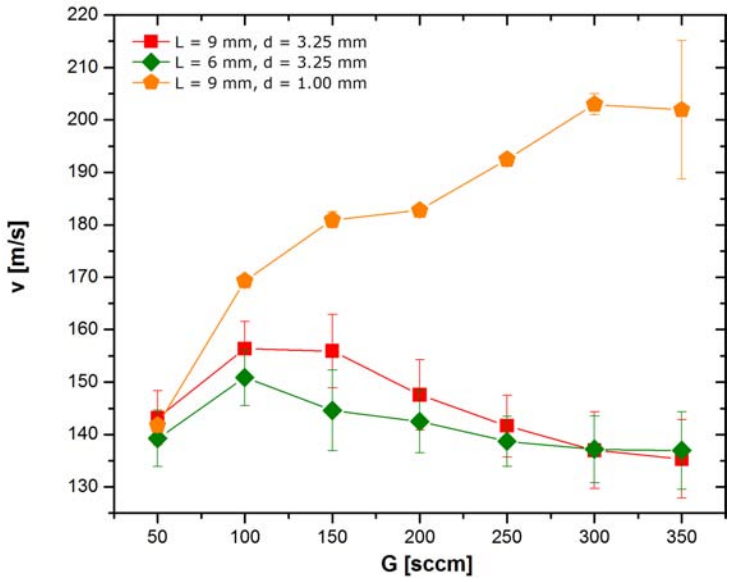

Figure 3.15: Velocity of 7 nm $Ag_{0.85}Au_{0.15}$ clusters for various Ar flow rates G, for 40/45 skimmer geometries: two nozzle-skimmer distances L and two skimmer inlet diameters d were tested.

3.7 Comparison Between Experimental Results and Numerical Simulations

The results of the simulations and experimental studies of the cluster velocity in relation to the cluster diameter D are summarized in Fig 3.16. All together four skimmer geometries were used: three (7/30, 30/35, 40/45) skimmers with the inlet

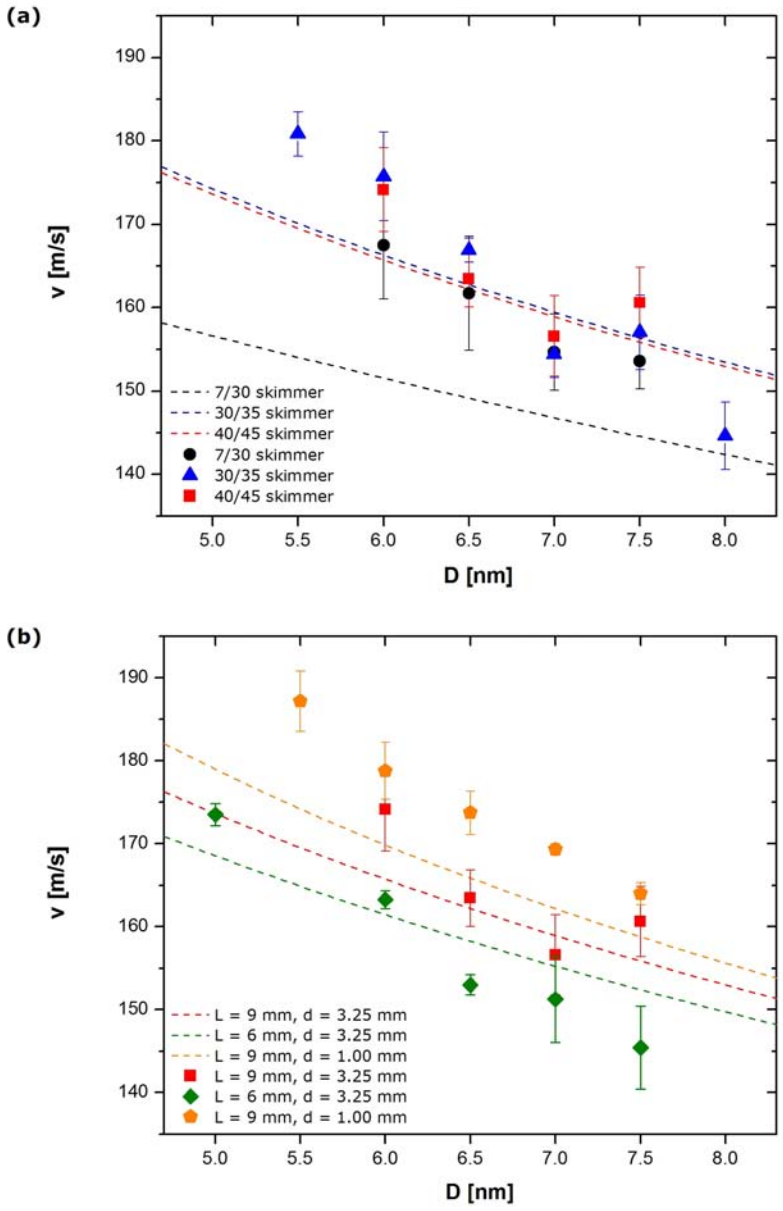

Figure 3.16: Numerical simulations with the deceleration effect taken into account (dashed curves) and experimental results (symbols) of the velocity of $Ag_{0.85}Au_{0.15}$ clusters of diameter D, for different skimmer geometries: (a) original 7/30, 30/35, and 40/45 skimmer, at $L = 9$ mm. (b) 40/45 skimmer at $L = 9$ mm and 6 mm, and a modified 40/45 skimmer at $L = 9$ mm. In all cases the Ar flow rate was $G = 100$ sccm.

diameter of $d = 3.25$ mm and an additional 40/45 skimmer with a smaller inlet diameter of $d = 1$ mm. They were all used in the longer nozzle-skimmer configuration with $L = 9$ mm, but we also studied a configuration with $L = 6$ mm in the case of the wider 40/45 skimmer. The Ar flow rate here was fixed at $G = 100$ sccm.

In general, both numerical simulations and experiments show that the cluster velocity tends to drop as the cluster diameter D is increased, for all the skimmer geometries investigated. As can be seen in Fig. 3.16 (a), there seems to be no gain in the cluster velocity when the new 30/35 and 40/45 skimmers with the inlet diameter of $d = 3.25$ mm were used. This is in contrast with the simulation results that suggested a significant increase of the velocity when the wider skimmers are used. However, when the modified 40/45 skimmer ($d = 1$ mm) was installed (see Fig. 3.16 (b)), it consistently gave velocity values that are greater than in any other case. At the same time, the background gas pressure in the mass-selection chamber was significantly lowered (see Table 3.2). These results suggest that the background gas has a considerable deceleration effect on the cluster motion in the mass-selection chamber, causing the clusters to lose their velocity and, implicitly, to deviate more from the beam centerline.

The agreement between the experimentally determined values of the cluster velocity and the results of the modeling is quite good – the measured values are within 10% of the calculated ones. Bearing in mind that the exact values of some parameters were unknown e.g. the temperature of the Ar gas in the source chamber (see Fig 3.2) or the length of the cluster trajectory inside the mass-selection chamber (assumed to be 1 m), the consistency of the results are pleasing.

It is especially interesting to compare the cluster velocity behaviour when the Ar flow rate G was varied across the range 50–350 sccm, for the cluster diameter set to $D = 7$ nm. For that reason the simulation and experimental data are replotted in Fig. 3.17. The modeling results suggested a significant negative influence of the background gas on the cluster velocities for all skimmer geometries; nevertheless, some differences between the measured values for various skimmer geometries were expected. However, the new 30/35 and 40/45 skimmers with the inlet diameter $d = 3.25$ mm produced results very similar to those obtained for the original 7/30 skimmer (see Fig. 3.17 (a)) and considerably below the simulated values of the velocity – even if the deceleration effect of the background gas is taken into account. It should be noted that not all of the mass-selection chamber pressure values were known (see Table 3.1) so that estimates had to be made for higher Ar flow rates. Moreover, even some of the measured values were quite close to the upper limit of the ion gauge range so they should be viewed with some suspicion. Therefore, it is possible that the values of the background gas pressure used as input parameters in

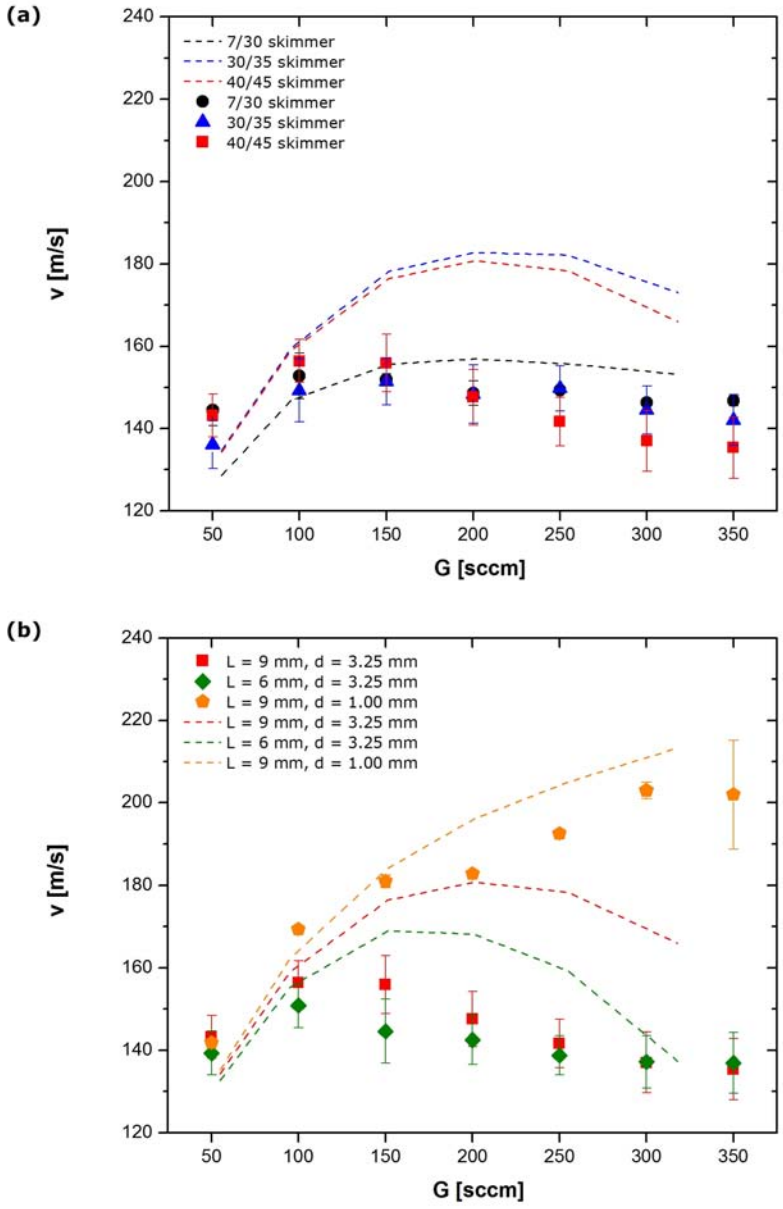

Figure 3.17: Velocity of 7 nm $Ag_{0.85}Au_{0.15}$ clusters for various Ar flow rates G, for different skimmer geometries used in our experiments: (a) original 7/30, 30/35, and 40/45 skimmer, at $L = 9$ mm. (b) 40/45 skimmer at $L = 9$ mm and 6 mm, and a modified 40/45 skimmer at $L = 9$ mm.

the simulations were underestimated; consequently, the numerical simulations gave higher cluster velocity values. Interestingly, in the case of the original 7/30 skimmer where almost all pressure values were measured, the match between the simulations and experimental results is very good.

As can be seen in Fig. 3.17 (b), the experimentally measured velocities in the case of the 40/45 skimmer with a smaller inlet diameter of $d = 1$ mm are significantly higher than in any other case. Obviously, a smaller diameter allows less Ar to pass through to the mass-selection chamber and therefore the deceleration of

clusters due to collisions with the background gas particles is less pronounced, resulting in relatively high cluster velocities (up to 50% higher than for other skimmer geometries). In that case we get quite good agreement between the experimental values of the velocity and the modeled values calculated by taking into account the negative effect of the background gas. Note that, due to the small Ar flux through the skimmer, we were again able to measure the mass-selection chamber pressure in the whole range of the Ar flow rates (see Table 3.2) – this may explain the good match between modeling and experimental results that we see for this skimmer.

3.8 Impact of Wider Skimmers on Cluster Size Distribution

As stated at the beginning of the chapter, one of the goals of these studies was to increase the flux of sub-5 nm clusters by installing wider-internal-angle skimmers. As can be seen in Fig. 3.18, when the new 30/35 and 40/45 skimmers with the inlet diameter $d = 3.25$ mm were installed in the system, cluster size distribution measurements showed a significant improvement of the flux of ∼7 nm clusters, in line with the modeling results presented in § 3.3. However, no visible improvement of the sub-5 nm cluster intensity was observed. The likely reason for that may

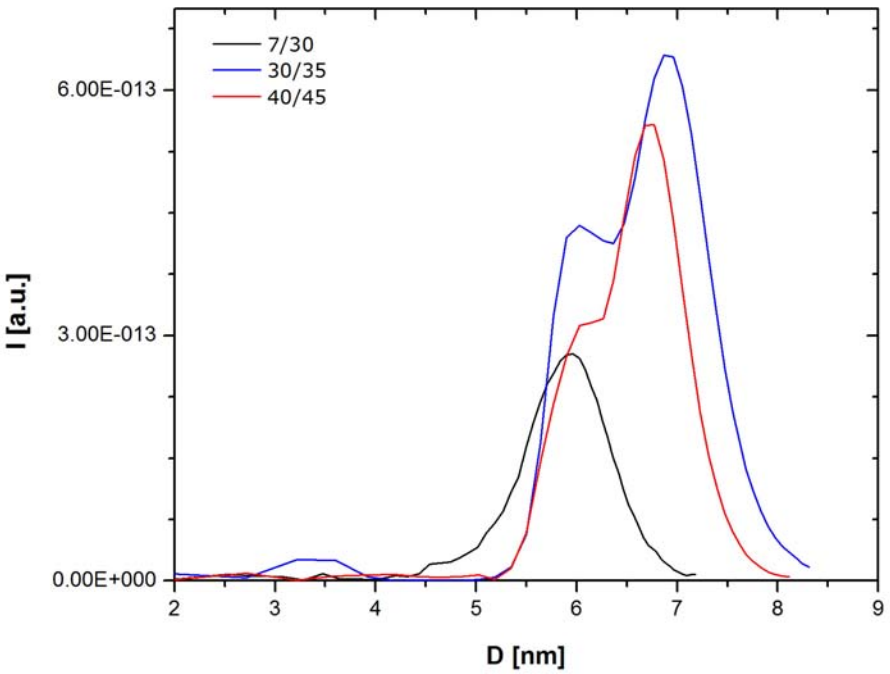

Figure 3.18: $Ag_{0.85}Au_{0.15}$ cluster size distribution for various skimmer geometries. The experimental parameters were as follows: $AL = 8$ cm, $G_{Ar} = 100$ sccm, $G_{He} = 0$ sccm, $P = 25$ W.

lay in the fact that, in case of these new skimmers, the mass-selection pressure increased so much (see Table 3.1) that it counterbalanced any benefits that the wider skimmer geometry may have had on the sub-5 nm cluster flux – most of these clusters were likely scattered on the background gas particles and deviated from the beam centerline, resulting in the loss of the flux.

The increase of the total cluster flux was also evident from the film thickness monitor: the cluster deposition rate increased from 0.02 Å/s in the case of 7/30 skimmer to 0.16 Å/s and 0.15 Å/s in the case of 30/35 and 40/45 skimmer, respectively.

On the other hand, the modified 40/45 skimmer with $d = 1$ mm did significantly decrease the mass-selection chamber pressure (see Table 3.2) – in general this should decrease the lateral deviations of sub-5 nm cluster trajectories so some increase of the sub-5 nm cluster flux was expected in this case. However, it was found experimentally that the cluster beam was extremely sensitive to the nozzle-skimmer alignment. Moreover, by adjusting the alignment it was possible to find two distinct positions that resulted in two regimes of the cluster deposition – one in which the cluster intensity was maximized (measured by the mass filter) and the second one in which the cluster deposition rate was maximized (measured by the film thickness monitor). Fig. 3.19(a) shows the cluster size distributions when each of these regimes was realized: in the case of maximum intensity, the size distribution was centered around $D = 8.5$ nm and was relatively narrow, while in the case of maximum deposition rate it was centered around $D = 14$ nm and was much broader. The latter size distribution indicated the presence of $D > 15$ nm clusters, which obviously caused the deposition rate to become considerably higher than in the case of maximum cluster intensity (0.38 Å/s to 0.08 Å/s, respectively). However, the TEM image (see Fig. 3.19(b)) of a low surface coverage sample ($\theta \lesssim 3\%$) deposited in the maximum deposition rate regime shows an unusually high proportion of joined clusters for such a small surface coverage, which can not be explained by post-deposition coalescence. This suggests that the "maximum deposition rate" position of the nozzle-skimmer configuration caused a turbulent flow of Ar and clusters through the skimmer, resulting with cluster collisions in the beam and cluster scattering in the skimmer region. This was additional supported by evidence of a cosiderable cluster deposition on the skimmer walls, as can be seen in Fig. 3.19(c).

Based on these observations, it seems unlikely that sub-5 nm clusters can successfully pass through the skimmer without suffering a large deflection from the beam centerline, most probably caused by the turbulent Ar flow and/or stronger aerodynamic drag when the skimmer's inlet diameter is only $d = 1$ mm.

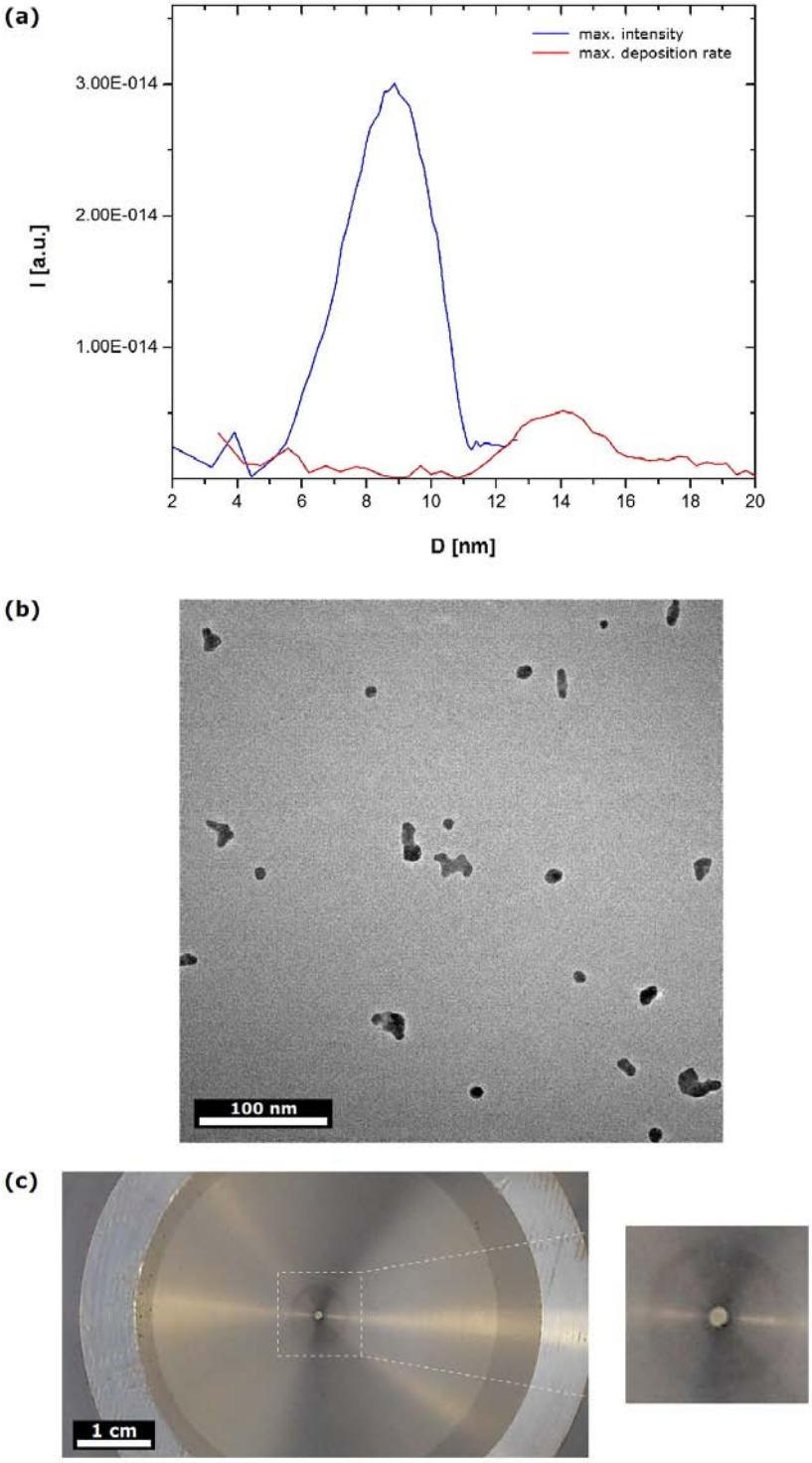

Figure 3.19: (a) $Ag_{0.85}Au_{0.15}$ cluster size distributions for the 40/45 skimmer skimmer with the inlet diameter of $d = 1$ mm, showing two distinctive regimes of the nozzle-skimmer alignment: "maximum intensity" and "maximum deposition rate". The experimental parameters were as follows: $AL = 13$ cm, $G_{Ar} = 150$ sccm, $G_{He} = 0$ sccm, $P = 25$ W. (b) TEM image of a low surface coverage ($\theta \lesssim 3\%$) $Ag_{0.85}Au_{0.15}$ sample fabricated under "maximum deposition rate" regime, showing a high proportion of joined clusters. (c) Photo of the inner side of the 40/45 skimmer with the inlet diameter of $d = 1$ mm. A significant deposit of material can be seen just around the inlet, suggesting considerable dispersion of clusters in that region.

3.9 Conclusions and Outlook

In this chapter we presented results of the Ag-Au nanocluster velocity determination for clusters produced in our IGA magnetron sputtering system. Initially, direct simulation Monte Carlo (DSMC) modeling was used to study behaviour of cluster velocities with respect to cluster diameter D and inert gas flow G, for different skimmer geometries used in the system. It was found that the cluster velocity could potentially be enhanced if skimmers with wider internal/external angles were utilized. More importantly, the simulation results indirectly implied that it would be possible to increase the flux of sub-5 nm clusters if certain combinations of these new skimmer geometries and Ar flow rates are realized in the system.

Experimental investigation revealed that the cluster velocity values obtained for the new 30/35 and 40/45 skimmers remained at the same level as for the original 7/30 skimmer, contrary to the initial modeling results. This was attributed to the presence of the background gas within the mass-selection chamber: in the case of the new skimmers, the Ar flow to the mass-selection chamber was significantly increased which raised the pressure in that part of the system, causing deceleration of clusters through collisions with the background gas. As a result, the flux of smaller clusters was mostly lost on their $\sim$1 m trajectory through the mass-selection chamber.

By installing a modified 40/45 skimmer with a smaller inlet diameter $d = 1$ mm, the passage of Ar to the mass-selection chamber was significantly lowered, which minimized the background gas pressure. Consequently, the cluster velocity increased considerably – up to 50% higher than for any other skimmer geometry. However, no increase of the flux of sub-5 nm clusters was observed; most likely due to a stronger effect of the aerodynamic drag for the inlet with $d = 1$ mm.

It seems there is a competition between two effects: on the one hand, a wider skimmer minimizes the aerodynamic drag, which is generally beneficial for cluster flux (especially for the sub-5 nm cluster flux). On the other hand, a wider skimmer allows for more Ar to pass through and increase the mass-selection chamber pressure, which is in general detrimental for the cluster flux (especially for the sub-5 nm cluster flux).

Based on the experimental observation, in future work one might consider using a wider skimmer at a nozzle-skimmer distance $L > 9$ mm, in order to exploit the benefits of a wider skimmer whilst keeping the mass-selection pressure at relatively low values. Of course, one of the solutions for minimizing the background pressure would be to use a pump of a greater pumping rate than the current one installed in the system (Pfeiffer Turbo with the pumping rate of 900 liters per second).

Chapter 4

Experimental Studies of $Ag_{0.85}Au_{0.15}$ Nanoclusters

A comprehensive study of $Ag_{0.85}Au_{0.15}$ clusters and cluster-based thin films was conducted in order to identify their structural, morphological, and compositional properties, as well as their stability over longer periods. Samples produced in the IGA magnetron sputtering system were systematically investigated by transmission electron microscopy (TEM) over a period of more than two years. Here we present the results of the study, propose the dynamics of time-dependent changes in samples and discuss their implications on catalytic performance of such noble metal alloy clusters.

4.1 Alloy Nanoclusters

Over the last couple of decades metallic nanoclusters have attracted much attention: their unusual and exciting size dependent properties[125,126] have opened new fields of research, such as plasmonics[127,128] or nanocatalysis[129], as well as generated much activity in modeling[130–132]. Within the subject of metallic nanoclusters we have recently seen an increased interest in alloy nanoclusters[133,134] whose characteristics seem fascinating from many standpoints. Moreover, due to a huge number of possibilities in choosing their size and composition, one could expect a plethora of different properties for each nanoalloy system under consideration. For this reason, it is very likely that some of these nanoalloys will be specially appealing from the point of view of applications. For instance, it has been demonstrated that Fe-Pt nanoclusters posses magnetic Fe cores while having catalytically active Pt shells[135]. Another interesting case is the Ag-Au system which, for example, shows synergistic effects in catalysis[136]. The latter nanoalloy system is the main subject of our

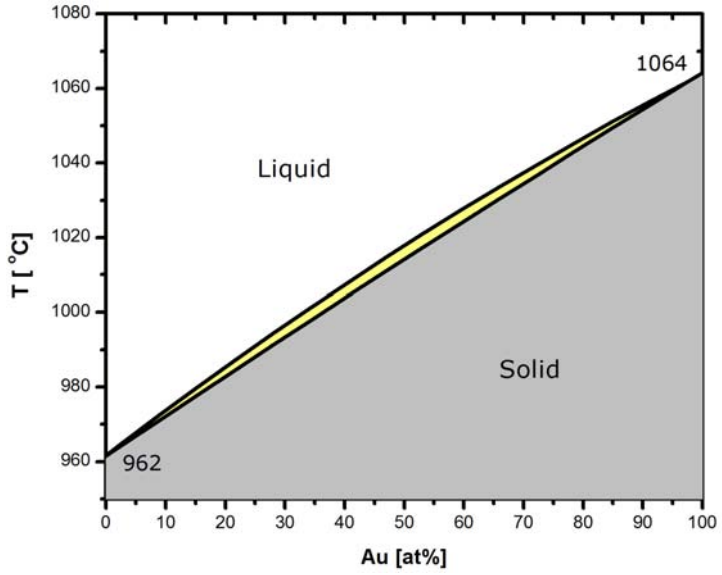

Figure 4.1: Phase diagram of bulk Ag-Au system showing full miscibility of Ag and Au.[138]

investigation whose results will be presented throughout this chapter.

4.2 Ag-Au Nanoclusters - Overview

In this section we introduce the topic of alloy nanoclusters with emphasis on nanosystems that contain Ag and/or Au. We outline the major research advances that have happened in this fast-growing field of physical sciences over the last few decades.

4.2.1 Ag-Au System

Ag and Au are precious metals known to humans for millennia that have firstly been used as ornaments and jewelery. Their remarkable physical properties – they are very ductile, malleable, and soft – made them very suitable for early metal processing which, combined with their high value, resulted in a widespread usage as currency coins for many centuries. With the technological advances the mankind has made it became obvious that other physical properties of these noble metals are even more appealing, such as their high electrical conductivity and corrosion resistivity. These properties made them very desirable in many applications, e.g. as contacts in many electronic devices.

Ag and Au are transition noble metals, both crystallize in the face centered cubic (FCC) lattice and have a very similar lattice parameter (a_{Ag} = 4.08 Å, a_{Au} = 4.09 Å)[137]. As a result, bulk Ag and Au show full miscibility at any composition, as can be seen in their phase diagram given in Fig. 4.1.

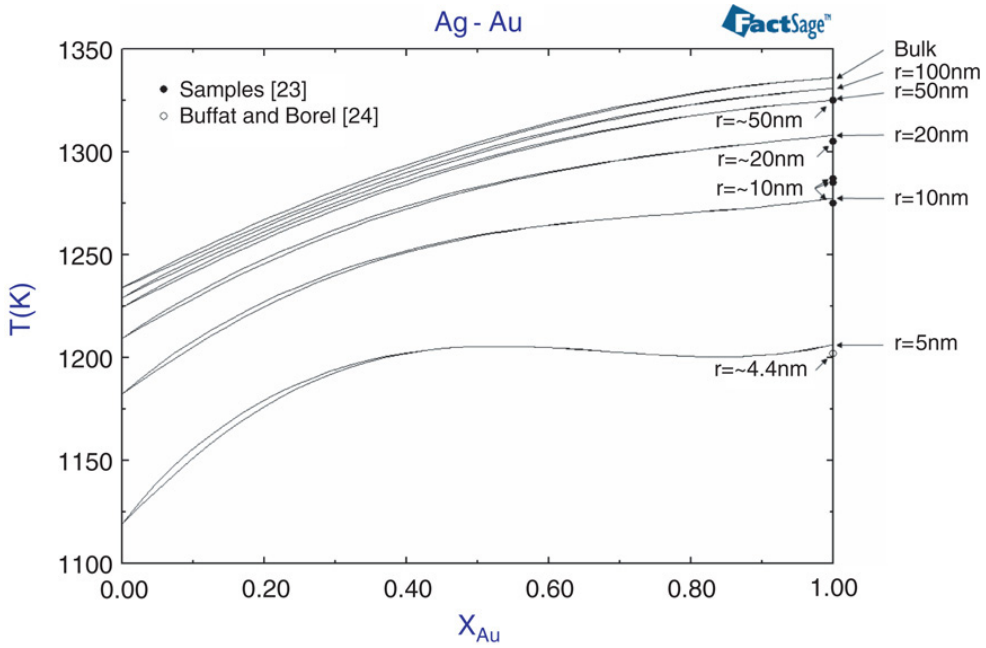

Figure 4.2: Calculated nanoscale phase diagram of Ag-Au system showing full miscibility of Ag and Au for systems with $D \geq 5$ nm. Note however that the melting point decreases as the size of the system gets smaller, which agrees well with experimental observations for Au nanoclusters. [139]

4.2.2 Nanoscale Ag-Au System

However, it became obvious that, as a system gets smaller, its bulk phase diagram may not be valid any more. For example, Buffat and Borel[1] showed experimentally that the melting temperature of Au nanoclusters drops as their size is decreased: the drop was observed for clusters as big as $D \sim 10$ nm and was highly pronounced for those with $D < 5$ nm. This behaviour indicates that the concept of a phase diagram needs to be reconsidered so that a nanoscale system of any size has an associated "nano" phase diagram. Some computational attempts have recently been made for the case of nanoscale Ag-Au system – Park and Lee[139] constructed several size-dependent diagrams (see Fig. 4.2) by applying the CALPHAD method in the case of the nanoscale Ag-Au system. Their nano phase diagrams show a good agreement with the experimental results of Buffat and Borel for pure Au clusters. Note that the calculated Ag-Au phase diagram suggests a significant drop of the melting temperature as the system gets smaller than $D = 10$ nm, for all compositions.

The calculations of Park and Lee is a very good example of the modeling studies performed on nanoscale Ag-Au systems – the next section gives a brief overview of this topic.

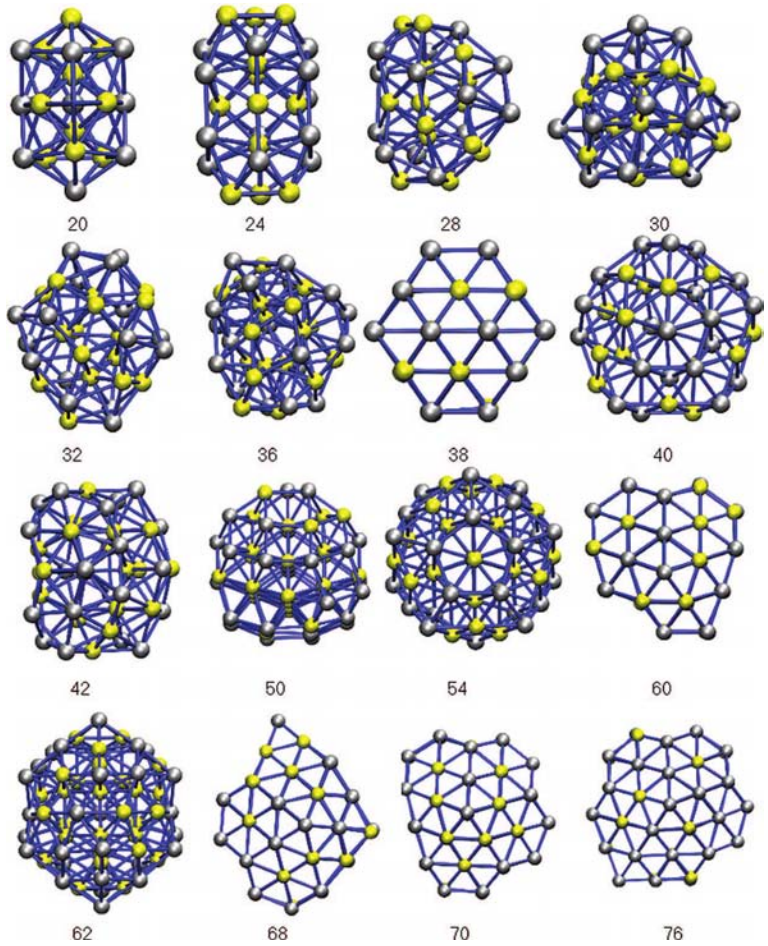

Figure 4.3: Energetically most favourable structures of small Ag-Au clusters. Au atoms are depicted yellow.[144]

Modeling of Ag-Au Nanoclusters

The most comprehensive modeling of Ag-Au nanoclusters was performed by Chen and Johnston[140–144] whose studies mainly dealt with structural characteristics of alloy clusters consisting of a relatively small number of atoms (< 300). They were trying to answer the question of thermodynamically most stable structures for a given number of Ag and Au atoms, including possible phase segregation into core-shell structures. For example, by using a genetic algorithm (GA) approach and density functional theory (DFT) calculations for Ag-Au clusters of ratio close to 1:1 in the range of 20-150 atoms, they identified 34 decahedra (Dh), 31 icosahedra (Ih) and 2 close-packed structures as energetically most favourable[144]. Also, their results indicate that all of these alloy nanoclusters are fully and randomly alloyed, as visible in Fig. 4.3. Note however that the size of the clusters under scrutiny was in the range 1 nm $< D <$ 2 nm with the composition chosen close to 1:1.

Similarly, Qi and Lee[145] investigated preferred structures in somewhat larger

Ag-Au clusters, containing 561 atoms. Their calculations also showed that, for the Ag:Au atomic ratios of 253:308 and 308:253, a fully alloyed structure is preferred over core-shell, when the structural motif was predefined as cuboctahedral (cOh); additionally, very similar results were obtained for Ih, Dh, or even spherical nanoclusters of similar Ag:Au ratios.

Rossi et al.[146] used a somewhat different approach: they set the number of atoms in the cluster to 34 and 38 and then varied the composition across a wider range to study the optimal structures of these small clusters. It was found that the atomic ordering would strongly depend upon the composition and that various structures could be obtained, including an amorphous Ag-Au core-shell. In general, their calculations revealed the tendency of Ag atoms to be located on the vertex and edge sites in these clusters.

Very recently, Ringe et al.[147] applied the Wulff construction on Ag-Au nanoclusters with $D = (3, 7, 15, 30)$ nm to examine the fraction of Au atoms on the surface of these clusters, for various Ag:Au compositions. Their results show that the number of Au atoms on the surface stays close to zero even if the total fraction of the Au component is as high as $\sim$97%, in the case of 30 nm clusters. Moreover, even in the case of 3 nm clusters, complete surface segregation of Ag atoms is observed when the total Au content is $\sim$70%. Hence, their study of nanoclusters suggests a Au-Ag core-shell structure over a wide range of total Au content. A similar conclusion was obtained by Negreiros et al.[148] based on their atomistic study of Ag-Au nanocluster formation using the Bozzolo-Ferrante-Smith (BFS) method for alloys.

Another notable modeling study is the one from Michaelian and Garzon[149] who observed a major difference in the melting behaviour of alloy Ag-Au clusters, compared to the pure Ag and Au clusters: the melting transition was much wider, suggesting that some sort of pre-melting of alloy nanoclusters may occur prior to their complete melting.

As mentioned in the introduction, one of the most appealing properties of Ag-Au nanoclusters is their very good catalytic performance, e.g. in CO oxidation. In that sense some modeling has been performed in order to better understand the processes behind such high catalytic activity. The recent works of Popolan et al.[150] and Kim et al.[151] indicate that high flexibility of Ag-Au nanocluster structure (see Fig. 4.4) may be responsible for the increased catalytic activity of Ag-Au nanoclusters in CO oxidation.

It should be emphasized though that all theoretical studies presented in this section involved modeling of free unsupported clusters in vacuum, containing no impurities except for those deliberately added (such as CO). Furthermore, in most of the studies the cluster size was relatively small compared to our standard size

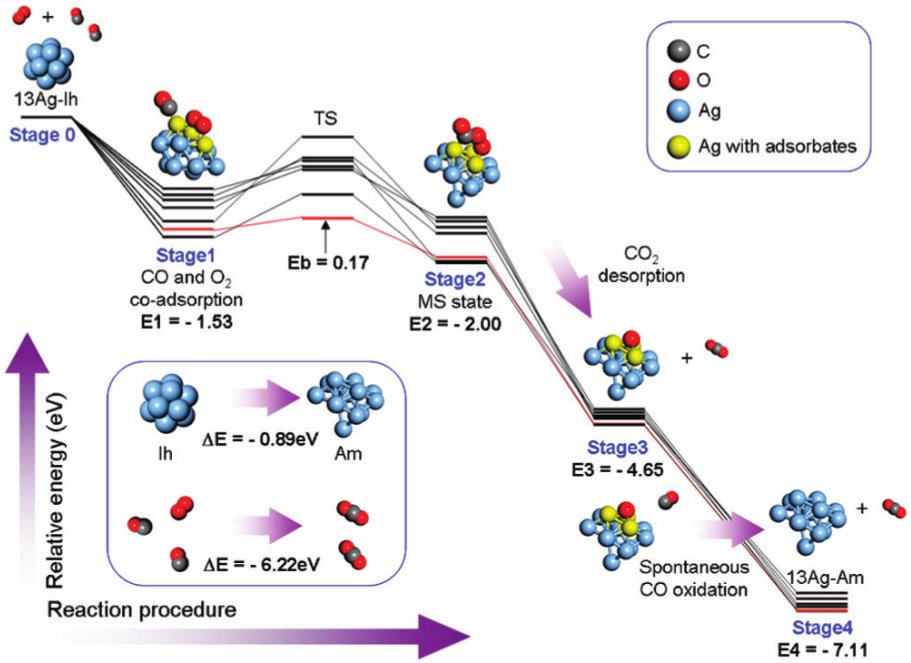

Figure 4.4: Proposed mechanism of CO oxidation on Ag-Au clusters. Note the change of the cluster structure during the process.[151]

range (3 nm $< D <$10 nm). The realistic conditions on the other hand are quite different to the ideal clean environment considered in the modeling studies; for instance, it was shown that a single impurity atom significantly affects the melting temperature of otherwise pure Ag nanoclusters[152].

Hence, these computational results should be considered with some reserve since these might significantly differ from experimental results. Hopefully, future modeling studies of alloy nanoclusters will take into account at least some more realistic conditions which will bridge the gap between the theory and experiments that exists today.

Previous Experimental Studies of Ag-Au Nanoclusters

The vast majority of experimental investigations are related to Ag-Au nanoclusters synthesized by means of wet chemistry[153–183]. Such methods include production of colloidal Ag-Au clusters, dispersed in a solution and regularly capped with some kind of surfactant which prevents their agglomeration. Therefore, the final properties of wet-synthesized nanoclusters, such as their shape or structure, might be strongly influenced by the environmental conditions in which the synthesis takes place.

In this sense, the question of equilibrium Ag-Au nanocluster structure is rather controversial: fully alloyed nanoclusters[167–169] have been reported, as well as Ag-Au[170–173] and Au-Ag[174–176] core-shell structures (see Fig. 4.5); moreover, onion-like

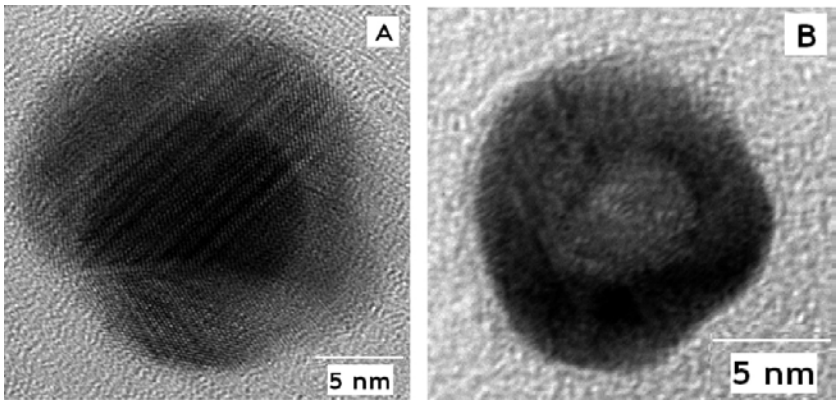

Figure 4.5: HRTEM image of Au-Ag (a) and Ag-Au (b) core-shell nanoclusters prepared by wet synthesis.[166]

Au-Ag-Au and Au-Ag-Au-Ag nanoclusters were produced by Rodriguez-Gonzalez et al[177]. Furthermore, Li et al.[178] showed composition dependent structural behaviour: for 4 nm seeded alloy clusters with Ag:Au ratio of 1:2 the observed structure was Ag-rich core and Au-rich shell, while those with ratio of 2:1 did not exhibit a core-shell structure. Recently, Gonzalez et al.[179] suggested that the ordering of Ag and Au atoms depended on the environment in which the clusters were synthesized. In addition, several experimental attempts were made to induce alloying in core-shell clusters: Hodak et al.[180] used laser radiation to alloy initially Au-Ag core-shell clusters; Shore et al.[181] achieved the same effect by heating Au-Ag core-shell clusters. Similarly, Wang et al.[182] heated Ag-Au core-shell clusters and turned them into fully alloyed particles.

Interestingly, Shibata et al.[183] showed that initially Au-Ag core-shell nanoclusters synthesized in methanol undergo *spontaneous* size dependent alloying over time. This result raises the question of long-term structural stability of Ag-Au nanoclusters, which is likely to depend on conditions in which the nanoclusters are stored.

Apart from wet chemistry syntheses, several other experimental techniques have been applied for production of Ag-Au nanoclusters. Cottancin's group used inert gas aggregation (IGA) from laser-vapourized alloy targets[184,185] to fabricate nanoclusters of various Ag-Au concentrations and then investigated their optical properties. Lidgi-Guigui et al.[186] investigated the growth of alloy Ag-Au nanoclusters by evaporating Ag atoms onto size selected Au clusters implanted in graphite surfaces; Au clusters used in their experiment were produced by IGA magnetron sputtering and size selected in the mass-filter of von Issendorff-Palmer type[30]. Similarly, Okazaki et al.[187] managed to produce alloy Ag-Au nanoclusters by co-deposition of sputtered Ag and Au atoms onto ionic liquids. More recently, Pena et al.[175] reported that sequential implantation of Ag and Au ions into a silica matrix led to the formation

of Au-Ag core-shell nanoclusters.

So far there have been a few reports of the use of magnetron sputtering IGA systems to produce alloy nanoclusters: Peng et al.[188] used such a system to fabricate Fe-Pt nanoclusters by co-sputtering from two targets; similarly, Wang et al.[135] obtained Fe-Pt core-shell nanoclusters by using an alloy target; regarding the Au alloys, Perez-Tijerina et al.[189] studied Au-Pd nanoclusters – interestingly, their study found that the average Au content in the alloy Au-Pd nanoclusters was 19 at.%, although the sputter target's composition was $Au_{0.5}Pd_{0.5}$; recently, Mayoral et al.[190] used the same IGA magnetron sputtering system to deposit Au-Co nanoclusters. To our best knowledge, our study is the first one that uses the IGA magnetron sputtering method to fabricate nanoclusters from a $Ag_{0.85}Au_{0.15}$ alloy target.

As an exotic method of Ag-Au nanocluster production, it is worth mentioning the effort of Govindaraju et al.[191] who utilized proteins from *Spirulina platensis* to obtain Ag-Au nanoclusters by means of biological reduction and extracellular synthesis.

When it comes to experimental studies of catalytic activity of Ag-Au nanoclusters, it has been demonstrated by Wang's group[164,192,193] that this system gives good results for low temperature CO oxidation. In addition, promising outcomes were seen in glucose oxidation[170] and very recently in catalytic reduction of 4-nitrophenol by $NaBH_4$ in water[136]. The latter study also suggests that Au-Ag core-shell nanoclusters are catalytically more active than fully alloyed or monometallic Ag or Au nanoclusters.

4.2.3 Diffusion of Nanoclusters on Substrates

In this section we describe the behaviour of nanoclusters that were deposited onto substrates and exposed to O or air for a period of time. As early as 1992, it was observed that cubic Au nanoclusters deposited onto NaCl underwent spontaneous dissolution when left in a dry box for 7 months[194]. Interestingly, the number of multiply twinned particles (MTPs) in the sample remained stable over the same period. Group of Gerthsen[14–16] studied the behaviour of Au nanoclusters deposited onto a-C films. It was found that after several months Au nanoclusters agglomerated into larger islands with thickness of 4 to 8 monolayers; futhermore, Au nanoclusters that had been stored for 32 months showed visible coarsening, which was attributed to Ostwald ripening (OR). Very recently, Bardotti et al.[13] showed that mass-selected Au and Pt nanoclusters deposited onto highly ordered pyrolytic graphite (HOPG) spontaneously organized into various structures, depending on the cluster size and environmental conditions. Jose-Yacaman et al.[195] studied the coalescence of Au,

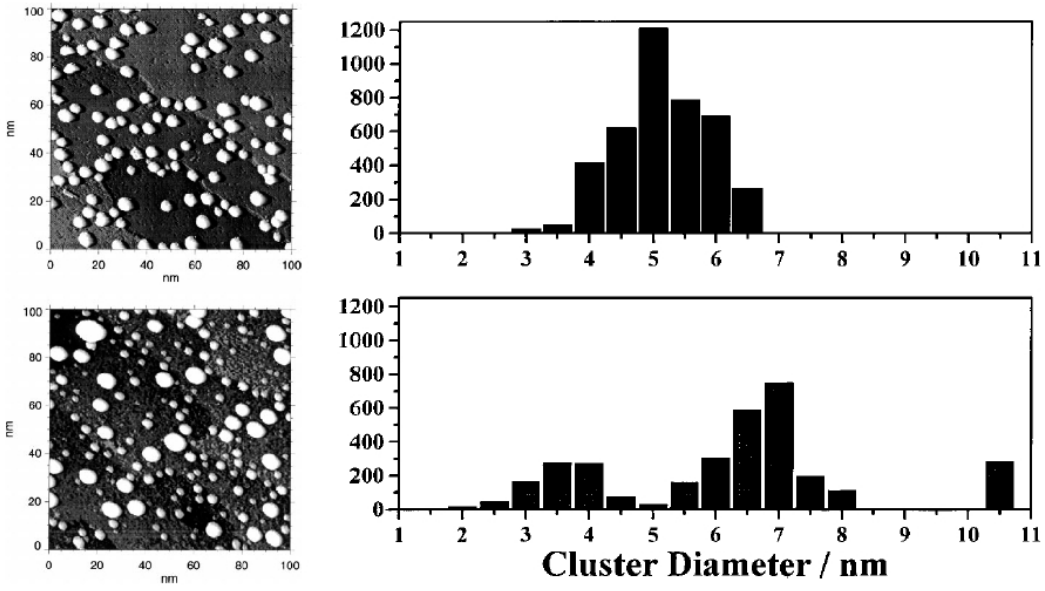

Figure 4.6: STM images of Ag nanoclusters on TiO_2 and corresponding size distribution histograms, for a fresh sample (top) and the one exposed to 10 Torr of O_2 for 2 hours (bottom).[196]

Pd, and alloy Au-Pd nanoclusters on a-C films and emphasized the role of surface layer atoms that showed high mobility in the process.

The influence of O on the behaviour of Ag nanoclusters and thin films seems to be particularly interesting from our point of view. Lai et al.[196] conducted a scanning tunneling microscopy (STM) study of Ag nanoclusters deposited onto TiO_2 (see Fig.4.6). It was found that exposure of Ag clusters to 10 Torr of O_2 for 2 hours changed the initial uniform size distribution into a bimodal one; the observed morphology change was attributed to OR.

A similar, but more comprehensive STM study was done by Layson's group[197–199] who investigated the influence of O_2 on thin Ag/Ag(1,0,0) films of sub-monolayer surface coverage (θ). They demonstrated (see Fig. 4.7) that the addition of O_2 led to the coarsening and smoothing of Ag islands and proposed that dissociation of molecular O_2 on kink sites in the islands was causing formation of Ag_xO *adspecies*. Such adspecies were susceptible to easy diffusion on the substrate due to a lowered energetic barrier compared to Ag. Consequently, the film morphology went from initially numerous smaller islands into sparse bigger smoother islands, as shown in Fig. 4.7 (a-c).

Lando and coworkers[200–203] investigated formation of Ag dendrites on graphite surfaces and observed that the addition of O_2 during the deposition of Ag led to pearling of fractal structures (see Fig. 4.8). They too concluded that the addition of O_2 was increasing the diffusion of Ag clusters on substrates.

When it comes to aging of Ag clusters in air, two reports are worth mentioning:

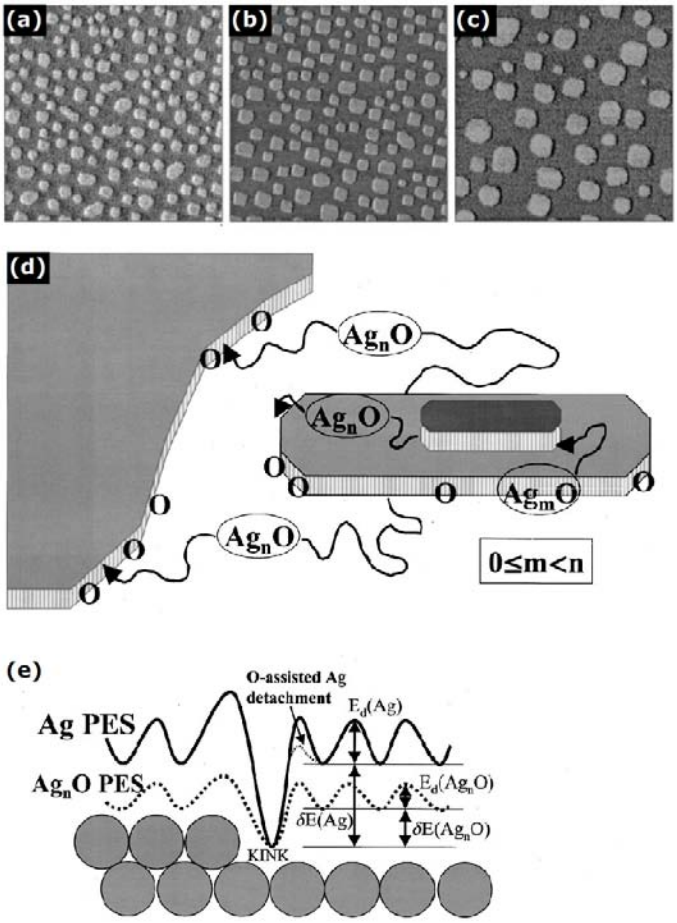

Figure 4.7: (a-c) Sequence of STM images of Ag/Ag(1,0,0) thin film (θ = 30%): (a) freshly deposited, without O_2; (b) 160 minutes after deposition, without O_2; (c) 167 minutes after deposition and exposure to 20 Langmuir of O_2. (d) Proposed mechanism for diffusion of Ag on the substrate through formation of highly mobile Ag_xO adspecies. (e) Explanation of the observed effect though energetic considerations: Ag_xO adspecies formed at kink sites have a lower energetic barrier (dotted line) for diffusion on the surface than pure Ag (solid line). The temperature was 250 K. [198]

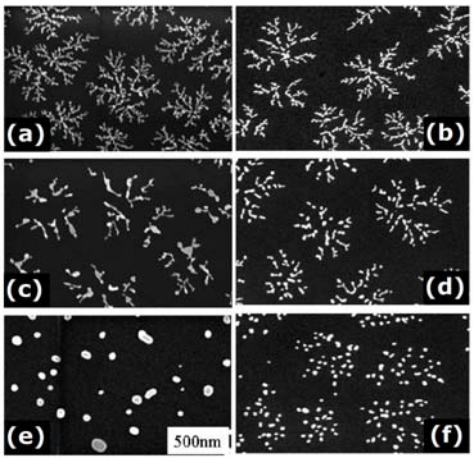

Figure 4.8: SEM images of Ag nanostructures on HOPG: (a-b) Fresh dendrites; (c,e) annealed at 200 °C and 300 °C for 1 hour; (d,f) with addition of 0.2% and 0.5% of O during Ag deposition. [201]

Peng et al.[204] investigated the behaviour of Ag nanoclusters deposited onto glass and witnessed a time dependent change of nanocluster morphology: initially uniformly spread clusters formed larger spherical and rod-like structures. Similar results were seen by Li et al.[205] when imaging Ag nanoclusters deposited onto TEM grids over the period of 7 months. Interestingly, Magdassi et al[206] demonstrated that a drop of cationic polymer poly(diallyldimethylammoniumchloride) caused a major sintering in Ag nanocluster-based films, showing liquid-like behaviour of Ag nanoclusters.

4.3 HRTEM Image Analysis

Since a large part of this thesis is based on acquiring information about nanoclusters through HRTEM imaging, in this section we briefly outline the basic principles of HRTEM image analysis that helped us to identify nanocluster types and uncover evidence of phase segregation within nanoclusters.

Starting from the early reports on multiply twinned particles (MTPs) of Au and Ag[2–4], there have been many studies dealing with the topic of recognition of various types of nanoclusters by means of HRTEM in combination with image simulations[207–216]. As a prerequisite for a successful analysis, it is necessary to obtain HRTEM images of a high quality that will reveal information about nanocluster structures. In order to identify the nanocluster type, we adopted a template based on the extensive work of Koga and Sugawara[216], whose meticulous efforts in HRTEM imaging of Au nanoclusters and subsequent micrograph analysis are much appreciated.

In their comprehensive study, Koga and Sugawara first used HRTEM to acquire images of over 4000 Au nanoclusters. These images were later on compared to computer generated images obtained by multislice modeling, in order to identify the nanocluster structures (see Figs. 4.9 and 4.10). With this approach, in addition to readily observed face centered cubic (FCC) nanoclusters, they were able to identify icosahedral (Ih) and decahedral (Dh) nanoclusters of various sizes and inclination angles relative to the electron beam.

However, if one looks for signs of phase segregation in alloy nanoclusters, the structural information obtained from bright field HRTEM might not always be sufficient. For that purpose a complementary technique – high angle annular dark field (HAADF) STEM – is often used. In short, this technique relies on scattering of electrons from objects under scrutiny: elements with a higher atomic number Z tend to deflect more electrons from the beam than elements of a lower atomic number. The intensities I stemming from different elements (A, B) in the sample

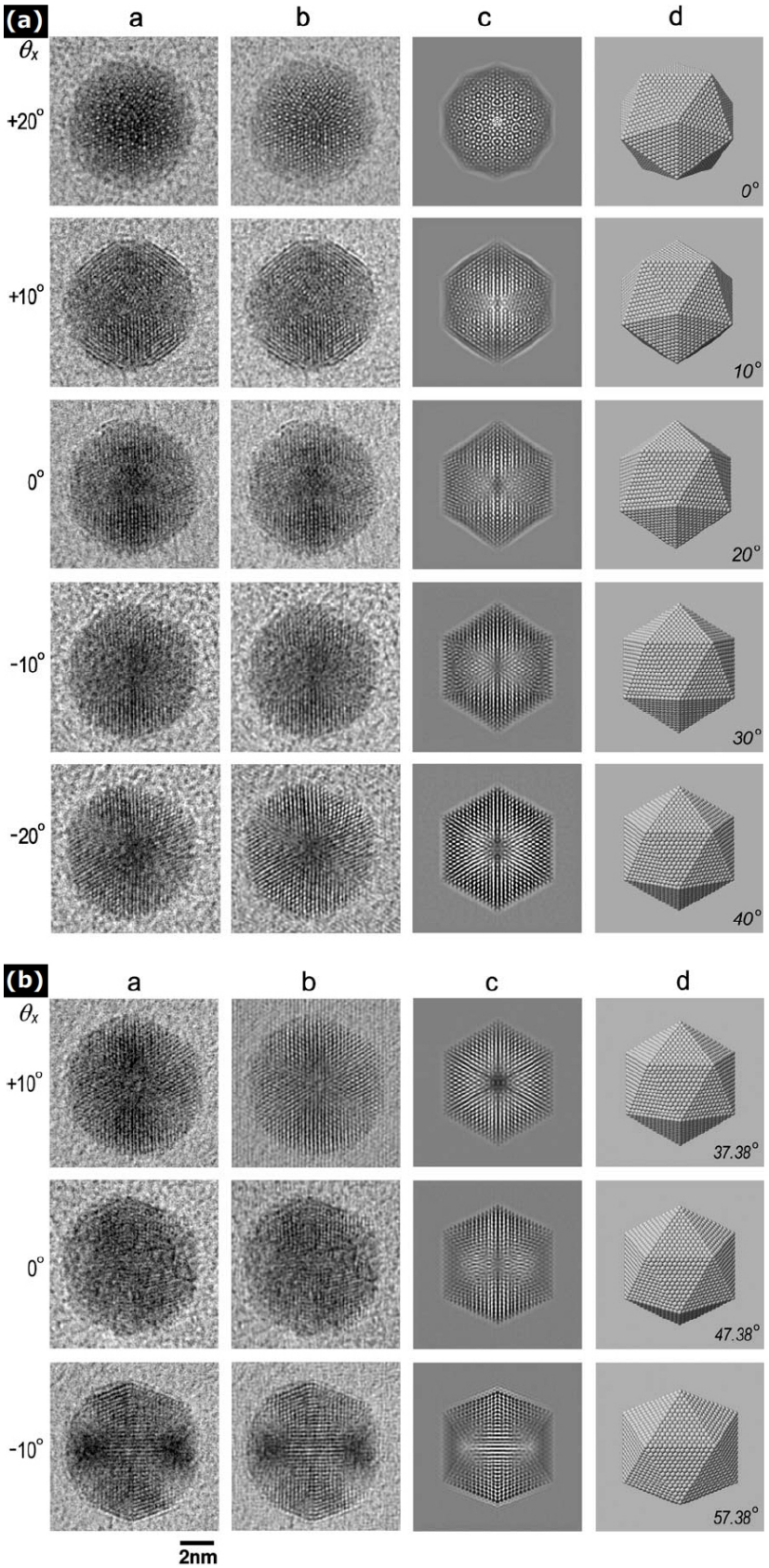

Figure 4.9: Series of experimental and simulated HRTEM images of two nanoclusters obtained by rotation around one of the axes by various angles, revealing their Ih structure: raw (column *a*) and filtered (column *b*) HRTEM images; simulated HRTEM images (column *c*) and corresponding views on a 3D ball model (column *d*).[216]

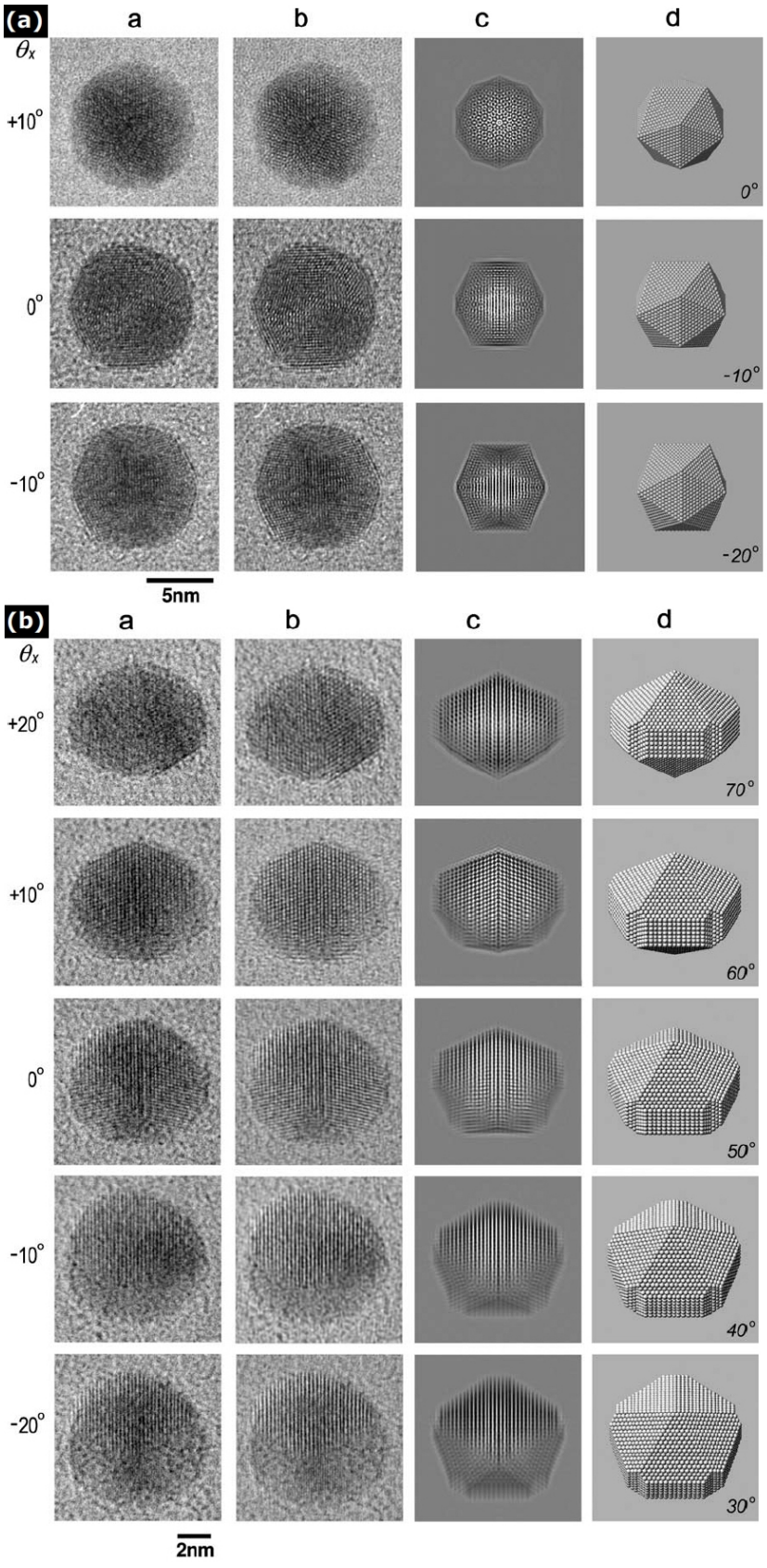

Figure 4.10: Series of experimental and simulated HRTEM images of an Ih nanocluster (a) and a Dh nanocluster (b) obtained by rotation around one of the axes by various angles: raw (column *a*) and filtered (column *b*) HRTEM images; simulated HRTEM images (column *c*) and corresponding views on a 3D ball model (column *d*).[216]

will be measured by a HAADF detector according to the following relation[104]:

$$\frac{I_A}{I_B} \approx \left(\frac{Z_A}{Z_B}\right)^{1.7} \tag{4.1}$$

As an example of HAADF STEM image analysis, we present a figure from Li et al.[217] (see Fig. 4.11) which depicts Au-Ag and Ag-Au core-shell nanoclusters (compostion 1:1). The line profiles taken across the nanoclusters in these two samples clearly differ, exhibiting the inversion of elements within the clusters. These profiles are in a good agreement with simulated intensities based on a simple geometrical model, as seen in Fig. 4.11(c) and (d).

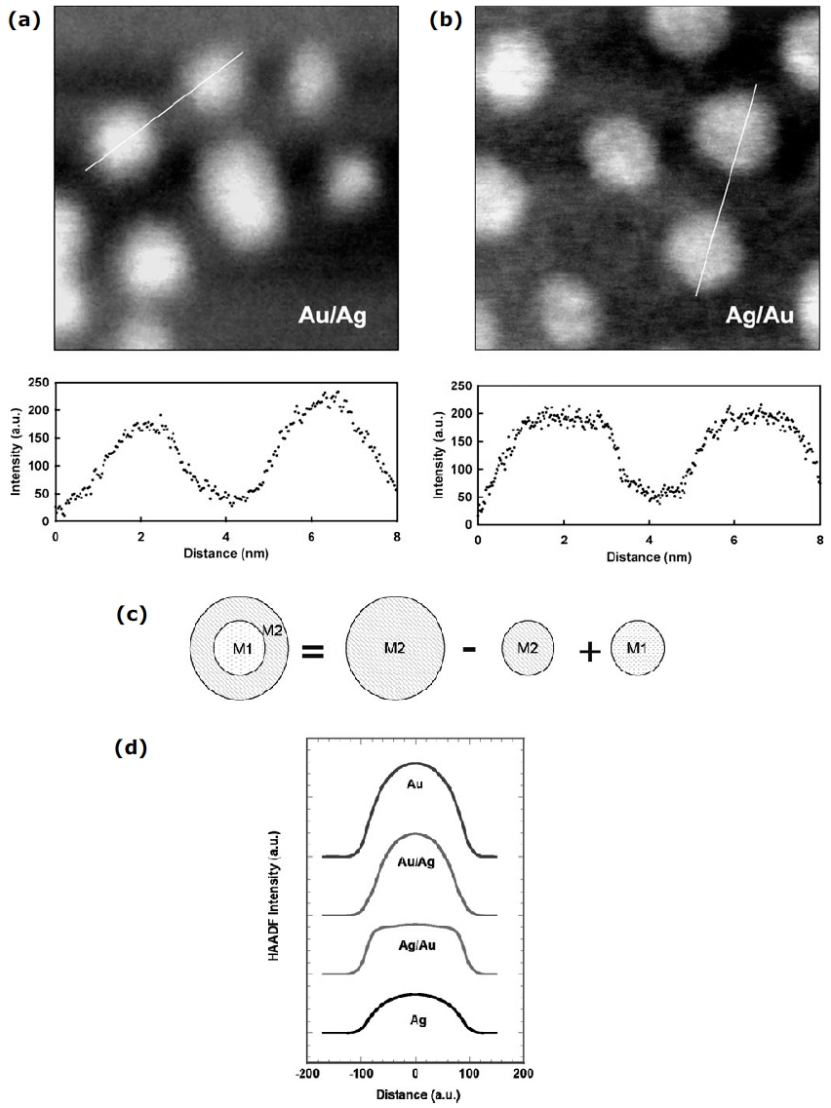

Figure 4.11: (a-b) HAADF STEM images of Au-Ag and Ag-Au core-shell nanoclusters, with corresponding line profiles. (c) Geometrical model of a core-shell nanoparticle that served as a basis for simulated HAADF intensities of core-shell nanoclusters (d).[217]

4.4 Results of $Ag_{0.85}Au_{0.15}$ Nanocluster Study

In the previous sections we outlined some of the most interesting results of computational and experimental studies of Ag-Au nanoclusters. We also stressed the importance of HRTEM as a valuable characterization technique that enables gathering information about the nanocluster structural properties. Here we present results of our experimental study of $Ag_{0.85}Au_{0.15}$ nanoclusters produced by IGA method in our magnetron sputtering system (see Chapter 2 for details). All together 192 samples of nanoclusters of various sizes were deposited at different surface coverages and characterized at various stages of aging. We again emphasize the advantages of using the IGA method for sample fabrication – independent control of the cluster size D and surface coverage θ, and absence of ligands/surfactants.

4.4.1 Fresh $Ag_{0.85}Au_{0.15}$ Nanoclusters

The first goal was to investigate the structure of isolated $Ag_{0.85}Au_{0.15}$ nanoclusters. For that purpose samples of clusters with sizes in the range 3 nm $< D <$ 10 nm were prepared by the recipes we developed over the course of the study, presented earlier in § 2.3.3. These nanoclusters were deposited onto a-C TEM grids and transferred to the TEM in ambient atmosphere, in a period of $t <$ 15 minutes – such samples are denoted "*fresh*" throughout the study.

Fig. 4.12 shows typical HRTEM images from 3 samples containing clusters of different sizes deposited at low surface coverage ($\theta \lesssim 5\%$) that allowed for investigation of individual clusters. The size distribution histograms were constructed from over 700 HRTEM images taken on these samples, with the total number of imaged nanoclusters in excess of 1700. The nanocluster size D is obtained from the following relation:

$$D = 2\sqrt{\frac{A}{\pi}} \tag{4.2}$$

where A is the projected area of nanoclusters in HRTEM images. By using the approximation that nanoclusters are spheres of diameter D one can overcome the difficulties arising from the irregular cluster shapes and simplify the analysis of images performed in ImageJ software[105].

HRTEM images of these fresh $Ag_{0.85}Au_{0.15}$ samples did not show any contrast within the nanoclusters in the bright field imaging mode (compare to Fig. 4.5), suggesting that they were completely alloyed.

Each of the nanoclusters in the images was carefully analyzed and its fringing pattern was compared with the patterns from the study of Koga and Sugawara[216]

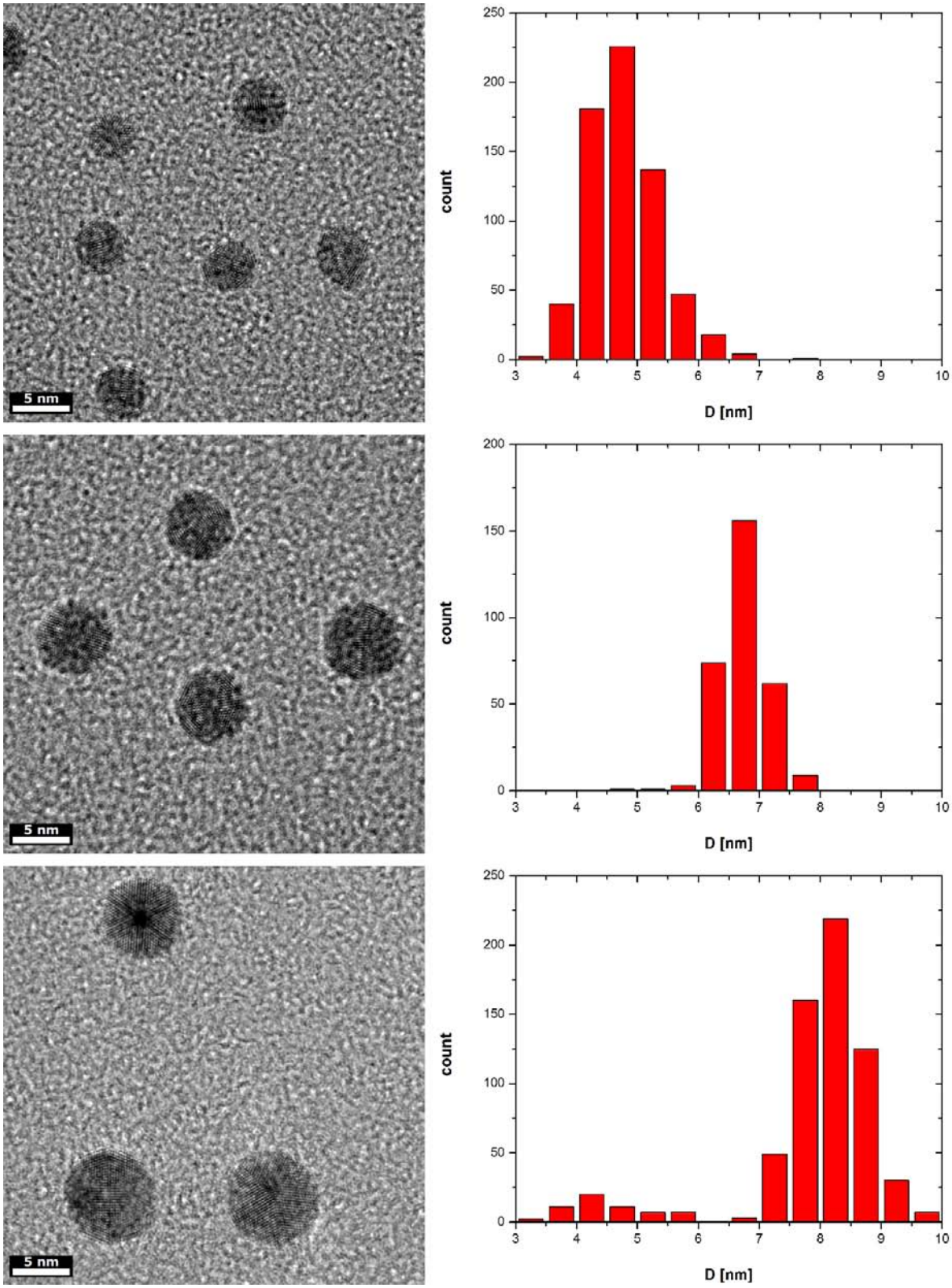

Figure 4.12: Representative HRTEM images of three $Ag_{0.85}Au_{0.15}$ samples containing clusters of different sizes, with corresponding size distribution histograms obtained by counting the particles of each size. Surface coverage in all samples presented here was $\theta \lesssim 5\%$.

Structure	Number	Percent
Icosahedral	1489	87.2
Decahedral	157	9.2
Other	61	3.6
Total	1707	100.0

Table 4.1: Results of HRTEM image analysis of fresh $Ag_{0.85}Au_{0.15}$ nanoclusters.

in order to identify the nanocluster structure. Additionally, the patterns were also compared with reports of Kirkland et al.[208], Ascencio et al.[211], and Flores et al.[213] to cross-check the results and identify those nanoclusters that did not seem to match any of the patterns from the work of Koga and Sugawara.

The results of the HRTEM image analysis are given in Table 4.1. We observed that the vast majority (>87%) of fresh $Ag_{0.85}Au_{0.15}$ nanoclusters in the range 3 nm $< D <$ 10 nm were of Ih structure (see Fig. 4.13). These were followed by Dh nanoclusters which amounted to $\sim$ 9% of the total number – 10$\times$ less than the number of Ih nanoclusters. All other structures, including the ambiguous patterns,

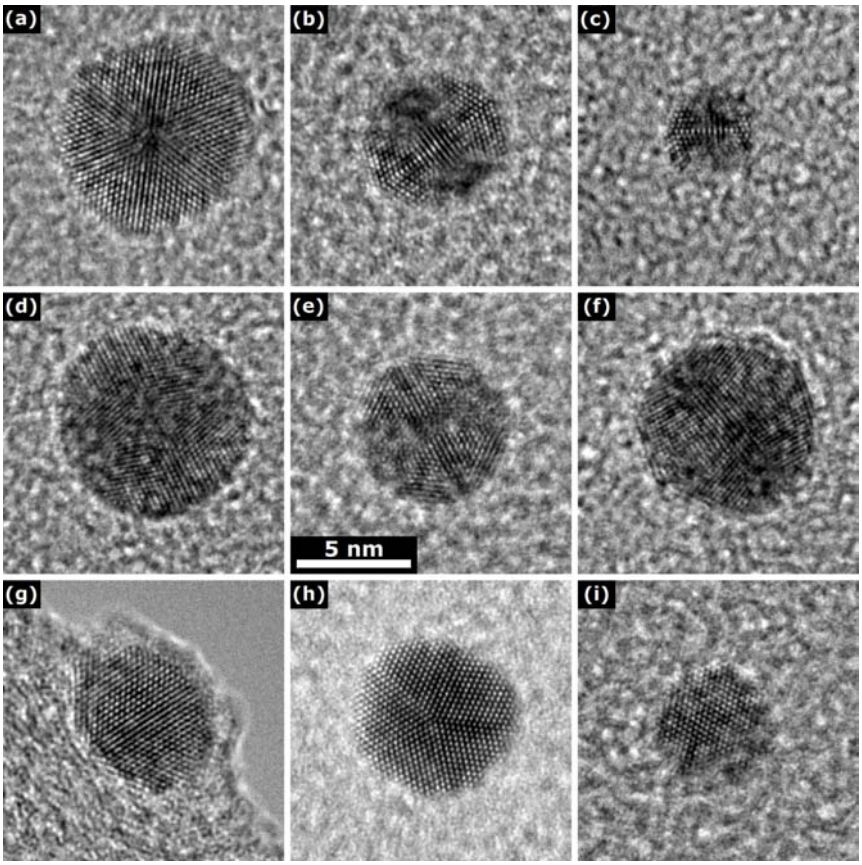

Figure 4.13: HRTEM images showing the most common fringing patterns obtained during imaging: (a-f) patterns revealing the Ih structure of nanoclusters; (g-h) patterns originating from Dh nanoclusters; (i) micrograph of a FCC nanocluster.

comprised less than 4% of the total number of nanoclusters. Surprisingly, FCC nanoclusters were very rare: at most there was 2% of them at any cluster size.

Although the percentage of structures other than Ih is relatively small, the fact that we had imaged and analyzed over 1700 nanoclusters means that the number of these other structures is nevertheless relatively high, which allows for statistically significant population distributions to be obtained. Fig. 4.14 shows a plot of the population of fresh $Ag_{0.85}Au_{0.15}$ nanocluster structures as a function of the cluster size. One can see that the clusters with size in the range 3.5 nm $< D <$ 8 nm are predominantly Ih, with a very small number (at least an order of magnitude less) of nanoclusters of any other structure. However, as the clusters get bigger than $D \sim 8$ nm, the fraction of Ih starts to drop quite quickly, whereas the percentage of Dh nanoclusters rises quite quickly in the same cluster size range. Based on this figure, one can expect similar number of Ih and Dh structures for clusters with the size $D \sim 9$ nm. For clusters bigger than that the Dh structure seems to be dominant. It should be said however that the number of clusters of the size $D > 9$ nm encountered during the HRTEM image analysis was relatively low (see Fig. 4.12) compared to the number of smaller clusters (and hence has a large uncertainty); nevertheless the trend that the Dh nanocluster population rises as the cluster size increases is clearly visible.

It is interesting to compare these results for $Ag_{0.85}Au_{0.15}$ alloy nanoclusters with the results of Koga and Sugawara[216] obtained for pure Au nanoclusters. In their

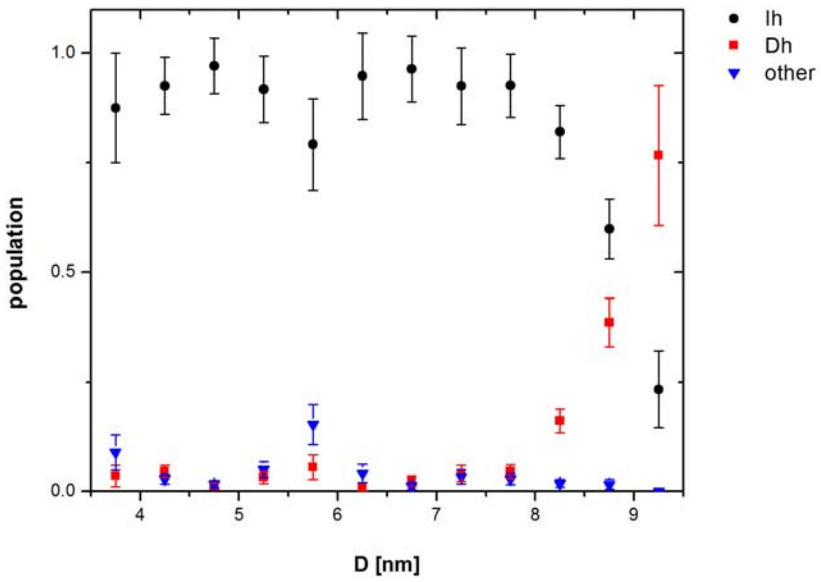

Figure 4.14: Population distribution of fresh $Ag_{0.85}Au_{0.15}$ nanoclusters, based on the HRTEM image analysis of 1707 nanoclusters. The uncertainty is calculated as $\frac{\sqrt{N}}{N}$ where N is the number of nanoclusters of a given type at a given size.

case, the population distribution showed similar behaviour: the percentage of Ih clusters dropped as the cluster size got bigger; at the same time the percentage of Dh clusters rose. However, in their case the transition was much smoother with the Dh population never exceeding 40% for the clusters in the size range 3 nm $< D <$ 18 nm, meaning that Ih were always in majority i.e. no population inversion was observed.

Our results seem surprising in the light of work of Reinhard et al.[218] who performed electron diffraction studies of unsupported 3-11 nm Ag nanoclusters and detected both FCC and Ih nanoclusters in the cluster beam. However, since their study also showed that, for certain experimental conditions in the IGA system, more FCC than Ih nanoclusters were obtained, our results suggest that the structure of nanoclusters in this size range is (partially) governed by the experimental conditions (e.g. Ar and He flow). From the standpoint of energetics it would mean that, under our experimental conditions, $Ag_{0.85}Au_{0.15}$ nanoclusters may have been kinetically trapped in the Ih (or Dh) structure so that consequently very few FCC clusters were observed. These results may also indicate that one structure might tend to be more abundant because the experimental conditions favor a *local* energetic minimum corresponding to that structure, although another structure (corresponding to the *global* energy minimum) might be energetically most stable. This behaviour would be in line with the model proposed by Marks and Ajayan[6], presented in Fig. 1.1 (b). Note that the trend that we observed (transition from Ih to Dh, with very few FCC clusters) is much more similar to the structural phase diagram for Ag nanoclusters modeled by Doye and Calvo[7], which shows that the FCC structure is favoured only for clusters with $D \gtrsim 11$ nm.

4.4.2 Fresh $Ag_{0.85}Au_{0.15}$ Nanocluster-based Thin Films

In addition to samples deposited at low surface coverage ($\theta \lesssim 5\%$) that were suitable for HRTEM imaging of individual nanoclusters, samples of higher surface coverages were also studied. A couple of representative TEM images showing samples with $\theta = 30\%$ and $\theta = 100\%$ are presented in Fig. 4.15. One can see that at higher surface coverages coalescence of nanoclusters is pronounced so that larger aggregates are formed - in the case of $\theta = 30\%$ a discontinuous thin film of $Ag_{0.85}Au_{0.15}$ islands is created, while for the case $\theta = 100\%$ one attains continuous, percolating thin films. HRTEM images of these islands and films reveal that they are of polycrystalline nature, showing features which are very similar to the original nanocluster structures i.e. Ih and Dh features, or even down to their basic Th building blocks.

Energy-dispersive X-ray (EDX) spectra were taken on 3 high coverage samples

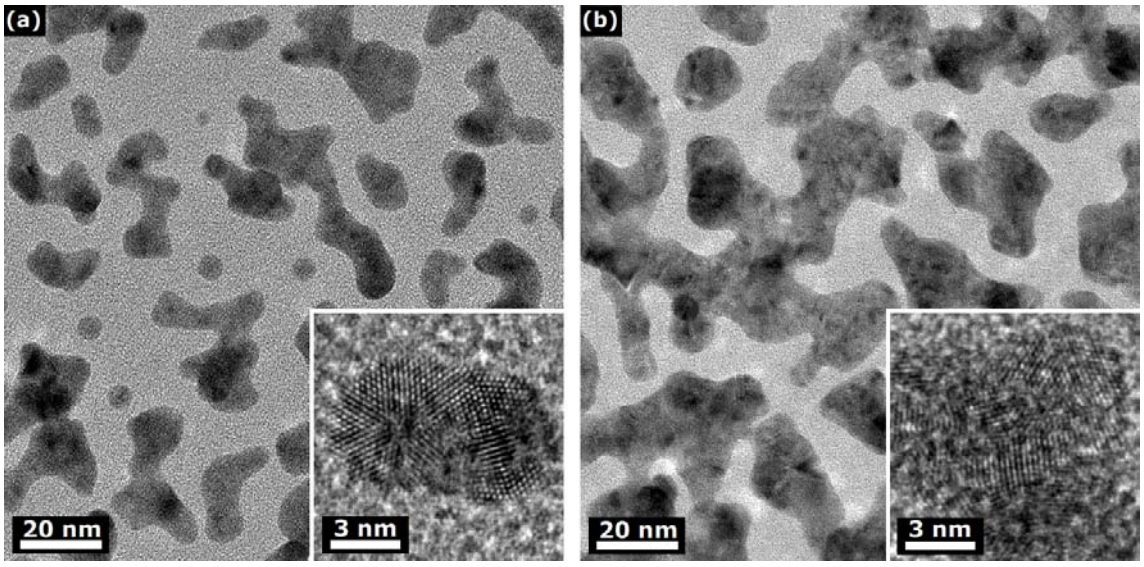

Figure 4.15: TEM images of fresh thin $Ag_{0.85}Au_{0.15}$ nanocluster-based films deposited onto a-C at various surface coverages: (a) $\theta = 30\%$; (b) $\theta = 100\%$. In both cases the size of the deposited clusters was $D = 6\pm1$ nm. HRTEM images are shown in the insets.

from 22 different areas on the TEM grids (Fig 4.16 shows a typical spectrum). Based on these measurements we found that the average Au content in the samples was 14±1 at.%, which agrees well with the sputter target composition used in the IGA system. Hence, throughout this thesis we denote our alloy Ag-Au samples as $Ag_{0.85}Au_{0.15}$.

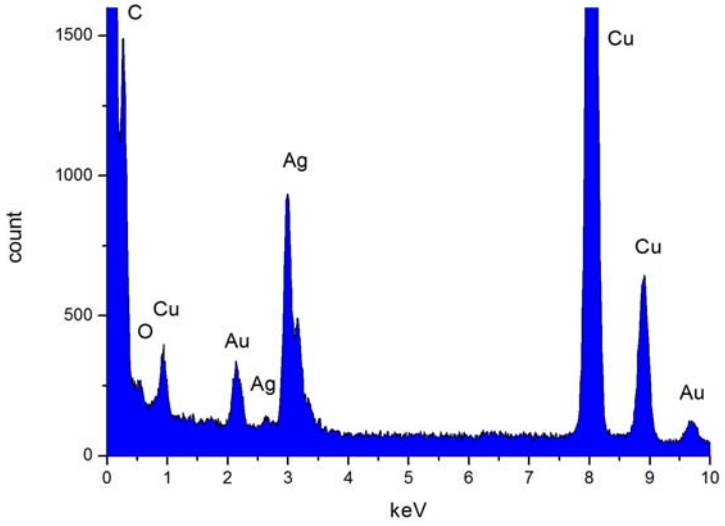

Figure 4.16: EDX spectrum of $Ag_{0.85}Au_{0.15}$ nanocluster-based film ($D = 6\pm1$ nm; $\theta = 100\%$). Cu and C signals originate from the TEM grid. Note a small amount of O that is either adsorbed on the TEM grid or is present as gas inside the TEM column.

4.4.3 Aged $Ag_{0.85}Au_{0.15}$ Nanoclusters

Once imaged in the TEM, the fresh $Ag_{0.85}Au_{0.15}$ samples were brought back and stored in plastic container boxes in darkness, under ambient conditions in the laboratory. During repeated imaging over subsequent weeks, it became obvious that the structure and morphology of the nanoclusters and thin films had changed over time. For that reason the samples were subjected to systematic periodic TEM imaging in order to study their unusual time-dependent behaviour.

Figs. 4.17 and 4.18 show a sequence of TEM and HRTEM images taken at different stages of aging of a low surface coverage $Ag_{0.85}Au_{0.15}$ nanocluster sample. The investigation covered the period between the first imaging of the initially fresh

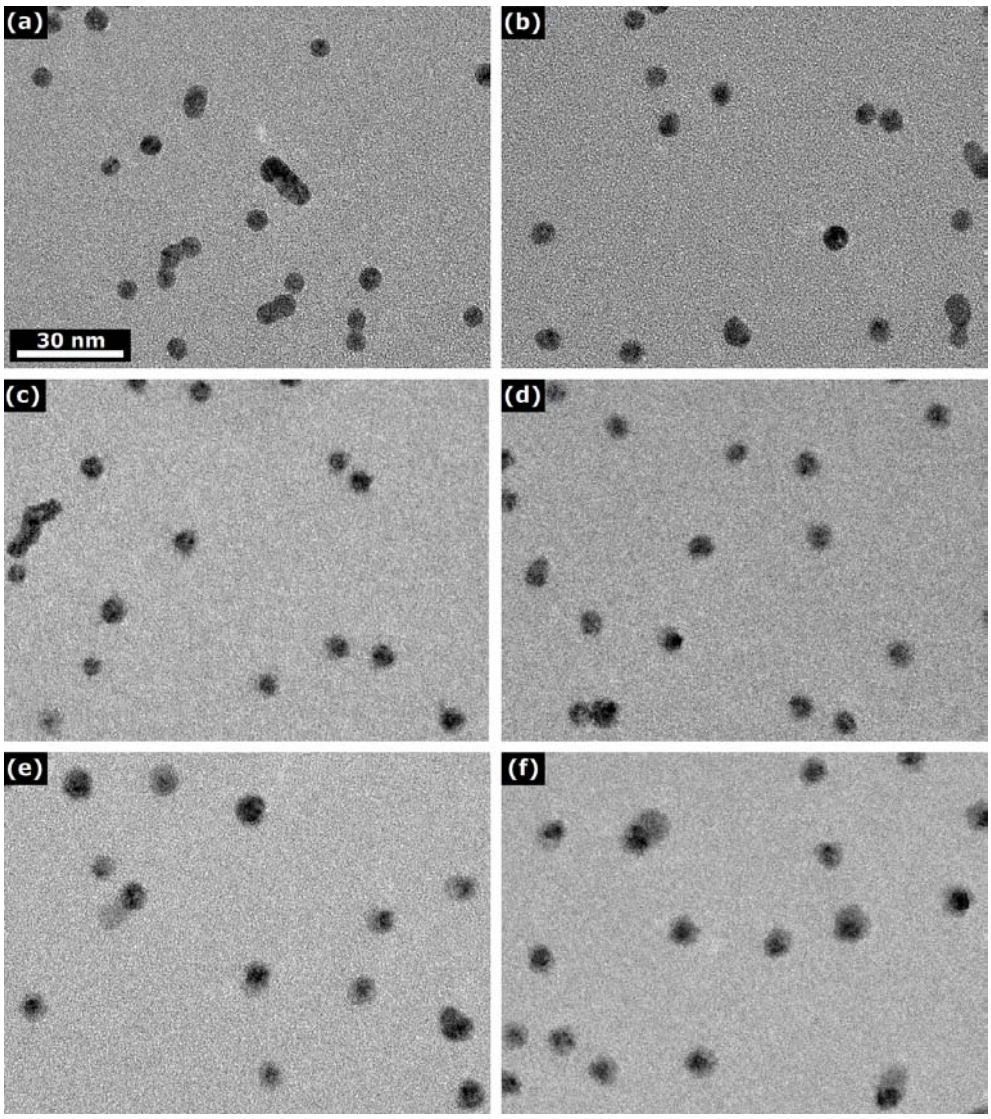

Figure 4.17: Sequence of TEM images taken on the same $Ag_{0.85}Au_{0.15}$ sample ($D = 6\pm1$ nm; $\theta \lesssim 5\%$) over a period of time: (a) initially fresh nanoclusters; (b) 14 days old; (c) 19 days old; (d) 28 days old; (e) 38 days old; (f) 52 days old.

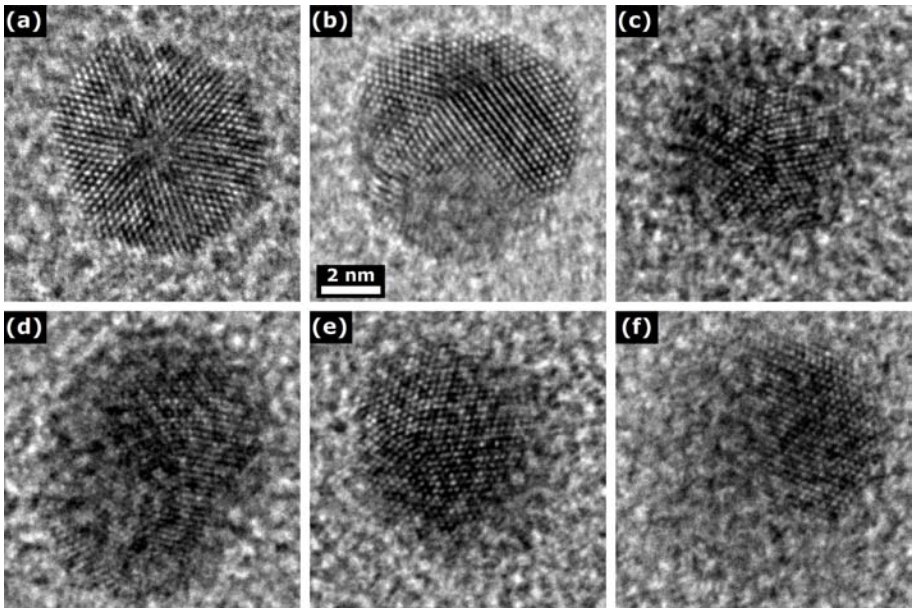

Figure 4.18: Sequence of HRTEM images taken on the same sample as in Fig. 4.17 over a period of time: (a) initially fresh nanocluster; (b) 14 days old; (c) 19 days old; (d) 28 days old; (e) 38 days old; (f) 52 days old.

sample (presented in Fig. 4.17 (a)) and the last imaging which happened 52 days later (presented in Fig. 4.17 (f)). Since the sample had a low surface coverage of $\theta \lesssim 5\%$, the average distance between the clusters was relatively big – this implied that any change of the cluster shape or structure in that period is a property of each individual nanocluster, rather than a property of the whole ensemble of nanoclusters. In other words, the diffusion of Ag and Au atoms on the surface of the a-C film was negligible compared to the perturbation of atoms within the individual clusters or rare groups of joined clusters (note that these clusters were joined during the deposition, most likely due to landing on top of one another – not to be confused with a relatively slow post-deposition coalescence).

As can be seen in Figs. 4.17 (a) and 4.18 (a), the fresh sample contained faceted nanoclusters with well-defined, sharp edges that provided a good contrast between the clusters and a-C film in TEM images. In time, the nanocluster edges start to appear less defined and the initially good contrast between the nanoclusters and a-C film is slowly lost. It suggests that some structural changes happened in the atomic layers close to the cluster's surface, making them less dense and less ordered, while the clusters were aging in ambient atmosphere. After approximately 3 weeks of aging (see Fig. 4.17 (c)), first signs of some kind of phase segregation became visible: a thin surface layer had developed on some of the clusters, turning their homogeneous structure into core-shell. Furthermore, it also became apparent that the clusters had grown bigger so that their average size increased.

As the aging continued, thickness of the shells grew. Moreover, in some nanoclusters the shell seemed to be formed asymmetrically so that Janus-like structures were created. After the 52 day period (see Fig. 4.17 (f)), it was observed that literally all of the nanoclusters had changed their appearance: most of them exhibited a clear core-shell structure that was fairly concentric, while some of the clusters formed Janus structures with a round "head" and elongated "body". As a consequence of the nanocluster "swelling", the increase in their average size is more than obvious.

Interestingly, the appearance of the nanoclusters did not significantly change after that period, suggesting that they reached some sort of steady state and that any further change of the shape or structure was not energetically favorable. Fig 4.19 shows a HAADF STEM image[a] taken approximately 10 months after the samples were fabricated and stored in darkness in ambient conditions. It can be seen that nanoclusters here have a very similar structural form – core-shell and Janus – as those from the sample that had aged for 52 days.

Based on the line profile taken across one of the nanoclusters, it is possible to roughly estimate the ratio of HAADF intensities between the core and the shell:

$$\frac{I_{shell}}{I_{core}} \approx \frac{80}{200} = 0.4$$

where I_{core} and I_{shell} were estimated at distances of 6 nm and 11 nm (see Fig. 4.19 (b)), respectively, which is approximately equidistant from the opposite edges of the nanocluster, so that any thickness-related issues are minimized.

Now, if one assumes that the shell mostly consists of silver(I)oxide (Ag_2O), and

[a]STEM imaging performed by R.L. Chantry and Z.Y. Li, Nanoscale Physics Research Laboratory, University of Birmingham, UK

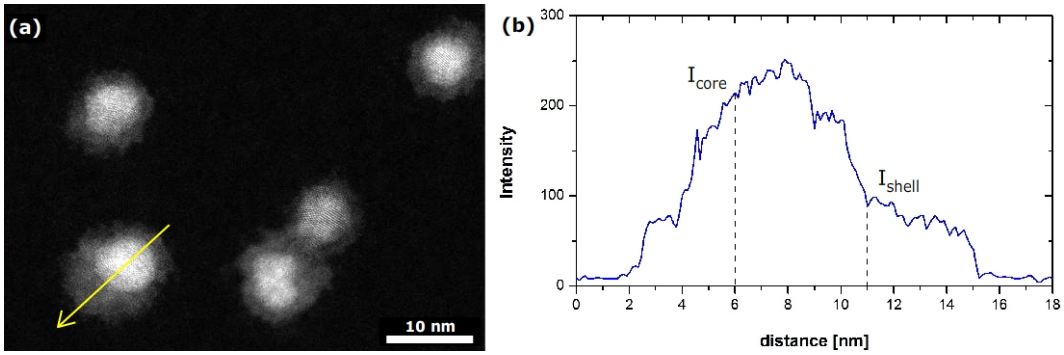

Figure 4.19: (a) HAADF STEM image of $Ag_{0.85}Au_{0.15}$ nanoclusters 10 months after deposition (initially: $D = 6\pm1$ nm; $\theta \lesssim 5\%$). (b) HAADF intensity line profile along the arrow in image (a).

the core is 1:1 alloy (AgAu), then equation 4.1 yields:

$$\frac{I_{shell}(Ag_2O)}{I_{core}(AgAu)} = \left(\frac{Z_{eff}(Ag_2O)}{Z_{eff}(AgAu)}\right)^{1.7} = \left(\frac{(94+8)/3}{(47+79)/2}\right)^{1.7} = 0.35$$

which agrees very well with the observed intensity. Note that this is a very rough calculation where some long-shot assumptions about the elemental composition of the core (AgAu) and shell (Ag_2O) had to be made.

Bright field HRTEM and HAADF STEM performed on the aged samples indicate that the structure of the clusters depends on their size. In smaller clusters ($D < 8$ nm), like in the one presented in Fig. 4.20, the cores and shells seem highly concentric. The shells are relatively thin and exhibit no long range atomic ordering, suggesting that they are amorphous. In contrast, most of the cores show a fivefold symmetry that is very similar to that of fresh Dh nanoclusters. Interestingly, the fraction of aged clusters with these Dh-like cores is considerably higher (at least by a factor of 2) than the fraction of fresh Dh nanoclusters, indicating that the formation of shells may have caused an Ih to Dh transition in some of the cores, in a way similar to the cooperative slip dislocation proposed by Koga and Sugawara[220]. The line profiles of HAADF intensity (see Fig. 4.20 (c) and (d)) across the atomic columns in the core appear random, suggesting that the core is randomly alloyed[219].

In larger Janus-like clusters ($D > 8$ nm), like the one presented in Fig. 4.21, the cores are polycrystalline, while shells appear partially crystalline; the amorphous cloak around the whole nanocluster still seems to exist. Image analysis of the crystalline part of shell in Fig. 4.21 reveals interplanar distances $d_1 = 3.3\pm0.1$ Å and $d_2 = 2.7\pm0.1$ Å with the angle between them $\alpha = 33\pm2°$. These distances and the angle match the distances and the angle between {1,1,0} and {1,1,1} planes in Ag_2O (isostructural with Cu_2O; lattice parameter $a_{Ag_2O} = 4.74$ Å)[221], suggesting that oxidation of Ag in the outer nanocluster layers is mainly responsible for the observed morphological and structural changes.

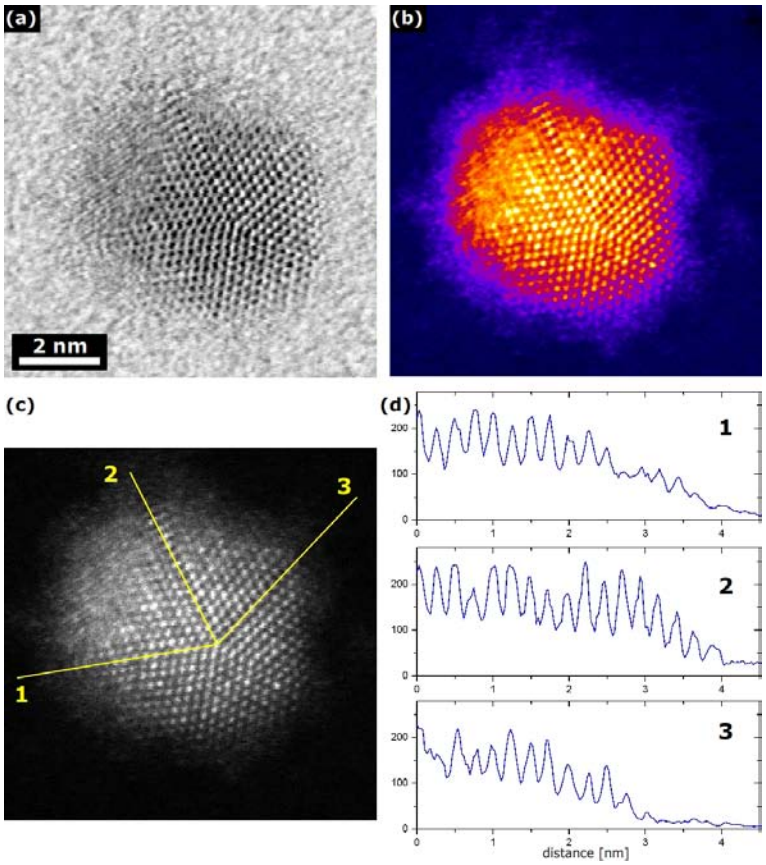

Figure 4.20: Bright field (a) and HAADF (b-c) STEM images of an aged $Ag_{0.85}Au_{0.15}$ nanocluster revealing its core-shell structure. (d) HAADF intensity line profiles across the core indicating it is fully alloyed[219]. The atomic spacing $d = 2.4\pm0.1$ Å corresponds to the distance between {1,1,1} planes in FCC Ag or Au.

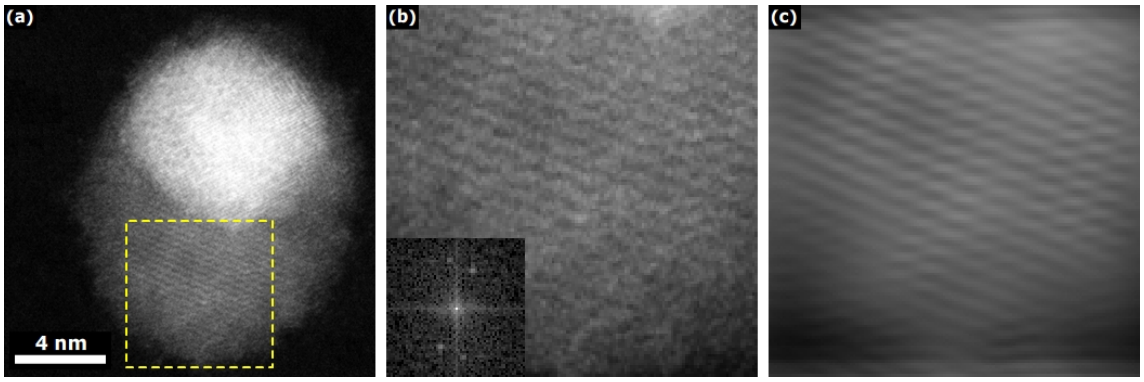

Figure 4.21: (a) HAADF STEM image of an aged Janus-like nanocluster. A crystal lattice can be seen in the elongated shell. (b) Close-up of the selected area from (a) and its fast Fourier transform (FFT) shown in the inset. (c) Filtered and reconstructed image from (b) showing fringes that correspond to {1,1,0} and {1,1,1} planes in Ag_2O with interplanar distances of $d_1 = 3.3\pm0.1$ Å and $d_2 = 2.7\pm0.1$ Å, respectively; measured angle 33±2°, calculated angle 35.5°. Here the zone axis of Ag_2O is [1,-1,0].

4.4.4 Aged $Ag_{0.85}Au_{0.15}$ Nanocluster-based Thin Films

We have seen that $Ag_{0.85}Au_{0.15}$ nanoclusters in the low surface coverage samples over time changed their morphological and structural characteristics: initially faceted and homogeneously alloyed nanoclusters turned into rounder core-shell objects with size dependent appearance. Since the distances between the clusters in such low coverage samples were quite big, we could ascribe the observed changes to individual clusters.

In the case of high surface coverage samples nanoclusters make up thin films, as seen in Fig. 4.15. Therefore, if these samples undergo any structural or morphological change when left to age exposed to ambient conditions, it should be seen as the property of the whole ensemble of nanoclusters.

Just like in the case of low surface coverage samples, we conducted a systematic study of aging of high surface coverage samples. Two sets of samples were produced with the same cluster size ($D = 6\pm1$ nm) at a different surface coverage ($\theta_1 = 30\%$ and $\theta_2 = 100\%$) and were periodically imaged in the TEM.

Samples with $\theta = 30\%$

Fig. 4.22 shows a sequence of TEM images taken at various stages of aging of an $Ag_{0.85}Au_{0.15}$ sample with $\theta = 30\%$. Initially, the sample contained a discontinuous thin film of relatively big islands formed by coalescence of nanoclusters during their deposition and immediately after. Between the islands it was possible to see individual nanoclusters that had not coalesced, but their number was relatively low.

However, after being exposed to atmosphere for a week (see Fig. 4.22 (b)), the morphology of the sample was visibly changed: the number of individual particles had risen considerably (more than 10×) and the majority of them were significantly smaller than the originally deposited nanoclusters. Furthermore, the edges of the bigger islands became less sharp and the contrast in the TEM images was consequently decreased, similar to what was seen in individual nanoclusters in aged low surface coverage samples. Over time (see Fig. 4.22 (c-f)), the number and size of the smaller particles grew bigger while, at the same time, the number and size of initially big islands decreased. The observed process could be described as crumbling of the initial $Ag_{0.85}Au_{0.15}$ islands. Note however that, although the morphology clearly changed in the period of investigation, there were no signs of phase segregation in any of these objects – not even after a prolonged period of 11 weeks! This is a major difference between the aging process of a high surface coverage sample and the one of a low surface coverage sample.

Fig. 4.23 shows HRTEM images of the smaller particles from a 2 week old high surface coverage sample. It is obvious that their size is smaller than the size of the

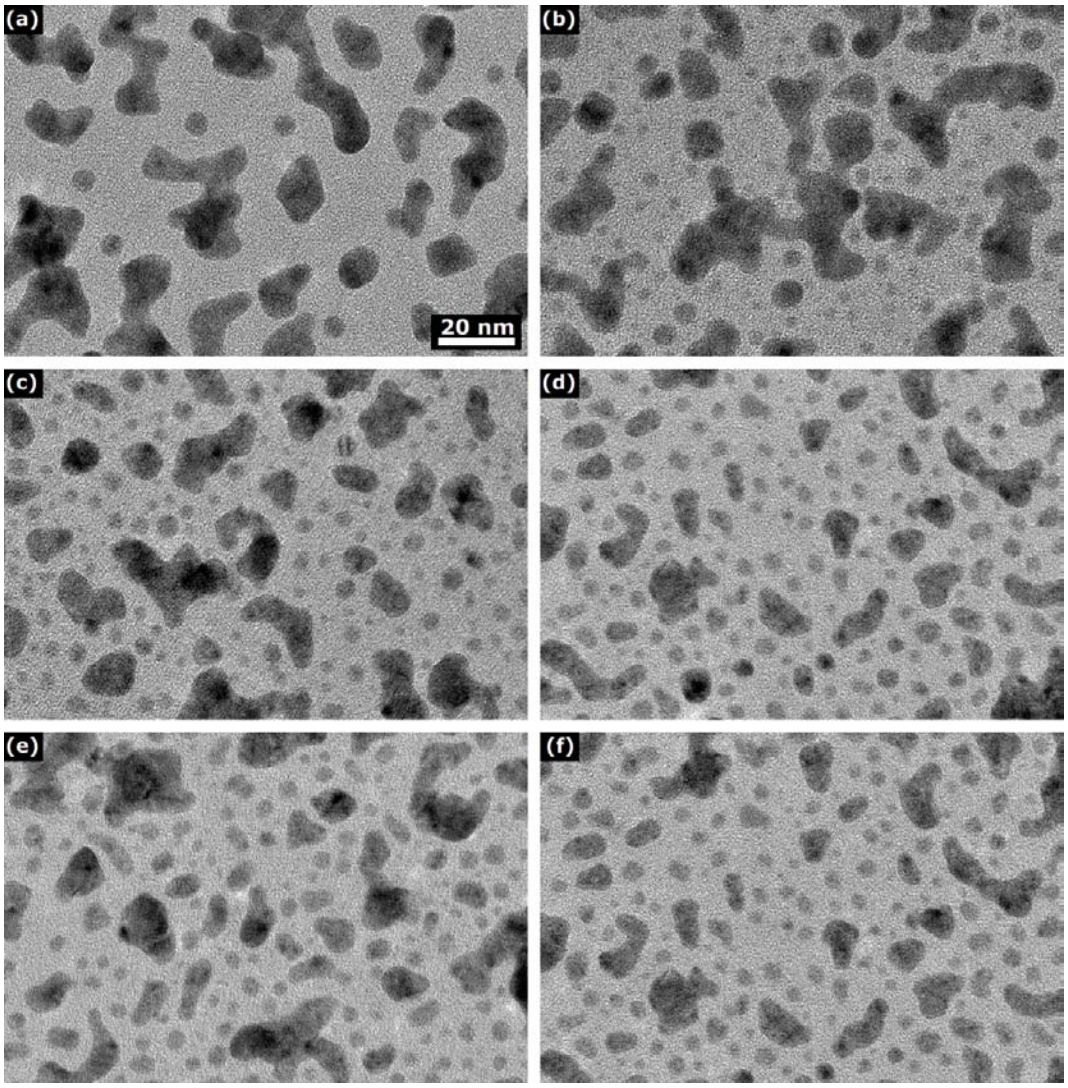

Figure 4.22: Sequence of TEM images taken on the same $Ag_{0.85}Au_{0.15}$ sample ($D = 6\pm1$ nm; $\theta = 30\%$) over a period of time: (a) initially fresh nanoclusters; (b) 1 week old; (c) 2 weeks old; (d) 3 weeks old; (e) 6 weeks old; (f) 11 weeks old.

originally deposited nanoclusters. Furthermore, although nanoclusters of a fivefold symmetry were commonly observed, there was a high fraction of FCC clusters – much more (at least an order of magnitude) than in a standard fresh low surface coverage sample with nanoclusters in the range 3 nm $< D <$ 10 nm (compare to Fig. 4.14). Moreover, the structure of these sub-3 nm clusters was fluctuating during the TEM imaging, in a similar fashion as reported by Ascencio et al.[222] for passivated Au nanoclusters under electron beam irradiation. Note that the interplanar distances in these smaller clusters in Fig. 4.23 match the interplanar distances in FCC Ag or Au.

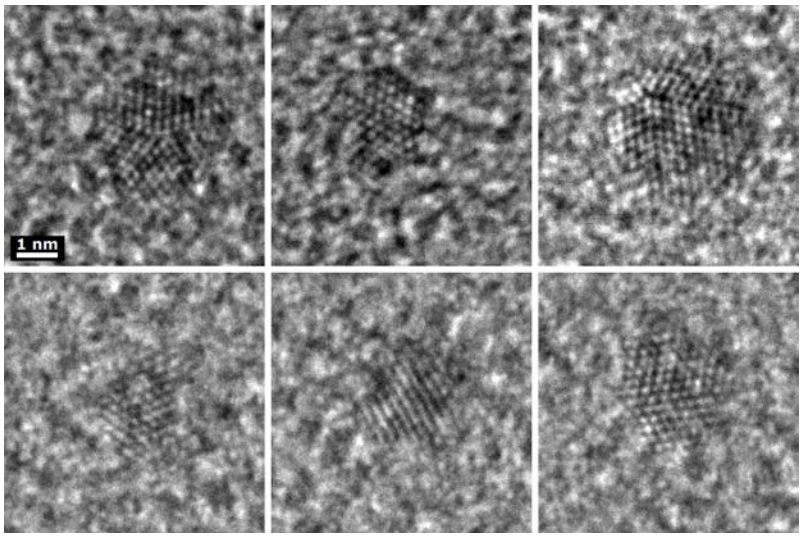

Figure 4.23: HRTEM images of small nanoclusters formed in an aged high surface coverage sample (t = 2 weeks, $D = 6\pm1$ nm, $\theta = 30\%$) presented in Fig. 4.22 (c).

To elucidate the dynamics of the aging process that resulted with the fragmentation of the $Ag_{0.85}Au_{0.15}$ islands deposited onto a-C film, we had to establish whether the exposure to ambient atmosphere was necessary for the observed morphology change. For that purpose, in addition to the samples that had been left exposed to air, on the same day we prepared a set of identical samples ($D = 6\pm1$ nm; $\theta = 30\%$) that were kept stored in the deposition chamber (see § 2.1.4), in darkness and isolated from the atmosphere, at the pressure of $p \sim 10^{-6}$ Torr. For 3 consecutive weeks one of these samples was taken out of the chamber and transferred to the TEM in a period of $t < 15$ min. The TEM images obtained from these samples are presented in Fig. 4.24 (right column) alongside TEM images of the sample that was aging in air for the same period of time (left column). As can be seen, unlike the sample exposed to air, the samples stored in vacuum did not exhibit any visible changes of their morphology – their appearance is very similar to the initial morphology of the sample left to age in air. Interestingly, once taken out of the chamber and left exposed to air, these samples underwent the same fragmentation process (not shown here) as the first sample, but with a delay. Simply said, the morphologies of samples that spent equal period of time exposed to air are very similar to one another, regardless of the period spent in vacuum of the deposition chamber.

All of this is strong evidence that environmental conditions are responsible for the fragmentation of alloy islands, implying that this is not a process that simply depends on the passage of time. To further support this claim, an aged sample was characterized by EDX in order to search for any foreign elements that were not present in the fresh samples.

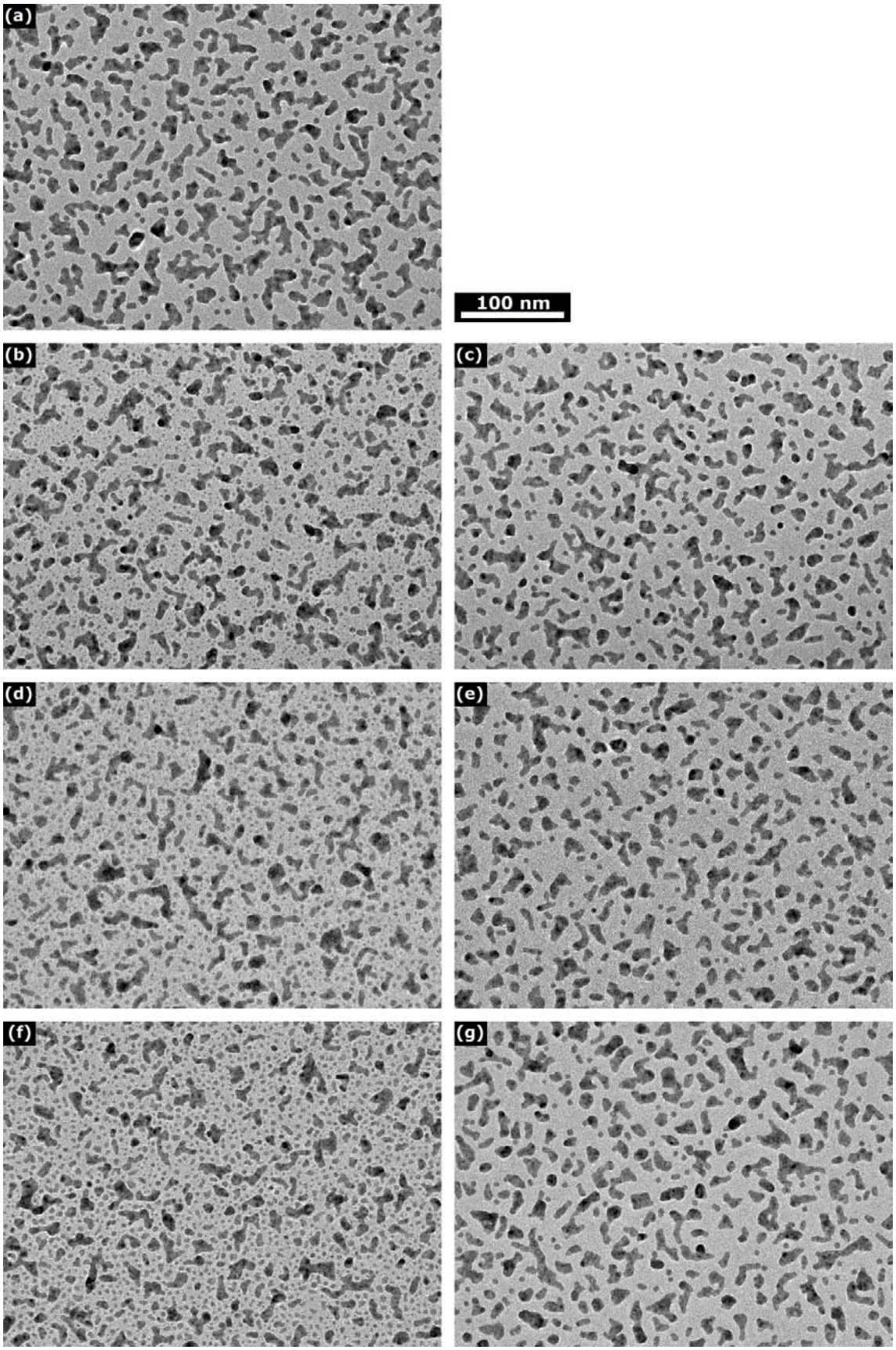

Figure 4.24: TEM images of high surface coverage samples exposed to air (left column) and stored in vacuum (right column), at various stages of aging: (a) fresh sample; (b-c) $t = 1$ week; (d-e) $t = 2$ weeks; (f-g) $t = 3$ weeks.

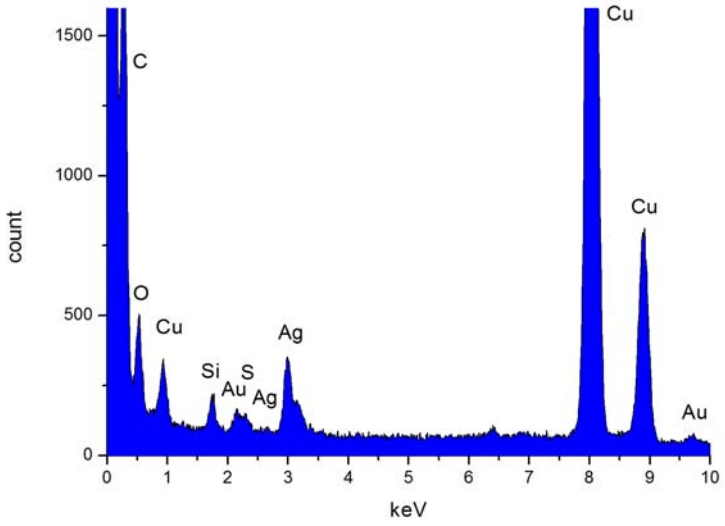

Figure 4.25: EDX spectrum of an aged high surface coverage sample ($t = 11$ weeks, $D = 6\pm1$ nm, $\theta = 30\%$), showing significant amount of O and Si in the sample, as well as traces of S.

16 EDX spectra were taken on various areas in the sample to get statistically significant results. If one compares a typical EDX spectrum of the aged sample ($t = 11$ weeks) presented in Fig. 4.25 with a typical EDX spectrum of a fresh sample given in Fig. 4.16, several things become clear:

(a) the O peak has grown significantly so that the amount of O rose over $10\times$

(b) a Si peak has appeared; in general, Si peaks could be artificial features of Si EDX detectors, but since it was not present in the fresh sample, we can not attribute it to the EDX detector installed in our TEM nor the Si-containing grease used in the TEM. This may suggest that some Si was incorporated in our samples during aging in ambient atmosphere, which would be quite surprising.

(c) a small S peak is also detected (note that it partially overlaps with an Au peak); naturally present in atmosphere, S is known to slowly corrode objects made of Ag, from cutlery silverware to nanowires[223]. Hence, it is possible that some S was incorporated into our alloy nanostructures during prolonged aging.

These EDX measurements suggest that a slow incorporation of O from air into $Ag_{0.85}Au_{0.15}$ nanoclusters and islands might be the main cause of the morphology change in these samples. However, before giving the final explanation of the observed phenomena, we conducted another set of experiments and expanded our study to samples with even higher surface coverage of $\theta = 100\%$.

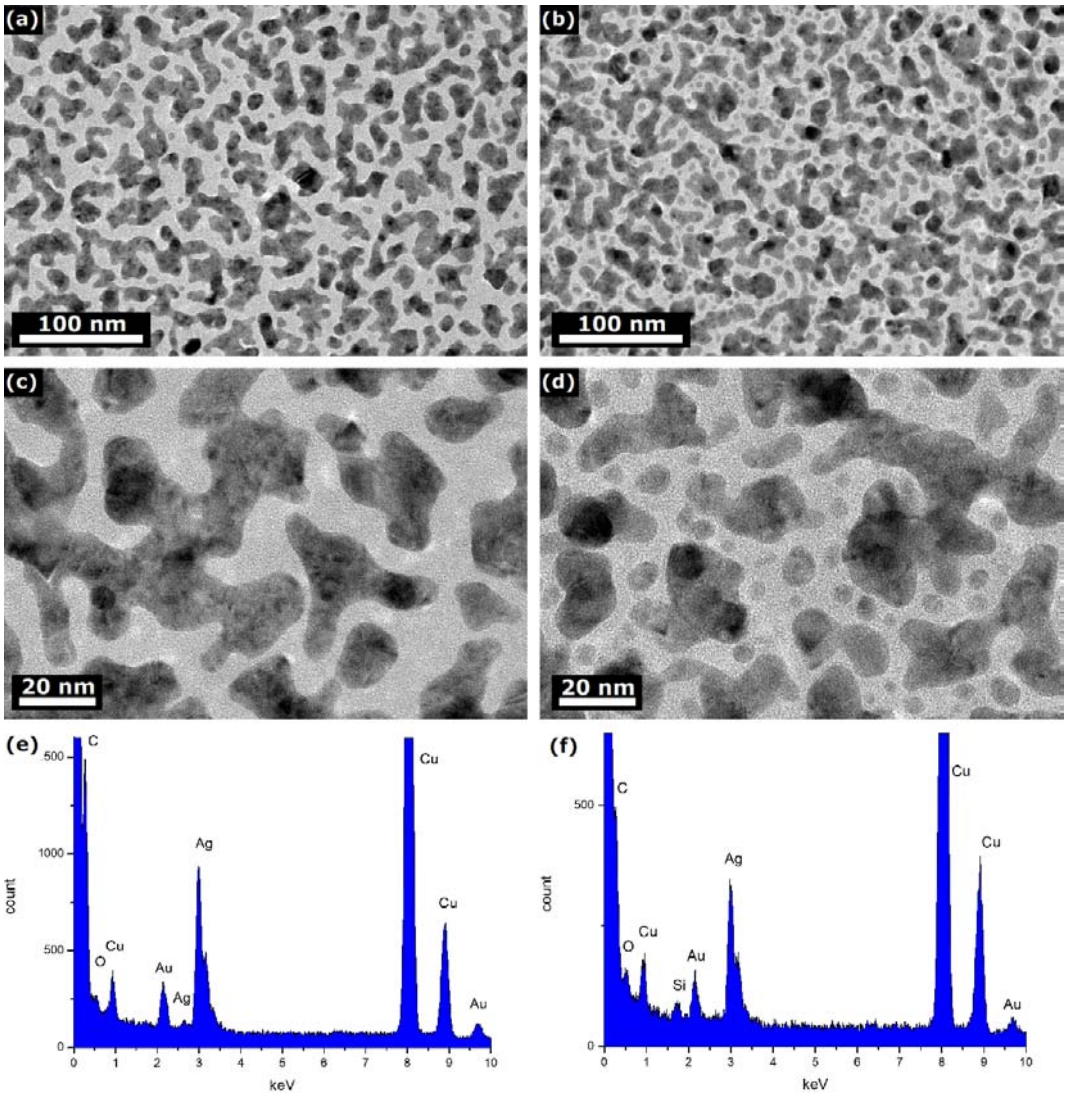

Figure 4.26: TEM images and corresponding EDX spectra of a high surface coverage $Ag_{0.85}Au_{0.15}$ sample ($D = 6\pm1$ nm, $\theta = 100\%$): fresh sample (left column) and the same sample after $t = 6$ weeks (right column).

Samples with $\theta = 100\%$

We used the same procedure in investigation of these samples as for the case of $\theta = 30\%$ samples. For the sake of simplicity we only show the comparison between the initial, fresh sample (left column in Fig. 4.26) and the same sample after $t = 6$ weeks in ambient atmosphere (right column). One can see that the morphology change over time is quite similar to the case of $\theta = 30\%$ samples i.e. the initally bigger islands started to fragment into smaller particles. Again, no signs of phase segregation were observed, suggesting the same dynamics as in $\theta = 30\%$ samples.

The EDX spectra of the aged sample (Fig. 4.26 (e-f)) showed the following:

(a) an increase in the O level by a factor of ∼3.5

(b) a Si peak appeared

(c) no traces of S

Note that the relative intensities of O and Si peaks in the aged $\theta = 100\%$ sample (Fig. 4.26 (f)) are quite similar to those seen in the $\theta = 30\%$ sample (Fig. 4.25).

4.4.5 Phase Segregation in Aged $Ag_{0.85}Au_{0.15}$ Nanocluster-based Thin Films

As we could see in the previous sections, although over time considerable morphology changes occurred in the $Ag_{0.85}Au_{0.15}$ nanocluster-based thin films that were exposed to air, no phase segregation was observed. However, the period of investigation was relatively short – it covered $t \sim 3$ months – which might be too short for the morphological and structural modifications to finish completely. Therefore, some of the high coverage sample were subjected to a longer investigation.

Fig. 4.27 shows TEM images of one of such samples ($D = 4.5 \pm 0.8$ nm, $\theta = 30\%$) taken over a period of 1 year. The morphology of the sample at $t = 6$ days shows a similarity to the images of other high coverage samples at that stage of aging with particles smaller than the deposited nanoclusters appearing in the sample after it was exposed to ambient conditions. After 6 months the morphology of the sample was quite different – core-shell and Janus nanoclusters were abundantly present, very much resembling the aged low surface coverage samples. However, another interesting feature was seen – all over the surface there were signs of cluster agglomeration into bigger *patches* with 20-50 nm in size. These patches seemed to be consisted of particles sitting on a smooth thin layer of material, quite similar to what was reported for Au nanoclusters on a-C[14,16]. Interestingly, the last imaging of this sample performed at $t = 12$ months showed that the morphology had further changed – the patches disappeared leaving behind Janus nanoclusters of very elongated bodies with tens of nanometers in length. Surprisingly, some of these elongated bodies showed signes of fragmentation, as indicated by the arrows in the inset of Fig. 4.27 (c).

The same type of fragmentation was observed in all HRTEM images of high surface coverage samples that had been aging for $t \gtrsim 12$ months: at least 11 samples of various original nanocluster sizes and surface coverages (but they all had $\theta \geq 13\%$) showed this behaviour (e.g. see Fig. 4.28 (a)). Moreover, HAADF STEM imaging

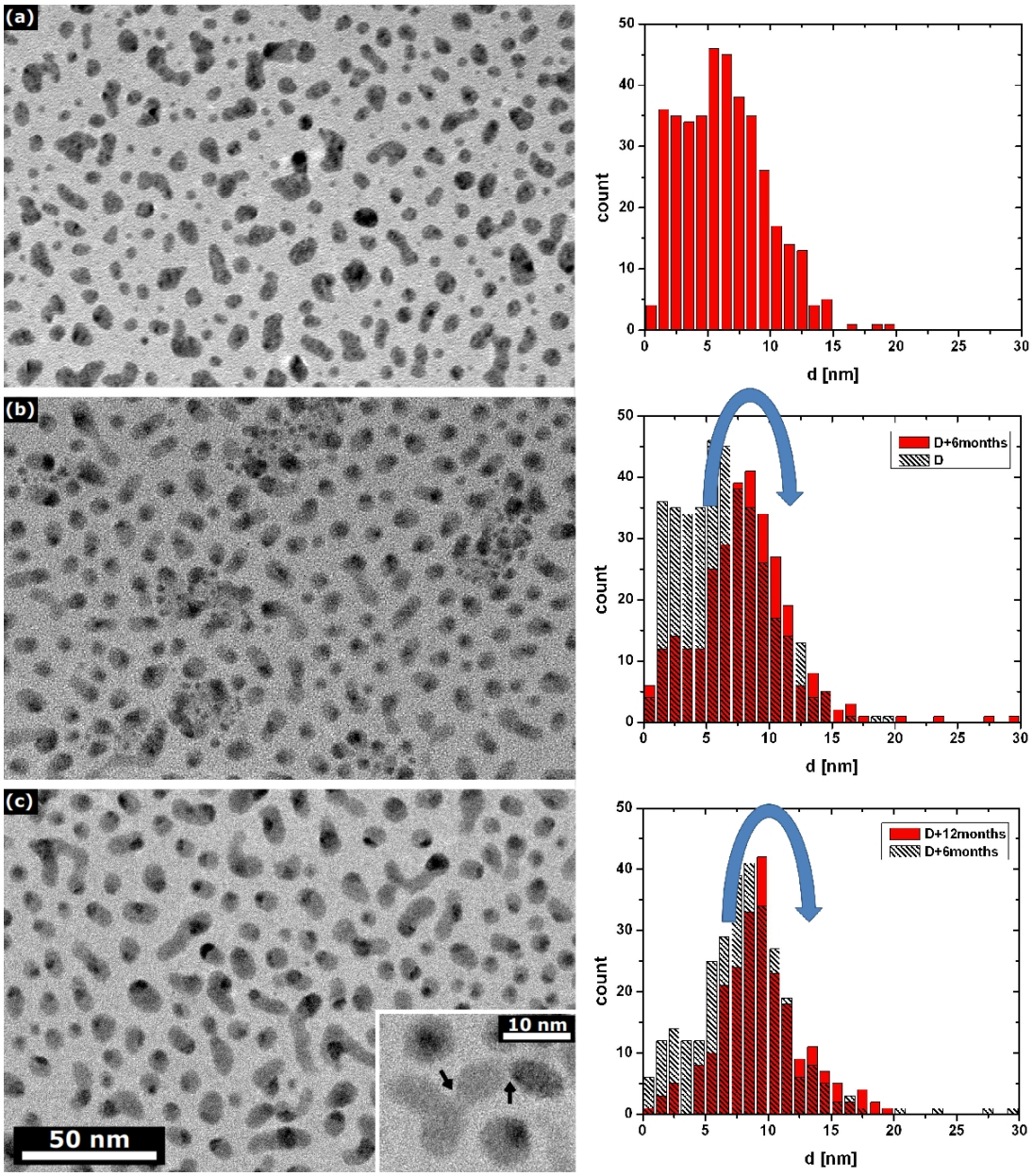

Figure 4.27: TEM images of $Ag_{0.85}Au_{0.15}$ sample ($D = 4.5 \pm 0.8$ nm, $\theta = 30\%$) at various stages of aging: (a) $t = 6$ days; (b) $t \sim 6$ months; (c) $t \sim 12$ months; close-up of an elongated island showing sings of fragmentation is given in the inset. Corresponding histograms describe show that over time the number of smaller particles decreased while the mean particle size increased from $d \sim 6$ nm to $d \sim 9$ nm.

provided insights into the composition of the fragments – it seems the elongated Janus nanoclusters separate into two (or more) fragments in such a way that one of the fragments is Au-rich, whereas the other one is Ag-rich. This is a relatively slow process which had not finished by the time of the last imaging. However, some of the images captured the fragmentation at various stages of the process – the HAADF STEM image given in Fig. 4.28 (b) is a perfect example, showing signs of early neck

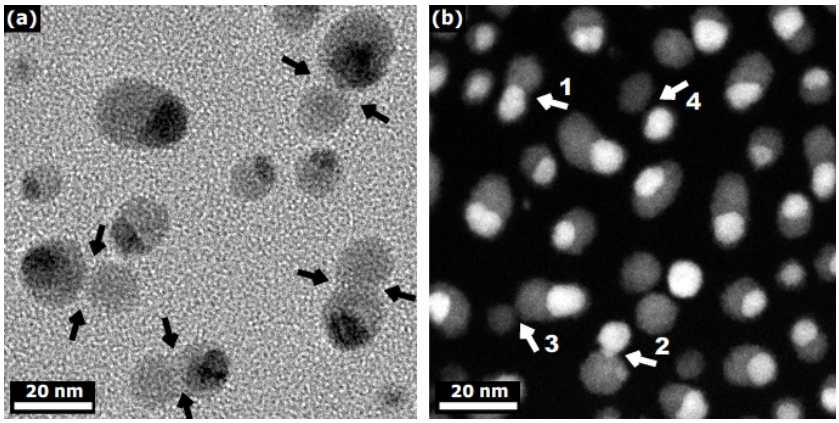

Figure 4.28: (a) TEM image of an aged $Ag_{0.85}Au_{0.15}$ sample (t = 18 months, D = 6±1 nm, θ = 13%). (b) HAADF STEM image of another aged $Ag_{0.85}Au_{0.15}$ sample (t = 12 months, D = 3.0±0.4 nm, θ = 30%), showing nanoclusters at various stages of segregation: 1 – neck formation; 2 – neck narrowing; 3 – neck breaking; 4 – separate clusters.

formation, neck narrowing, and splitting into separate nanoclusters.

4.5 Discussion of Results

In the previous sections it was shown that major structural and morphological changes occurred in $Ag_{0.85}Au_{0.15}$ nanoclusters and nanocluster-based thin films when they were exposed to ambient atmosphere for a longer period. The control samples that were stored in the deposition chamber of the IGA system did not show such alterations of their morphology in the same period, which is strong evidence that environmental conditions must have played a key role in the process.

HRTEM images of the aged low coverage samples showed that nanoclusters over time turned into core-shell objects, either being concentric or Janus-like. The shells seemed to be mostly amorphous; however, in some of the Janus nanoclusters the shells were partially crystalline which allowed for the lattice spacings to be analyzed. The analysis showed that the interplanar distances and angles were consistent with the Ag_2O structure. In addition, EDX measurements showed the presence of significant amount of O in the aged samples – considerably more than in the case of fresh samples. Moreover, the level of O seemed to be growing over time, indicating its incorporation into the nanoclusters and thin films.

Based on these information, we propose the following model. Initially, fresh $Ag_{0.85}Au_{0.15}$ nanoclusters and nanocluster-based films are homogeneously alloyed. When left exposed to air, the surface of clusters and islands starts to oxidize so that the topmost layers become O-rich. At first, the incorporation of O into the Ag-Au system is not stoichiometric, i.e. amorphous Ag_xO is formed over the surface

of clusters and islands. As was seen experimentally by Layson et al.[197–199], the incorporation of O may lead to the lowering of the energetic barrier for surface diffusion of Ag via formation of highly mobile Ag_xO adspecies (see Fig. 4.7). In the case of Ag/Ag(1,0,0), surface diffusion was relatively quick ($t \sim$ days) which is not surprising since the substrate in their case was relatively smooth. Similar results were obtained when Ag nanoclusters deposited onto Ti_2O were exposed to O[196] or when O was added in the source[200–203]. In our case though, the a-C film that $Ag_{0.85}Au_{0.15}$ nanoclusters were deposited onto is much rougher, making the energetic barrier for any surface diffusion considerably higher. However, this may simply mean that the diffusion rate will be decreased and, consequently, it will take more time for any observable morphological change to occur.

The interesting thing here is the difference in the way the low and high surface coverage samples undergo such morphological and structural changes. The former samples contained individual clusters with relatively big distances between them. In that case no obvious signs of surface diffusion were ever observed in the TEM investigations. All of the nanoclusters in these samples were growing bigger in time (as seen in Fig. 4.17), which is a bit surprising from the point of view of surface diffusion via Ag_xO adspecies. However, there exists a competing process – Ostwald ripening – so that any of these adspecies which may have been wandering around the surface of a-C film was most probably added to a nearby nanocluster rather quickly, forming an amorphous Ag_xO shell around the alloyed core. Consequently, we could observe only growth of the nanoclusters through the incorporation of O atoms, but not their reduction in size nor formation of smaller particles in the samples.

In the high surface coverage samples though, the amount of material available for creation of Ag_xO adspecies was much higher. Therefore, their concentration (number of adspecies per unit area) on the surface of a-C film was relatively high. In fact, it is likely that over time the surface of the film got saturated with these adspecies so that some of them agglomerated into clusters – those are the clusters one can readily see in TEM images after $t \gtrsim 1$ week. These clusters grew bigger over time, eventually forming core-shell and Janus structures, just like the ones seen in the low surface coverage samples. Note that it is possible that some Au also takes part in the redistribution of atoms via this type of surface diffusion.

Once the nanoclusters have formed sufficiently thick Ag_xO shell, some of this amorphous material starts to slowly crystallize into thermodynamically more stable form of silver oxide – Ag_2O[224] – and an elongated body starts to form giving Janus-like appearance to the cluster.

In bigger Janus clusters of fragmented islands, the presence of highly mobile amorphous Ag_xO may lead to redistribution of atoms *within* the entity shaping a

form that will minimize its surface energy. This process is very much similar to Rayleigh instability[225] and is know to happen in nanoscale objects[20,226,227]. Therefore, any elongated entity is likely to eventually split into fragments, just as it can be seen in Figs. 4.27 (c) and 4.28.

Since a small amount of S was detected in the aged samples, it is also likely that some incorporation of S into the nanoclusters had occurred during the prolonged aging of samples in atmosphere so that some Ag_2S was also formed[223]. The latest (October 2011) HRTEM imaging and selected area electron diffraction (SAED) of samples as old as 27 months did show (see Fig. 4.29) that the particles with a crystal structure corresponding to monoclinic Ag_2S ($a = 4.23$ Å, $b = 6.91$ Å, $c = 7.87$ Å, $\beta = 99.58°$)[228] were also present in some of the samples.

However, in the early stages of aging ($t \lesssim 10$ weeks) no such lattice was found in any of the samples and the EDX spectra showed no traces of S, while the O level steadily increased in that period, corroborating the claim that O caused the observed morphological changes.

Although not presented in this work, for the sake of completeness it should be said that very similar structural and morphological changes were observed for monometallic Ag and alloy $Ag_{0.9}Au_{0.1}$ nanoclusters.

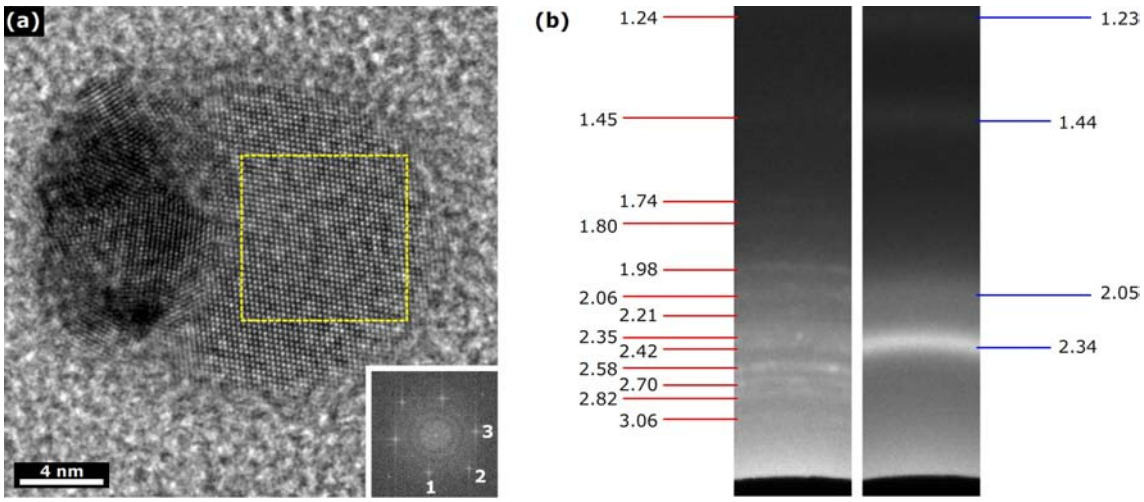

Figure 4.29: (a) HRTEM image of a Janus nanocluster from an aged sample ($t = 27$ months, $D = 6\pm1$ nm, $\theta = 13\%$) showing a polycrystalline core/head and partially crystallized shell/body. FFT pattern of the selected area is shown in the inset; spots 1,2, and 3 correspond to interplanar distances $d_1 = 2.6\pm0.1$ Å, $d_2 = 2.1\pm0.1$ Å, and $d_3 = 2.5\pm0.1$ Å, which in combination with the measured angles $\alpha_{1-2} = 56\pm2°$, $\alpha_{2-3} = 49\pm2°$ reveals that these planes match[228] {1,2,0}, {0,2,3}, and {-1,0,3} planes in monoclinic Ag_2S, respectively. Here the zone axis of Ag_2S is [6,-3,2]. (b) SAED pattern of the aged sample from (a) exhibiting rings that correspond to interplanar distances in FCC Ag(Au) and also rings that are consistent with monoclinic Ag_2S (see Frueh[228]); SAED pattern of a fresh $Ag_{0.85}Au_{0.15}$ sample showing only rings from FCC Ag(Au) is presented for comparison. Values are given in Å.

4.6 Electron Beam Effect

As mentioned earlier, sub-3 nm clusters were quite unstable under the electron beam in the TEM, showing signs of structural fluctuations, as well as a loss of material. This issue was not limited only to such small clusters – every cluster would sooner or later exhibit some kind of a structural and/or morphological transition when irradiated with electrons for a longer period of time. The rate of the change seemed to depend on the electron beam intensity, size of nanoclusters, and their composition. Fortunately, under usual HRTEM imaging conditions, clusters with $D > 4$ nm were stable for at least a few minutes, even at a high electron beam intensity, which was long enough to capture high quality images of their initial structures.

As an example of the electron beam induced morphological and structural transition, in Fig. 4.30 we present a case of a Janus nanocluster imaged at a relatively high electron beam intensity i.e. at a high TEM magnification ($M = 800$ k×). Initially, it had an alloy Ag-Au core of FCC structure and a partially crystalline shell, most

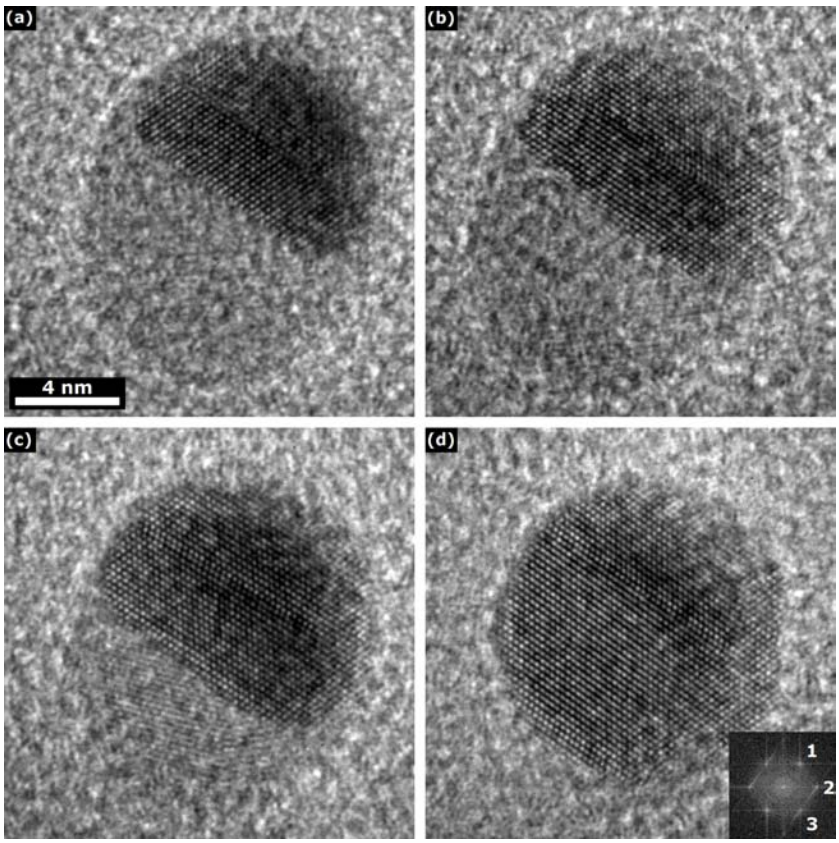

Figure 4.30: Sequence of HRTEM images of an initially phase segregated Janus nanocluster that experienced a structural and morphological change when irradiated with the electron beam: (a) $t = 2$ minutes; (b) $t = 4$ minutes; (c) $t = 8$ minutes; (d) $t = 10$ minutes. FFT of the cluster given is in the inset of (d): spots 1,2, and 3 correspond to {1,-1,1}, {0,0,2}, and {-1,1,1} planes in FCC Ag or Au, respectively.

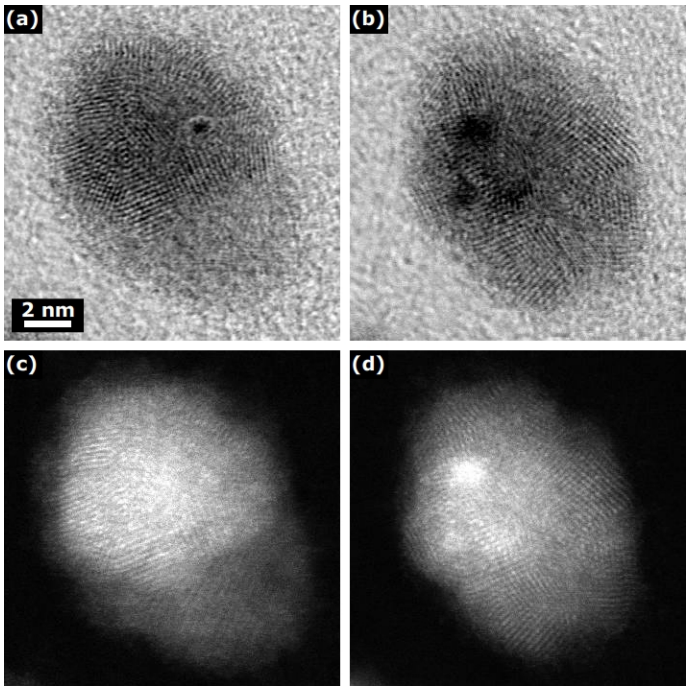

Figure 4.31: BF HRTEM (a-b) and HAADF (c-d) STEM images showing evolution of a Janus nanocluster under the electron beam irradiation. The images in the right column were acquired approximately 9 minutes after the images in the left column.

likely made of Ag_2O. During a prolonged exposure to the electron beam, the shell reduces in size, while the FCC core grows by recrystallizing the shell. At the end of the process, approximately 10 minutes into imaging, the shell almost completely disappeared, resulting with a rounder, smaller FCC nanocluster. Interestingly, although structurally the cluster seems homogeneous, there exist a contrast within the cluster – a lighter, 1-2 nm thin shell is visible around a darker core – which suggest that compositionally the cluster may not be homogeneously alloyed i.e. possibly a thin Ag shell developed around the Ag-Au core.

Similar effect was seen in the bright field and HAADF STEM images presented in Fig. 4.31 where an initially phase-segregated Janus cluster (left column) changed into a more homogeneous polycrystalline object (right column) after approximately 9 minutes of electron beam irradiation.

As was seen, the prolonged exposure to the electron beam may lead to morphological and structural changes in phase segregated nanoclusters, so caution is needed when imaging such objects. As long as the beam intensity was relatively low and the imaging time was short, the above mentioned changes were negligible.

4.7 Conclusions

This chapter outlined the results of a comprehensive study of alloy Ag-Au nanoclusters and nanocluster-based thin films generated in the IGA magnetron sputtering system and deposited onto a-C films. The study focused on examination of structural, morphological and compositional properties of these nanoscale systems, with the main goal of identifying the nanocluster structure and looking for any signs of phase segregation between the constituent elements.

Deposition of low surface coverage samples ($\theta \lesssim 5\%$) allowed for investigation of individual nanoclusters with sizes in the range 3 nm $< D <$ 10 nm. A thorough TEM characterization of these samples, performed immediately after the deposition ($t <$ 15 minutes), produced over 700 high-quality HRTEM images, containing over 1700 individual nanoclusters. The meticulous analysis of these images revealed that the vast majority of $Ag_{0.85}Au_{0.15}$ nanoclusters were icosahedral ($> 87\%$), followed by decahedral structure ($> 9\%$) as the second largest type. Interestingly, very few FCC nanoclusters ($< 2\%$) were observed at any cluster size. The population distribution of the nanocluster type turned out to be size dependent: the fraction of Ih clusters steadily decreases for clusters with $D > 8$ nm; at the same time the fraction of Dh cluster rises, and the fraction of FCC clusters remained very low. This behaviour suggests that the experimental conditions (primarily the Ar flow) used during inert gas aggregation of alloy $Ag_{0.85}Au_{0.15}$ nanoclusters may have left the nanoclusters in a state where they were kinetically trapped in the form of Ih or Dh, but not FCC. In addition, no phase segregation was seen in any of these fresh clusters.

Once left exposed to ambient conditions, in time these samples underwent surprising structural and compositional transitions: initially faceted Ih and Dh nanoclusters turned into core-shell and Janus nanoclusters. HRTEM and HAADF STEM characterization of these aged samples indicate that the cores are alloyed (Ag-Au) and of a fivefold symmetry, similar to the initial structure, while the shells are made up of mostly amorphous Ag_xO, although partially crystalline shells are also seen in Janus-like nanoclusters. The incorporation of atmospheric O is further supported by the evidence of the increased level of O observed in the EDX spectra of the aged samples.

High surface coverage samples contained larger islands of $Ag_{0.85}Au_{0.15}$, forming either discontinuous (for $\theta \sim 30\%$) or continuous (for $\theta \sim 100\%$) nanocluster-based films. When these samples were stored in ambient atmosphere, they too exhibited morphological and structural changes; however, the pathway and the rate of the changes was quite different than in the case of low surface coverage samples. In less than a week after being exposed to air, the number of smaller, individual particles

soared, indicating pronounced surface diffusion of Ag (and possibly Au). Since the control samples stored in vacuum did not show the same morphological transition over that period, it was obvious that environmental conditions were a key factor in the observed phenomenon. Similar to the low surface coverage case, the exposure to atmospheric O most likely led to the creation of highly mobile Ag_xO adspecies that enhanced the surface diffusion of material on the a-C film. Over a period of time, the particles grew bigger and formed core-shell and Janus-like structures, leaving the initially bigger islands completely fragmented. At the end, the morphology of high surface coverage samples that were aging for $t \gtrsim 12$ months was very much similar to the morphology of the aged low surface coverage samples where core-shell and Janus structures were readily observed. However, there was a difference: some of the elongated particles in the high surface coverage samples began to fragment into Ag_xO-rich and Ag-Au rich clusters in a fashion similar to Plateau-Rayleigh instability. Possibly the presence of highly mobile Ag_xO enhanced the redistribution of material within these elongated particles so that they eventually split into separate entities. In the low surface coverage samples though there seemed to be no particles elongated enough to undergo this type of fragmentation.

The study of $Ag_{0.85}Au_{0.15}$ nanoclusters therefore encompassed not only the properties of initial individual clusters, but also the long term stability of nanoclusters and nanocluster-based thin films. Since the Ag-Au nanoclusters are very appealing from the point of view of catalysis, these findings might prove valuable if real world applications are to be achieved e.g. in the design of catalytic reactors.

Chapter 5

Studies of $Ni_{0.85}Cu_{0.15}$ Nanoclusters and Carbon Nanotubes

This chapter describes an investigation of $Ni_{0.85}Cu_{0.15}$ nanoclusters generated in our IGA magnetron sputtering system. We produced samples containing nanoclusters of various sizes and surface coverages, deposited onto different substrates suitable for SEM or TEM characterization. In addition, we prepared $Ni_{0.85}Cu_{0.15}$ samples that were used as catalysts in syntheses of single-wall carbon nanotubes (SWCNTs) and multi-wall carbon nanotubes (MWCNTs) by catalytic chemical vapour deposition (CVD). A preliminary study of CNT growth was conducted in order to optimize both $Ni_{0.85}Cu_{0.15}$ nanocluster size and CVD growth experimental conditions for a straightforward synthesis of SWCNT and MWCNTs. These initial studies serve to prepare the ground for future work where the goal will be to try to tailor the chirality of CNTs by using nanoclusters of certain characteristics combined with appropriate CNT growth conditions.

5.1 $Ni_{0.85}Cu_{0.15}$ Nanoclusters

This section outlines basic facts about Ni-Cu systems, starting from the bulk alloys, to thin Ni-Cu films, to recent advances in nanoscale Ni-Cu systems, comprising both modeling and experimental results.

5.1.1 Bulk Ni-Cu alloys

Both Ni and Cu are metals that are widely used in many applications. While Ni is relatively hard and corrosion-resistant with a relatively high melting point

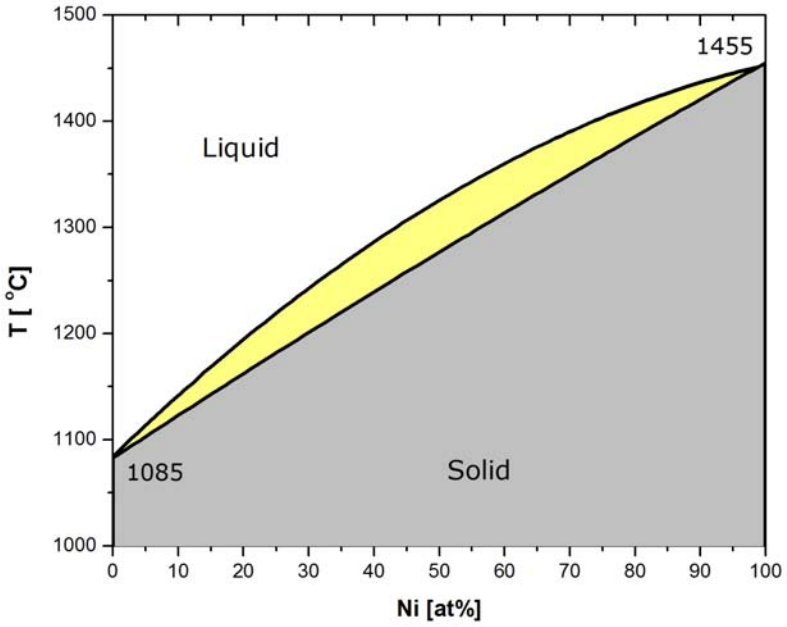

Figure 5.1: Phase diagram of a bulk Ni-Cu system, showing full miscibility of Ni and Cu. Note that a solid and liquid phase coexist prior to complete melting of the system. [138]

temperature (1455°C), Cu is ductile, soft and very conductive with a lower melting point temperature (1083°C). When combined together, these two metals give alloys of very appealing properties - being conductive and corrosion-resistant in sea water makes them ideal for use in many harsh industrial environments.

The phase diagram of a bulk Ni-Cu system presented in Fig. 5.1 reveals that Ni and Cu are fully miscible at any composition. In a way this is expected since both Ni and Cu crystallize in face centered cubic (FCC) lattice with a very small mismatch between the lattice parameter ($a_{Ni} = 3.52$ Å, $a_{Cu} = 3.61$ Å)[137]. However, there is evidence that the phase diagram presented in Fig. 5.1 may not be valid near the alloy surface. For example, it was found experimentally that at 550 °C Cu showed a tendency to enrich (1,1,1) surface layers up to 54 at.% in a bulk Ni-Cu alloy containing only 5 at.% of Cu, gradually decreasing to the bulk composition in the first 13 surface layers[229]. These early experimental results were later backed up by a Monte Carlo simulation study of Ni-Cu alloys at 800 K that showed an increased concentration of Cu atoms in the surface layers (see Fig. 5.2) for various crystal facets and bulk alloy compositions[230]. Similar results were obtained in a more recent simulation study of Ni-Cu alloys that covered a wider range of Cu concentration ($Ni_{0.25}Cu_{0.75}$, $Ni_{0.5}Cu_{0.5}$, and $Ni_{0.75}Cu_{0.25}$)[231]. It was found that at 1000 K the Cu concentration increases in the top 5 surface layers for (1,0,0) facets, with the top layer consisting of pure Cu.

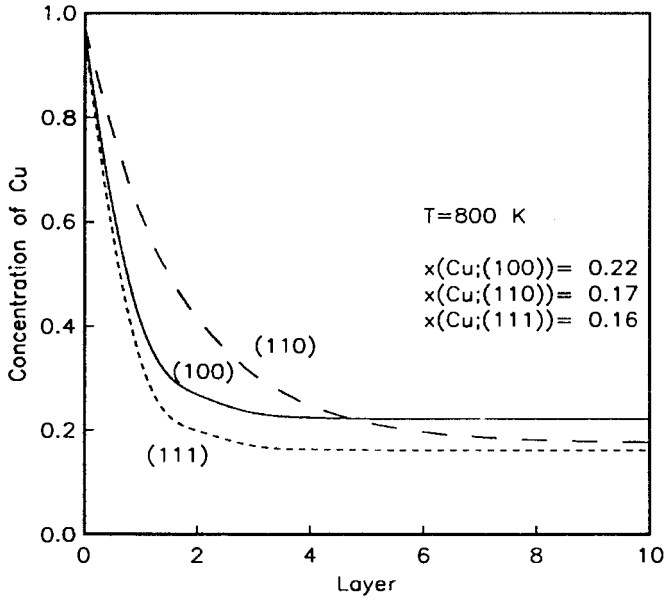

Figure 5.2: Simulation results showing concentration of Cu atoms in (1,1,1), (1,1,0), and (1,0,0) surface layers of bulk Ni-Cu alloys.[230]

5.1.2 Nanoscale Ni-Cu Alloys

Obviously, the presence of a crystal boundary can significantly influence the atomic arrangement in the Ni-Cu system. While for bulk Ni-Cu alloys this affects only a minor fraction of the total number of atoms, in nanoscale alloys it should play an important role in determining the structure, shape and composition of the system. Therefore, there is a need for establishing not just one but a whole set of size-dependent nanoalloy phase diagrams – some modeling of these is under way, although experimental verifications of proposed diagrams may be quite difficult and time-consuming.

Modeling of Nanoscale Ni-Cu Alloys

Early attempts to model the ordering in Ni-Cu nanoalloys were limited to systems with a relatively small number of atoms; nevertheless some valuable insights into the nanocluster structure and phase segregation were obtained. Montejano-Carrizales et al.[232] used the embedded-atom method (EAM) to model the ordering in 147 atom Ni-Cu clusters. They found that an icosahedral (Ih) structure is favoured over cuboctahedral (cOh), with Cu atoms showing a tendency to segregate to the surface, achieving the smallest possible number of neighboring atoms. Similarly, by introducing a bond-order simulation (BOS) model, Zhu and DePristo[233] showed a preferential surface segregation of Cu atoms in a 201-atom Ni-Cu (cOh) cluster containing 101 Ni atoms (see Fig. 5.3); Mainardi and Balbuena[234] computationally

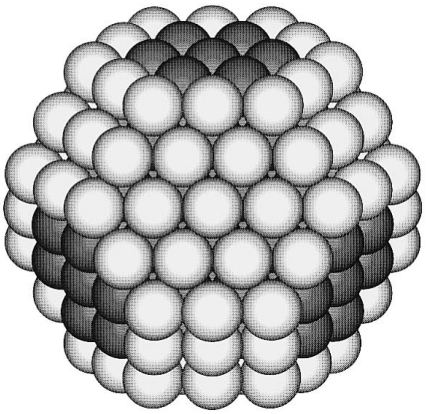

Figure 5.3: Simulation results for a 201-atom Ni-Cu cluster exhibiting preferential segregation of Cu atoms to the sites with the least neighbors. Ni and Cu atoms are represented by darker and lighter spheres, respectively.[233]

investigated FCC Ni-Cu clusters comprising 125–729 atoms, with the Cu content varying from 5 to 95 at%. They too found a strong tendency for Cu to segregate to the lowest coordination number sites, for all considered temperatures. Recently, Hristova et al.[235] confirmed the Cu segregation in small Ni-Cu clusters ($N \leq 38$), as well as Cui-Ju et al.[236] in very small Ni-Cu clusters ($N \leq 10$).

The issue of size-dependent melting temperature of Ni-Cu nanoclusters is very interesting, particularly in our case where Ni-Cu nanoclusters are to be used as catalysts in high-temperature CVD synthesis of CNTs. Huang and Balbuena[237] used molecular dynamics (MD) simulations to study the melting behaviour in 343 and 1000-atom Ni-Cu clusters of two compositions: $Ni_{0.75}Cu_{0.25}$ and $Ni_{0.5}Cu_{0.5}$. Their results (see Fig. 5.4) suggest that, depending on the size and composition, the melting temperature of Ni-Cu nanoclusters is in the range 700–900 K – significantly lower than the melting temperature of bulk Ni-Cu alloys seen in Fig. 5.1. Moreover, their study indicates that the melting of surface Cu atoms starts at temperatures as low as 400 K.

More recently, similar values of Ni-Cu nanocluster melting temperature were obtained by Li et al.[238] who additionally tried to construct a phase diagram of a nanoscale Ni-Cu system in the case of 682 and 1048-atom clusters (see Fig. 5.5). Based on their MD studies, the solidus and liquidus curves of the nanoscale Ni-Cu phase diagram are significantly lower than for the bulk Ni-Cu alloy. As the cluster size decreases, both the solidus and liquidus curves exhibit a shift to lower values of temperature. This downward shift from the bulk curves is visible even in the case of relatively big Ni-Cu clusters having a diameter of 60 nm, as calculated by Shirinyan et al.[239].

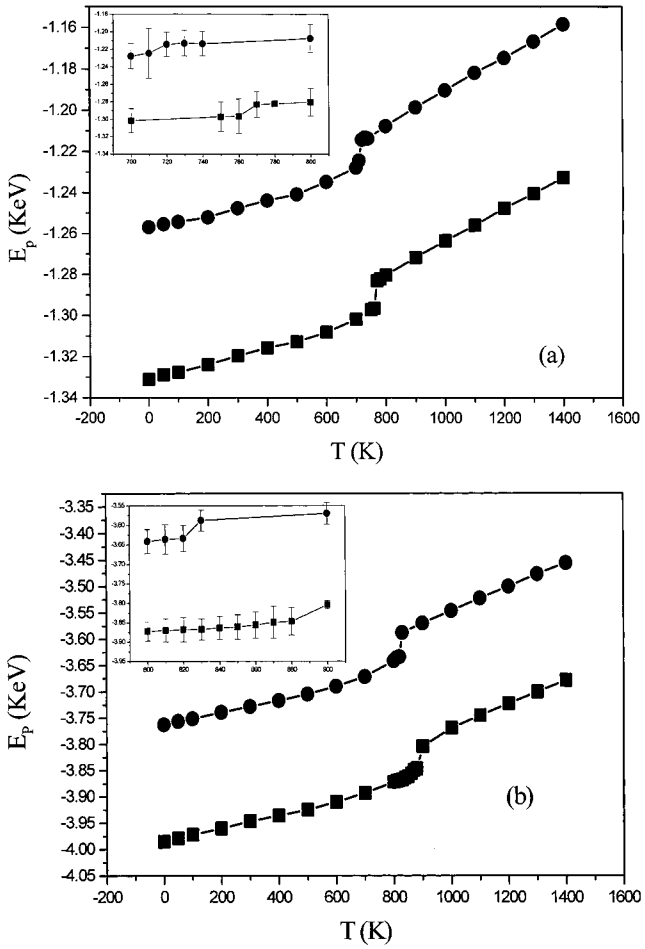

Figure 5.4: MD simulation results of Ni-Cu nanocluster potential energy as a function of temperature, for a 343-atom cluster (a) and for a 1000-atom cluster (b). Squares and circles correspond to $Ni_{0.75}Cu_{0.25}$ and $Ni_{0.5}Cu_{0.5}$, respectively. Insets show the region near the melting point.[237]

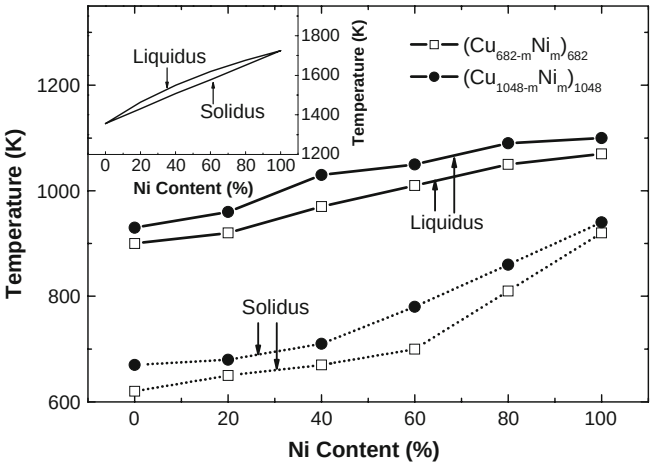

Figure 5.5: Nanoscale phase diagram of Ni-Cu system. Inset is the phase diagram for the bulk Ni-Cu alloy.[238]

Previous Experimental Studies of Nanoscale Ni-Cu alloys

Early experimental work in the field of Ni-Cu alloys included studies of objects with dimensions between bulk and nanoscale, such as thin films or powders. For example, Van Ingen et al.[240] studied polycrystalline thin (down to 100 nm) Ni-Cu and Ni-Ag films prepared by laser ablation deposition from bulk alloy targets. By x-ray diffraction (XRD) it was found that the Ni-Cu films were homogeneous, showing the presence of only one solid phase, indicating a formation of polycrystalline Ni-Cu solid solution. Interestingly, while the composition of deposited Ni-Cu thin films matched the composition of targets used in the experiment, Ni-Ag films were richer with Ni than the starting alloy target.

Pabi and collaborators[241] prepared Ni-Cu nanocrystals by mechanical milling of elemental powders. XRD characterization revealed the creation of ∼30 nm crystals of solid Ni-Cu solution, after 20 hours of milling. During that time, the difference between the lattice parameters of Ni and Cu steadily decreased indicating a gradual formation of solid Ni-Cu solution (see Fig. 5.6).

One of the first attempts to fabricate and characterize Ni-Cu nanoclusters came from Cattaruzza and coworkers[242] by means of ion implantation of Ni and Cu into silica substrates. Their synchrotron x-ray absorption spectroscopy (XAS) investigation revealed the presence of $Ni_{0.5}Cu_{0.5}$ nanoclusters embedded in the substrate, additionally confirmed by TEM observations and optical absorption spectra measurements.

Further advances in the field of Ni-Cu nanoclusters came through research based on wet chemical syntheses. Damle and Sastry[243] firstly utilized fatty acid matrices to synthesize Ni and Cu cluster films and then used low temperature annealing at 100 °C to produce alloyed Ni-Cu nanoclusters, ranging 15-50 nm in diameter. XRD study showed that the lattice parameter of the formed Ni-Cu nanoclusters had a

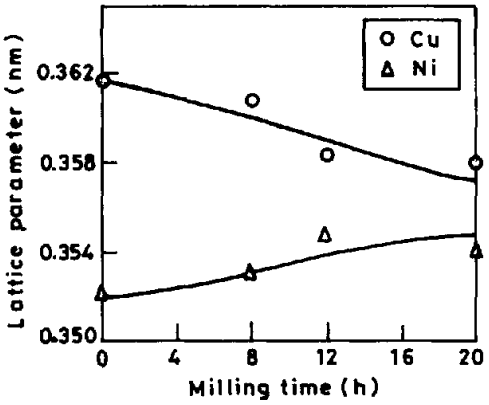

Figure 5.6: Time-dependent change of Ni and Cu lattice parameters during mechanical alloying.[241]

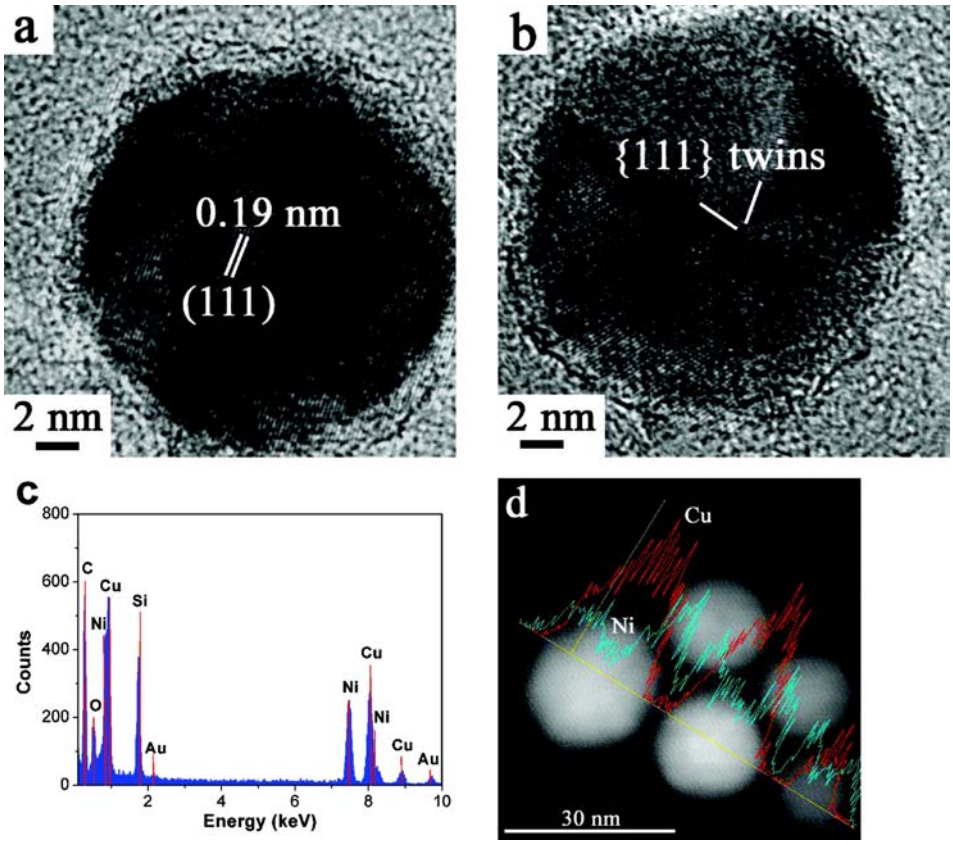

Figure 5.7: (a-b) HRTEM images of $Ni_{0.5}Cu_{0.5}$ nanoclusters.(c) EDX spectrum of $Ni_{0.5}Cu_{0.5}$ nanoclusters (Au originates from the TEM grid). (c) ADF image of nanoclusters indicating Cu-Ni core-shell structure.[244]

value between those for pure Ni and Cu, which is consistent with the results of Pabi et al[241], presented in Fig. 5.6.

More recently, Zhang et al.[244] and Yamauchi et al.[245] synthesized Cu-Ni core-shell nanoclusters (see Fig. 5.7). This structure is very appealing from the standpoint of a possible use in chemical catalysis. For instance, Zhang et al.[244] used these nanoclusters as catalysts for generation of H_2 by means of thermal hydrolysis of $NaBH_4$. The study revealed increased catalytic activity of the Cu-Ni core-shell nanoclusters compared to the monometallic Ni catalyst, suggesting strong synergistic effects.

In addition, Yamauchi et al.[245] studied oxidation of Cu-Ni core-shell nanoclusters. It was shown that, when exposed to air, the surface of Ni-Cu nanoclusters tended to oxidize quite easily, creating thin patchy oxide layers, as can be seen in Fig. 5.8.

When it comes to production of Ni-based clusters by means of inert gas aggregation (IGA), only a few attempts have been reported so far. Zhou et al.[246] investigated structural characteristics of Ni-NiO core-shell nanoclusters. Interestingly, their TEM images showed very high proportion ($\geq 90\%$) of cubic nanoclusters. More recently,

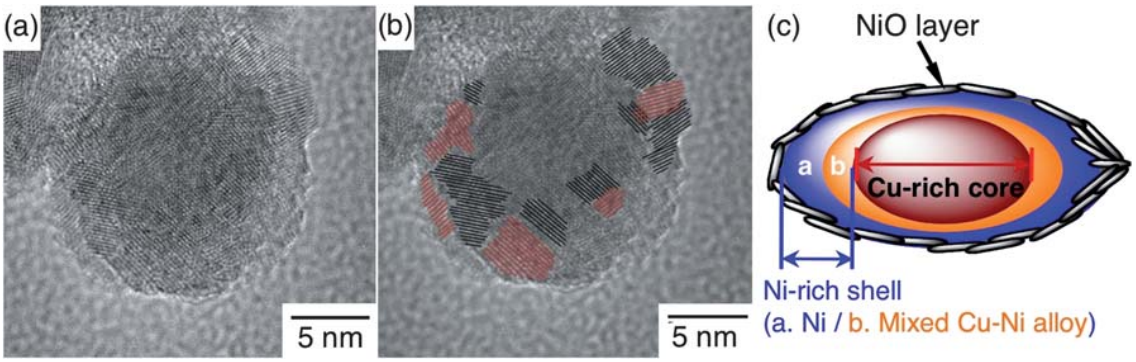

Figure 5.8: (a-b) HRTEM images of an oxidized $Cu_{0.4}Ni_{0.6}$ nanocluster, with the lattice spacings indicated by red (2.43 Å) and black lines (2.07 Å) that correspond to (1,1,1) and (2,0,0) interplanar distances in FCC NiO (a = 4.14 Å), respectively. (c) Illustration of the nanocluster structure. [245]

D'Addato's group conducted an intensive study of Ni nanocluster films[247], as well as Ni-MgO core-shell[248] and Ni-NiO core-shell[249] nanoclusters. The latter work shows that fresh Ni nanoclusters ranging 4-8 nm in diameter are predominantly Ih (see Fig. 5.9), chemically and structurally stable when exposed to air for a relatively long period of time (up to 15 hours). Furthermore, it was shown that over time a patchy NiO shell had formed around the Ni core, which is consistent with the work of Yamauchi et al[245]. However, in this case the NiO shell adopted the Ih structure of the core and remained structurally stable during the early stage of oxidation.

Similarly, there are only a few reports on Cu nanoclusters produced by IGA methods. Our group at the University of Canterbury previously studied Cu nanocluster-based devices[25], with the emphasis on their electrical properties. Apart from our group, it is worthwhile mentioning the latest effort from Gracia-Pinilla et al. [250] who managed to produce size-controlled Cu nanoclusters ranging 1-5 nm in diameter, using their IGA sputtering system.

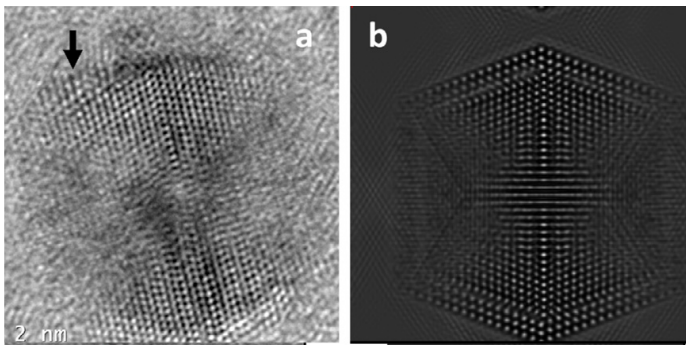

Figure 5.9: (a) HRTEM image of an oxidized Ni nanocluster, with the black arrow pointing to the possible presence of NiO nanocrystalline island formed on the Ni core. (b) Simulation of a Ni-NiO core-shell Ih nanocluster. Note the difference between the lattice spacings in the core and shell. [249]

5.2 Results of $Ni_{0.85}Cu_{0.15}$ Nanocluster Study

This section contains results of our investigation of $Ni_{0.85}Cu_{0.15}$ nanoclusters produced in the IGA magnetron sputtering system (see Chapter 2 for details). In total 139 $Ni_{0.85}Cu_{0.15}$ samples of various cluster sizes and surface coverages were produced during the study. Firstly, samples were deposited onto various TEM grids and characterized *ex-situ* at different stages of aging, using a Philips CM200 analytical HRTEM, located at UCEM. Secondly, sets of $Ni_{0.85}Cu_{0.15}$ samples were deposited onto Si_3N_4/Si substrates suitable for CNT growth experiments – results of those experiments are presented later in the chapter.

5.2.1 Fresh $Ni_{0.85}Cu_{0.15}$ Nanoclusters

Just like in the case of $Ag_{0.85}Au_{0.15}$ nanoclusters presented in the previous chapter, *fresh* $Ni_{0.85}Cu_{0.15}$ nanoclusters were characterized shortly after their deposition with minimum exposure to air (<15 minutes) during the transfer from the deposition chamber to the TEM. A typical TEM image of a low surface coverage sample ($\theta \leq 3\%$) is shown in Fig. 5.10. At this surface coverage coalescence of clusters is negligible which allows for an investigation of properties of individual nanoclusters. In addition, it allows for an efficient determination of the cluster size distribution (see Fig. 5.11), calculated from the cluster's projected area, with an assumption that the clusters are spherical.

HRTEM images of the $Ni_{0.85}Cu_{0.15}$ samples revealed that the nanoclusters are either of Ih structure, as can be seen in Fig. 5.10 (b), or they retain their bulk FCC structure, visible in Fig. 5.10 (c). Furthermore, both Ih and FCC clusters exhibited lattice spacings $d = 2.0 \pm 0.1$ Å, which closely match the distance between {1,1,1} planes in Ni or Cu. Note that this spacing is also similar to the distance between {2,0,0} planes in FCC NiO ($a_{NiO} = 4.18$ Å); however, based on the reported Ni nanocluster oxidation rate[249], it is not likely that complete oxidation of fresh $Ni_{0.85}Cu_{0.15}$ took place during the transfer from the IGA system to the TEM.

5.2.2 Aged $Ni_{0.85}Cu_{0.15}$ Nanoclusters

Fig. 5.12 shows TEM images of a $Ni_{0.85}Cu_{0.15}$ sample that had been left exposed to atmosphere for 24 hours before it was imaged. From this figure it is evident that $Ni_{0.85}Cu_{0.15}$ nanoclusters deposited onto a-C do not coalesce easily, unlike the case of $Ag_{0.85}Au_{0.15}$ nanoclusters presented in § 4.4.2; instead, they tend to form patches of a nanocluster-based film where the original nanoclusters are still visible as the main building blocks. In addition, Fig. 5.12 (b) shows that some $Ni_{0.85}Cu_{0.15}$ nanoclusters

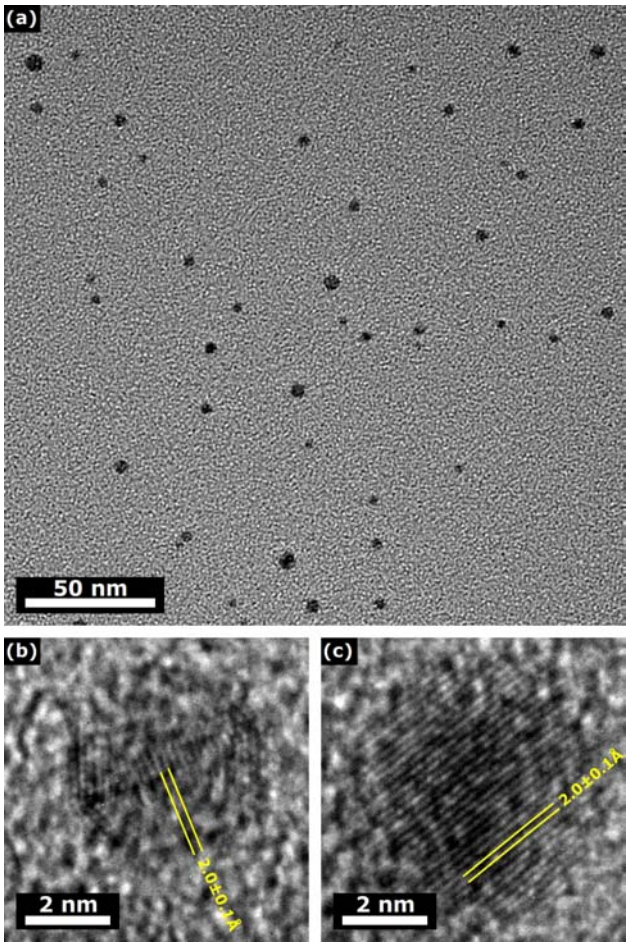

Figure 5.10: (a) TEM image of fresh $Ni_{0.85}Cu_{0.15}$ clusters deposited onto a-C at low surface coverage ($\theta \leq 3\%$). (b) HRTEM image of an icosahedral Ni-Cu cluster, showing the interplanar distance of 2.0±0.1 Å that corresponds to {1,1,1} planes in FCC Ni (or Cu). (c) HRTEM image of a FCC Ni-Cu cluster, exhibiting the same interplanar distance as in (b).

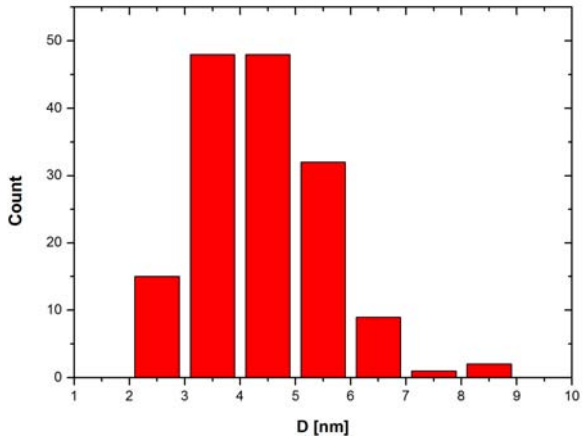

Figure 5.11: Size distribution of $Ni_{0.85}Cu_{0.15}$ clusters from the low surface coverage sample presented in Fig. 5.10. Total number of counted clusters was $N = 155$.

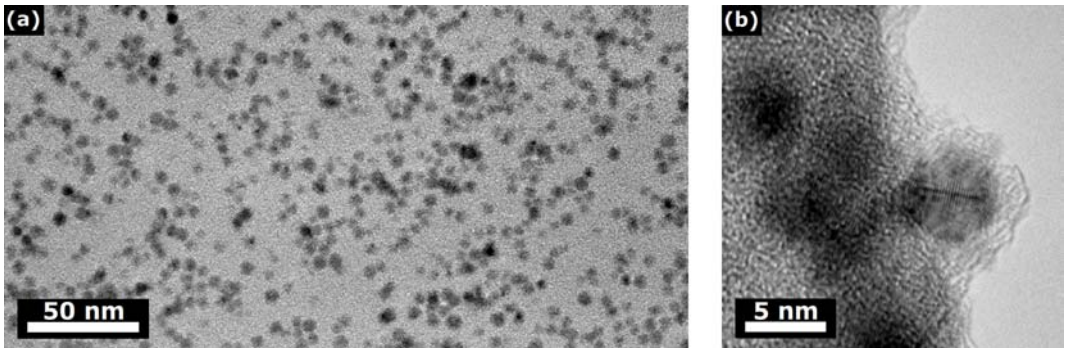

Figure 5.12: TEM (a) and HRTEM (b) images of an aged $Ni_{0.85}Cu_{0.15}$ sample with clusters of diameter $D = 5\pm1$ nm, deposited onto holey a-C. Surface coverage was $\theta \sim 30\%$.

retained their initial Ih structure even after such prolonged exposure to air, with the lattice spacings corresponding to Ni and Cu, but not NiO nor Cu_2O. Note also that these clusters have an amorphous shell with thickness of $\lesssim 2$ nm. The shell is most likely made of a-C that diffused over the clusters' surface from the support film, since it does not seem very plausible that such a thick amorphous shell could be formed by oxidation of Ni or Cu from the clusters while the Ni-Cu core preserved its Ih structure with no visible distortions.

When the surface coverage was further increased up to 2 monolayers ($\theta \sim$2 ML or 200%) we obtained continuous nanocluster-based thin films. Fig. 5.13 presents one such high surface coverage film which was had been exposed to air for a week before being taken to the TEM. Again, this figure shows the original nanoclusters as the building blocks of the film, suggesting that the coalescence of (oxidized) Ni-Cu

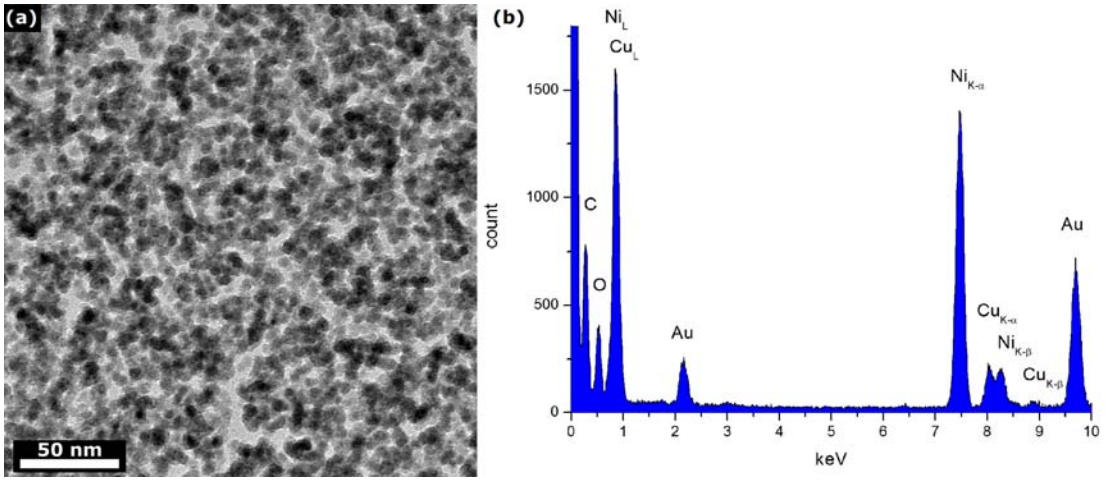

Figure 5.13: (a) TEM image of a thin $Ni_{0.85}Cu_{0.15}$ nanocluster film deposited onto a-C on Au mesh. Cluster size in the beam was $D = 6\pm1$ nm; surface coverage was 200% (∼12 nm). (b) EDX spectrum taken from the same sample, showing the average Cu content of 12.1±0.4 at.%.

nanoclusters is fairly slow. The energy dispersive X-ray spectroscopy (EDX) profiles (see Fig. 5.13 (b)) showed that the average Cu content in the nanocluster-based film was 12.1±0.4 at.%, which is quite close to the starting composition of the sputter target ($Ni_{0.85}Cu_{0.15}$). For this reason we denote our nanoclusters' composition as $Ni_{0.85}Cu_{0.15}$ throughout this thesis. Note also that the EDX spectrum indicates the presence of O in the film, which is not surprising since, as mentioned earlier, this sample had been exposed to atmosphere for a week before the characterization.

5.2.3 $Ni_{0.85}Cu_{0.15}$ Nanoclusters on HOPG

The coalescence of $Ni_{0.85}Cu_{0.15}$ nanoclusters deposited onto substrates is interesting from many standpoints. For example, when used in catalysis, in order to maximize the efficiency of the catalytic reactor, it would be beneficial to achieve a high surface density of Ni-Cu clusters. However, with the possibility of surface diffusion and coalescence of the clusters, one has to be very careful when increasing the surface coverage: the Ni-Cu catalytic activity is likely to be size-dependent and therefore any agglomeration of clusters may severely affect the performance of such a catalytic reactor. A similar thing has to be considered when Ni-Cu clusters are used as catalysts in thermal CVD growth of CNTs – the coalescence rate of clusters may be additionally enhanced since the growth usually occurs in the temperature range of 500-1000 °C. Therefore, an investigation of coalescence of $Ni_{0.85}Cu_{0.15}$ nanoclusters deposited onto various substrates seems worthwhile.

As the first step, it is useful to study the coalescence of clusters during and immediately after the deposition (at room temperature). To further investigate the influence of substrate on the coalescence of $Ni_{0.85}Cu_{0.15}$ nanoclusters, we deposited samples onto home-made TEM grids containing HOPG as a support for the clusters. HOPG is known as a material that has relatively big ($\sim\mu m^2$) terraces of a very flat surface and is widely used in the field of surface science as a substrate[13,200,201,203,251–253]. Our HOPG support was made by peeling off flakes from a commercially available bulk pieces of HOPG. The peeled flakes were then suspended over oyster TEM grids (see Table 2.1) and firmly clamped to secure them from falling off.

A typical TEM image of a fresh $Ni_{0.85}Cu_{0.15}$ nanocluster sample deposited onto such a grid is presented in Fig. 5.14. In this case the surface coverage was increased to $\theta \sim 10$ % in order to get more clusters available for coalescence, but still kept relatively low to avoid formation of a thin nanocluster-based film. One can see that $Ni_{0.85}Cu_{0.15}$ nanoclusters diffused on the flat surfaces of the support and formed localized assemblies of clusters. These assembiles however did not merge forming

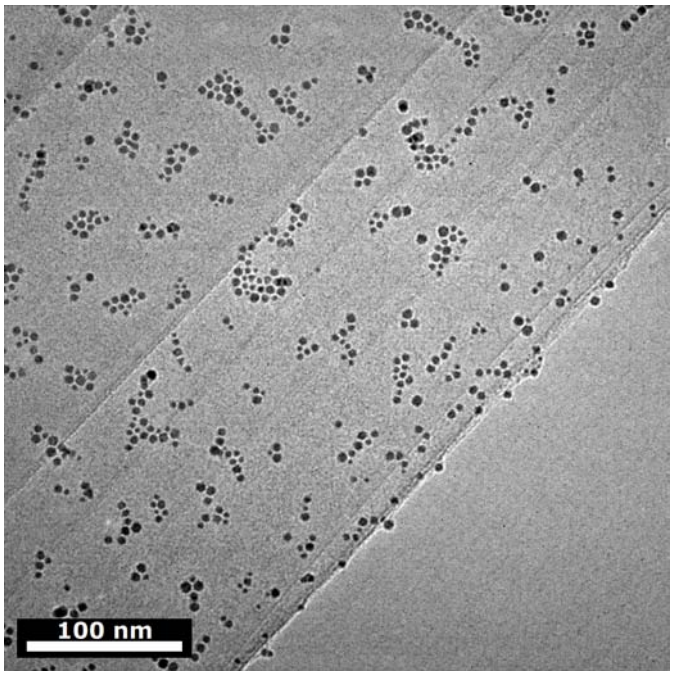

Figure 5.14: TEM image of fresh $Ni_{0.85}Cu_{0.15}$ nanoclusters deposited onto a home-made HOPG flake. Nanoclusters formed localized assemblies on the stepped terraces, but did not coalesce. Nanocluster size was $D = 6\pm1$ nm; surface coverage was $\sim$10%. Note the change of image contrast as the thickness of the substrate gradually decreases, starting from the upper left corner.

larger islands, as was for example seen in the case of Ag-Au nanoclusters. On the contrary, the appearance of these clusters is very similar to typical images of nanocluster TEM samples prepared by evaporating a drop of chemically-synthesized cluster-containing solution on the TEM grid[254–258]. However, our nanoclusters do not contain any surfactants, unlike the clusters in the samples prepared by wet synthesis. Based on this observation we can conclude that our surfacant-free $Ni_{0.85}Cu_{0.15}$ nanoclusters do not readily coalesce into larger islands, even when they are deposited onto a substrate with a very smooth surface, such as HOPG, where the diffusion of clusters is pronounced.

One possible explanation of this behaviour may lay in the fact that Ni and Cu posses higher cohesive energies than Ag and Au, meaning that it is more difficult to move over Ni and Cu atoms on the surface of nanoclusters so that necks between the clusters can be formed. In another words, it might be energetically more expensive to form bigger islands in the case of Ni-Cu nanoclusters than in the case of Ag-Au nanoclusters. It is also possible that the surface layer of deposited Ni-Cu nanoclusters got (partially) oxidized during the course of deposition and transfer to the TEM laboratory ($\sim$15 min), so that some sort of oxidized "buffer" surface layers were created that additionally hampered the coalescence of clusters into larger clumps or islands. Since the oxidation rate of Ag is much slower than the oxidation

rate of either Ni or Cu, there were no such obstacles present for Ag-Au nanoclusters and hence they coalesced fairly easy, compared to Ni-Cu nanoclusters.

These results seem very promising for possible realizations of Ni-Cu nanocluster catalytic reactors of high efficiency, where a high surface-to-volume ratio is desired.

As can be seen in Fig. 5.14, some of the clusters were residing on the terraces near the edge which are in general significantly thinner than those further from it. These thin regions, some of which contained <10 layers of graphite/graphene, allowed better imaging of our clusters, since the substrate contribution to the image is relatively weak there. Fig. 5.15 shows one such HRTEM image of a $Ni_{0.85}Cu_{0.15}$ nanocluster: one can resolve the cluster's Ih structure, as well as a somewhat ordered pattern of the supporting HOPG layers (e.g. in the bottom right corner in (a)). The latter approach could be utilized in the image analysis in order to subtract the substrate contribution to the micrograph by filtering the FFT pattern, making the cluster's structure somewhat clearer in the inverse FFT image (Fig. 5.15 (c)).

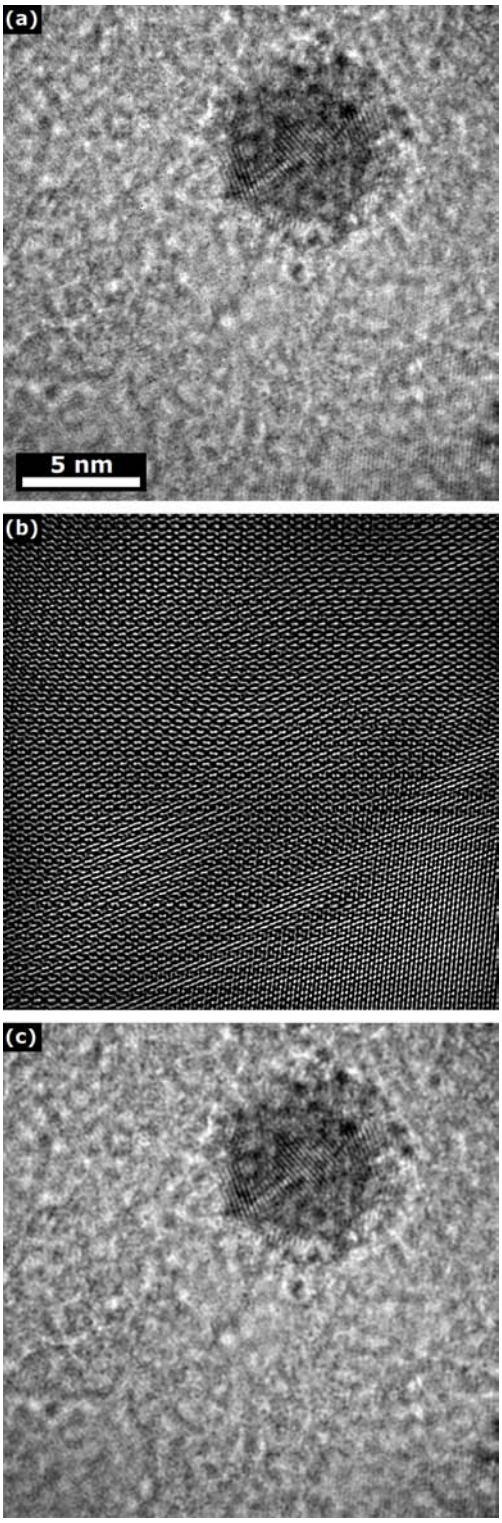

Figure 5.15: (a) HRTEM image of an Ih $Ni_{0.85}Cu_{0.15}$ nanocluster deposited onto a HOPG flake. Note the hexagonal lattice of the HOPG substrate in the bottom right corner. (b) Substrate contribution to the micrograph showing some regularity – a feature that is not visible in a-C substrates. The contrast was additionally increased, for the sake of clarity. (c) HRTEM image from (a) after subtraction of the substrate contribution.

5.2.4 Behaviour of $Ni_{0.85}Cu_{0.15}$ Nanoclusters Under Electron Beam Irradiation

As can be seen in Fig. 5.14, some of the deposited $Ni_{0.85}Cu_{0.15}$ nanoclusters slid to the outer edge of the HOPG support and were left hanging practically in vacuum, making them even more suitable for HRTEM imaging. However, when the TEM magnification was increased to $M > 500\ 000\ \times$, a time-dependent change of the nanocluster shape and structure was observed: one or more artifacts started to grow on the cluster's surface, usually perpendicular to the electron beam direction. These artifacts were crystalline with the FCC lattice, no matter whether the nanocluster that they grew on was Ih or FCC. We took many TEM images of this process for various $Ni_{0.85}Cu_{0.15}$ nanoclusters – one such sequence is presented in Fig. 5.16.

It was found experimentally that the growth rate of these objects depended on the intensity of the electron beam; under standard imaging conditions the growth

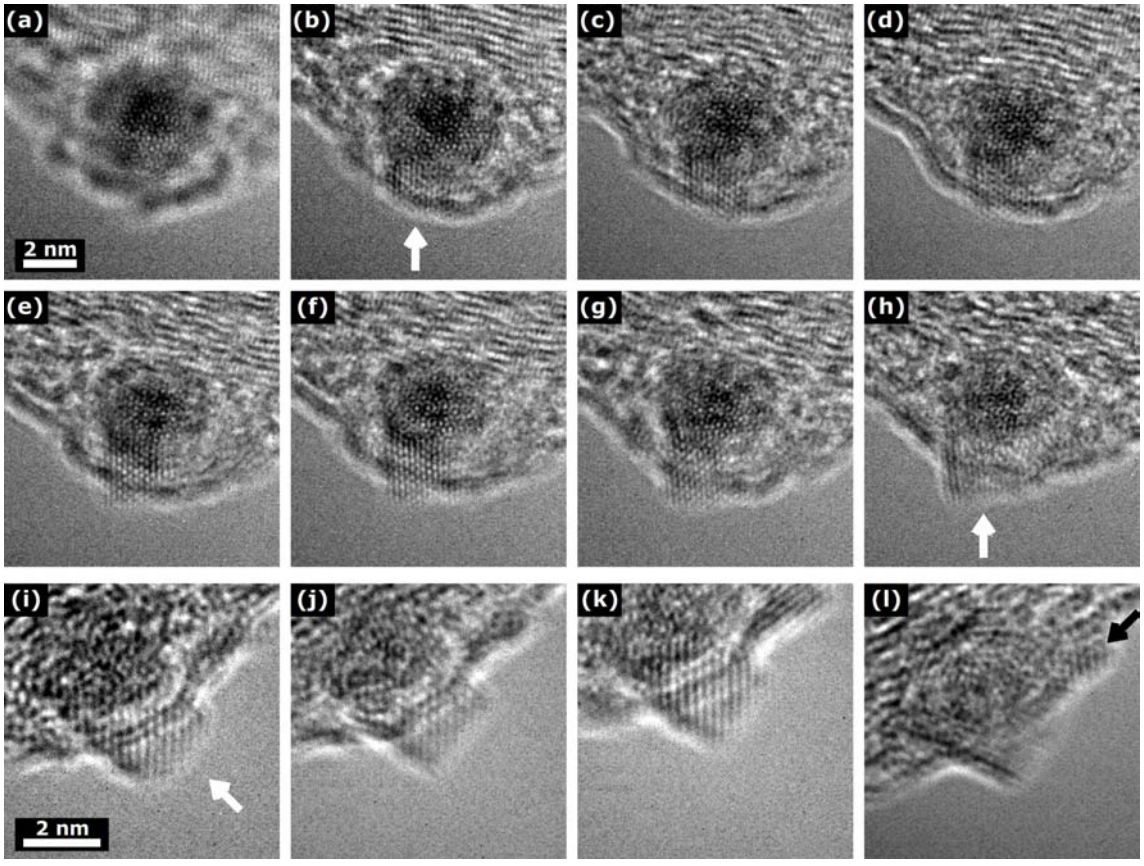

Figure 5.16: Series of HRTEM images of an Ih $Ni_{0.85}Cu_{0.15}$ nanocluster showing the growth of a "nanochimney" (indicated by the white arrow) under the influence of electron beam. Note the increase in TEM magnification for images (i)–(l), accompanied by a counter-clockwise rotation of the image by ∼45°. After the principal nanochimney reached its maximum length (k), a smaller nanochimney (indicated by the black arrow) started to grow along the edge of the HOPG substrate (l).

occurred over the period of 10–15 minutes. The process was advancing in 3 stages:

1. Dormancy stage – no visible growth of any artifacts occurs, although some changes in the cluster outer region may be visible. This stage usually lasts for < 3 minutes.

2. Growth of the artifact (we call it "nanochimney" due to its growth on top of the cluster) that usually extends 2-3 nm from the cluster's surface, although extensions up to 5 nm in length were observed in some cases. This stage lasts 3-15 minutes, depending on the electron beam intensity and size of the starting $Ni_{0.85}Cu_{0.15}$ nanocluster (the bigger the cluster, the longer the growth).

3. End stage – by this time the starting cluster has lost most of its initial structural characteristics, usually turning into a polycrystalline FCC object (see Fig. 5.16 (l)). The principal "nanochimney" starts to expand in width at the expense of its length, followed by a side growth of other, smaller "nanochimneys" at the base of the principal one. Interestingly, these side "nanochimneys" exhibit a tendency to grow along the edge of the HOPG substrate (but the same thing was seen in the case of holey a-C supports), in a fashion that may be described as a "creeping mode".

A detailed examination of these HRTEM images (see Fig. 5.17) revealed that the nanochimney's lattice spacings and directions corresponded to the NiO structure, although the starting nanocluster's structure was a fivefold Ih with spacings corresponding to non-oxidized Ni or Cu.

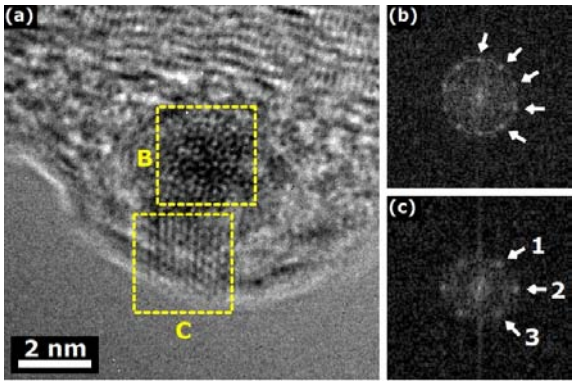

Figure 5.17: HRTEM image (same as Fig. 5.16 (e)) of a $Ni_{0.85}Cu_{0.15}$ cluster with a "nanochimney" growing sideways. (b) FFT of the $Ni_{0.85}Cu_{0.15}$ cluster, exhibiting a fivefold symmetry with all spots corresponding to interplanar distances of 2.0±0.1Å. (c) FFT of the "nanochimney", exhibiting the FCC structure with spots denoted 1,2, and 3 revealing interplanar distances of 2.5±0.1 Å, 2.0±0.1 Å, and 2.5±0.1 Å, respectively, that correspond to those between the {1,1,1}, {2,0,0}, and {1,-1,-1} planes in NiO.

This effect may be explained in the following way: the surface of $Ni_{0.85}Cu_{0.15}$ nanocluster was (partially) oxidized during the transfer to the TEM, but most of the cluster retained its original structure. However, when irradiated by the electron beam, the surface oxide layer starts to absorb energy that is sufficient for a significant diffusion of O and Ni (Cu) atoms over the surface so that they form energetically more stable structures – FCC NiO nanochimneys. The growth continues as long as there is a supply of Ni and O atoms from the cluster. It is possible that some Cu atoms also incorporated into the nanochimneys, but the fraction of Cu atoms in the clusters is relatively small so it is reasonable to assume that nanochimneys mostly consist of Ni and O. Further investigation may be required to elucidate the role of Cu in this process.

5.3 $Ni_{0.85}Cu_{0.15}$ Study - Conclusions

We have presented results of an experimental study of Ni-Cu nanoclusters, with emphasis on their structural properties. The clusters ranging from 3–10 nm in diameter were successfully produced in the IGA magnetron sputtering system from an alloy ($Ni_{0.85}Cu_{0.15}$) target and deposited onto various substrates, suitable for TEM and synchrotron XRD characterization.

TEM EDX measurements showed that the average Cu content in the clusters was 12.1±0.1 at.%, which agrees well with the alloy target's composition. HRTEM imaging of low surface coverage samples revealed that the majority of fresh nanoclusters possesed the Ih structure, although single-crystal FCC clusters were also observed. No visible phase segregation in these fresh clusters was detected in the bright field HRTEM – even if there was some segregation, a similar lattice parameter and atomic number of Ni and Cu (28 and 29, respectively), as well as a relatively low Cu content, prevented us from observing it. However, during the aging of samples, amorphous shells developed around the Ih cores, indicating a formation of surface NiO or Cu_2O.

It was observed that $Ni_{0.85}Cu_{0.15}$ nanoclusters do not coalesce easily at room temperature, even in the case of a very smooth substrate, such as HOPG. Moreover, in the high surface coverage samples thin nanocluster-based films were created, retaining their granular structure without coalescing significantly. This behaviour was attributed to higher cohesive energies of Ni and Cu than in the case of Ag and Au, where coalescence is pronounced. Also, the oxidation of Ni and Cu, which is faster than in the case of Ag, may additionally hamper the coalescence. These results seem encouraging from the point of view of a possible usage of $Ni_{0.85}Cu_{0.15}$ nanoclusters in high-efficient catalytic reactors where a large surface area is desired.

Under the influence of the electron beam during HRTEM imaging of samples, crystalline artifacts ("nanochimneys") started to grow on the nanoclusters' surfaces, usually perpendicular to the beam, with a structure consistent with NiO. It was hypothesized that the energy input from the electron beam causes the redistribution of surface Ni and O atoms so that they form single crystal FCC NiO nanostructures.

The results of $Ni_{0.85}Cu_{0.15}$ nanocluster study and experience obtained from it proved to be very helpful in the next step – investigation of their usage as catalysts in CVD syntheses of CNTs, presented in the following sections of this chapter.

5.4 Carbon Nanotubes

Here we outline the basic facts about carbon nanotubes (CNTs) and recent advances in this booming field of physical sciences. The latest experimental and modeling results are presented, including a brief overview of the usage of Ni and Cu as catalysts in CNT growth.

5.4.1 Overview of Carbon Nanotubes

First reported in the early 1950s in the Soviet Union[259], the discovery of CNTs went unnoticed for years. Occasionally a CNT-related work would be published, such as the one from Abrahamson[260], until a great interest in the subject of CNTs was sparked in 1991. when the seminal paper from Iijima[261] was published. Since then there have hundreds of books[8–10] and thousands of papers[262] covering many aspects of this subject, ranging from the preparation of catalysts[38,39,67,263–266] and substrates[72,264,267], to CNT growth[268–270], to characterization[271–275] and applications[262,276–285] in various fields.

From our point of view, the most interesting issue is the usage of alloy Ni-Cu nanoclusters as catalysts in the CNT growth by CVD and thermal decomposition of PMMA. The ultimate goal is to try to correlate some of the catalysts' properties, such as shape, size, and composition, to some of the CNTs' properties, such as inner diameter and possibly chirality. This will ideally lead to fabrication of CNTs with predefined electrical characteristics, which is highly advantageous for possible applications of CNTs in electronic devices. In order to better understand the influence of nanocatalysts' properties on CNT growth, we need to revisit some of the basic information about CNTs and recent advances in this subject.

Types of CNTs

Carbon is known to exist in a form of 1D sheets of covalently bonded atoms ordered in a hexagonal lattice – graphene. The distance between neighboring C atoms in a sheet is $a = 1.42$ Å and, if layered together to form multi-layer graphene/graphite, the distance between successive sheets is $d = 3.35$ Å. Due to its extraordinary properties[286–290], graphene has drawn much attention over the last decade[291,292], establishing a large subject for itself. If however, these graphene sheets are rolled, one gets CNTs – either as single-wall (SWCNT) or multi-wall (MWCNT) nanoscale objects (see Fig. 5.18). Each type of CNTs has its own properties which are suitable for possible usage in different applications. For instance, semiconducting SWCNTs utilized in SWCNT-based transistors exhibit favorable I–V characteristics making

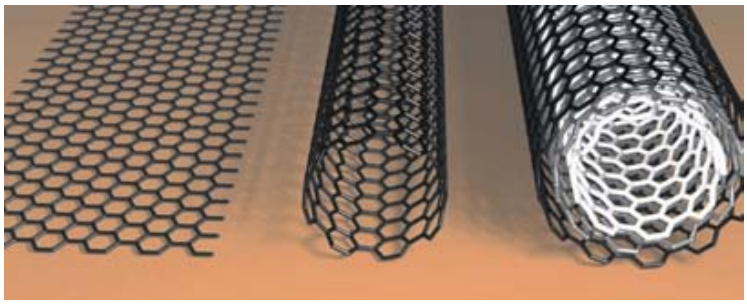

Figure 5.18: Illustration of a graphene sheet (left) which, when rolled, can give a SWCNT (center) or, if more than one graphene sheet is rolled, a concentric MWCNT (right).[285]

them useful in electronics[293]; metallic SWCNTs may be used as flexible electrodes[284], whereas MWCNT with their high surface-area-to-mass ratio may find applications in the field of photovoltaics[282] or energy storage[281].

SWCNT Chirality – Semiconducting vs. Metallic Tubes

What determines whether a SWCNT is metallic or semiconducting is the way the graphene sheet is rolled. To explain this, one has to look at a SWCNT as a molecule whose structure is defined by a chiral vector $\vec{C}_{n,m} = n\vec{a_1} + m\vec{a_2}$, where $\vec{a_1}$ and $\vec{a_2}$ are unit vectors of the graphene lattice, with magnitude $a = 2.46$ Å (see Fig. 5.19). In this notation, every SWCNT can be described by a set of (n, m) indices – the SWCNT is formed by rolling of the graphene sheet from (0, 0) to (n, m) in the

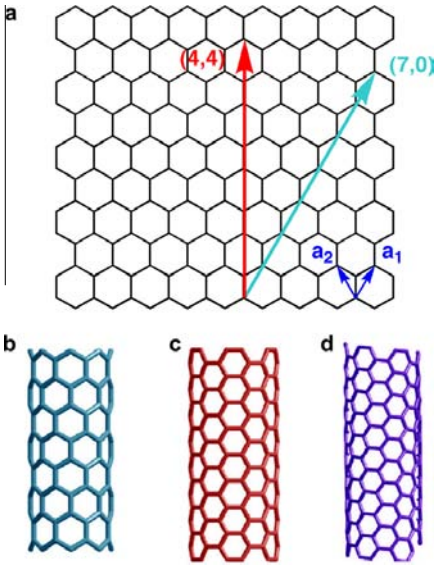

Figure 5.19: SWCNT chirality is defined by the way the 2D graphene sheet (a) is rolled: rolling along (n, 0) direction produces *zigzag* tubes (b); rolling along (n, n) direction creates *armchair* tubes (c); any other direction gives *chiral* tubes (d).[269]

direction of the chiral vector $\vec{C}_{n,m}$. SWCNTs of a general type (n, 0) are called *zigzag*; SWCNTs designated by (n, n) are referred to as *armchair* and all other (n, m) SWCNTs are called *chiral*. The set of indices (n, m) also describes whether a particular SWCNT is semiconducting or metallic, according to the following rules:

$$(n-m) = 3z \quad \Rightarrow \quad \text{metallic tube}$$
$$(n-m) = 3z \pm 1 \quad \Rightarrow \quad \text{semiconducting tube}$$

where z is an integer. A comprehensive set of (n, m) indices is presented in Fig. 5.20 indicating whether a particular (n, m) SWCNT is metallic or semiconducting. The angle δ between a chiral vector $\vec{C}_{n,m}$ and zigzag axis (n, 0) is referred to as *chiral angle* and can be calculated from the following relation:

$$\tan\delta = \frac{\sqrt{3}m}{2n+m}$$

In addition, if the (n, m) of the SWCNT is known, its diameter will then be:

$$d = \frac{a}{\pi}\sqrt{n^2+nm+m^2}$$

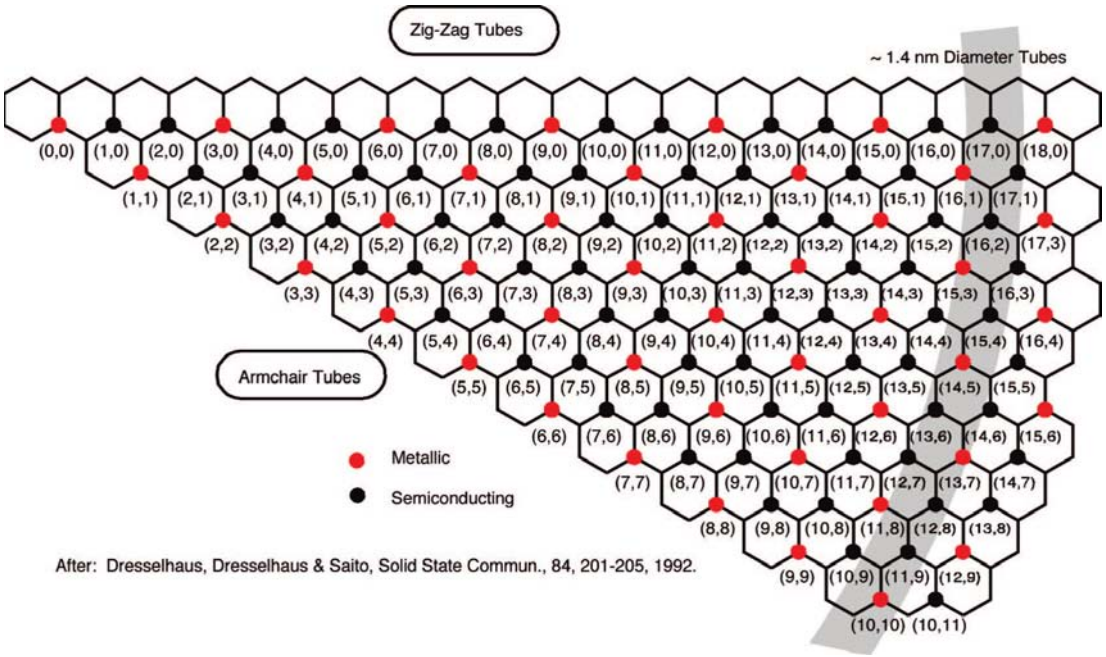

Figure 5.20: Set of (n, m) indeces indicating whether a particular SWCNT is metallic or semiconducting. Note that all armchair SWCNTs are metallic, whereas most (but not all!) zigzag SWCNTs are semiconducting. [11]

5.4.2 Growth of CNTs

CNTs can be produced in numerous ways which all have the same basic principle – C atoms are taken from a source and are rearranged in a tubular nanostructure (see Fig. 5.18) with an input of externally added energy. Some of popular and less popular methods are listed in Table 5.1.

In order to better understand CNT growth, including the influence of catalysts, substrates, carbon sources and growth conditions, numerous computational and experimental studies have been conducted over the couple of decades; here we give a brief overview of the most recent results and advances in this exciting subject, with focus on Ni- and Cu-catalyzed CVD synthesis.

Modeling Studies

Apart from Fe and Co, Ni is one of the most widely used elements in catalytic CVD synthesis of CNTs. Abdi et al.[294] modeled the annealing of Ni thin films and subsequent nucleation of Ni nanoclusters on a substrate, examining the influence of the annealing temperature on the size of nucleated clusters. A group of Amara et al. conducted an extensive investigation of CNT nucleation on Ni nanoclusters[295–298], with a focus on the Ni-C interaction. They found that the solubility and diffusion of C atoms in Ni nanoclusters governed the initial stages of CNT nucleation i.e. the formation of C caps on Ni surfaces. In addition, they observed that the self-organization of C atoms on the Ni surface depends on the temperature, with higher temperatures (>1500 K) propagating creation of NiC, which is detrimental for CNT growth. Similarly, Shin and Hong[299] studied the diffusion of C around the edges of Ni nanoclusters; it was found that C atoms diffuse more on the (1,1,0) surface, compared to the (1,1,1) and (1,0,0) surfaces. Note the importance of this result if faceted Ih nanoclusters, similar to the one seen in Fig. 5.10 (b), are used as catalysts in the CNT growth. Furthermore, Lyalin et al.[300] took another approach to the Ni-C nanosystem: instead of looking at the influence of Ni clusters on C atoms and

Method	C Source	Energy	Catalyst
arc discharge	solid (soot, graphite, ...)	electric	no
laser ablation	solid (graphite target)	laser radiation + thermal	optional
ball milling	solid	mechanical + thermal	yes
thermal CVD	gaseous (C_2H_2, CH_4, ...)	thermal	optional
PECVD	gaseous	thermal + electric	yes
polymer treatment	solid (PMMA)	thermal	yes
microwave growth	solid(polystyrene)	microwave radiation	yes

Table 5.1: Some popular and alternative methods for CNT production.

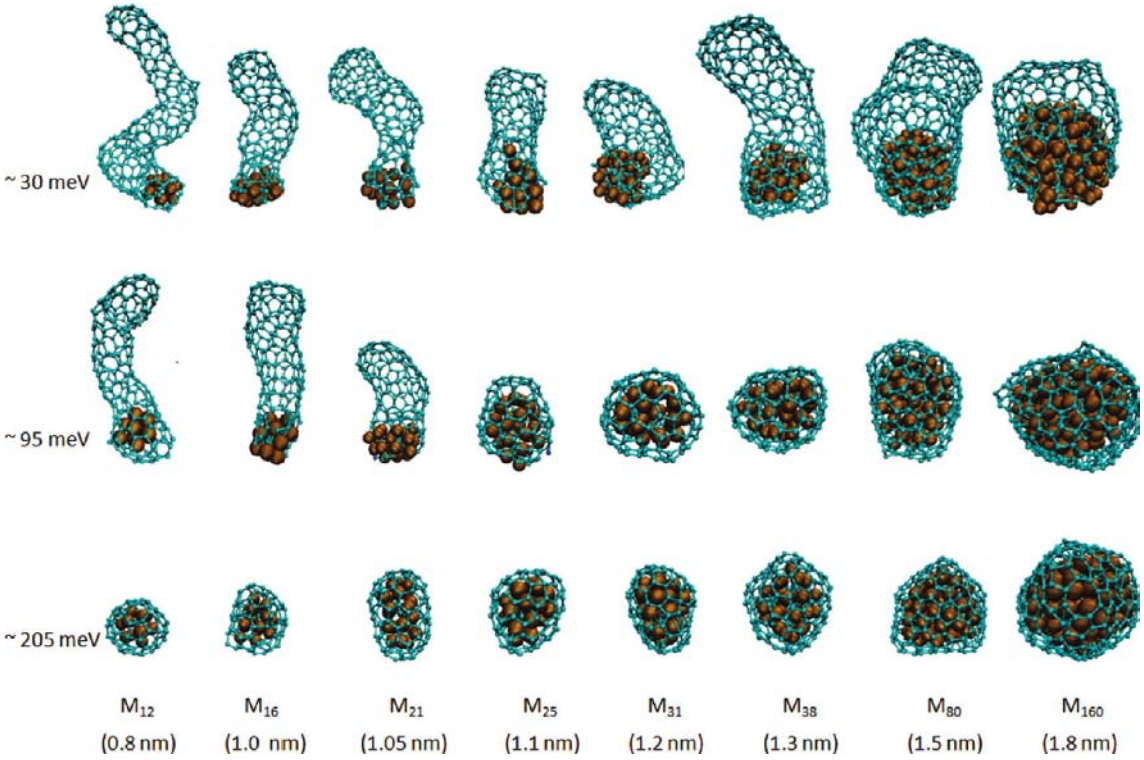

Figure 5.21: Influence of nanocluster size and adhesion between the nanocluster and C-cap on SWCNT growth.[302]

CNT growth, they examined the influence of C on the Ni clusters. They see that the addition of a single C atom to the 147-atom Ni cluster significantly influences its thermodynamic properties, such as the melting temperature. Banerjee et al.[301] studied the CNT growth modes (tip vs. base growth) and found that Ni nanoclusters preferentially yielded tip growth, whereas Fe nanocatalysts favored base growth.

However, the most important issue in catalytic CVD synthesis of CNTs seem to be the influence of nanocluster size and adhesion forces between a nanocluster and the adhered C atoms. Burgos et al.[302] found that these parameters determine the behaviour of the Ni-C system: weak adhesion and smaller nanoclusters lead to a C-cap lift-off and formation of SWCNT, while stronger adhesion and relatively big nanoclusters prefer encapsulation of the Ni catalyst (see Fig. 5.21). Similar studies were conducted by Larsson et al.[303] and Wang et al.[304]; the latter concludes that the strain relief between a nanocluster surrounded by a C-cap is responsible for the extrusion and growth of CNT. Furthermore, Yazyev and Pasquarello[12,305] theoretically investigated how the choice of metallic nanocatalysts influenced the CNT growth; it was found that coinage metals (Cu in particular) favored low temperature CVD growth forming CNTs with narrow chirality distributions.

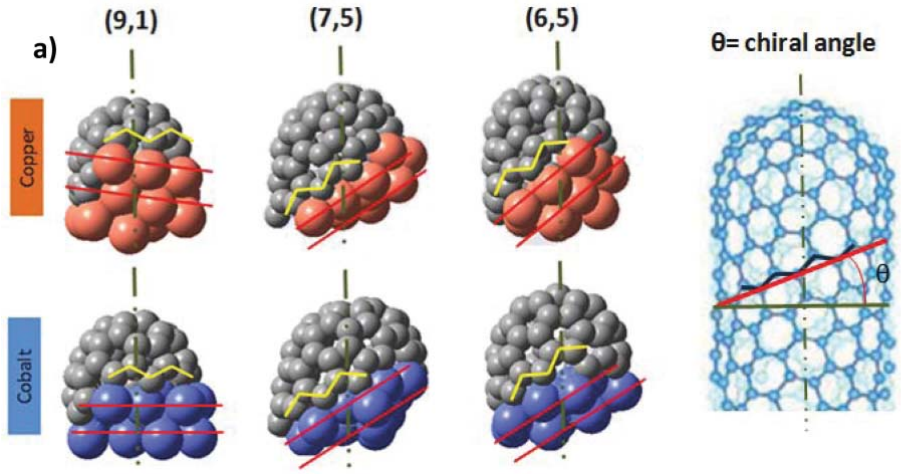

Figure 5.22: Schematic representation of the influence of nanocatalyst shape on the chirality of nascent SWCNT: the chiral angle of the tube is associated with the angle between the planes (red) and direction of the tube growth. These results suggest possibility of tailoring SWCNT chirality and consequently some of its physical properties, by using the appropriately shaped nanocatalysts. [309]

The issue of CNT chirality was also studied by Ding et al. [79] and Dumlich and Reich [306–308], but the most comprehensive report from Gomez-Gualdron [309] investigated the influence of the Co nanocatalysts' shape and the type of carbonaceous gas on the chirality of grown CNTs. Their DFT and MD calculations show (see Fig. 5.22) that zigzag chains of C atoms are preferentially formed on (2,1,1) surfaces, while armchair chains favor (3,2,1) stepped surfaces, thus suggesting that the nanocluster shape can affect the chirality of the SWCNT grown on it.

Experimental Studies

Out of many experimental studies of CNTs, we will here focus on recent advances in Ni or Cu catalyzed CVD growth, with a brief overview on the possibility of modifying CNT chirality by using alloy catalysts of various compositions.

Siegal et al. [47,56,58,61,66] extensively studied the influence of experimental conditions, such as temperature and growth time, on Ni-catalyzed CVD synthesis of CNTs. In their most recent paper [47] they report on the linear correlation between the number of walls and growth temperature (see Fig. 5.23).

Hofmann's group at Cambridge, UK has conducted comprehensive research on this topic over the last decade, by using both plasma-enhanced (PE) CVD [43,44,59] and thermal CVD [59,67,266]. Utilizing an environmental transmission electron microscope (ETEM) they managed to capture images of the initial stages of CNT growth (see Fig. 5.24), as well as to observe the state of nanocatalysts during the growth. Recently, Terrrado and al. [310] investigated the influence of temperature and time

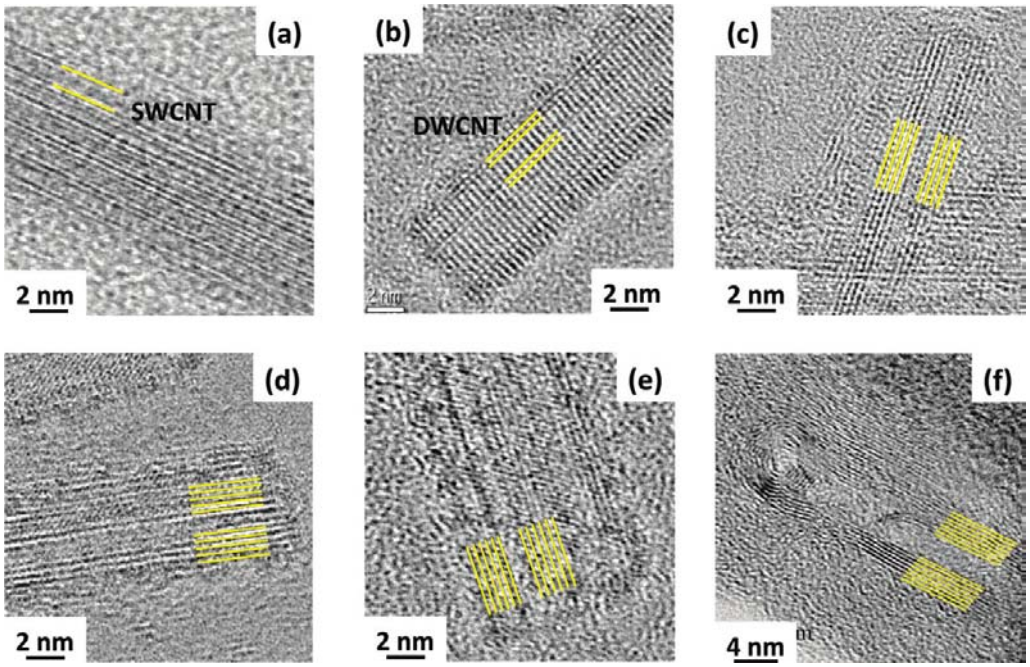

Figure 5.23: HRTEM images of CNTs produced by thermal CVD. The number of CNT walls grows linearly with increasing temperature: (a) 530 °C; (b) 550 °C; (c) 570 °C; (d) 590 °C; (e) 610 °C; (f) 630 °C.[47]

of catalyst reduction and pretreatment on the CNT growth, while Santiago et al. studied the effect of SiO_2/Si substrate on a nanocatalyst and consequently on CNT growth. The latter group found evidence of metal silicide formation, which surprisingly, showed the same catalytic activity as metal nanocatalysts, without inhibiting the CNT growth at all.

When it comes to usage of alloy nanocatalysts in CNT synthesis, investigation has been largery centered around Co-based systems, such as Co-Pd[40] or Co-Mo[71,267].

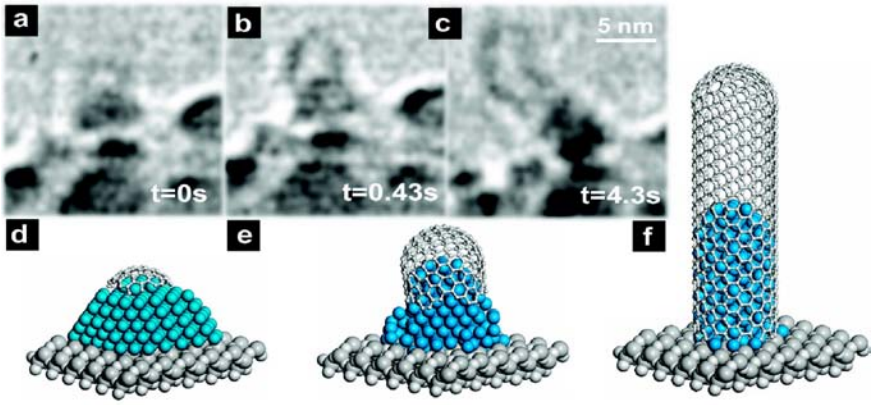

Figure 5.24: Real-time HRTEM observation of initial CNT growth stage (a-c) and illustration of it (d-f).[67]

However, some advances have recently come in the field of Ni-based alloys: Sharma et al.[263] experimented with the addition of Au, finding that a small amount of Au can increase the catalytic activity of Ni nanoclusters, despite the fact that Au tends to segregate on Ni. Gonzalez et al.[311] investigated the effect of Cu on the catalytic activity of Ni nanoclusters: although the rate of catalytic cracking of CH_4 on Ni-Cu nanocatalyst was somewhat increased compared to pure Ni, the growth of CNTs was not affected by the presence of Cu. A more detailed study of Ni-Cu nanocatalyzed MWCNT synthesis came from Thiruvengadachari and Ajmera[88] who investigated the influence of experimental conditions on the nanotube growth, finding a strong correlation between the nanocatalyst size and the average outer diameter of the grown MWCNTs.

It should be noted though that, in all of the experimental studies presented so far, both monometallic and alloy nanocatalysts were created in situ by annealing of thin metallic films that had previously been sputtered onto various substrates.

In contrast, Chiang and Sankaran[41,265,312] have pioneered the usage of pre-designed alloy nanoclusters in SWCNT growth: they showed that by varying the composition of Ni_xFe_{1-x} nanoclusters one can preferentially obtain SWCNT of a certain chirality (see Fig. 5.25). The chirality-selective behaviour of these alloy nanoclusters was explained by the observed increase in the {1,1,1} interplanar distance when Fe was added (a_{Ni} = 2.0 Å, $a_{Ni_xFe_{1-x}}$ = 2.1 Å), influencing the Ni-C interactions in a similar fashion as predicted by Reich[307].

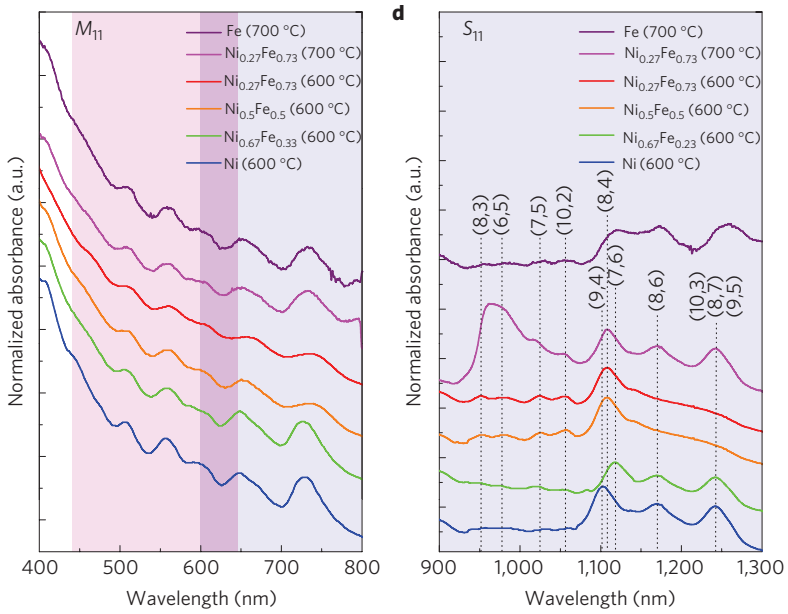

Figure 5.25: Absorbance spectra of SWCNTs synthesized on compositionally tailored 2 nm Ni_xFe_{1-x} nanoclusters showing correlation between SWCNT chirality (n, m) and the nanocatalyst composition.[265]

5.5 Results of CNT study

In this section we present the results of preliminary CVD syntheses that utilized $Ni_{0.85}Cu_{0.15}$ nanocluster samples prepared in the IGA magnetron sputtering system as catalysts for the CNT growth. SWCNT growth experiments (design, syntheses, characterization, and interpretation of Raman spectra) were carried out by Kirsten Edgar at the School of Chemical and Physical Sciences, VUW. MWCNT growth experiments (design and syntheses) were performed by Jin Ke and Vladimir Golovko at the Department of Chemistry, UC, while the author characterized the samples and interpreted the results.

5.5.1 SWCNT Growth and Characterization

A set of identical, low surface coverage $Ni_{0.85}Cu_{0.15}$ samples ($D = 6\pm1$ nm, $\theta = 0.1\%$) was deposited onto Si_3N_4/Si substrates; these clusters were then utilized as catalysts in thermal CVD growth (see Chapter 2 for details), with the aim of producing SWCNTs. Firstly, the influence of temperature on CVD growth was investigated in a temperature range 900–1050 °C. SEM images presented in Fig. 5.26 show that the samples grown at lower temperatures (T = 900 °C and 975 °C) feature only spherical objects that somewhat resemble C-nanocages. However, the sample that underwent the highest temperature CVD growth (T = 1050 °C) contain tubular-like nanoscale objects – presumably SWCNTs[313,314], in addition to the spherical objects that are also present in a relatively high number.

These results are quite similar to an experimental study that has been reported by Lin et al.[89] which showed that SWCNTs preferentially grew on Ni nanoclusters of $D \leq 6$ nm, whereas larger clusters tended to form C-nanocages – this behaviour has recently been backed up by the results of a modeling study of Burgos et al.[302] that showed encapsulation of larger clusters (see Fig. 5.21). In addition, one has to bear in mind that at such high temperatures a partial or complete melting of $Ni_{0.85}Cu_{0.15}$ nanoclusters is possible, as predicted by Huang and Balbuena[237] and Li et al.[238], which may significantly reduce the average size of clusters in the sample.

In the light of these findings, we propose an explanation for the observations: deposited at a low surface coverage, initially 6±1 nm $Ni_{0.85}Cu_{0.15}$ clusters likely started to diffuse considerably on the substrate at such high temperatures, partially melting at the same time; over time they formed larger aggregates ($D > 6$ nm), completely changing the initial size distribution; such big nanoclusters were then suitable for the growth of C-nanocages, but not SWCNTs. However, at the highest temperature used, the size distribution of these aggregates was shifted toward a smaller diameter, due to 2 reasons: initially 6±1 nm $Ni_{0.85}Cu_{0.15}$ clusters melted more at this tem-

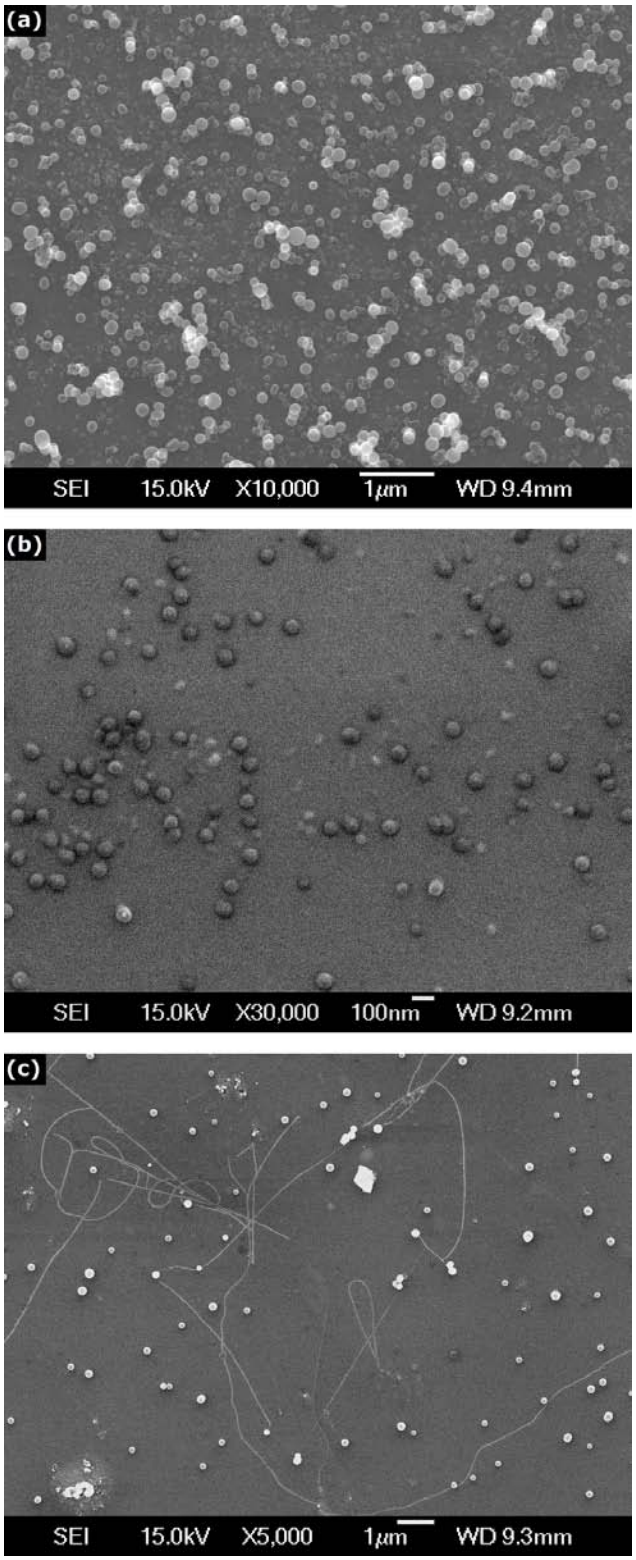

Figure 5.26: SEM images (credits: K. Edgar, VUW) of $Ni_{0.85}Cu_{0.15}$ samples after the CVD growth at various temperatures: (a) 900 °C; (b) 975 °C; (c) 1050 °C. Features similar to C-nanocages were formed at all temperatures, but only the highest temperature sample gave tubular-like nanoobjects. Note that the surface density of spherical objects drops with increasing temperature.

perature even before aggregating into clumps; additionally, these clumps may have partially melted and further decreased the size distribution. In the latter case some of the clumps were small enough to initiate the SWCNT growth, as indicated by Fig. 5.26 (c). Note from Fig. 5.26 that the surface density of C-nanocages gradually decreased as the temperature was increased, supporting the claim that partial melting of $Ni_{0.85}Cu_{0.15}$ nanoclusters had occurred prior to introducing the carbonaceous gas.

To overcome the problems stemming from the evidence of a significant surface diffusion, aggregation and possibly melting of $Ni_{0.85}Cu_{0.15}$ nanoclusters supported on Si_3N_4/Si, an alternative approach was taken. Samples were spincoated with a thin layer of Poly(methyl methacrylate) (PMMA) whose presence should ideally decrease the diffusion and aggregation of nanoclusters, keeping their size $D \leq 6$ nm, favorable for SWCNT growth. The sample preparation procedure was as follows: a drop of PMMA solution (996,000 MW, 4 wt.% in toluene), was cast onto the $Ni_{0.85}Cu_{0.15}$ samples; three spinning rates ν were used: 1000, 2000, and 3000 rotations/minute (rpm) in order to obtain PMMA films of different thicknesses, ready for CVD synthesis. Since it was seen that the highest temperature yielded the most promising results, the CVD growth conditions used in this set of experiments were the same as in that experimental run.

Results of CVD syntheses using the newly prepared PMMA-coated $Ni_{0.85}Cu_{0.15}$ samples are presented in Fig. 5.27. One can see that all samples contained tubular-like nanoobjects, while the occurrence and size of spherical features dropped considerably in comparison with the non-PMMA-coated samples. The sample that had the thickest PMMA film on (produced by the lowest spinning rate $\nu = 1000$ rpm) shows the highest density of CNTs – dense enough to form a network. Note that, unlike the other samples from this set, nanotubes here are covered with a relatively thick layer of material, possibly a-C that originated from the thick PMMA film which thermally decomposed during the experiment. The sample spincoated at $\nu =$ 2000 rpm also shows CNTs, although their density seems significantly less than in the first sample. The sample that contained the thinnest PMMA layer (spincoated at $\nu = 3000$ rpm) shows very few CNTs. However, unlike the other two samples, these CNTs appear much longer.

As was seen, by depositing a relatively thick PMMA layer ($\nu = 1000$ rpm) over the $Ni_{0.85}Cu_{0.15}$ nanoclusters one can increase the number of tubular-like objects that form during the CVD synthesis. It seems that thicker PMMA layers give better results in terms of quantity, but at the expense of quality since nanotubes are covered with a layer of a-C.

In order to confirm the formation of SWCNTs, the sample that showed the high-

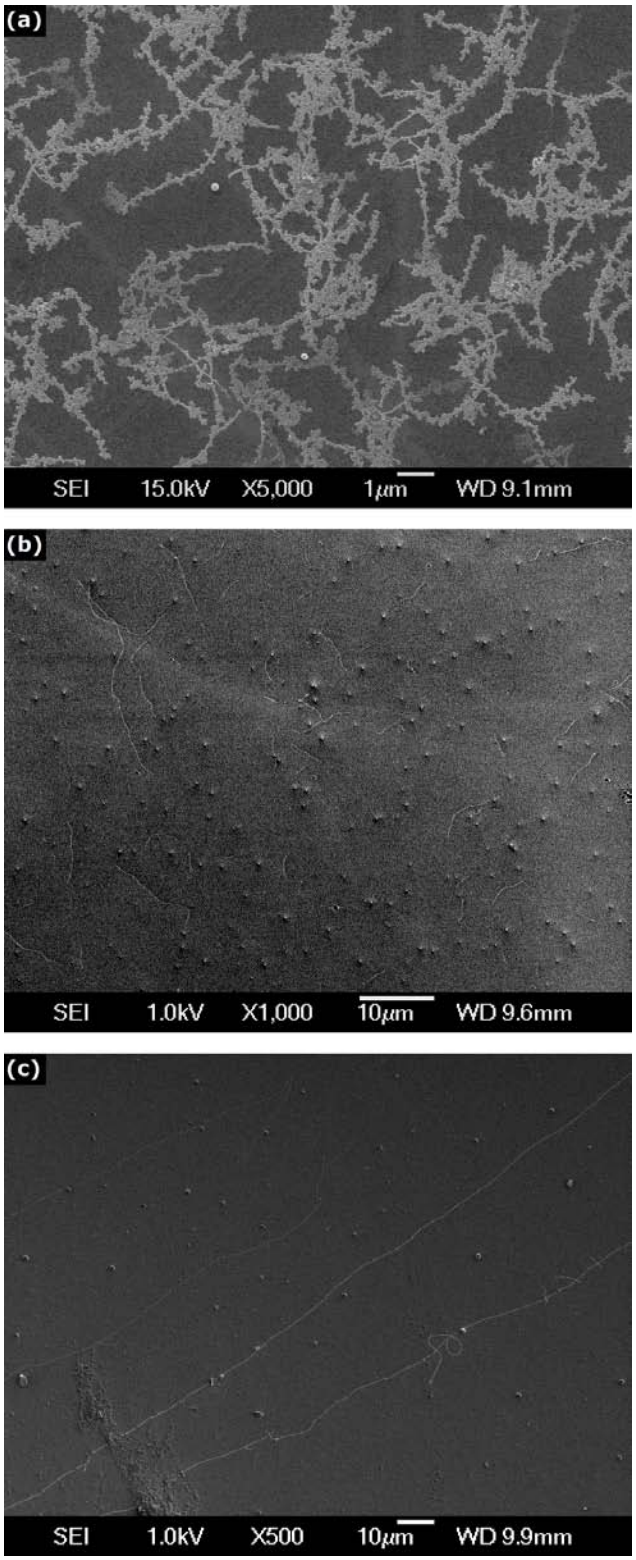

Figure 5.27: SEM images (credits: K. Edgar, VUW) of $Ni_{0.85}Cu_{0.15}$ samples after the CVD growth. Samples were spincoated with PMMA at various spinning rates: (a) $\nu = 1000$ rpm; (b) $\nu = 2000$ rpm; (c) $\nu = 3000$ rpm. The temperature in these experiments was $T = 1050$°C.

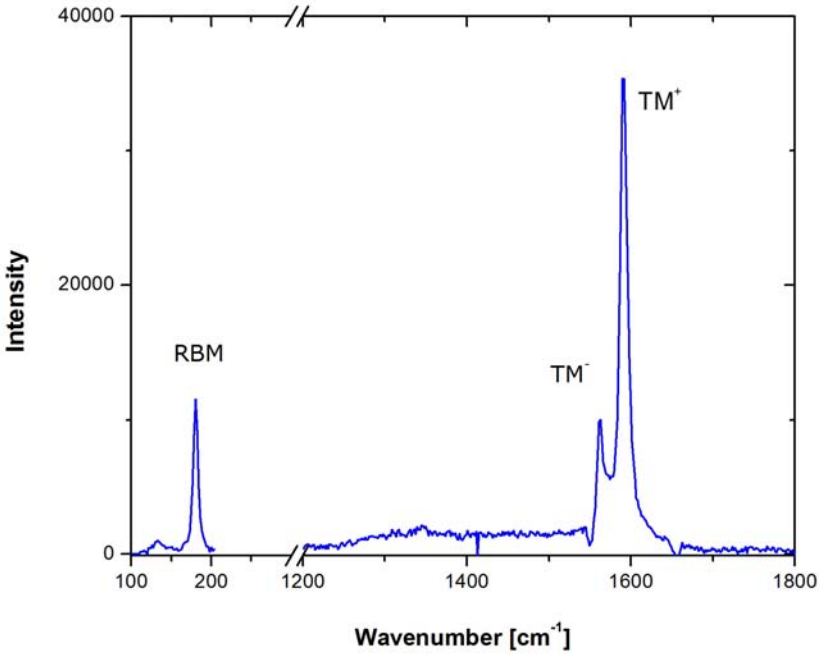

Figure 5.28: Raman spectrum (credits: K. Edgar, VUW) of the CNT sample shown in Fig. 5.27 (a) revealing the presence of non-bundled well-graphitized semiconducting SWCNTs in the sample.

est density of tubular-like nanobjects was subjected to characterization by Raman spectroscopy. The initial Raman spectra indicated a high amount of a-C, in line with the observation from Fig. 5.27 (a). To decrease the amount of a-C in the sample, a low temperature (400 °C) burn off in air was performed. This enabled the acquisition of Raman spectra originating from the tubular-like objects – a typical spectrum is presented in Fig. 5.28.

The Raman spectra show a strong peak at $\omega_{RBM} = 181$ cm^{-1} which corresponds to the excitation frequency of the radial breathing modes (RBM) of SWCNTs, confirming their presence in the sample. Furthermore, two strong Lorentzian-like peaks at $\omega_{RBM} \sim 1600$ cm^{-1} that correspond to the excitation frequencies of tangential modes (TM$^-$ and TM$^+$) indicate well-graphitized semiconducting non-bundled SWCNTs[315,316]. It is also possible to estimate the diameter of the SWCNTs from the positions of these peaks[317–319]:

$$\omega_{RBM} = \frac{248}{D(nm)}$$

$$\omega_{TM^-} = 1592 - \frac{41.4}{D(nm)}$$

For the spectrum presented in Fig. 5.28, one obtains quite consistent values of SWCNT diameter: $D_{RBM} = 1.37$ nm and $D_{TM^-} = 1.43$ nm.

SWCNT Growth – Conclusions

An preliminary experimental study of $Ni_{0.85}Cu_{0.15}$-catalyzed CVD syntheses of SWCNTs was conducted for temperatures ranging 900–1050 °C. It was found that tubular-like nanoobjects were produced only at the temperature of 1050 °C, whereas for temperatures below that one gets spherical features that resemble C-nanocages. These results suggested that clusters may have agglomerated into larger clumps during the growth as such high temperatures, which likely enhanced the production of nanocages, but was detrimental to SWCNT growth.

To overcome these issue, the samples were spincoated with a layer of PMMA. As a results, the catalytic activity of $Ni_{0.85}Cu_{0.15}$ nanoclusters seemingly increased – the number of tubular-like objects in these samples increased. The most likely reason was that more clusters had a size favorable for SWCNT growth[89] ($D \leq 6$ nm), possibly due to suppressed cluster surface diffusion and agglomeration because of the PMMA coating. After a low temperature burn off in air, the presence of low-defect SWCNTs of diameter $D \sim 1.4$ nm was confirmed by Raman spectroscopy.

This preliminary study showed that, under favoring experimental conditions, $Ni_{0.85}Cu_{0.15}$ nanoclusters can be used as catalysts in CVD growth of SWCNTs. Moreover, the fabricated SWCNTs are well-graphitized, non-bundled and predominantly semiconducting.

5.5.2 MWCNT Growth and Characterization

In this part of study, the main goal was to prove the concept that alloy $Ni_{0.85}Cu_{0.15}$ nanoclusters could be used as catalysts in low-temperature CVD growth of MWCNTs. Since these were very first CVD experiments undertaken at the Department of Chemistry[96], University of Canterbury, the goal was also to investigate a wider range of experimental conditions in order to optimize the CVD process for future usage. For that purpose, various samples of $Ni_{0.85}Cu_{0.15}$ nanoclusters were deposited onto Si_3N_4/Si substrates (see Table 5.2) and used for catalytic CVD growth of MWCNTs (see Chapter 2 for details on CVD growth).

Initial MWCNT Growth Experiments

Initially, samples of a relatively high surface coverage ($\theta \lesssim 3\%$) were used in the experiments: this coverage is low enough to suppress coalescence of nanoclusters during the deposition, yet high enough to provide a relatively high number of possible catalytic centers for CNT growth that would consequently increase the number of CNTs, which would be beneficial for initial SEM and TEM characterization.

Sample Set	Cluster Size [nm]	Surface Coverage [%]	Substrate Type
193	5.7 ± 0.8	$\lesssim$3	Si_3N_4/Si
195	5.7 ± 0.8	$\lesssim$3	Si_3N_4/Si
210	5.7 ± 0.8	∼0.1	Si_3N_4/Si
211	5.7 ± 0.8	∼0.1	Si_3N_4/Si
213	4.0 ± 0.2	∼0.1	Si_3N_4/Si
214	4.0 ± 0.2	∼0.1	Si_3N_4/Si
253	4.2 ± 0.4	∼0.1	Si_3N_4/Si
254	4.2 ± 0.4	∼0.1	Si_3N_4/Si

Table 5.2: Characteristics of $Ni_{0.85}Cu_{0.15}$ samples prepared for thermal CVD experiments. Each set contained 4 samples, denoted *a*-*d* throughout this chapter.

A diagram showing the experimental conditions used for this set of samples is given in Fig. 5.29. After a low temperature reduction of oxidized $Ni_{0.85}Cu_{0.15}$ samples, CNT growth was carried out at the temperature of 650 °C. Note that this temperature is significantly lower than the ones used in the SWCNT growth experiments, presented in the previous section. SEM images of a typical sample from this set is presented in Fig. 5.30 – before (a) and after (b) the CNT growth. One can see that a dense spaghetti-like network of tubular nanostructures had grown on top of the sample, with a relatively wide range of diameters (10 nm $\lesssim D_{CNT} \lesssim$ 50 nm) that were considerably larger than the initial cluster size (D = 5.8±0.8 nm) – this was the first indication of MWCNTs.

Interestingly, another sample containing identical $Ni_{0.85}Cu_{0.15}$ nanocluster that was subjected to the same CVD synthesis gave a very similar spaghetti-like network of tubular structures, but with a more uniform diameter (10 nm $\lesssim D_{CNT} \lesssim$ 20 nm) (see Fig. 5.30 (c)). The only difference between these two samples was in the way the

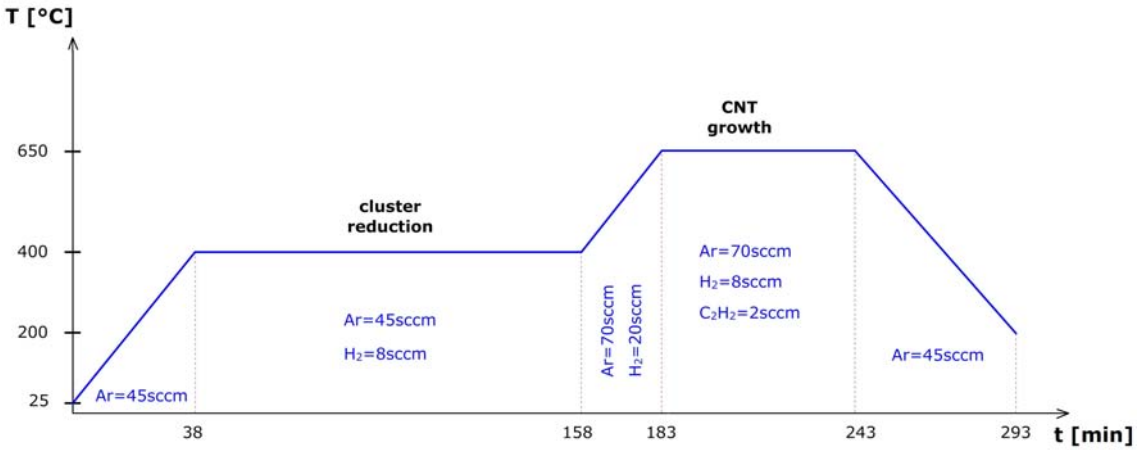

Figure 5.29: CNT growth conditions – *initial* $Ni_{0.85}Cu_{0.15}$ samples 193 and 195. Credits: J. Ke and V. Golovko, UC

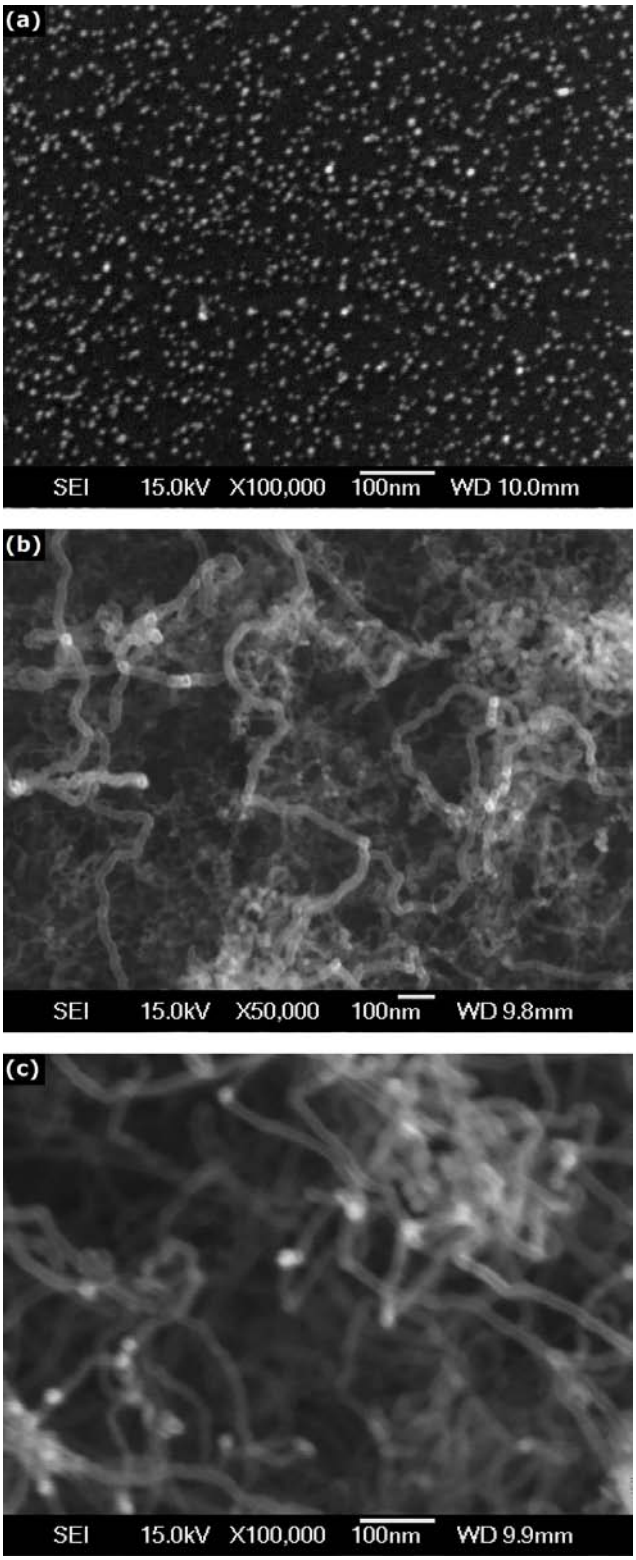

Figure 5.30: (a) SEM image of $Ni_{0.85}Cu_{0.15}$ sample 195 before the CNT growth; $D = 5.8 \pm 0.8$nm, $\theta \lesssim 3\%$. (b) SEM image of the sample from (a) after the CNT growth, showing CNTs with a wide range of diameter. (c) SEM image of CNTs grown on $Ni_{0.85}Cu_{0.15}$ sample 193 ($D = 5.8 \pm 0.8$ nm, $\theta \lesssim 3\%$).

Si_3N_4/Si substrates were cleaned prior to the deposition of $Ni_{0.85}Cu_{0.15}$ nanoclusters: in sample 193 the substrate was washed with isopropyl alcohol (IPA) in an ultrasonic bath, whereas sample 195 was washed with low grade acetone. In the latter case the presence of impurities on the substrate left after the cleaning procedure may have influenced the CNT growth, either by enhancing the surface diffusion and aggregation of $Ni_{0.85}Cu_{0.15}$ clusters resulting with a wider range of nanocatalyst size, or simply by affecting the nanocatalyst-substrate interaction, which is known to have a significant impact on the CNT growth[267].

In order to unambiguously show the existence of MWCNTs in these samples, several TEM specimens were prepared (see Chapter 2 for details on preparation methods) and imaged at UCEM (see Fig. 5.31). One can see that the samples

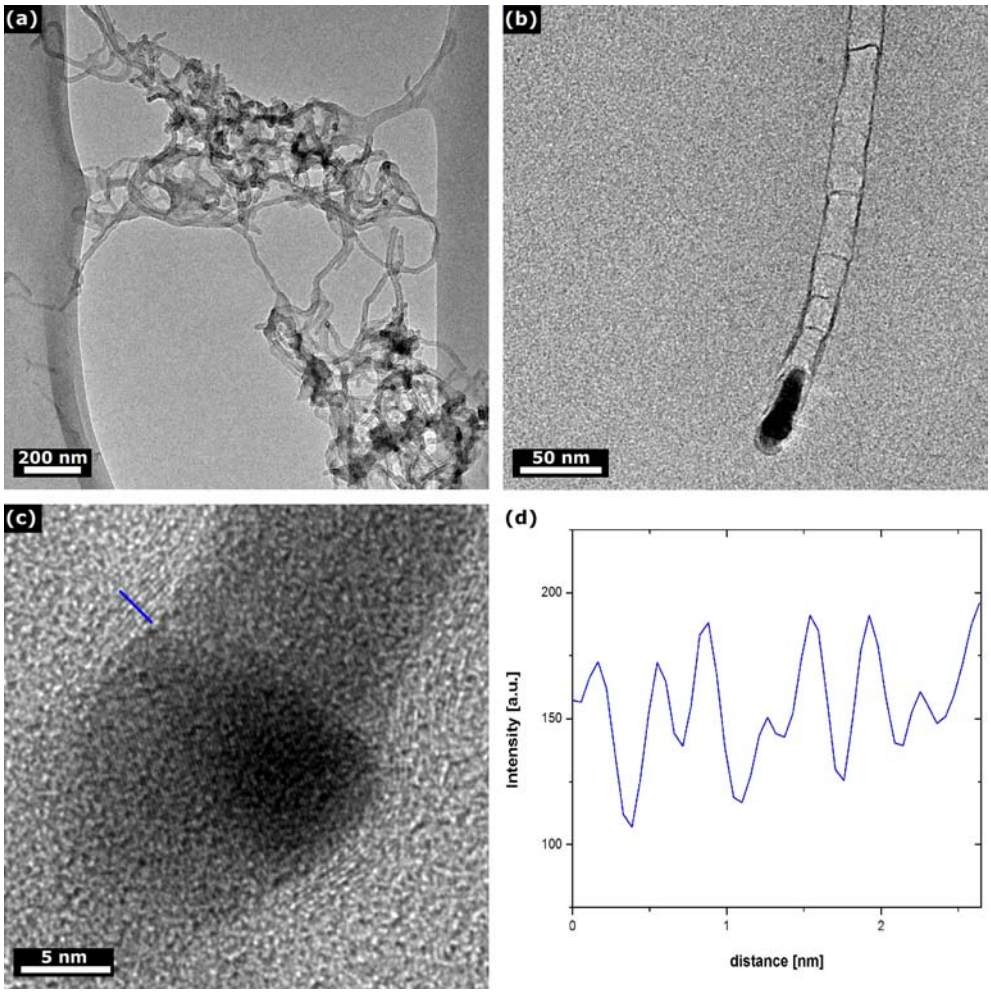

Figure 5.31: (a) TEM image of sample 193 showing entangled CNTs and CNFs. (b) TEM image of a bamboo-like MWCNT containing a nanocatalyst at its end. (c) HRTEM of the same MWCNT; individual walls can be seen clearly, as well as fringes of the nanocatalyst with a spacing of $d = 2.1 \pm 0.1$ Å that corresponds to the distance between {1,1,1} planes in FCC Ni or Cu. (d) Plot profile of CNT walls along the line in (c), giving the average spacing between the walls $d_{CNT} = 3.3 \pm 0.1$ Å.

contained MWCNTs as well as carbon nanofibres (CNFs) i.e. nanostructures made of graphene sheets in the form of stacked cones that, unlike CNTs, do not have cylindric symmetry. Based on the TEM observation, it appears that CNFs were in majority in this sample. Both MWCNT and CNFs were relatively thick, ranging 10 nm $\lesssim D_{CNT} \lesssim$ 40 nm in outer diameter, which is in a good agreement with the SEM observations from Fig. 5.30.

Very few nanoclusters were observed during the imaging of CNT samples – this was common for all samples we imaged during our MWCNT study, regardless of the CVD growth conditions or the method of TEM sample preparation. This suggests that there was a relatively strong adhesion of nanocatalysts to the substrate; in addition it also suggests that one dealt with the base growth of CNTs.

In some cases nanocatalyst were observed, but quite often their size was significantly bigger than the initial size of deposited $Ni_{0.85}Cu_{0.15}$ nanoclusters, implying that some aggregation of nanoclusters into bigger clumps had occurred during the CNT growth. Note that even these bigger clumps seem to be catalytically active (as suggested by Fig. 5.31 (b)), since most of them were found at the ends of CNTs.

In the case of our initial samples, some of MWCNTs had a bamboo-like structure, as can be seen in Fig. 5.31 (b). HRTEM images allowed for the walls to be resolved, and the average distance between the walls was found to be $d_{CNT} = 3.3 \pm 0.1$ Å, in very good accordance with the commonly reported value[10] of $d_{CNT} = 3.4$ Å. In addition, HRTEM images showed fringes in the nanocatalysts with a spacing of $d = 2.1 \pm 0.1$ Å that correspond to distances between {1,1,1} planes in FCC Ni or Cu.

The results obtained in the preliminary stage of our study were quite promising – MWCNTs were synthesized using our $Ni_{0.85}Cu_{0.15}$ nanoclusters proving the concept that these alloy nanoclusters can be used as catalyst in CVD growth, which was our primary goal.

Optimization of MWCNT Growth

In the initial attempts the samples for CNT growth had a relatively high nanocluster surface coverage and the CNT growth time was deliberately chosen to be quite long ($t = 1$ hour) to increase the number and size of nanostructures which would make our characterization easier. As it was seen, a dense entangled network of relatively thick CNTs and CNFs was formed allowing for good imaging. However, it is likely that a prolonged period of CVD growth also caused some of MWCNTs to be coated with a-C during the last stages of growth.

In the next step of our study $Ni_{0.85}Cu_{0.15}$ samples of lower surface coverage

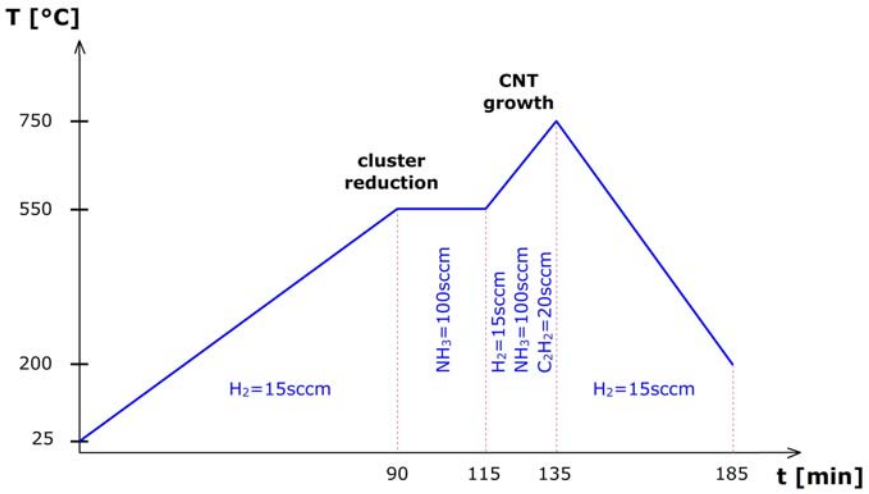

Figure 5.32: CNT growth conditions used in samples 210a and 213a. Credits: J. Ke and V. Golovko, UC

were used to decrease the number of grown nanostructures which would enable for characterization of individual CNTs. Similarly, the growth time was shortened to $t = 20$ minutes (see Fig. 5.32) to decrease the average thickness of the CNTs. In addition, it was presumed that a shorter reduction of clusters at a higher temperature might be advantageous for MWCNT growth.

In order to investigate the influence of cluster size on the CNT growth, two samples of different cluster sizes ($D_1 = 5.7\pm0.8$ nm, $D_2 = 4.0\pm0.2$ nm) were simultaneously exposed to same CVD growth conditions. SEM images of this pair of samples, presented in Fig. 5.33, show that the sample with larger nanoclusters did not yield any CNTs/CNFs (see Fig. 5.33 (a)), whereas the sample with smaller

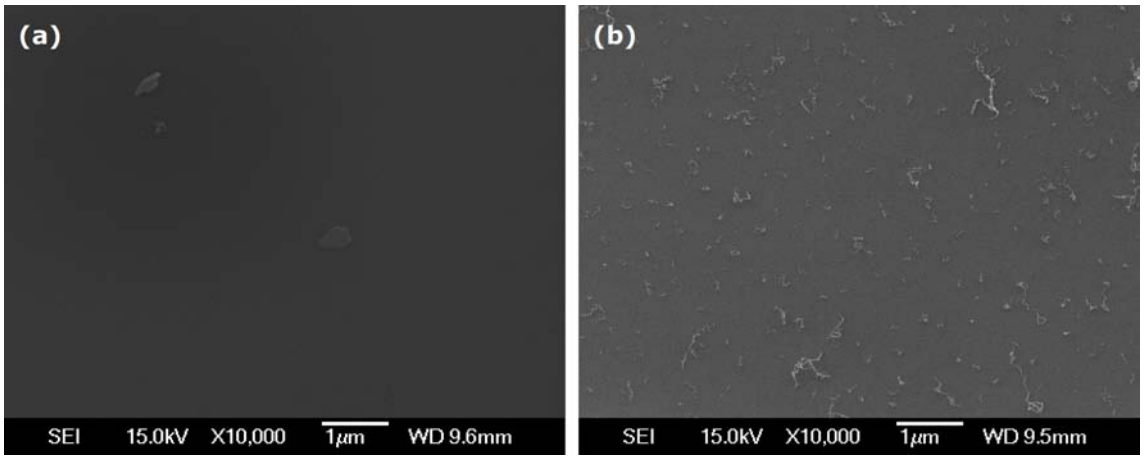

Figure 5.33: SEM images of two $Ni_{0.85}Cu_{0.15}$ samples (210a & 213a) after the CVD synthesis (Fig 5.32): (a) sample that contained $D_1 = 5.7\pm0.8$ nm clusters; (b) sample that contained $D_2 = 4.0\pm0.2$ nm clusters.

nanoclusters contains a large number of tubular-like nano-objects seen all over the surface (see Fig. 5.33 (b)). As expected, their number and length decreased significantly in comparison with the initial samples so that individual structures could be observed in high resolution SEM images. Unfortunately, it was found that no usable TEM specimens could be prepared from such a sample using our methods. Hence, no TEM images of this sample could be obtained to confirm the presence of MWCNTs. However, high resolution SEM images did show tubular-like structures, similar in diameter to the ones from the initial samples, although much shorter.

These results indicate that the nanocluster size played the key role in this experimental run – the sample containing $D_2 = 4.0 \pm 0.2$ nm $Ni_{0.85}Cu_{0.15}$ clusters showed good catalytic activity for CNT/CNF synthesis, whereas the sample with $D_1 = 5.7 \pm 0.8$ nm $Ni_{0.85}Cu_{0.15}$ clusters seemed completely inactive under these experimental conditions.

Next, the influence of temperature on CNT growth was investigated: another pair of $Ni_{0.85}Cu_{0.15}$ samples was used in the CVD synthesis given in Fig. 5.34 which very much resembles the previous one, except that the reduction and CNT growth temperature was raised by 100 °C. The increase in temperature would presumably increase the CNT growth rate so that longer CNTs could be grown, which should enable preparation of TEM specimens using our standard methods. Again, the samples were of two cluster sizes: $D_1 = 5.7 \pm 0.8$ nm and $D_2 = 4.0 \pm 0.2$ nm. Fig. 5.35 shows that the increase in temperature had a detrimental effect on the CNT growth: again, the sample with bigger clusters did not show any activity, while in the sample with smaller clusters tubular-like nano-objects could be seen, although in a considerably

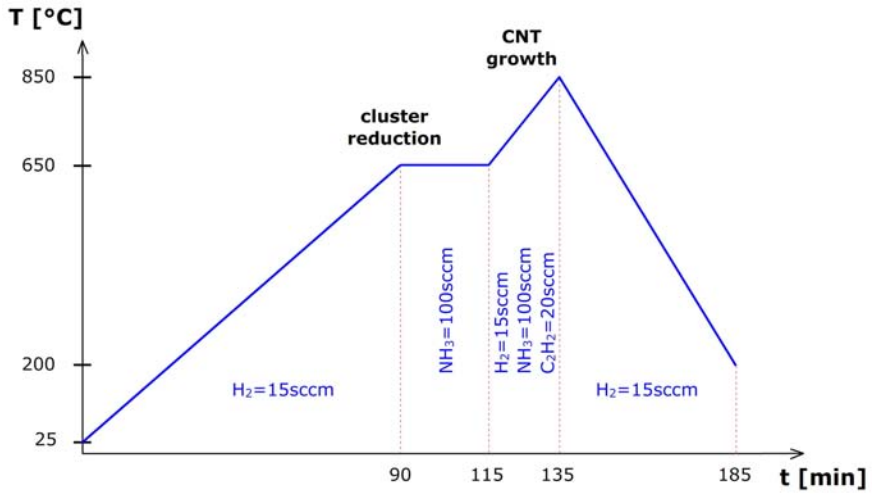

Figure 5.34: CNT growth conditions used in samples 210d and 213d. Credits: J. Ke and V. Golovko, UC

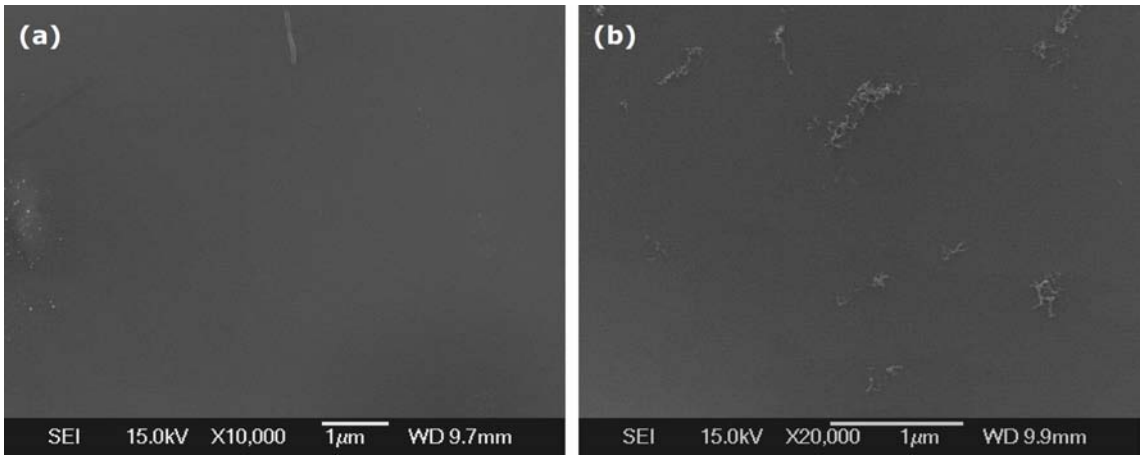

Figure 5.35: SEM images of two $Ni_{0.85}Cu_{0.15}$ samples (210d & 213d) after the CVD synthesis (Fig 5.34): (a) sample that contained $D_1 = 5.7 \pm 0.8$ nm clusters; (b) sample that contained $D_2 = 4.0 \pm 0.2$ nm clusters.

smaller number than in the case of lower temperature (compare to Fig. 5.33). This experiment suggests that the increase of CVD growth temperature above 750 °C yields poor results when 4–6 nm $Ni_{0.85}Cu_{0.15}$ clusters are used as catalysts.

In the next attempt the CNT growth temperature was brought down to 750 °C and the reduction temperature was increased to the same value (see Fig. 5.36). Note also that the reduction time was decreased to 5 minutes. Again, two samples of different nanocluster size were simultaneously subjected to CVD synthesis.

As can be seen in Fig. 5.37, these conditions were favorable for CNT/CNF growth: in both samples tubular-like structures had been grown; interestingly, under those growth conditions the sample with bigger clusters seem to be more catalyti-

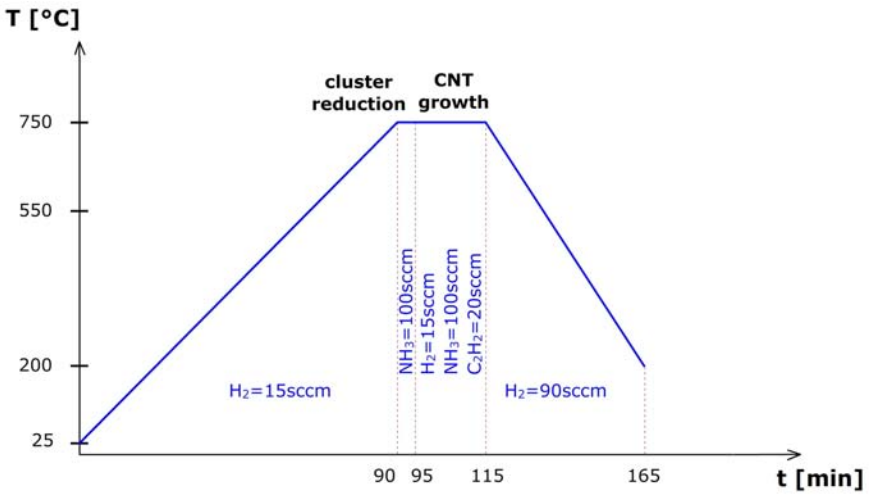

Figure 5.36: CNT growth conditions used in samples 211c and 214c. Credits: J. Ke and V. Golovko, UC

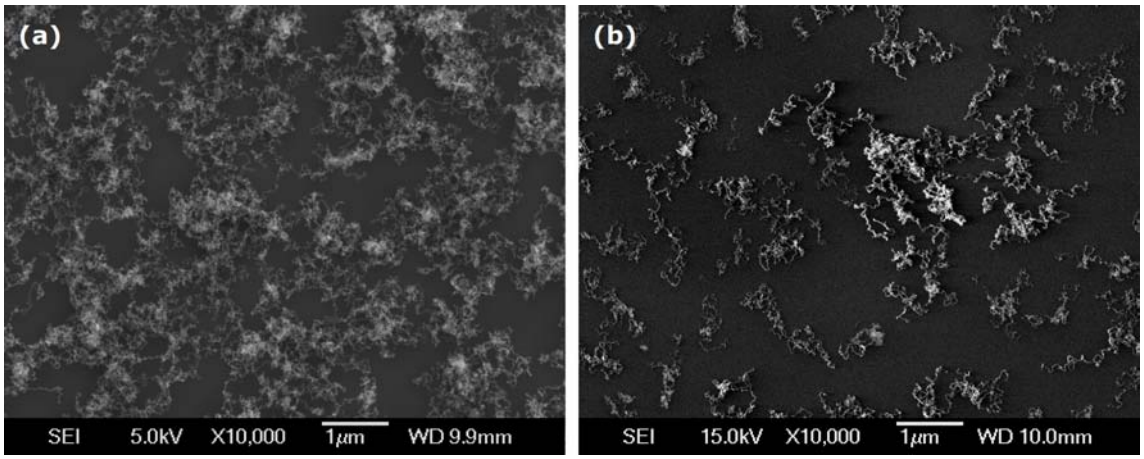

Figure 5.37: SEM images of two $Ni_{0.85}Cu_{0.15}$ samples (211c & 214c) after the CVD synthesis (Fig 5.36): (a) sample that contained $D_1 = 5.7 \pm 0.8$ nm clusters; (b) sample that contained $D_2 = 4.0 \pm 0.2$ nm clusters.

cally active than the sample with smaller clusters. It is possible that the reduction of nanoclusters prior to the CNT growth was not complete when they were reduced at 550 °C or 650 °C for 20 minutes, as in the previous two experiments.

This claim was additionally supported by the results obtained when the reduction and CNT growth temperatures were lowered to 600 °C, as presented in Fig. 5.38. The SEM images showed that no CNTs had grown on the sample that contained bigger clusters (see Fig. 5.39 (a)), while in the sample with smaller clusters sparse features were observed (see Fig. 5.39 (b)) – much less than in the case of 750 °C. Note also that the high resolution SEM image of the sample with bigger clusters showed the presence of clusters with no carbon structures grown on them, indicating

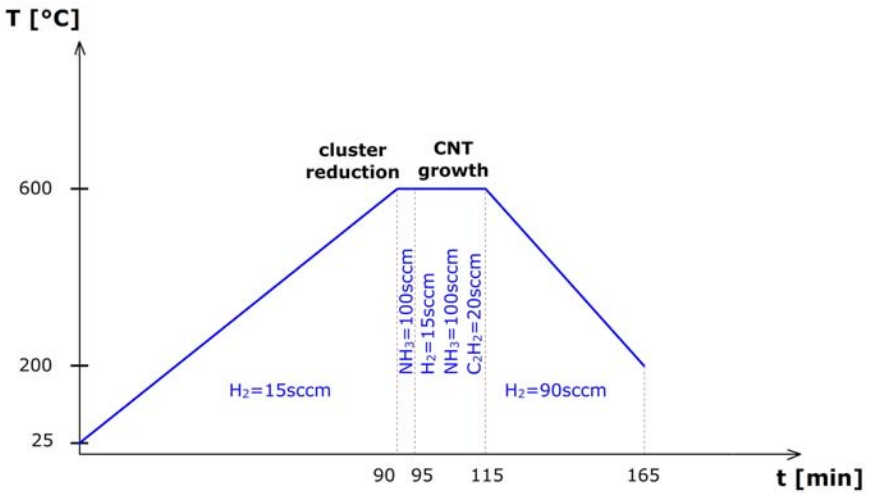

Figure 5.38: CNT growth conditions used in samples 211d and 214d. Credits: J. Ke and V. Golovko, UC

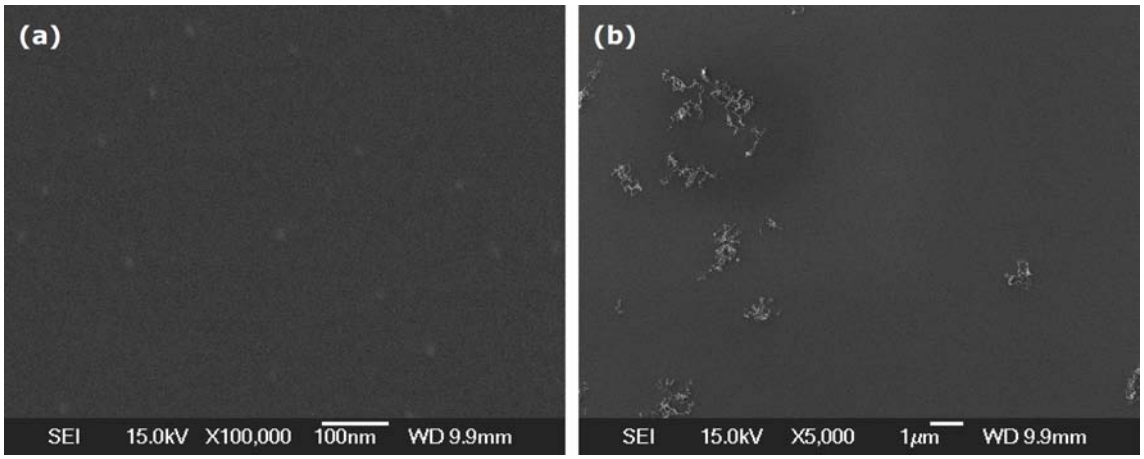

Figure 5.39: SEM images of two $Ni_{0.85}Cu_{0.15}$ samples (211d & 214d) after the CVD synthesis (Fig 5.38): (a) sample that contained $D_1 = 5.7\pm0.8$ nm clusters; (b) sample that contained $D_2 = 4.0\pm0.2$ nm clusters.

that they were catalytically inactive.

So far the results of MWCNT syntheses study have suggested that the optimal temperature for producing a relatively large number of long CNTs/CNFs is 750 °C, for that set of experimental conditions. However, it seems that the reduction step prior to the CNT growth is also an important factor in obtaining a favorable outcome. Hence, the next goal was to optimize the reduction of nanoclusters. For that purpose another reduction step was added: before a 5 minute reduction with NH_3, the clusters were exposed to H atmosphere for 20 minutes (see Fig. 5.40).

The results for this run, presented in Fig. 5.41, show that again a relatively large number of tubular-like structures were grown. The sample that had bigger clusters

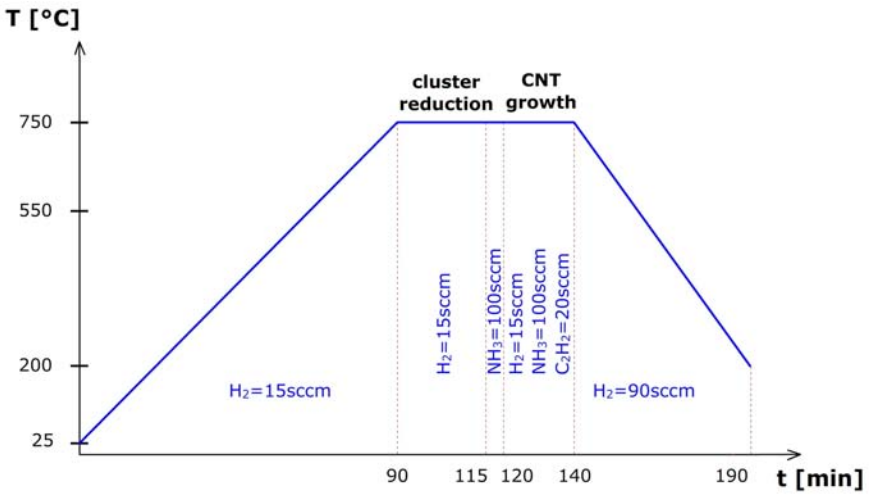

Figure 5.40: CNT growth conditions used in samples 210c and 213c. Credits: J. Ke and V. Golovko, UC

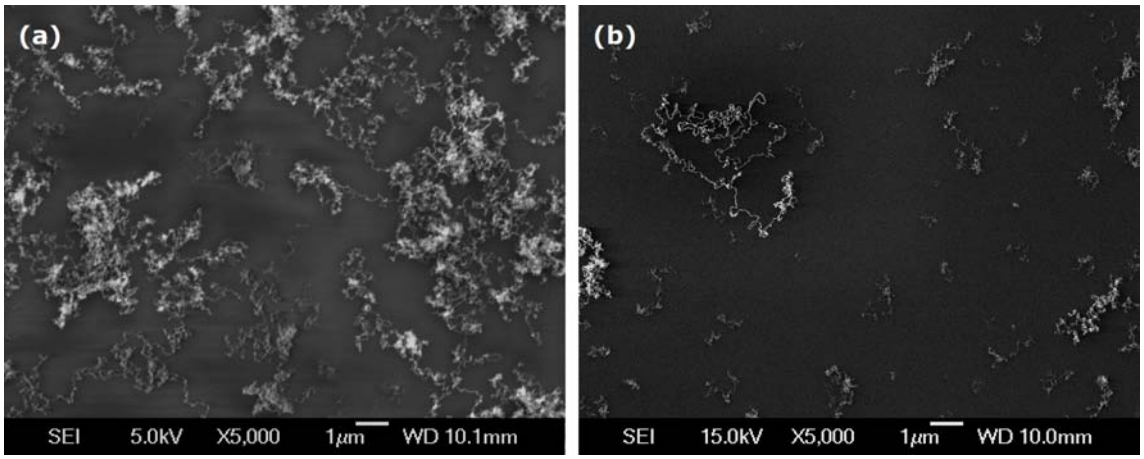

Figure 5.41: SEM images of two $Ni_{0.85}Cu_{0.15}$ samples (210c & 213c) after the CVD synthesis (Fig 5.38): (a) sample that contained $D_1 = 5.7\pm0.8$ nm clusters; (b) sample that contained $D_2 = 4.0\pm0.2$ nm clusters.

yielded better results than the sample with smaller clusters, similar to what was seen for samples 211c and 214c in Fig. 5.37. However, when the surface density of CNTs/CNFs from Fig. 5.41 is compared to those samples, one can see that a longer reduction time had a detrimental effect on the growth. A possible reason is that a prolonged time that the clusters spent at such a high temperature may have caused partial or complete melting of clusters which reduced their size and number.

One can see that in all experiments presented so far relatively low gas flow rates were used. Since the volume of the glass tube used in the experimental set-up (see Fig. 2.25) was ∼1 litre, it is possible that the tube had not been completely flushed from air prior to reduction and CNT growth. This of course means that the efficiency of the cluster reduction might have been seriously affected. It is also possible that the usage of such partially oxidized nanocatalysts will impact the growth of CNTs/CNFs, which may have happened to some extent in all experimental trials so far. For that reason in the next experimental run the tube was firstly flushed from air with a high flow of Ar for half an hour (see Fig. 5.42). In addition, based on observation from the previous run, the temperature of the reduction and CNT growth was lowered to 650 °C.

Fig. 5.43 shows the results of this experimental run, when a sample containing smaller $Ni_{0.85}Cu_{0.15}$ clusters ($D = 4.2\pm0.4$ nm) was used: the CNT/CNF surface density and length were quite similar to the sample with smaller clusters from the previous case (compare to Fig. 5.41 (b)), even though the reduction and CNT growth temperatures were considerably lower here, and more similar to the ones for sample 214d which had less structures grown on it (see Fig. 5.39 (b)). This suggests that the glass tube had not been properly flushed in the previous experiments, which influ-

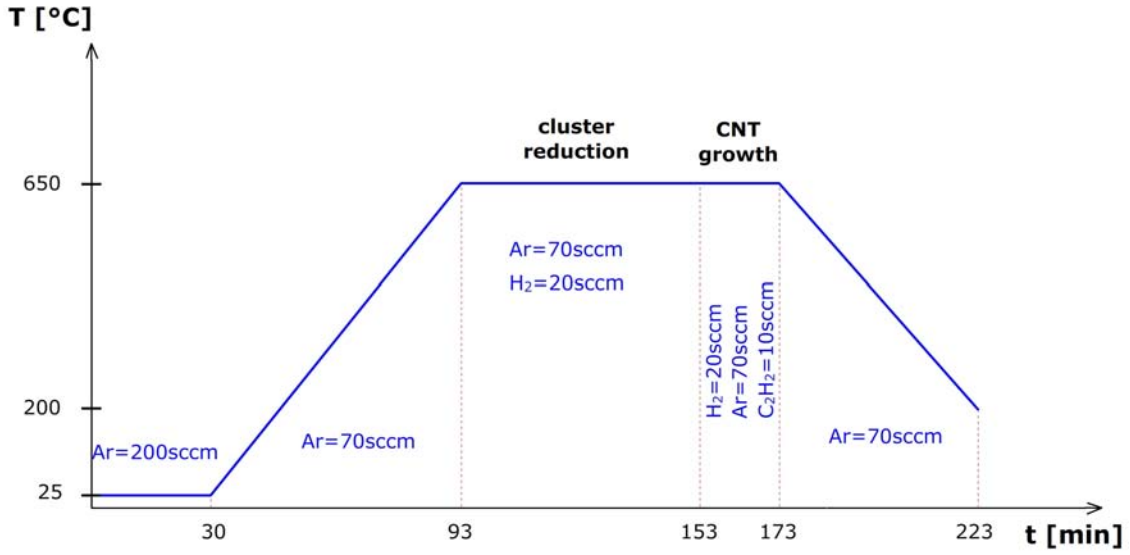

Figure 5.42: CNT growth conditions used in sample 253. Credits: J. Ke and V. Golovko, UC

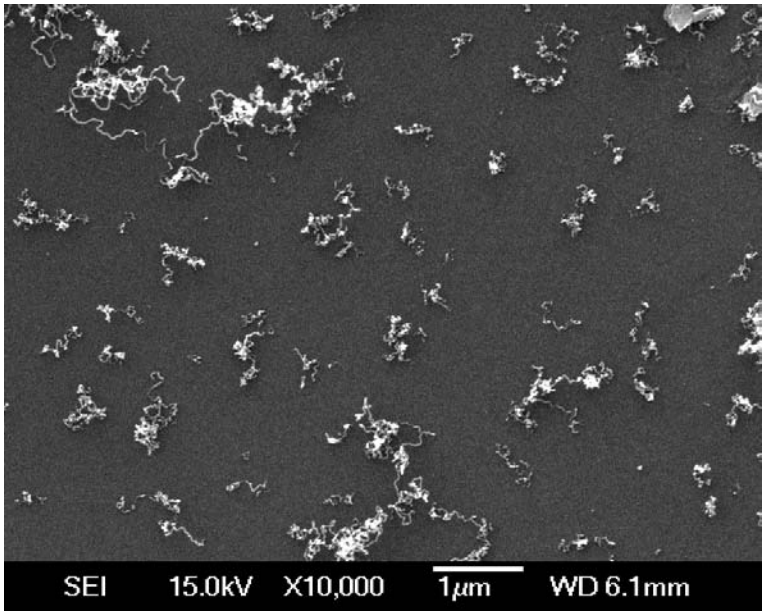

Figure 5.43: SEM image of $Ni_{0.85}Cu_{0.15}$ sample 253 after the CVD synthesis (Fig 5.42). This sample contained $D = 4.2 \pm 0.4$ nm clusters.

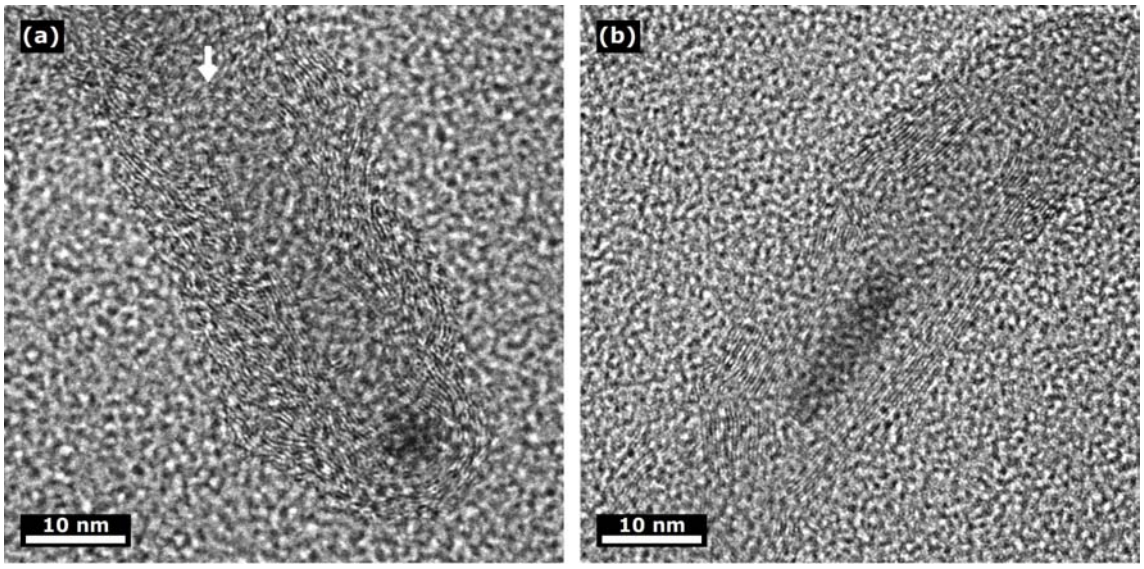

Figure 5.44: HRTEM images of $Ni_{0.85}Cu_{0.15}$ sample 253. (a) MWCNT grown on a cluster of the initial size. Note that the inner 4-5 cylinders of the MWCNT were closed, as pointed by the arrow. (b) MWCNT filled with an elongated nanocatalyst.

enced the degree of nanocluster reduction. Furthermore, this run showed that with the increase in the Ar flow one can obtain good results even for lower temperatures. This consequently means that the possibility of modification of as-deposited clusters (change of their (Ih) structure, partial/complete melting, surface diffusion and agglomeration into bigger clumps) during the reduction stage is lowered, allowing for higher chances of tailoring of CNT properties by the initial cluster characteristics.

With a lot of effort invested we were able to obtain a TEM specimen from this sample, which enabled us to confirm the presence of MWCNTs. Fig. 5.44 shows a couple of HRTEM images of this sample: MWCNTs were relatively thin with the outer diameter in the range 10 nm $\lesssim D_{CNT} \lesssim$ 25 nm. It also appeared that the relative number of CNTs to CNFs had increased, supporting the notion that clusters were well reduced before the CNT growth. Although the number of nanocatalyst observed was again quite low (2-3 per hour of imaging), it seems that their average size was much smaller than for those seen in the sample 193 (see Fig. 5.31).

Finally, in the last CNT growth attempt, experimental conditions were somewhat modified from the previous run in order to test the influence of Ar during the reduction of nanoclusters. Unlike the previous case, this time no Ar was present during much of the reduction stage (see Fig. 5.45). As a consequence, SEM images (see Fig. 5.46) showed that the number of nanostructures was considerably smaller than in the previous case when argon was present during the whole course of nanocluster reduction. Furthermore, it is also visible that the length of the CNTs was shorter in comparison with the previous run.

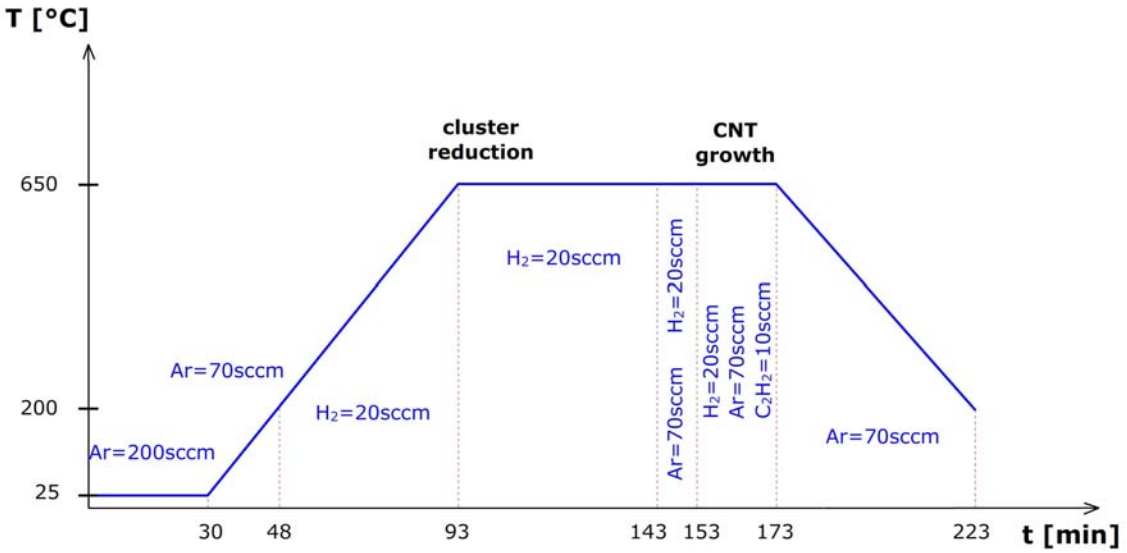

Figure 5.45: CNT growth conditions used in sample 254. Note that no argon was added during much of the reduction stage. Credits: J. Ke and V. Golovko, UC

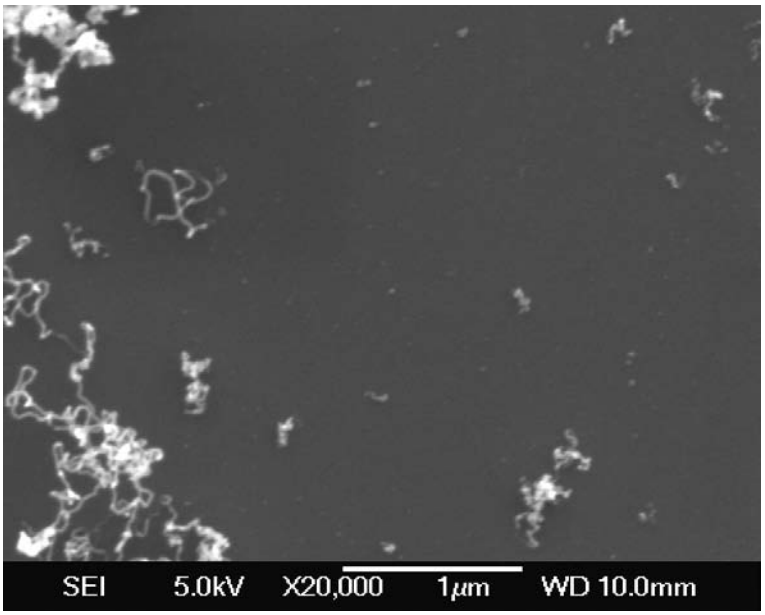

Figure 5.46: SEM image of $Ni_{0.85}Cu_{0.15}$ sample 254 after the CVD synthesis (Fig 5.45). This sample also contained $D = 4.2 \pm 0.4$ nm clusters.

Nevertheless, the sample was good enough to provide a TEM specimen so that HRTEM images could be obtained. As can be seen in Fig. 5.47, MWCNTs were definitely present in the sample; their diameter however varied a lot, in line with the SEM observations of this sample. Again, a small number of MWCNTs contained the nanocatalysts: some of them were many times bigger than the initially deposited clusters, as the one presented in Fig. 5.47 (a), suggesting that cluster aggregation into larger clumps had occurred during the growth. Surprisingly, even such large clumps seemed to have catalyzed MWCNTs – moreover, these MWCNTs appear to contain

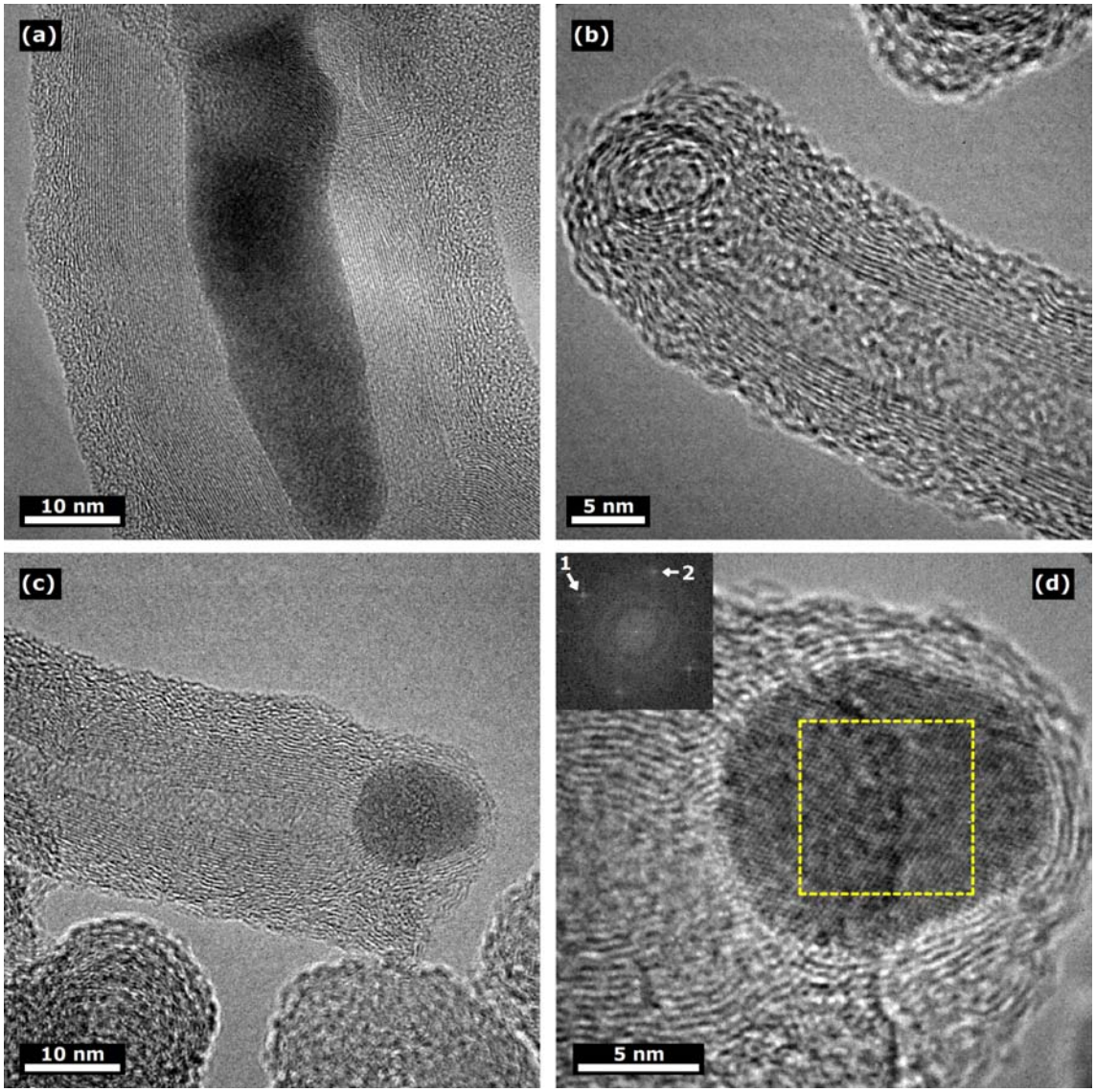

Figure 5.47: HRTEM images of $Ni_{0.85}Cu_{0.15}$ sample 254. (a) MWCNT containing ∼30 well-graphitized walls, filled with a nanocatalyst much larger than the as-deposited clusters. (b) MWCNT with a cavity at the end. MWCNTs like this one were the most numerous. (c) MWCNT containing a nanocatalyst at the end. (d) The same nanocatalyst at high-resolution with FFT of the selected area shown in the inset; spots 1 and 2 correspond to {1,1,1} and {1,-1,1} planes in FCC Ni, with interplanar distances $d = 2.1 \pm 0.1$ Å; measured angle 72±2°, calculated angle 70.5°.

tens of well-graphitized walls. However, a large majority of the MWCNTs observed had an empty cavity at the end, suggesting that the adhesion of the clusters to the substrate was much stronger than their adhesion to the CNT walls: most probably during the preparation of TEM specimens these catalysts remained on the substrate while MWCNTs were transferred onto the TEM grid. This is sound evidence of the base CNT growth.

Still, we were able to find several examples of nanocatalysts sitting at the end (or beginning) of a CNT, just like the one presented in Fig. 5.47 (c) and (d). An analysis of these images revealed that the nanocatalyst structure was consistent with FCC Ni or Cu, suggesting that the nanocatalysts had been fully reduced prior to the CNT growth.

MWCNT Growth – Conclusions

A preliminary experimental study of MWCNT growth using $Ni_{0.85}Cu_{0.15}$ nanoclusters as catalysts was carried out in order to:

(a) Prove the concept of using these alloy clusters as catalysts for MWCNT growth.

(b) Optimize the growth conditions for straightforward production of MWCNTs containing a relatively small number of walls ($N \lesssim 10$), ideally with as few defects as possible.

Initial attempts of MWCNT growth using samples with a relatively high nanocluster surface coverage were quite fruitful: SEM imaging showed that a dense network of entangled, spaghetti-like nano-objects ranging 10 nm $\lesssim D_{CNT} \lesssim$ 40 nm in outer diameter was fabricated on the samples. TEM investigation confirmed the presence of both MWCNTs and CNFs, with the latter being in majority, which proved our concept of utilizing $Ni_{0.85}Cu_{0.15}$ nanoclusters as catalysts in CNT (and CNF) growth.

In the second part of the study, a series of experiments were conducted in order to find the optimal conditions that would increase the number of MWCNTs relative to the number of CNFs. Pairs of samples containing clusters of different sizes ($D_1 = 5.7 \pm 0.8$ nm and $D_2 = 4.0 \pm 0.2$ nm) were simultaneously put in the CVD experimental set-up so that any size dependent behaviour could be observed. In each run a different set of experimental conditions was used; the parameters that were investigated were the reduction and growth temperatures, reduction and growth times, and presence of argon during the reduction.

Although the early attempts suggested that the optimal temperature for CNT growth was 750 °C, the latest experimental results show that a relatively good yield of MWCNTs can be achieved even at the temperature of 650 °C if the glass tube

in which the CVD synthesis takes place is flushed with a high flow of argon. This is an important result since it is known that the $Ni_{0.85}Cu_{0.15}$ nanocluster melting point drops with their size, meaning that smaller clusters might be lost for catalytic purposes. In addition, a lower temperature will decrease the surface diffusion of clusters and their aggregation into larger clumps. Even though these larger aggregates showed some evidence of catalytic activity for MWCNT growth, their properties such as size and shape strongly differ from the initial cluster characteristics. Consequently, if one aims for tailoring of the CNTs properties (such as chirality) by using nanocatalysts of specific characteristics (such as shape), any modification of these should be avoided during the synthesis. In that sense certain progress has been achieved over the course of the investigation and some future work on $Ni_{0.85}Cu_{0.15}$ nanocluster usage in CNT growth might benefit from these findings.

Chapter 6

Conclusion and Outlook

In the final chapter of the thesis we summarize the results of our research which was comprised of four subjects: modeling and experimental work on the cluster motion, Ag-Au nanocluster study, Ni-Cu nanocluster study, and CNT growth experiments. The prospective work in each of these topics is also outlined.

Cluster Velocity Measurements

We performed cluster velocity measurements in our IGA magnetron sputtering deposition system in order to improve the flux of sub-2 nm clusters. The basic idea was that by increasing the cluster velocity one might be able to minimize their lateral deviations and hence enhance the cluster flux in the deposition chamber. The initial modeling of cluster motion, performed by P. Skovorodko, identified the important role of skimmer's geometry on the cluster velocities and trajectories. It suggested that the use of skimmers with wider internal/external angles (30/35°and 40/45°, as opposed to the original 7/30° skimmer) might be beneficial for the flux of sub-2 nm clusters. For that reason a set of new skimmers was designed, machined, and installed in the system to experimentally investigate the impact of skimmer geometry on cluster velocities.

The experimental results showed no significant gains in the cluster velocities compared to the values obtained for the old skimmer. This was attributed to the increased flux of the carrier gas (Ar) through the newly designed wider skimmers that increased the mass selection chamber pressure. The clusters were most probably decelerated by collisions with the background gas particles so that the gain in the cluster flux through the skimmer was offset by the deflection of clusters on their path through the mass selection chamber.

This claim was supported with the experimental results obtained for the wide skimmer with a narrower aperture that reduced the Ar flow into the mass selection

chamber, which kept the background gas pressure low. In that case the cluster velocities were considerably higher than for any other skimmer. However, we observed dispersion of clusters in the skimmer, which most likely caused a loss of the flux of sub-2 nm clusters so that the overall performance of the skimmer was again compromised.

Our investigation identified the mass selection chamber pressure as one of the key factors for deflection of clusters that caused the loss of their flux. Hence, in the next step of the system development one should aim for reducing the mass selection chamber pressure, either by increasing the nozzle-skimmer distance or by installing a turbo pump with a greater pumping rate.

$\mathbf{Ag_{0.85}Au_{0.15}}$ Nanoclusters

The study of $Ag_{0.85}Au_{0.15}$ nanoclusters is the central part of the thesis. $Ag_{0.85}Au_{0.15}$ nanocluster samples of various cluster sizes (3 nm $< D <$10 nm) and surface coverages were produced in the IGA magnetron sputtering system and comprehensively characterized by TEM and STEM.

HRTEM images of fresh samples indicated that $Ag_{0.85}Au_{0.15}$ clusters are fully alloyed; their elemental composition was found to match the starting composition of the sputter target used in the experiment; their structure was found to be size dependent: clusters smaller than 8 nm in diameter were predominantly icosahedral, while those bigger than 8 nm are decahedral. Interestingly, very few single crystal FCC nanoclusters were observed. When compared with previous reports for Ag and Au nanocluster structures, our results indicate that the fresh $Ag_{0.85}Au_{0.15}$ nanocluster might have been kinetically trapped in structures which do not represent the global energy minimum for such systems.

When left to age in air, initially faceted and fully alloyed $Ag_{0.85}Au_{0.15}$ nanoclusters in low coverage samples underwent slow transformation into more spherical core-shell or Janus-like particles. It was found that the cores/heads of such particles were Au-rich, whereas shells/bodies were Ag-rich. It was hypothesized that the absorption of O from air and formation of highly mobile Ag_xO was responsible for the witnessed phenomena.

Similar transition was observed in high coverage samples: initially bigger and uniformly alloyed coalesced islands of nanoclusters transformed into rounder core-shell and Janus particles when left stored in darkness in air, albeit at a much slower transformation rate. It was seen that the fragmentation of these islands started within a week from when they had been exposed to air. On the other hand, the control samples kept in UHV for the same period did not show such behaviour –

their morphology remained the same, indicating that the exposure to atmospheric O triggers the fragmentation. However, in aged samples one can also see evidence of Ag_2S formation, whose role in the morphology change is yet to be investigated.

Therefore, in prospective work one might try storing the samples in various environments (e.g. in dry air, H_2S, ...) in order to clarify the role of various gases on the structural and morphological characteristics of Ag-Au nanoclusters and thin films.

$Ni_{0.85}Cu_{0.15}$ Nanoclusters

We successfully fabricated samples of $Ni_{0.85}Cu_{0.15}$ nanoclusters ranging 4-10 nm in diameter by using our deposition system. The compositional characterization revealed that the average Cu content in the samples matched the Cu content in the sputter target. HRTEM investigation of fresh samples showed the presence of five-fold symmetrical clusters, but single crystal FCC clusters were also observed.

When irradiated with an electron beam, $Ni_{0.85}Cu_{0.15}$ nanoclusters underwent structural and morphological changes producing extremely small nanorods with dimensions <4 nm. The analysis of HRTEM images showed that the crystal structure of such nanorods corresponds to the structure of NiO. Since NiO is deemed to be one of the most promising materials for nanotechnological applications (e.g. in supercapacitors), future work might include more comprehensive studies of NiO nanorods growth over pure Ni nanoclusters deposited on C substrates, that may also allow for electrical characterization aiming for possible applications.

Carbon Nanotubes

In the first instance, we wanted to prove that alloy nanoclusters ($Ni_{0.85}Cu_{0.15}$ in particular) could be used as nanocatalyst in CNT growth. This proof-of-concept study was successful: both SWCNTs and MWCNTs were produced by thermal CVD syntheses using $Ni_{0.85}Cu_{0.15}$ nanocatalysts.

In the next step, the goal was to try to selectively produce SWCNTs of certain chirality or, in the case of MWCNTs, to be able to produce nanotubes of a certain diameter and length. This was to be achieved by experimenting with various parameters used in the CVD growth, such as temperature, atmosphere composition, or growth time. Although some progress has been achieved, there still remain many open questions regarding the optimal experimental conditions, as well as the appropriate $Ni_{0.85}Cu_{0.15}$ nanocluster size and surface coverage for the samples used in these experiments. Nevertheless, future studies of tailored CNT growth using $Ni_{0.85}Cu_{0.15}$ nanoclusters might benefit from the initial findings outlined in this thesis.

Acknowledgements

I am thankful to my supervisor Dr Simon Brown for giving me the opportunity to pursue toward the degree of doctor of natural philosophy on such an exciting and beautiful subject. His guidance throughout these years, academic freedom he provided me with and his high level of tolerance for my Mediterranean temperament are very much appreciated and will not be forgotten. I also appreciate efforts from my co-supervisors Dr Pawel Kowalczyk and Dr Pierre Convers whose assistance with the experiments and discussions of the results were very helpful.

I would like to thank the technical staff at the Department of Physics and Astronomy for their support: Graeme Kershaw and Stephen Hemmingsen from the mechanical workshop who designed and machined the skimmers and other parts of the experimental set-up; Bob Flyngering from the cryogenics laboratory for maintaining the interrupted supply of so much needed liquid nitrogen; Helen Devereux and Gary Turner from the Nanofabrication lab for providing the access to their equipment and chemicals. The experimental work presented in this thesis would not be possible without them.

I am indebted to the people who made it possible for me to become so skilled in electron microscopy: Dr Sujay Prabakar and Dr Richard Tilley from Victoria University of Wellington for introducing me to TEM; Dr Takanori Sato, Dr Milo Kral, and Mike Flaws from the Department of Mechanical Engineering for providing a high-quality TEM and SEM training and access to their electron microscopes. That part of my PhD I enjoyed the most.

I thank people from other institutions worldwide who helped with various parts of my nanocluster research: Dr Petr Skovorodko from the Institute of Thermophysics in Novosibirsk whose extensive work on modeling of clusters motion in the deposition system allowed for further improvements of our research; Dr Ziyou Li and Ruth Chantry from the University of Birmingham for providing high-class STEM data that allowed for better understanding of structures and morphology of Ag-Au nanoclusters; Dr Kirsten Edgar from Victoria University of Wellington for her efforts on CNT syntheses and sample characterization; Dr Christian Dotzler and Dr Michael Toney from Stanford Linear Accelerator, as well as Dr Bridget Ingham from

Industrial Research Ltd in Lower Hutt for the synchrotron characterization of samples; Dr Shaun Hendy's group at IRL for their modeling of alloy nanoclusters that initiated the whole project in the first place.

I enjoyed collaborating with Jin Ke and Dr Vladimir Golovko from the Department of Chemistry on the CNT growth experiments - thank you guys.

Thanks to the past and present members of the nanocluster group: Dr David McCarthy, Tom Watson, Emily Dahlberg, Sven Dönges, Dr David Mackenzie for proofreading the thesis and being a man of his word; Dr Abdul Sattar, Ojas Mahapatra, Jack Grigg, Rick Montgomery, Dr Nadia Grillet, Dr Shawn Fostner, Dr Haifeng Ma, and Amol Nande. Thank you all for making this journey more pleasurable with all the laughs.

I owe my gratitude to Kate Ferguson for the positive influence she had on my PhD and life in New Zealand.

Lastly, special thanks to my family and friends from Croatia for their continuous support throughout my life.

Bibliography

1. Buffat, P. and Borel, J. P. *Physical Review A* **13**, 2287 (1976).
2. Ino, S. *Journal of the Physical Society of Japan* **21**, 346 (1966).
3. Ino, S. and Ogawa, S. *Journal of the Physical Society of Japan* **22**, 1365 (1967).
4. Marks, L. D. and Howie, A. *Nature* **282**, 196 (1979).
5. Ajayan, P. M. and Marks, L. D. *Physical Review Letters* **60**, 585 (1988).
6. Ajayan, P. M. and Marks, L. D. *Physical Review Letters* **63**, 279 (1989).
7. Doye, J. P. K. and Calvo, F. *Physical Review Letters* **86**, 3570 (2001).
8. Loiseau, A. *Understanding Carbon Nanotubes: From Basics to Applications.* Springer, Berlin, (2006).
9. Martin, D. A. *Trends in Nanotubes Research.* Nova Science Publishers, New York, (2006).
10. Harris, P. J. F. *Carbon Nanotubes and Related Structures: New Materials for the Twenty-first Century.* Cambridge University Press, Cambridge, UK, (1999).
11. Dresselhaus, M. S., Dresselhaus, G., and Saito, R. *Solid State Communications* **84**, 201 (1992).
12. Yazyev, O. V. and Pasquarello, A. *Physica Status Solidi (b)* **245**, 2185 (2008).
13. Bardotti, L., Tournus, F., eacute, linon, P., Pellarin, M., and Broyer, M. *Physical Review B* **83**, 035425 (2011).
14. Wanner, M., Werner, R., and Gerthsen, D. *Surface Science* **600**, 632 (2006).
15. Popescu, R., Schneider, R., Gerthsen, D., Bttcher, A., Lffler, D., Weis, P., and Kappes, M. M. *Surface Science* **603**, 3119 (2009).

16. Werner, R., Wanner, M., Schneider, G., and Gerthsen, D. *Physical Review B* **72**, 045426 (2005).

17. Lifshitz, I. M. and Slyozov, V. V. *Journal of Physics and Chemistry of Solids* **19**, 35 (1961).

18. Wagner, C. Z. *Zeitschrift fur Elektrochemie* **65**, 581 (1961).

19. Nichols, F. A. and Mullins, W. W. *Transactions of AIME* **233**, 1840 (1965).

20. Karim, S., Toimil-Molares, M. E., Balogh, A. G., Ensinger, W., Cornelius, T. W., Khan, E. U., and Neumann, R. *Nanotechnology* **17**, 5954 (2006).

21. Reichel, R., Partridge, J. G., Dunbar, A. D. F., Brown, S. A., Caughley, O., and Ayesh, A. *Journal of Nanoparticle Research* **8**, 405 (2006).

22. Reichel, R., Partridge, J. G., Natali, F., Matthewson, T., Brown, S. A., Lassesson, A., Mackenzie, D. M. A., Ayesh, A. I., Tee, K. C., Awasthi, A., and Hendy, S. C. *Applied Physics Letters* **89**, 213105 (2006).

23. Ayesh, A. I., Lassesson, A., Brown, S. A., Dunbar, A. D. F., Kaufmann, M., Partridge, J. G., Reichel, R., and van Lith, J. *Review of Scientific Instruments* **78**, 053906 (2007).

24. Partridge, J. G., Reichel, R., Ayesh, A., Mackenzie, D. M. A., and Brown, S. A. *Physica Status Solidi (a)* **203**, 1217 (2006).

25. Tee, K. C. *Cluster Devices - Interconnects for Nanotechnology.* PhD thesis, University of Canterbury, (2008).

26. Ayesh, A. I., Brown, S. A., Awasthi, A., Hendy, S. C., Convers, P. Y., and Nichol, K. *Physical Review B* **81**, 195422 (2010).

27. Sattar, A. *Electrical Characterization of Cluster Devices.* PhD thesis, University of Canterbury, (2012).

28. Ayesh, A. *Device Fabrication Using Bi Nanoclusters.* PhD thesis, University of Canterbury, (2007).

29. Reichel, R. *Nano Scale Cluster Devices.* PhD thesis, University of Canterbury, (2007).

30. Issendorff, B. v. and Palmer, R. E. *Review of Scientific Instruments* **70**, 4497 (1999).

31. Watson, T. F., Belić, D., Convers, P. Y., Boyd, E. J., and Brown, S. A. *The European Physical Journal D - Atomic, Molecular, Optical and Plasma Physics* **61**, 81 (2011).

32. Watson, T. F. Master's thesis, University of Canterbury, (2009).

33. Gelatt, C. D., J., Ehrenreich, H., and Watson, R. E. *Physical Review B* **15**(4), 1613 (1977).

34. Qi, W. H., Wang, M. P., and Xu, G. Y. *Chemical Physics Letters* **372**, 632 (2003).

35. Attarian Shandiz, M., Safaei, A., Sanjabi, S., and Barber, Z. H. *Solid State Communications* **145**, 432 (2008).

36. Vanithakumari, S. C. and Nanda, K. K. *Physics Letters A* **372**, 6930 (2008).

37. Wang, H. and Ren, Z. F. *Nanotechnology* **22**, 405601 (2011).

38. Behr, M. J., Gaulding, E. A., Mkhoyan, K. A., and Aydil, E. S. *Journal of Applied Physics* **108**, 053303 (2010).

39. Behr, M. J., Mkhoyan, K. A., and Aydil, E. S. *ACS Nano* **4**, 5087 (2010).

40. Berenguer, A., Cantoro, M., Golovko, V. B., Hofmann, S., Wirth, C. T., Johnson, B. F. G., and Robertson, J. *Physica Status Solidi (b)* **246**, 2436 (2009).

41. Chiang, W.-H. and Sankaran, R. M. *Advanced Materials* **20**, 4857 (2008).

42. Srivastava, S., Vankar, V., Kumar, V., and Singh, V. *Nanoscale Research Letters* **3**, 205 (2008).

43. Ducati, C., Alexandrou, I., Chhowalla, M., Robertson, J., and Amaratunga, G. A. J. *Journal of Applied Physics* **95**, 6387 (2004).

44. Hofmann, S., Ducati, C., Robertson, J., and Kleinsorge, B. *Applied Physics Letters* **83**, 135 (2003).

45. Chhowalla, M., Teo, K. B. K., Ducati, C., Rupesinghe, N. L., Amaratunga, G. A. J., Ferrari, A. C., Roy, D., Robertson, J., and Milne, W. I. *Journal of Applied Physics* **90**, 5308 (2001).

46. Aksak, M. and Selamet, Y. *Applied Physics A: Materials Science and Processing* **100**, 213 (2010).

47. Siegal, M. P., Overmyer, D. L., Provencio, P. P., and Tallant, D. R. *The Journal of Physical Chemistry C* **114**, 14864 (2010).

48. Kobayashi, K., Kitaura, R., Kumai, Y., Goto, Y., Imagaki, S., and Shinohara, H. *Carbon* **47**, 722 (2009).

49. Mudimela, P. R., Nasibulin, A. G., Jiang, H., Susi, T., Chassaing, D., and Kauppinen, E. I. *The Journal of Physical Chemistry C* **113**, 2212 (2009).

50. Qi, X., Deng, Y., Zhong, W., Yang, Y., Qin, C., Au, C., and Du, Y. *The Journal of Physical Chemistry C* **114**, 808 (2009).

51. Zhang, C., Pisana, S., Wirth, C. T., Parvez, A., Ducati, C., Hofmann, S., and Robertson, J. *Diamond and Related Materials* **17**, 1447 (2008).

52. Bhaviripudi, S., Mile, E., Steiner, S. A., Zare, A. T., Dresselhaus, M. S., Belcher, A. M., and Kong, J. *Journal of the American Chemical Society* **129**, 15167 (2007).

53. Moshkalev, S. A. and Verissimo, C. *Journal of Applied Physics* **102**, 044303 (2007).

54. Porro, S., Musso, S., Giorcelli, M., Chiodoni, A., and Tagliaferro, A. *Physica E: Low-dimensional Systems and Nanostructures* **37**, 16 (2007).

55. Yao, Y., Li, Q., Zhang, J., Liu, R., Jiao, L., Zhu, Y. T., and Liu, Z. *Nature Materials* **6**, 283 (2007).

56. Kaatz, F. H., Siegal, M. P., Overmyer, D. L., Provencio, P. P., and Tallant, D. R. *Applied Physics Letters* **89**, 241915 (2006).

57. Lolli, G., Zhang, L., Balzano, L., Sakulchaicharoen, N., Tan, Y., and Resasco, D. E. *The Journal of Physical Chemistry B* **110**, 2108 (2006).

58. Kaatz, F. H., Siegal, M. P., Overmyer, D. L., Provencio, P. P., and Jackson, J. L. *Materials Science and Engineering: C* **23**, 141 (2003).

59. Ducati, C., Alexandrou, I., Chhowalla, M., Amaratunga, G. A. J., and Robertson, J. *Journal of Applied Physics* **92**, 3299 (2002).

60. Lee, Y. T., Park, J., Choi, Y. S., Ryu, H., and Lee, H. J. *The Journal of Physical Chemistry B* **106**, 7614 (2002).

61. Siegal, M. P., Overmyer, D. L., and Provencio, P. P. *Applied Physics Letters* **80**, 2171 (2002).

62. Harutyunyan, A. R., Chen, G., Paronyan, T. M., Pigos, E. M., Kuznetsov, O. A., Hewaparakrama, K., Kim, S. M., Zakharov, D., Stach, E. A., and Sumanasekera, G. U. *Science* **326**, 116 (2009).

63. Khavrus, V. O., Ibrahim, E. M. M., Leonhardt, A., Hampel, S., Oswald, S., Taschner, C., and Buchner, B. *The Journal of Physical Chemistry C* **114**, 843 (2009).

64. Kasumov, Y. A., Shailos, A., Khodos, I. I., Volkov, V. T., Levashov, V. I., Matveev, V. N., Guron, S., Kobylko, M., Kociak, M., Bouchiat, H., Agache, V., Rollier, A. S., Buchaillot, L., Bonnot, A. M., and Kasumov, A. Y. *Applied Physics A: Materials Science and Processing* **88**, 687 (2007).

65. Mizuno, K., Hata, K., Saito, T., Ohshima, S., Yumura, M., and Iijima, S. *The Journal of Physical Chemistry B* **109**, 2632 (2005).

66. Siegal, M. P., Overmyer, D. L., and Kaatz, F. H. *Applied Physics Letters* **84**, 5156 (2004).

67. Hofmann, S., Sharma, R., Ducati, C., Du, G., Mattevi, C., Cepek, C., Cantoro, M., Pisana, S., Parvez, A., Cervantes-Sodi, F., Ferrari, A. C., Dunin-Borkowski, R., Lizzit, S., Petaccia, L., Goldoni, A., and Robertson, J. *Nano Letters* **7**, 602 (2007).

68. Hernadi, K., Knya, Z., Siska, A., Kiss, J., Oszk, A., Nagy, J. B., and Kiricsi, I. *Materials Chemistry and Physics* **77**, 536 (2003).

69. O'Byrne, J. P., Li, Z., Tobin, J. M., Larsson, J. A., Larsson, P., Ahuja, R., and Holmes, J. D. *The Journal of Physical Chemistry C* **114**, 8115 (2010).

70. Santiago, E., Whelan, C. M., and Maex, K. *Nanotechnology* **18**, 015602 (2007).

71. Liao, X. Z., Serquis, A., Jia, Q. X., Peterson, D. E., Zhu, Y. T., and Xu, H. F. *Applied Physics Letters* **82**, 2694 (2003).

72. Wright, A. C., Xiong, Y., Maung, N., Eichhorn, S. J., and Young, R. J. *Materials Science and Engineering: C* **23**, 279 (2003).

73. Edgeworth, J. P. and et al. *Nanotechnology* **21**, 105605 (2010).

74. Homma, Y., Liu, H., Takagi, D., and Kobayashi, Y. *Nano Research* **2**, 793 (2009).

75. Liu, B., Ren, W., Liu, C., Sun, C.-H., Gao, L., Li, S., Jiang, C., and Cheng, H.-M. *ACS Nano* **3**, 3421 (2009).

76. Marchand, M., Journet, C., Guillot, D., Benoit, J.-M., Yakobson, B. I., and Purcell, S. T. *Nano Letters* **9**, 2961 (2009).

77. Marcus, M. S., Simmons, J. M., Baker, S. E., Hamers, R. J., and Eriksson, M. A. *Nano Letters* **9**, 1806 (2009).

78. Nie, J., Qian, W., Zhang, Q., Wen, Q., and Wei, F. *The Journal of Physical Chemistry C* **113**, 20178 (2009).

79. Ding, L., Yuan, D., and Liu, J. *Journal of the American Chemical Society* **130**, 5428 (2008).

80. Kang, J. L., Li, J. J., Du, X. W., Shi, C. S., Zhao, N. Q., Cui, L., and Nash, P. *Journal of Alloys and Compounds* **456**, 290 (2008).

81. Li, H., Zhao, N., He, C., Shi, C., Du, X., and Li, J. *Journal of Alloys and Compounds* **465**, 51 (2008).

82. Li, H., Zhao, N., He, C., Shi, C., Du, X., Li, J., and Cui, Q. *Materials Science and Engineering: A* **476**, 230 (2008).

83. Puretzky, A. A. and et al. *Nanotechnology* **19**, 055605 (2008).

84. Verissimo, C., Gobbi, A. L., and Moshkalev, S. A. *Applied Surface Science* **254**, 3890 (2008).

85. Yoshida, H., Takeda, S., Uchiyama, T., Kohno, H., and Homma, Y. *Nano Letters* **8**, 2082 (2008).

86. Lin, M., Tan, J. P. Y., Boothroyd, C., Loh, K. P., Tok, E. S., and Foo, Y.-L. *Nano Letters* **7**, 2234 (2007).

87. Reina, A., Hofmann, M., Zhu, D., and Kong, J. *The Journal of Physical Chemistry C* **111**, 7292 (2007).

88. Thiruvengadachari, B. and Ajmera, P. K. *Materials Letters* **61**, 4301 (2007).

89. Lin, M., Ying Tan, J. P., Boothroyd, C., Loh, K. P., Tok, E. S., and Foo, Y.-L. *Nano Letters* **6**, 449 (2006).

90. Takagi, D., Homma, Y., Suzuki, S., and Kobayashi, Y. *Surface and Interface Analysis* **38**, 1743 (2006).

91. Huh, Y., Green, M. L. H., and Jin Lee, C. *Diamond and Related Materials* **15**, 239 (2005).

92. Hata, K., Futaba, D. N., Mizuno, K., Namai, T., Yumura, M., and Iijima, S. *Science* **306**, 1362 (2004).

93. Cumings, J., Mickelson, W., and Zettl, A. *Solid State Communications* **126**, 359 (2003).

94. Zhang, R. Y., Amlani, I., Baker, J., Tresek, J., Tsui, R. K., and Fejes, P. *Nano Letters* **3**, 731 (2003).

95. Harris, P. J. *Carbon Nanotube Science: Synthesis, Properties and Applications*. Cambridge University Press, New York, (2009).

96. Ke, J. *Design and Fabrication of the Catalysts Systems for the Control of Sintering of Metal Nanoparticles During the Growth of Carbon Nanotubes*. PhD thesis, University of Canterbury, (2012).

97. Goldstein, J. *Scanning Electron Microscopy and X-Ray Microanalysis*. Springer, New York, (2003).

98. Zhou, W. and Wang, Z. L. *Scanning Microscopy for Nanotechnology: Techniques and Applications*. Springer, New York, (2006).

99. Williams, D. B. and Carter, C. B. *Transmission Electron Microscopy: A Textbook for Materials Science*. Springer, New York, (2009).

100. Haider, M., Rose, H., Uhlemann, S., Schwan, E., Kabius, B., and Urban, K. *Ultramicroscopy* **75**, 53 (1998).

101. Smith, D. J. *Microscopy and Microanalysis* **14**, 2 (2008).

102. Pennycook, S. J., Chisholm, M. F., Lupini, A. R., Varela, M., Borisevich, A. Y., Oxley, M. P., Luo, W. D., van Benthem, K., Oh, S.-H., Sales, D. L., Molina, S. I., Garcia-Barriocanal, J., Leon, C., Santamaria, J., Rashkeev, S. N., and Pantelides, S. T. *Philosophical Transactions of the Royal Society A: Mathematical, Physical and Engineering Sciences* **367**, 3709 (2009).

103. Pennycook, S. J. and Varela, M. *Journal of Electron Microscopy* **60**, S213 (2011).

104. Muller, D. A. *Nature Materials* **8**, 263 (2009).

105. http://rsbweb.nih.gov/ij (link valid in Feb. 2012.).

106. http://www.gatan.com/software/ (link valid in Feb. 2012.).

107. Partridge, J., Brown, S. A., Dunbar, A., Reichel, R., Kaufmann, M., Siegert, C., Scott, S., and Blaikie, R. J. *Nanotechnology* **15**, 1382 (2004).

108. Schmelzer, J., Brown, S. A., Wurl, A., Hyslop, M., and Blaikie, R. J. *Physical Review Letters* **88**, 226802 (2002).

109. Awasthi, A., Hendy, S. C., Zoontjens, P., Brown, S. A., and Natali, F. *Physical Review B* **76**, 115437 (2007).

110. Awasthi, A., Hendy, S. C., Zoontjens, P., and Brown, S. A. *Physical Review Letters* **97**, 186103 (2006).

111. Jensen, P. *Reviews of Modern Physics* **71**, 1695 (1999).

112. Yamada, I. *Materials Science and Engineering A* **217-218**, 82 (1996).

113. Insepov, Z. and Yamada, I. *Materials Science and Engineering A* **217-218**, 89 (1996).

114. Haberland, H., Insepov, Z., and Moseler, M. *Physical Review B* **51**, 11061 (1995).

115. Yamada, I. and Takaoka, G. H. *Japanese Journal of Applied Physics* **32**, 2121 (1993).

116. Wegner, K., Piseri, P., Tafreshi, H. V., and Milani, P. *Journal of Physics D: Applied Physics* **39**, R439 (2006).

117. Wang, X. and McMurry, P. H. *Aerosol Science and Technology* **40**, 320 (2006).

118. Wang, X., Kruis, F. E., and McMurry, P. H. *Aerosol Science and Technology* **39**, 611 (2005).

119. Piseri, P., Tafreshi, H. V., and Milani, P. *Current Opinion in Solid State and Materials Science* **8**, 195 (2004).

120. Piseri, P., Podesta, A., Barborini, E., and Milani, P. *Review of Scientific Instruments* **72**, 2261 (2001).

121. Fonzo, F. D., Gidwani, A., Fan, M. H., Neumann, D., Iordanoglou, D. I., Heberlein, J. V. R., McMurry, P. H., Girshick, S. L., Tymiak, N., Gerberich, W. W., and Rao, N. P. *Applied Physics Letters* **77**, 910 (2000).

122. Liu, P., Ziemann, P. J., Kittelson, D. B., and McMurry, P. H. *Aerosol Science and Technology* **22**, 314 (1995).

123. Broc, A., De Benedictis, S., Dilecce, G., Vigliotti, M., Sharafutdinov, R. G., and Skovorodko, P. A. *Journal of Fluid Mechanics* **500**, 211 (2004).

124. Bird, G. A. *Molecular Gas Dynamics and the Direct Simulation of Gas Flows*. Clarendon Press, Oxford, (1994).

125. Vollath, D. and Fischer, F. D. *Progress in Materials Science* **56**, 1030 (2011).

126. Baletto, F. and Ferrando, R. *Reviews of Modern Physics* **77**, 371 (2005).

127. Halas, N. J. *Nano Letters* **10**, 3816 (2010).

128. Noguez, C. and Garzon, I. L. *Chemical Society Reviews* **38**, 757 (2009).

129. Li, Y., Liu, Q., and Shen, W. *Dalton Transactions* **40**, 5811 (2011).

130. Barnard, A. S. *Reports on Progress in Physics* **73**, 086502 (2010).

131. Seyed-Razavi, A., Snook, I. K., and Barnard, A. S. *Journal of Materials Chemistry* **20**, 416 (2010).

132. Finney, E. E. and Finke, R. G. *Journal of Colloid and Interface Science* **317**, 351 (2008).

133. Ferrando, R., Jellinek, J., and Johnston, R. L. *Chemical Reviews* **108**, 845 (2008).

134. Jellinek, J. *Faraday Discussions* **138**, 11 (2008).

135. Wang, R., Dmitrieva, O., Farle, M., Dumpich, G., Acet, M., Mejia-Rosales, S., Perez-Tijerina, E., Yacaman, M. J., and Kisielowski, C. *The Journal of Physical Chemistry C* **113**, 4395 (2009).

136. Jiang, H.-L., Akita, T., Ishida, T., Haruta, M., and Xu, Q. *Journal of the American Chemical Society* **133**, 1304 (2011).

137. Ashcroft, N. and Mermin, N. *Solid State Physics*. Holt, Rinehart and Winstonl, New York, (1976).

138. Hansen, M. and Anderko, K. *Constitution of Binary Alloys*. McGraw-Hill, New York, (1958).

139. Park, J. and Lee, J. *Calphad* **32**, 135 (2008).

140. Chen, F. and Johnston, R. L. *Applied Physics Letters* **92**, 023112 (2008).

141. Chen, F. and Johnston, R. L. *Acta Materialia* **56**, 2374 (2008).

142. Chen, F. Y. and Johnston, R. L. *Applied Physics Letters* **90**, 153123 (2007).

143. Chen, Curley, B. C., Rossi, G., and Johnston, R. L. *The Journal of Physical Chemistry C* **111**, 9157 (2007).

144. Chen, F. and Johnston, R. L. *ACS Nano* **2**, 165 (2007).

145. Qi, W. H. and Lee, S. T. *The Journal of Physical Chemistry C* **114**, 9580 (2010).

146. Rossi, G., Ferrando, R., Rapallo, A., Fortunelli, A., Curley, B. C., Lloyd, L. D., and Johnston, R. L. *The Journal of Chemical Physics* **122**, 194309 (2005).

147. Ringe, E., Van Duyne, R. P., and Marks, L. D. *Nano Letters* **11**, 3399 (2011).

148. Negreiros, F. R., Soares, E. A., de Carvalho, V. E., and Bozzolo, G. *Physical Review B* **76**, 245432 (2007).

149. Michaelian, K. and Garzon, I. L. *The European Physical Journal D - Atomic, Molecular, Optical and Plasma Physics* **34**, 183 (2005).

150. Popolan, D. M., No, Mitric, R., Bernhardt, T. M., and Bonacic-Koutecky, V. *Physical Chemistry Chemical Physics* **12**, 7865 (2010).

151. Kim, H. Y., Kim, D. H., Ryu, J. H., and Lee, H. M. *The Journal of Physical Chemistry C* **113**, 15559 (2009).

152. Mottet, C., Rossi, G., Baletto, F., and Ferrando, R. *Physical Review Letters* **95**, 035501 (2005).

153. Chen, D.-H. and Chen, C.-J. *Journal of Materials Chemistry* **12**, 1557 (2002).

154. Devarajan, S., Bera, P., and Sampath, S. *Journal of Colloid and Interface Science* **290**, 117 (2005).

155. Douglas, F., Yanez, R., Ros, J., Marin, S., de la Escosura-Muniz, A., Alegret, S., and Merkoi, A. *Journal of Nanoparticle Research* **10**, 97 (2008).

156. Eccles, J. W. L., Bangert, U., Bromfield, M., Christian, P., and Harvey, A. J. *Journal of Applied Physics* **107**, 104325 (2010).

157. Gong, X., Yang, Y., and Huang, S. *The Journal of Physical Chemistry C* **114**, 18073 (2010).

158. Kahraman, M., Aydn, O., and Culha, M. *Plasmonics* **4**, 293 (2009).

159. Link, S., Wang, Z. L., and El-Sayed, M. A. *The Journal of Physical Chemistry B* **103**, 3529 (1999).

160. Liu, S., Chen, G., Prasad, P. N., and Swihart, M. T. *Chemistry of Materials* **23**, 4098 (2011).

161. Mallin, M. P. and Murphy, C. J. *Nano Letters* **2**, 1235 (2002).

162. Ramos, M. *Journal of Nanomaterials* **2011**, 374096 (2011).

163. Raveendran, P., Fu, J., and Wallen, S. L. *Green Chemistry* **8**, 34 (2006).

164. Wang, A.-Q., Chang, C.-M., and Mou, C.-Y. *The Journal of Physical Chemistry B* **109**, 18860 (2005).

165. Longo, A., Pepe, G. P., Carotenuto, G., Ruotolo, A., Nicola, S. D., Belotelov, V. I., and Zvezdin, A. K. *Nanotechnology* **18**, 365701 (2007).

166. Pande, S., Ghosh, S. K., Praharaj, S., Panigrahi, S., Basu, S., Jana, S., Pal, A., Tsukuda, T., and Pal, T. *The Journal of Physical Chemistry C* **111**, 10806 (2007).

167. Shang, L., Jin, L., Guo, S., Zhai, J., and Dong, S. *Langmuir* **26**, 6713 (2009).

168. Zhang, Q., Xie, J., Liang, J., and Lee, J. Y. *Advanced Functional Materials* **19**, 1387 (2009).

169. Rodriguez-Gonzalez, B., Sanchez-Iglesias, A., Giersig, M., and Liz-Marzan, L. M. *Faraday Discussions* **125**, 133 (2004).

170. Tokonami, S., Morita, N., Takasaki, K., and Toshima, N. *The Journal of Physical Chemistry C* **114**, 10336 (2010).

171. Chen, H. M., Liu, R. S., Jang, L. Y., Lee, J. F., and Hu, S. F. *Chemical Physics Letters* **421**, 118 (2006).

172. Srnova-Sloufova, I., Vlckova, B., Bastl, Z., and Hasslett, T. L. *Langmuir* **20**, 3407 (2004).

173. Srnova-Sloufova, I., Lednicky, F., Gemperle, A., and Gemperlova, J. *Langmuir* **16**, 9928 (2000).

174. Kim, K., Kim, K. L., Choi, J.-Y., Lee, H. B., and Shin, K. S. *The Journal of Physical Chemistry C* **114**, 3448 (2010).

175. Pena, O., Pal, U., Rodriguez-Fernaandez, L., Silva-Pereyra, H. G., Rodriguez-Iglesias, V., Cheang-Wong, J. C., Arenas-Alatorre, J., and Oliver, A. *The Journal of Physical Chemistry C* **113**, 2296 (2009).

176. Norris, C. B., Joseph, P. R., Mackiewicz, M. R., and Reed, S. M. *Chemistry of Materials* **22**, 3637 (2010).

177. Rodriguez-Gonzalez, B., Burrows, A., Watanabe, M., Kiely, C. J., and Liz Marzan, L. M. *Journal of Materials Chemistry* **15**, 1755 (2005).

178. Li, Z. Y., Yuan, J., Chen, Y., Palmer, R. E., and Wilcoxon, J. P. *Applied Physics Letters* **87**, 243103 (2005).

179. Gonzalez, C. M., Liu, Y., and Scaiano, J. C. *The Journal of Physical Chemistry C* **113**, 11861 (2009).

180. Hodak, J. H., Henglein, A., Giersig, M., and Hartland, G. V. *The Journal of Physical Chemistry B* **104**, 11708 (2000).

181. Shore, M. S., Wang, J., Johnston-Peck, A. C., Oldenburg, A. L., and Tracy, J. B. *Small* **7**, 230 (2011).

182. Wang, C., Peng, S., Chan, R., and Sun, S. *Small* **5**, 567 (2009).

183. Shibata, T., Bunker, B. A., Zhang, Z., Meisel, D., Vardeman, C. F., and Gezelter, J. D. *Journal of the American Chemical Society* **124**, 11989 (2002).

184. Cottancin, E., Lerme, J., Gaudry, M., Pellarin, M., Vialle, J. L., Broyer, M., Prevel, B., Treilleux, M., and Melinon, P. *Physical Review B* **62**, 5179 (2000).

185. Gaudry, M., Lerme, J., Cottancin, E., Pellarin, M., Prevel, B., Treilleux, M., Melinon, P., Rousset, J. L., and Broyer, M. *The European Physical Journal D - Atomic, Molecular, Optical and Plasma Physics* **16**, 201 (2001).

186. Lidgi-Guigui, N., Mulheran, P., and Palmer, R. E. *Applied Physics Letters* **93**, 123107 (2008).

187. Okazaki, K.-I., Kiyama, T., Hirahara, K., Tanaka, N., Kuwabata, S., and Torimoto, T. *Chemical Communications* (6), 691 (2008).

188. Peng, D. L., Hihara, T., and Sumiyama, K. *Applied Physics Letters* **83**, 350 (2003).

189. Perez-Tijerina, E., Pinilla, M. G., Mejia-Rosales, S., Ortiz-Mendez, U., Torres, A., and Jose-Yacaman, M. *Faraday Discussions* **138**, 353 (2008).

190. Mayoral, A., Mejia-Rosales, S., Mariscal, M. M., Perez-Tijerina, E., and Jose-Yacaman, M. *Nanoscale* **2**, 2647 (2010).

191. Govindaraju, K., Basha, S., Kumar, V., and Singaravelu, G. *Journal of Materials Science* **43**, 5115 (2008).

192. Wang, A.-Q., Liu, J.-H., Lin, S. D., Lin, T.-S., and Mou, C.-Y. *Journal of Catalysis* **233**, 186 (2005).

193. Wang, A.-Q., Hsieh, Y.-P., Chen, Y.-F., and Mou, C.-Y. *Journal of Catalysis* **237**, 197 (2006).

194. Jose-Yacaman, M. and Miki-Yoshida, M. *Physical Review B* **46**, 1198 (1992).

195. Jose-Yacaman, M., Gutierrez-Wing, C., Miki, M., Yang, D. Q., Piyakis, K. N., and Sacher, E. *The Journal of Physical Chemistry B* **109**, 9703 (2005).

196. Lai, X., P. St.Clair, T., and Wayne Goodman, D. *Faraday Discussions* **114**, 279 (1999).

197. Layson, A. R., Evans, J. W., Fournee, V., and Thiel, P. A. *The Journal of Chemical Physics* **118**, 6467 (2003).

198. Layson, A. R., Evans, J. W., and Thiel, P. A. *Physical Review B* **65**, 193409 (2002).

199. Layson, A. R. and Thiel, P. A. *Surface Science* **472**, L151–L156 (2001).

200. Lando, A., Kebaili, N., Cahuzac, P., Colliex, C., Couillard, M., Masson, A., Schmidt, M., and Brechignac, C. *The European Physical Journal D - Atomic, Molecular, Optical and Plasma Physics* **43**, 151 (2007).

201. Lando, A., Kebaili, N., Cahuzac, P., Masson, A., and Brechignac, C. *Physical Review Letters* **97**, 133402 (2006).

202. Brechignac, C., Cahuzac, P., Carlier, F., Colliex, C., Leroux, J., Masson, A., Yoon, B., and Landman, U. *Physical Review Letters* **88**, 196103 (2002).

203. Kebaili, N., Benrezzak, S., Cahuzac, P., Masson, A., and Brechignac, C. *The European Physical Journal D - Atomic, Molecular, Optical and Plasma Physics* **52**, 115 (2009).

204. Peng, H.-I., Krauss, T. D., and Miller, B. L. *Analytical Chemistry* **82**, 8664 (2010).

205. Li, J., Lin, Y., and Zhao, B. *Journal of Nanoparticle Research* **4**, 345 (2002).

206. Magdassi, S., Grouchko, M., Berezin, O., and Kamyshny, A. *ACS Nano* **4**, 1943 (2010).

207. Flueli, M., Spycher, R., Stadelmann, P., Buffat, P., and Borel, J.-P. *Europhysics Letters* **6**, 349 (1988).

208. Kirkland, A. I., Jefferson, D. A., Tang, D., and Edwards, P. P. *Proceedings of the Royal Society of London. Series A: Mathematical and Physical Sciences* **434**, 279 (1991).

209. Buffat, P.-A., Flueli, M., Spycher, R., Stadelmann, P., and Borel, J.-P. *Faraday Discussions* **92**, 173 (1991).

210. Marks, L. D. *Reports on Progress in Physics* **57**, 603 (1994).

211. Ascencio, J. A., Gutierrez-Wing, C., Espinosa, M. E., Marin, M., Tehuacanero, S., Zorrilla, C., and Jose-Yacaman, M. *Surface Science* **396**, 349 (1998).

212. Yacaman, M. J., Ascencio, J. A., Liu, H. B., and Gardea-Torresdey, J. *Journal of Vacuum Science and Technology B: Microelectronics and Nanometer Structures* **19**, 1091 (2001).

213. Flores, A. B., Robles, L. A., Arias, M. O., and Ascencio, J. A. *Micron* **34**, 109 (2003).

214. Buffat, P. A. *Philosophical Transactions of the Royal Society of London. Series A: Mathematical, Physical and Engineering Sciences* **361**, 291 (2003).

215. Reyes-Gasga, J., Tehuacanero-Nuez, S., Montejano-Carrizales, J., Gao, X., and Jose-Yacaman, M. *Topics in Catalysis* **46**, 23 (2007).

216. Koga, K. and Sugawara, K. *Surface Science* **529**, 23 (2003).

217. Li, Z. Y., Wilcoxon, J. P., Yin, F., Chen, Y., Palmer, R. E., and Johnston, R. L. *Faraday Discussions* **138**, 363 (2008).

218. Reinhard, D., Hall, B. D., Ugarte, D., and Monot, R. *Physical Review B* **55**, 7868 (1997).

219. Li, Z. Y., Young, N. P., Di Vece, M., Palomba, S., Palmer, R. E., Bleloch, A. L., Curley, B. C., Johnston, R. L., Jiang, J., and Yuan, J. *Nature* **451**, 46 (2008).

220. Koga, K., Ikeshoji, T., and Sugawara, K. *Physical Review Letters* **92**, 115507 (2004).

221. Tjeng, L. H., Meinders, M. B. J., van Elp, J., Ghijsen, J., Sawatzky, G. A., and Johnson, R. L. *Physical Review B* **41**, 3190 (1990).

222. Ascencio, J. A., Mendoza, M., Santamaria, T., Perez, M., Nava, I., Gutierrez-Wing, C., and Jose-Yacaman, M. *Journal of Cluster Science* **13**, 189 (2002).

223. Elechiguerra, J. L., Larios-Lopez, L., Liu, C., Garcia-Gutierrez, D., Camacho-Bragado, A., and Yacaman, M. J. *Chemistry of Materials* **17**, 6042 (2005).

224. Assal, J., Hallstedt, B., and Gauckler, L. J. *Journal of the American Ceramic Society* **80**, 3054 (1997).

225. Rayleigh, L. *Proceedings of the London Mathematical Society* **s1-10**, 4 (1878).

226. Karim, S., Toimil-Molares, M. E., Ensinger, W., Balogh, A. G., Cornelius, T. W., Khan, E. U., and Neumann, R. *Journal of Physics D: Applied Physics* **40**, 3767 (2007).

227. Molares, M. E. T., Balogh, A. G., Cornelius, T. W., Neumann, R., and Trautmann, C. *Applied Physics Letters* **85**, 5337 (2004).

228. Frueh, A. J. *Zeitschrift fur Kristallographie* **110**, 136 (1958).

229. Ng, Y. S., Tsong, T. T., and McLane, S. B. *Physical Review Letters* **42**, 588 (1979).

230. Good, B., Bozzolo, G., and Ferrante, J. *Physical Review B* **48**, 18284 (1993).

231. Ouannasser, S., Wille, L. T., Dreyss, eacute, and H. *Physical Review B* **55**, 14245 (1997).

232. Montejano-Carrizales, J. M., Iiguez, M. P., and Alonso, J. A. *Physical Review B* **49**, 16649 (1994).

233. Zhu, L. and DePristo, A. *The Journal of Chemical Physics* **102**, 5342 (1995).

234. Mainardi, D. S. and Balbuena, P. B. *International Journal of Quantum Chemistry* **85**, 580 (2001).

235. Hristova, E., Dong, Y., Grigoryan, V. G., and Springborg, M. *The Journal of Physical Chemistry A* **112**, 7905 (2008).

236. Cui-Ju, F., Yong-Hong, X., Xiao-Yan, Z., and Xiao-Chun, Z. *Chinese Physics B* **18**(4), 1436 (2009).

237. Huang, S.-P. and Balbuena, P. B. *The Journal of Physical Chemistry B* **106**, 7225 (2002).

238. Li, G., Wang, Q., Liu, T., Wang, K., and He, J. *Journal of Cluster Science* **21**, 45 (2010).

239. Shirinyan, A., Wautelet, M., and Belogorodsky, Y. *Journal of Physics: Condensed Matter* , 2537 (2006).

240. van Ingen, R., Fastenau, R., and Mittemeijer, E. *Journal of Applied Physics* **76**, 1871 (1994).

241. Pabi, S. K., Joardar, J., Manna, I., and Murty, B. S. *Nanostructured Materials* **9**, 149 (1997).

242. Cattaruzza, E., Battaglin, G., Polloni, R., Cesca, T., Gonella, F., Mattei, G., Maurizio, C., Mazzoldi, P., D'Acapito, F., Zontone, F., and Bertoncello, R. *Nuclear Instruments and Methods in Physics Research Section B: Beam Interactions with Materials and Atoms* **148**, 1007 (1999).

243. Damle, C. and Sastry, M. *Journal of Materials Chemistry* **12**, 1860 (2002).

244. Zhang, Y., Huang, W., Habas, S. E., Kuhn, J. N., Grass, M. E., Yamada, Y., Yang, P., and Somorjai, G. A. *The Journal of Physical Chemistry C* **112**, 12092 (2008).

245. Yamauchi, T., Tsukahara, Y., Sakata, T., Mori, H., Yanagida, T., Kawai, T., and Wada, Y. *Nanoscale* **2**, 515 (2010).

246. Zhou, Y. Z., Chen, J. S., Tay, B. K., Hu, J. F., Chow, G. M., Liu, T., and Yang, P. *Applied Physics Letters* **90**, 043111 (2007).

247. D'Addato, S., Gragnaniello, L., Valeri, S., Rota, A., di Bona, A., Spizzo, F., Panozaqi, T., and Schifano, S. F. *Journal of Applied Physics* **107**, 104318 (2010).

248. D'Addato, S., Grillo, V., Altieri, S., Frabboni, S., Rossi, F., and Valeri, S. *The Journal of Physical Chemistry C* **115**, 14044 (2011).

249. D'Addato, S., Grillo, V., Altieri, S., Tondi, R., Valeri, S., and Frabboni, S. *Journal of Physics: Condensed Matter* **23**, 175003 (2011).

250. Gracia-Pinilla, M., Martinez, E., Vidaurri, G., and Perez-Tijerina, E. *Nanoscale Research Letters* **5**, 180 (2010).

251. Scott, S. A. *Self-Assembly of Sb and Bi Nanostructures on Graphite*. PhD thesis, University of Canterbury, (2005).

252. Scott, S. A., Kral, M. V., and Brown, S. A. *Physical Review B* **72**, 205423 (2005).

253. Scott, S. A., Kral, M. V., and Brown, S. A. *Physical Review B* **73**, 205424 (2006).

254. Lou, W., Wang, X., Chen, M., Liu, W., and Hao, J. *Nanotechnology* **19**, 225607 (2008).

255. Zhang, Q., Xie, J., Yang, J., and Lee, J. Y. *ACS Nano* **3**, 139 (2008).

256. Li, Z. Y., Yuan, J., Chen, Y., Palmer, R. E., and Wilcoxon, J. P. *Advanced Materials* **17**, 2885 (2005).

257. Swami, A., Selvakannan, P. R., Pasricha, R., and Sastry, M. *The Journal of Physical Chemistry B* **108**, 19269 (2004).

258. Liz-Marzan, L. M. and Mulvaney, P. *The Journal of Physical Chemistry B* **107**, 7312 (2003).

259. Radushkevich, L. V. and Lukyanovich, V. M. *Soviet Journal of Physical Chemistry* **26**, 88 (1952).

260. Abrahamson, J., Wiles, P., and Rhoades, B. *Carbon* **37**, 1873 (1999).

261. Iijima, S. *Nature* **354**, 56 (1991).

262. Dresselhaus, M. S. *ACS Nano* **4**, 4344 (2010).

263. Sharma, R., Chee, S.-W., Herzing, A., Miranda, R., and Rez, P. *Nano Letters* **11**, 2464 (2011).

264. Banhart, F. *Nanoscale* **1**, 201 (2009).

265. Chiang, W.-H. and Mohan Sankaran, R. *Nature Materials* **8**, 882 (2009).

266. Hofmann, S., Blume, R., Wirth, C. T., Cantoro, M., Sharma, R., Ducati, C., Havecker, M., Zafeiratos, S., Schnoerch, P., Oestereich, A., Teschner, D., Albrecht, M., Knop-Gericke, A., Schlogl, R., and Robertson, J. *The Journal of Physical Chemistry C* **113**, 1648 (2009).

267. Wang, B., Yang, Y., Li, L.-J., and Chen, Y. *Journal of Materials Science* **44**, 3285 (2009).

268. Bodwell, G. J. *Nature Nanotechnology* **5**, 103 (2010).

269. Jasti, R. and Bertozzi, C. R. *Chemical Physics Letters* **494**, 1 (2010).

270. Nessim, G. D. *Nanoscale* **2**, 1306 (2010).

271. Marquardt, C. W., Grunder, S., Blaszczyk, A., Dehm, S., Hennrich, F., Lohneysen, H. v., Mayor, M., and Krupke, R. *Nature Nanotechnology* **5**, 863 (2010).

272. Chang, C. W., Okawa, D., Garcia, H., Majumdar, A., and Zettl, A. *Physical Review Letters* **99**, 045901 (2007).

273. Zhou, X., Park, J.-Y., Huang, S., Liu, J., and McEuen, P. L. *Physical Review Letters* **95**, 146805 (2005).

274. Yu, M.-F., Lourie, O., Dyer, M. J., Moloni, K., Kelly, T. F., and Ruoff, R. S. *Science* **287**, 637 (2000).

275. Kasumov, A. Y., Deblock, R., Kociak, M., Reulet, B., Bouchiat, H., Khodos, I. I., Gorbatov, Y. B., Volkov, V. T., Journet, C., and Burghard, M. *Science* **284**, 1508 (1999).

276. Kolpak, A. M. and Grossman, J. C. *Nano Letters* **11**, 3156 (2011).

277. Zhao, Y., Wei, J., Vajtai, R., Ajayan, P. M., and Barrera, E. V. *Scientific Reports* **1**, 1 (2011).

278. Dillon, A. C. *Chemical Reviews* **110**, 6856 (2010).

279. Herrmann, L. G., Portier, F., Roche, P., Yeyati, A. L., Kontos, T., and Strunk, C. *Physical Review Letters* **104**, 026801 (2010).

280. Hu, L., Hecht, D. S., and Gruner, G. *Chemical Reviews* **110**, 5790 (2010).

281. Lee, S. W., Yabuuchi, N., Gallant, B. M., Chen, S., Kim, B.-S., Hammond, P. T., and Shao-Horn, Y. *Nature Nanotechnology* **5**, 531 (2010).

282. Schriver, M., Regan, W., Loster, M., and Zettl, A. *Solid State Communications* **150**, 561 (2010).

283. Tang, D.-M., Yin, L.-C., Li, F., Liu, C., Yu, W.-J., Hou, P.-X., Wu, B., Lee, Y.-H., Ma, X.-L., and Cheng, H.-M. *Proceedings of the National Academy of Sciences* **107**, 9055 (2010).

284. Choi, D., Choi, M.-Y., Shin, H.-J., Yoon, S.-M., Seo, J.-S., Choi, J.-Y., Lee, S. Y., Kim, J. M., and Kim, S.-W. *The Journal of Physical Chemistry C* **114**, 1379 (2009).

285. Graham, A. P., Duesberg, G. S., Hoenlein, W., Kreupl, F., Liebau, M., Martin, R., Rajasekharan, B., Pamler, W., Seidel, R., Steinhoegl, W., and Unger, E. *Applied Physics A: Materials Science and Processing* **80**, 1141 (2005).

286. Novoselov, K. S., Geim, A. K., Morozov, S. V., Jiang, D., Zhang, Y., Dubonos, S. V., Grigorieva, I. V., and Firsov, A. A. *Science* **306**, 666 (2004).

287. Novoselov, K. S., Jiang, D., Schedin, F., Booth, T. J., Khotkevich, V. V., Morozov, S. V., and Geim, A. K. *Proceedings of the National Academy of Sciences of the United States of America* **102**, 10451 (2005).

288. Chen, J.-H., Li, L., Cullen, W. G., Williams, E. D., and Fuhrer, M. S. *Nature Physics* **7**, 535 (2011).

289. Koenig, S. P., Boddeti, N. G., Dunn, M. L., and Bunch, J. S. *Nature Nanotechnology* **advance online publication** (2011).

290. Waldmann, D., Jobst, J., Speck, F., Seyller, T., Krieger, M., and Weber, H. B. *Nature Materials* **advance online publication** (2011).

291. Soldano, C., Mahmood, A., and Dujardin, E. *Carbon* **48**, 2127 (2010).

292. Geim, A. K. and Novoselov, K. S. *Nature Materials* **6**, 183 (2007).

293. LeMieux, M. C., Roberts, M., Barman, S., Jin, Y. W., Kim, J. M., and Bao, Z. *Science* **321**, 101 (2008).

294. Abdi, Y., Mohajerzadeh, S., and Ezatollah, A. *Journal of Nanoparticle Research* **12**, 521 (2010).

295. Amara, H., Roussel, J. M., Bichara, C., Gaspard, J. P., and Ducastelle, F. *Physical Review B* **79**, 014109 (2009).

296. Amara, H., Bichara, C., and Ducastelle, F. *Physical Review Letters* **100** (2008).

297. Amara, H., Bichara, C., and Ducastelle, F. *Physical Review B* **73**, 113404 (2006).

298. Bolton, K., Brjesson, A., Zhu, W., Amara, H., and Bichara, C. *Nano Research* **2**, 774 (2009).

299. Shin, Y.-H. and Hong, S. *Applied Physics Letters* **92**, 043103 (2008).

300. Lyalin, A., Hussien, A., Solovyov, A. V., and Greiner, W. *Physical Review B* **79**, 165403 (2009).

301. Banerjee, S., Naha, S., and Puri, I. K. *Applied Physics Letters* **92**, 233121 (2008).

302. Burgos, J. C., Reyna, H., Yakobson, B. I., and Balbuena, P. B. *The Journal of Physical Chemistry C* **114**, 6952 (2010).

303. Larsson, P., Larsson, J. A., Ahuja, R., Ding, F., Yakobson, B. I., Duan, H., Ros, eacute, n, A., and Bolton, K. *Physical Review B* **75**, 115419 (2007).

304. Jian-Tao, W., Chen, C., Ohno, K., Wang, E., Chen, X.-L., Wang, D.-S., Mizuseki, H., and Kawazoe, Y. *Nanotechnology* **21**, 115602 (2010).

305. Yazyev, O. V. and Pasquarello, A. *Physical Review Letters* **100**, 156102 (2008).

306. Dumlich, H. and Reich, S. *Physical Review B* **82**, 085421 (2010).

307. Reich, S., Li, L., and Robertson, J. *Physica Status Solidi (b)* **243**, 3494 (2006).

308. Reich, S., Li, L., and Robertson, J. *Physical Review B* **72**, 165423 (2005).

309. Gomez-Gualdron, D. A., Zhao, J., and Balbuena, P. B. *Journal of Chemical Physics* **134**, 014705 (2011).

310. Terrado, E., Tacchini, I., Benito, A. M., Maser, W. K., and Martnez, M. T. *Carbon* **47**, 1989 (2009).

311. Gonzalez, I., De Jesus, J. C., de Navarro, C. U., and Garcia, M. *Catalysis Today* **149**, 352 (2010).

312. Chiang, W.-H. and Sankaran, R. M. *Diamond and Related Materials* **18**, 946 (2009).

313. Zhang, R. Y., Wei, Y., Nagahara, L. A., Amlani, I., and Tsui, R. K. *Nanotechnology* **17**, 272 (2006).

314. Homma, Y., Suzuki, S., Kobayashi, Y., Nagase, M., and Takagi, D. *Applied Physics Letters* **84**, 1750 (2004).

315. Dresselhaus, M. S., Jorio, A., Souza Filho, A. G., and Saito, R. *Philosophical Transactions of the Royal Society A: Mathematical, Physical and Engineering Sciences* **368**, 5355 (2010).

316. Dresselhaus, M. S., Dresselhaus, G., Jorio, A., Souza Filho, A. G., and Saito, R. *Carbon* **40**, 2043 (2002).

317. Paillet, M., Michel, T., Meyer, J. C., Popov, V. N., Henrard, L., Roth, S., and Sauvajol, J. L. *Physical Review Letters* **96**, 257401 (2006).

318. Meyer, J. C., Paillet, M., Michel, T., Morac, A., Neumann, A., Duesberg, G. S., Roth, S., and Sauvajol, J.-L. *Physical Review Letters* **95**, 217401 (2005).

319. Jorio, A., Pimenta, M. A., Souza Filho, A. G., Samsonidze, G. G., Swan, A. K., nl, M. S., Goldberg, B. B., Saito, R., Dresselhaus, G., and Dresselhaus, M. S. *Physical Review Letters* **90**, 107403 (2003).